Evaluation of sheet pile behavior based on Eemdijk monitoring data

F.L.E. Meijer

TU Delft

Witteveen + Bos

Evaluation of sheet pile behavior based on Eemdijk monitoring data

by

F.L.E. Meijer

to obtain the degree of Master of Science
at the Delft University of Technology,
to be defended publicly on Wednesday February 13, 2019 at 01:00 PM.

Student number:	4034708	
Project duration:	May 1, 2018 – February 5, 2019	
Thesis committee:	Prof. dr. ir. M. Kok,	TU Delft, supervisor
	Ir. H.J. Lengkeek,	Witteveen+Bos
	Dr. ir. D.J. Peters,	TU Delft
	Dr. M. Korff,	TU Delft

An electronic version of this thesis is available at `http://repository.tudelft.nl/`.

TU Delft Delft University of Technology

Witteveen+Bos

Preface

Full-scale tests as big as the Eemdijk test are very rare and I am delighted that I have had the chance to carry out this research. It has been a challenging and informative journey, which would not have been possible without help.

First, I want to thank my committee members. I am very grateful to my supervisor at Witteveen+Bos, Arny Lengkeek. I am thankful for his support, guidance and for giving me the opportunity to carry out this research. Always enthusiastic when I had a question or presented new results.

I wish to thank Dirk Jan Peters for his extensive feedback and critical view, which has elevated the quality of the report.

I gratefully thank my graduation professor Matthijs Kok for the interesting discussions during committee meetings.

I wish to express my gratitude to Mandy Korff for her course about deep excavations, which got me interested in sheet piling.

Furthermore, I want to thank Apostolos Bougioukos for his extensive help in setting up the finite element models.

I would like to thank my colleagues of the geotechnical and structural group of Witteveen+Bos in Rotterdam for the interesting discussions.

Finally, I would like to thank my beloved better half for listening to my thesis related problems for 9 months.

Contents

Symbols

A	cross-sectional area
E	Young's modulus (steel: $E = 2.1 \times 10^5 N/mm^2$)
F	force
F_c	critical buckling load
I	moment of inertia
I_{yy}	moment of inertia around x-axis
M	bending moment
M_e	elastic bending moment resistance
M_p	plastic bending moment resistance
M_r	resisting bending moment
M_s	driving bending moment
M_u	ultimate bending moment resistance
M_s	bending moment around x-axis
P	probability
T	temperature
EI	bending stiffness
a	distance between support and load introduction
b	width
b	flange width
f_u	ultimate strength
f_y	yield strength
h	height
h	step-size
l	length
t	time
t_f	flange thickness
u	horizontal displacement
u_y	displacement in y-direction
α	shape factor
ϵ	strain
ϵ_r	strain at the onset of strain hardening
ϵ_s	strain at the onset of strain-hardening
ϵ_u	ultimate strain
ϵ_y	yield strain
θ	angle
κ	curvature
κ_x	curvature in x direction
κ_y	curvature in y direction
$\mu\epsilon$	micro-strain
σ	normal stress
ϕ	rotation angle
$\mathcal{O}$	order of approximation

Abstract

From the 3500 kilometers of primary flood defenses in the Netherlands, a third does not comply with the current standards. As a result, over 700 kilometers will be strengthened in the upcoming years. Traditional strengthening of dikes consists of strengthening with soil and requires space that is often not available. Further strengthening of dikes, therefore, requires smart solutions, which increase the strength, without changing the dikes cross-sectional area.

One of these solutions is the use of sheet pile walls as stability screens. However, in contradiction to all commonly used design codes, including the Eurocode, the current design approach for stability screens in dikes does not allow for plastic calculation. Furthermore, a model factor of 1.1 is applied to the forces and moments, when the sheet pile is applied as a panel. These two aspects make the application of sheet piles as stability screens expensive to apply. A better understanding of the failure behavior is needed to clarify whether the current design approach is conservative. Within the scope of the Flood Protection Program, a cross-project exploration was formed between water boards and the national government at the end of 2014. This collaboration is called POV and the aim is to innovate dike reinforcement which will result in a better, faster and cheaper process. A separate branch of this organization, POVM, is focusing on macro-stability. Within this scope, the use of sheet pile walls as stability screens is investigated. In this context, the Eemdijk test has been performed. This consisted of two full-scale tests up to failure. Although the test was successful and led to many new insights, the reliability of strain measurement data is questionable. The strain distribution, however, is essential in understanding the failure behavior.

That is why this thesis addresses the reliability of the measurement data. This is done by means of comparing measurements of different sensor types. Each sensor is then classified using four classes that indicate the reliability. Subsequently, reliable data is used to obtain a curvature distribution. In order to convert strains into moments, a moment-curvature diagram is required, which relates curvatures to moments in the sheet pile. This relationship is obtained by means of finite element calculation of a 4-point bending test. Subsequently, the chosen model is calibrated by means of reproducing the measurement results of three real documented 4-point bending tests. Finally, the model is applied to the sheet pile profiles used in the Eemdijk test.

With the obtained moment distributions, conclusions are drawn with respect to the current design approach. Furthermore, recommendations are made with regards to the applied monitoring program and the influence of soil on local buckling.

1 Introduction

1.1. Problem description

Within the Netherlands, there is a large river delta. Furthermore, a large part of the land is situated below sea level. As a result, the country is highly prone to flooding. In order to cope with this, there are over 3500 kilometers of primary flood defense structures. Currently, the flood defense structures in the Netherlands are assessed every twelve years. A substantial part of the flood defense structures requires strengthening according to the assessments. This is shown in figure 1.1.

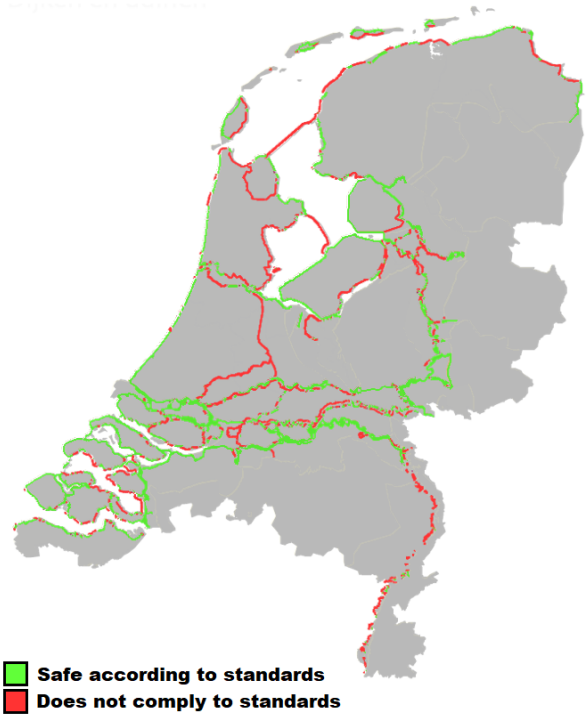

Figure 1.1: Assessment of flood defense structures

As a result, strengthening projects of dikes with a total length of more than 700 km will be performed in the upcoming years. Traditional dike reinforcement consists of increasing the cross-sectional area of the dikes, but often space is limited due to a high degree of urban density. For this reason, further strengthening of dikes often requires smart solutions. One of these solutions is the use of sheet pile walls as a stability screen.

With this solution, the stability is obtained, by a balance between active and passive earth pressures. Active earth pressures are exerted by the soil from which the sheet pile moves away, while passive earth pressures

are exerted by the soil at which the sheet pile is pressing up against. Intuitively it makes sense, that the latter is dominant. For this reason, the use of a sheet pile wall is an effective way of retaining a soil mass.

Since the application of sheet piles in dikes is relatively new, the experience and knowledge are still limited. This results in the use of very heavy and expensive sheet piles. Heavy sheet piles reduce the applicability due to the requirement of heavy machinery, while high costs cause this solution to be unattractive. As a result of the limited knowledge, the currently used design approach for dikes with stability screens might be conservative, since they don't allow for plastic calculation. Accordingly, a better understanding of the behavior could result in cheaper and lighter sheet piles.

1.2. Ideal test

To get this understanding, ideally, multiple full-scale test dikes should be loaded up to failure, within each test dike, a different sheet pile profile applied. This way both U and Z-profiles can be tested, but also profiles with a different cross-sectional classification. Furthermore, each test should be extensively monitored to allow for analysis and comparison. Unfortunately, there are some restrictions related to feasibility and budget.

1.3. Eemdijk test

With the restrictions in mind, the Eemdijk test was performed. Instead of multiple test dikes, this experiment consisted of one test dike (full-scale test), with additional pull-over tests. As a result of this setup, only one test dike is required, while a variety in profiles can be compared in the additional tests. The tests are shown in figure 1.2 and 1.3.

Figure 1.2: Full scale test

Figure 1.3: Pull-over test

1.4. Analysis

Both tests were successful and have brought lots of new insights. By analysis of the gathered data, a better understanding of the behavior during failure should be obtained. Subsequently, this will indicate whether the current design guidelines can be improved. However, the reliability of a small part of the measurement data is questionable. To capture the force distribution in the sheet piles, the strains have been monitored. To be as accurate and precise as possible, advanced fiber optic strain gauges have been used. The obtained measurements, however, contain a large scatter. A post-test inspection on the excavated sheet piles revealed that the glue fixating the fibers did not hold properly. This complicates the determination of the moment distribution in the sheet piles.

This thesis is focusing on sheet pile behavior and soil-structure interaction under extreme conditions. In order to investigate this, the moment distribution is required. In order to obtain this, the reliability of the strain data should be verified. Combined with other test results and knowledge obtained in previous experiments, this will provide an in-depth understanding of the technical aspects of a sheet pile wall in the soil. This understanding will serve a base for recommendations regarding the current design guideline.

1.5. Research questions

This thesis will aim to answer the following research question:

- How does an embedded sheet pile wall behave under extreme load conditions, based upon measurement results of the Eemdijk test?

In order to answer the research question, the following sub-questions are formulated:

1. What is the current design approach?
2. How are the curvatures and moments in the sheet pile distributed during the tests?
3. What conclusions can be drawn with regards to the design approach based on this?
4. Is it possible to relate curvature to moments by means of a finite element calculation?
5. What conclusions can be drawn with regards to the applied monitoring program?
6. Does the embedment of the sheet pile delay the onset of local buckling?

2

Research method

2.1. Introduction

In order to answer the research question, several steps have to be taken. First, the current design approach is analyzed. Subsequently, the Eemdijk test data is studied for comparison. To do so processing is required. The processed data can then be used to determine the strain and curvature distribution in the sheet pile wall. By means of a finite element calculation, a 4-point bending test is simulated in order to obtain a relation between curvature and moment. In these simulations, the soil-structure interaction with regards to buckling will be assessed. With the development of the moment distribution during the test, failure behavior can be analyzed. Furthermore, differences in behavior between mid and side piles will be investigated.

2.1.1. Axis definition

The chosen axis definition is shown in figure 2.1.

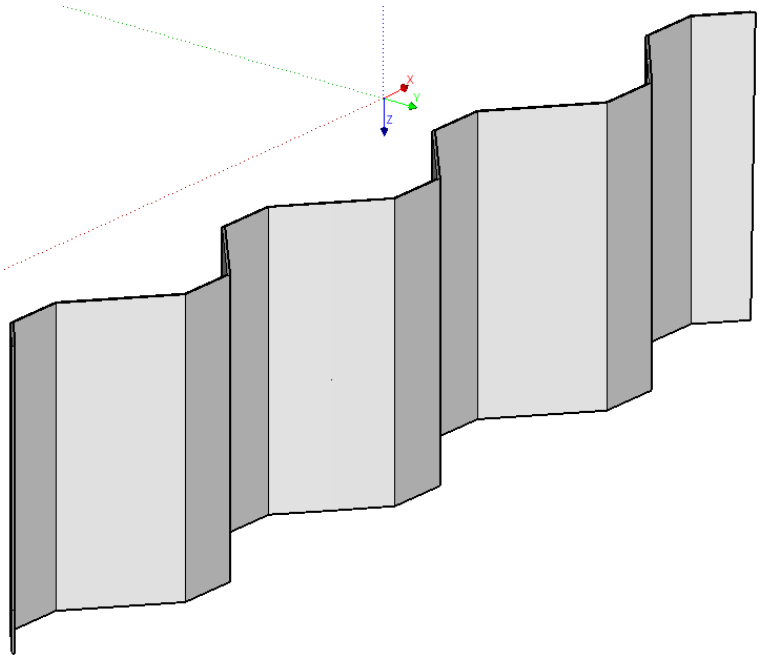

Figure 2.1: Axis definition sheet pile

2.2. Data processing

A considerable amount of data has been gathered during the tests. In order to extract the relevant data, several steps have to be taken. For the sheet piles, 14 inclinometers monitored deflections at 336 locations. Strains were measured by 660 strain gauges. Each sensor not only has a different location, but also the timestamps vary. For comparison between different sensors, advanced scripts have to be built.

2.3. Strain distribution

In order to investigate the behavior of the sheet pile, the force distribution is crucial. For this reason, a reliable strain distribution should be obtained from the measurement data. Since the raw measurement data is not reliable, a verification method will be constructed.

The glue fixing the fibre of the strain gauges could have failed at any time during the experiment and might even have failed during post-test excavation. For this reason, a verification has to be done in order to validate which part of the strain data is accurate. This verification will be performed by comparing strain measurements with results of different sensors. For the pull-over tests, the applied force is also measured. It is expected the strains will be positively correlated with the applied force. Comparison between the two should indicate if the strain gauges behave as expected. Furthermore, an estimation of the strains can be obtained from inclinometer measurements, which measure the deflection of the sheet pile. Since strain ϵ is related to the curvature κ of the sheet pile [2]:

$$\epsilon(x, y) = \epsilon + x\kappa_x + y\kappa_y \tag{2.1}$$

And the curvature κ can be expressed as the second derivative of the deflection u:

$$\kappa_y = -\frac{\mathrm{d}^2 u_y}{\mathrm{d}z^2} \tag{2.2}$$

By combining 2.1 and 2.2 the strain at the location of strain gauges can be estimated. This estimation will be used to verify which of the strain gauges were working properly. A method will be designed in order to perform this verification and it will be scientifically substantiated.

2.4. Moment distribution

The obtained strain distribution is converted into a curvature distribution. The curvature is then linked to the moment distribution. For small curvatures the Euler-Bernoulli beam theory still holds:

$$M_y = EI_{yy}\kappa_y \tag{2.3}$$

With Young's modulus E and moment of inertia I. For larger curvatures however an M-κ diagram is required, which relates curvatures to moments and can be obtained by performing a four-point bending test.

2.5. Finite element analysis

It will be investigated if the M-κ can be obtained by simulating a 4-points bending test in a finite element calculation. The chosen finite element package is DIANA.

2.6. Influence of soil on local buckling

Both class 2 and class 3 profiles have been tested. For a class 3 profile, it is expected that local buckling will not occur before the elastic limit is reached. However, the class derivation in the Eurocode only takes into account the geometric stability of the compression flange [14]. Since the sheet pile in the dike is embedded at both sides, there might be a delay in the onset of local buckling due to earth pressures. It will be investigated if this results in a higher moment and rotation capacity.

2.7. Edge effect

Instead of a continuous wall, sheet pile walls can also be applied as panels. Instead of connecting the panels, they are placed at a certain distance from each other. Due to arching in the soil, the panels will act as a continuous wall. However, a distinction has to be made between middle and side piles. This will introduce an edge effect because of the following reasons:

- Friction between soil particles results in more soil mobilization for edge piles
- Edge piles are unconstrained at one side since they are not connected to another pile

An illustration of the difference in soil mobilization is given in figure 2.2.

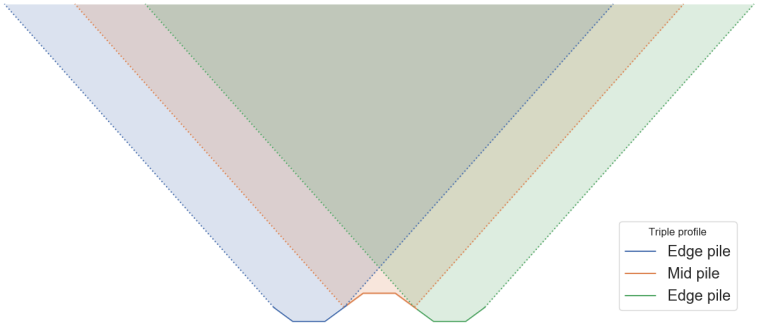

Figure 2.2: Edge effect: soil mobilization

During the tests mid and edge piles were monitored individually. A comparison of the obtained data may reveal if there is a significant edge effect and if this effect should be taken into account in the design approach.

3

Literature study

3.1. Introduction

A literature study has been conducted to get a better understanding of the use of sheet pile walls as dike reinforcement. The subject requires knowledge in a wide range of aspects and thus resulted in a large scope during the study. The following aspects have been explored:

- Safety standards and failure mechanisms
- Development of design guidelines
- Innovations in dike design
- Structural behavior of steel
- Monitoring

3.2. Safety standards and failure mechanisms

To better understand the need for sheet pile dike reinforcement, a closer look is taken at the approach for flood risk analysis and the failure mechanisms of dikes.

3.2.1. Old standards

Up to 2017, the safety standards were based on the Flood Water Law dating back to 2009. Before that, they were based on the approach of the first Delta Committee dating back to 1956. These standards were related to the exceedance probability of the water level. Since flooding is not only related to the water level this approach was not ideal and resulted in some parts of the flood defenses to be safer than other parts.[21][18]

3.2.2. New standards

Over time the understanding of failure mechanisms has grown. This enabled in the introduction of a safety standard based on flood risk in 2017. The risk is defined as follows:

$$Risk = Probability\ of\ Flooding * Consequence$$

In order to calculate the flood risk of a dike ring, a division is made into more or less homogeneous parts. For each section, the failure probability of different failure mechanisms is then calculated. This will result in the following table:

	Section 1	Section 2	Section j	Combined
Mechanism 1	P_{11}	P_{12}	P_{1j}	$P_{mech,1}$
Mechanism 2	P_{21}	P_{22}	P_{2j}	$P_{mech,2}$
Mechanism i	P_{31}	P_{32}	P_{ij}	$P_{mech,i}$
Combined	P_1	P_2	P_j	P_{flood}

Table 3.1: Example of presentation of results p_f failure probability calculation [18]

The total flood probability for an entire dike ring is in between the maximum sectional failure probability and the summation of all sectional failure probabilities, depending on the correlation. [18]

3.2.3. Failure mechanisms

A schematic overview of the different failure mechanisms is presented here:

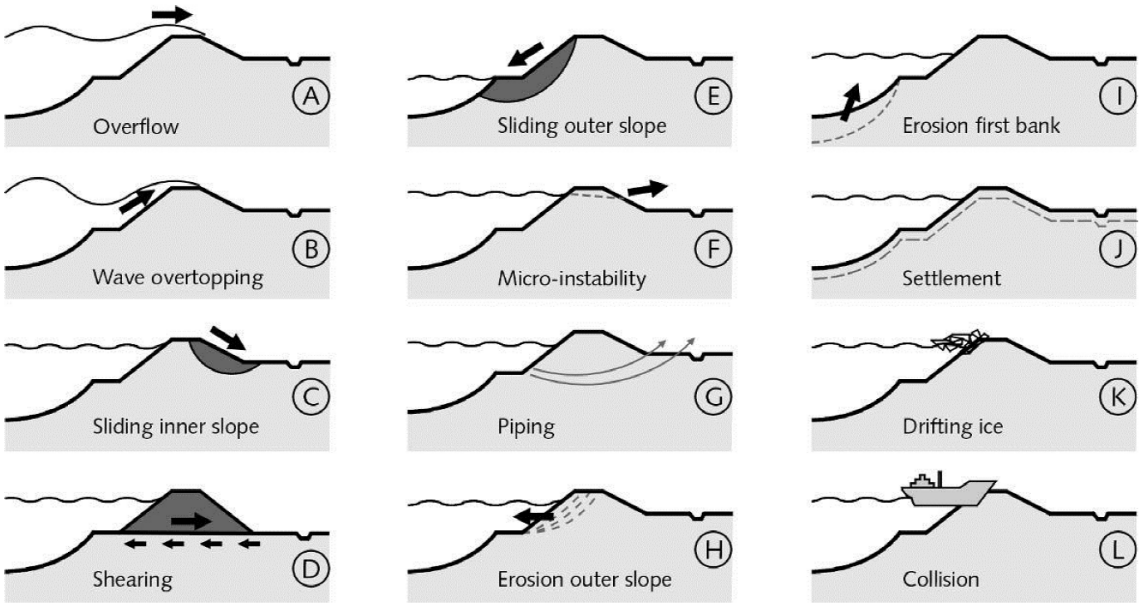

Figure 3.1: Schematic overview of the most relevant failure mechanisms of flood defences [18]

The most common stability problem for river dikes, and also the most relevant for this thesis, is sliding of the inner slope, also macro-stability.

Macro-stability

Long lasting high water levels cause saturation of the dike body. Saturation results in an increase of the pore pressure and thus a decrease of the effective stress. Eventually, the shear capacity is not sufficient to withstand sliding of the soil mass and failure occurs.

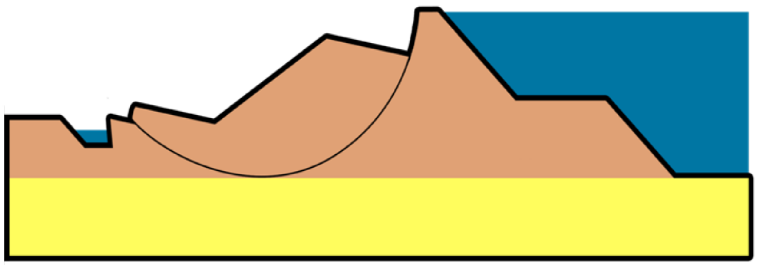

Figure 3.2: Macro-instability failure mechanism [18]

There are numerous methods for slope stability analysis. The most applied ones for dikes are Bishop and Fellenius. Both assume a circular slip surface above which the soil is divided into several slices as shown in figure 3.3.

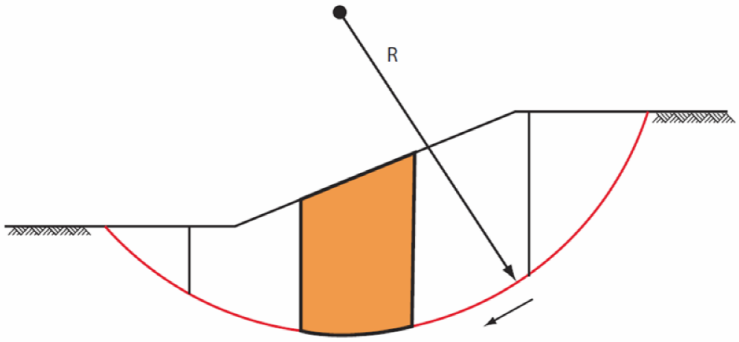

Figure 3.3: Slope stability analysis [22]

Each slice exerts a moment with respect to the center of the slip circle due to its weight. The driving moment M_s is exerted by the slices at the water-side, while the resisting moment M_r is exerted by the slices at the land-side in addition to the shear capacity at the slip surface. The factor of safety is then given by: [18] [22]

$$FoS = \frac{M_r}{M_s} \tag{3.1}$$

3.3. Development of design guidelines

This thesis investigates whether the current design process might be too conservative. A thoroughly study is done on the current and former guidelines.

3.3.1. Sources

In the Netherlands, the Expertise Netwerk Waterveiligheid (ENW) advises the government regarding water safety. This committee was founded in 1960 after a dike breach had occurred in Tuindorp.[8] The committee is assisted by the research institute Deltares and furthermore by the POV Macrostabiliteit. The latter is a cross-project exploration between water boards and the national government, which was formed in the scope of the Flood Protection Programme at the end of 2014.

3.3.2. Structure

The design guidelines for dikes are structured in three levels:

- General design guidelines (ontwerpinstrumentaria)
- Specific design guidelines (leidraden)
- Technical reports

General design guidelines

General design guidelines describe general aspects that apply to flood protection works in the entire country. For example, they describe how failure probabilities are calculated.

Specific design guidelines

Specific design guidelines describe guidelines that apply for a specific structure or area. For example, the "Leidraad Ontwerpen van Rivierdijken deel 2" describes the guidelines for river dikes that are located downstream of the river. Loads on these dikes are not only related to river discharge but also on the tide. For this reason, a separate design guideline is created.

Technical reports

The technical reports go in-depth on certain topics. For example, there is a technical report that deals with water pressures on dikes.

3.3.3. Publications

To fully understand the background of current design guidelines a summary has been made of all relevant reports on which the current guidelines are based. A timeline of publication is given first after which an elaboration is given on the most important publications.

Year	Publication	Abbreviation
1989	Leidraad Ontwerpen van Rivierdijken deel 2, Benedenrivierengebied	LOR2
2001	Technisch Rapport Waterkerende Grondconstructies	TRWG
2003	Leidraad Kunstwerken	LK
2003	Stabiliteits- en sterktecriteria bij lange damwanden in dijken	Kookboek
2007	Leidraad Rivieren en Addendum behorende bij TR Waterkerende Grondconstructies	LR
2010	Technisch Rapport Analyse dijken met Eindige Elementen Methode v1	TREEM 2010
2013	Ontwerprichtlijn stabiliteitsschermen in dijken v1	OSPW 2013
2014	Ontwerprichtlijn stabiliteitsschermen in dijken v2	OSPW 2014
2014	Addendum Ontwerprichtlijn stabiliteitsschermen	
2015	Technisch Rapport Analyse dijken met Eindige Elementen Methode v2	TREEM 2015

Table 3.2: Chronologic overview of guidelines in the Netherlands

Leidraad Ontwerpen van Rivierdijken deel 2, Benedenrivierengebied

In 1989 the second general design guideline of the ENW was published. This guideline contained design rules for dikes where storm surge or tides influence the water levels. The design approach is based on the different failure mechanisms of dikes. [19]

Leidraad Kunstwerken

This is the first guideline to cover the use of sheet pile walls in dikes. The safety approach is based on the failure mechanisms of the structure. For dimensioning of the sheet pile wall a reference is made to CUR166. The latter, however, recommends taking the dike requirements into account. This is not further elaborated on and therefore resulted in a wide range of dimensions based upon interpretation. [4] [12] [20]

Stabiliteits- en sterktecriteria bij lange damwanden in dijken

For a dike strengthening project in the Krimpenerwaard another methodology for the use of sheet pile walls in dikes was presented by Deltares. The safety approach, however, was based upon dike failure mechanisms. The reasoning for this was that the sheet pile failure is highly dependent on soil stability. Following this safety approach, the method is closely related to LOR2 and calculation was based upon a finite element method using Plaxis. [12] [9]

Technisch Rapport Analyse dijken met Eindige Elementen Methode

With calculation by means of the finite element method, there are numerous models to describe soil behavior. In order to unify calculation results, a clear guide was required. This step-by-step guide was presented in this technical report. [12] [13]

Ontwerprichtlijn stabiliteitsschermen in dijken

With time it became clear that some aspects of the guideline derived for the Krimpenerwaard were not properly addressed. As a result, Waterboard Rivierenland asked Deltares to produce a new guideline. This is the currently used design guideline for the use of sheet pile walls as dike strengthening. [12]

This thesis will address two aspects of this guideline, namely:

- In contradiction to the Eurocode and all other commonly used standards [10], it is not allowed to take into account the plastic capacity of structural elements and/or components.
- When the opening between structural elements is larger than the width (in length direction of the dike), a model factor of 1.1 should be applied on the calculated forces and moments.

The latter is explained by a rotation of the side pile of up to 5°, due to the unrestricted edge [3]. In figure 3.4 and 3.5, the resultant earth pressure and the rotation for the right outermost pile of a panel are illustrated respectively.

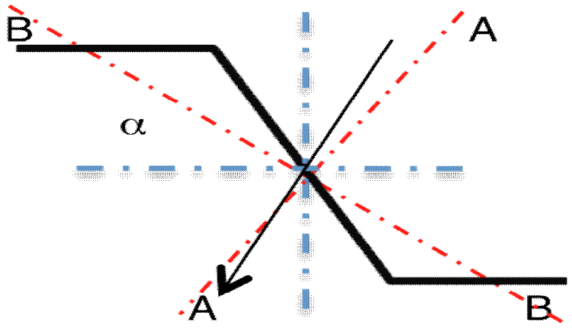

Figure 3.4: Resultant earth pressures [3]

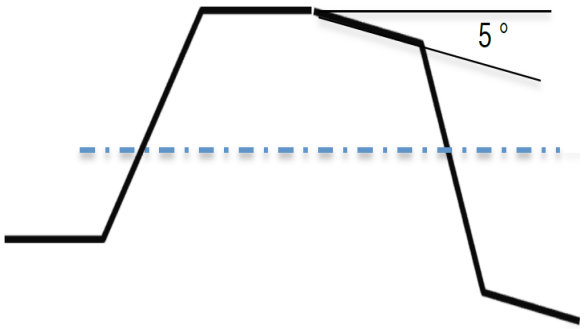

Figure 3.5: Rotation at the side of a panel [3]

As a result of the rotation, the stiffness increases. Since stiffer parts carry more load, this will lead to an increase of total stresses between 5 and 10%.

3.4. Innovation in dike design

Conventional dike reinforcement consists of increasing the cross-sectional area of the dikes, but often space is limited due to a high degree of urban density. For this reason, further strengthening of dikes often requires innovative solutions.

3.4.1. POVM

Within the scope of the Flood Protection Program, a cross-project exploration was formed between water boards and the national government at the end of 2014. This collaboration is called POV and the aim is to innovate dike reinforcement which will result in a better, faster and cheaper process. A separate branch of this organization, POVM, is focusing on macro-stability. Within this scope the following innovations are being investigated:

- Dike soil nailing
- Drainage techniques
- Soil improvements
- Sheet pile walls

Dike soil nailing

Dike nailing protects the dike against inner slope failure by inserting elements through the slip surface. The benefit of this solution is that it increases stability without changing the dike profile and furthermore it is possible to create steeper slopes. This makes the solution well suited for locations with limited space available.

Drainage techniques

Drainage techniques decrease the probability of macro instability by decreasing the pore pressure in a dike. A decrease in pore pressure results in an increase of effective stress and thus larger resisting shear stress. Since no changes to the dike profile are required, this solution is also well suited when only limited space is available.

Soil improvements

By means of vacuum consolidation, the effective vertical pressure is increased. This results in a permanent increase of the undrained shear strength of the soil and thus protects the dike against macro stability related failures. This results in a reduction of the required berm height to guarantee stability.

Sheet pile walls

The sheet pile wall functions as a stability screen and protects the dike against inner slope failure by intersecting the slip surface. Furthermore, it affects water flows, pressures, and the freatic line. These stability screens can be either applied with or without anchors. Application of sheet pile walls has been around for some time, so in that sense, it is not really an innovation. However, cost savings as a result of new insights can significantly increase the applicability.

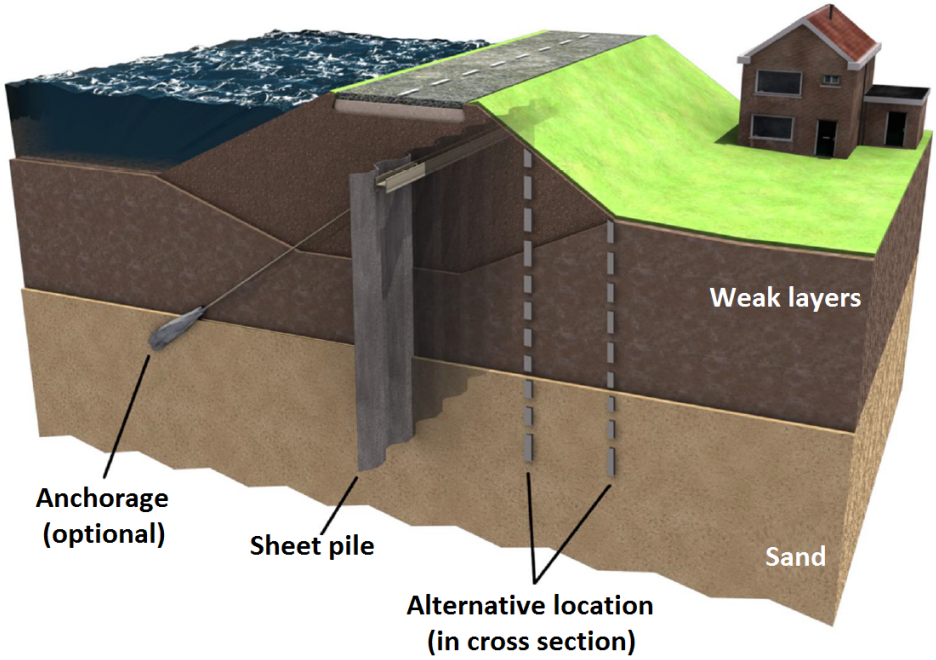

Figure 3.6: Use of a sheet pile wall as dike reinforcement [12]

3.5. Structural behavior of steel

To fully understand the behavior of the sheet pile wall, the structural behavior of steel is analyzed.

3.5.1. Stress-Strain behavior

The idealized stress-strain behavior of steel is illustrated in figure 3.7.

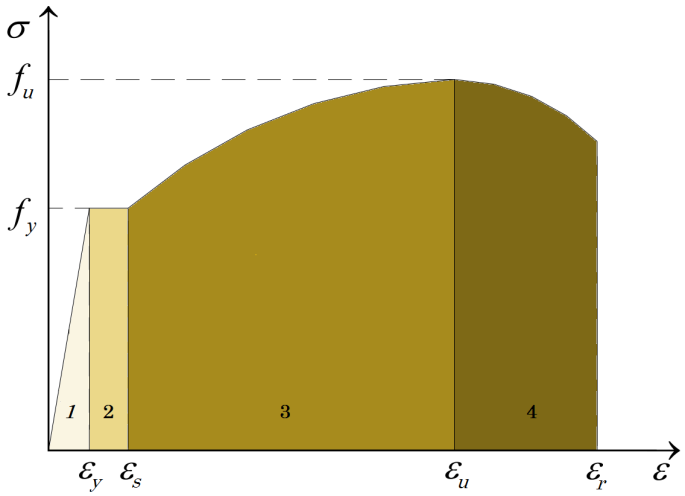

Figure 3.7: Idealized stress-Strain diagram for steel

From the stress-strain relation the behavior can be divided into four separate regions:

1. Up to the yield strength f_y, the stress-strain relations is linear elastic. Unloading at this stage will return the steel to the original state without deformations.
2. After the yield strength f_y is reached, yielding will occur at a constant stress level.
3. Strain hardening occurs when the strain is equal to about 10 times the yield strain. Additional stress is required to further deform the steel. This continues until the maximum stress f_u is reached.
4. Finally, the stress required to further yield the steel decreases until the failure occurs. (Necking)

3.5.2. Elastic analysis

With an elastic analysis, only the linear elastic part is taken into account. This is indicated in figure 3.8.

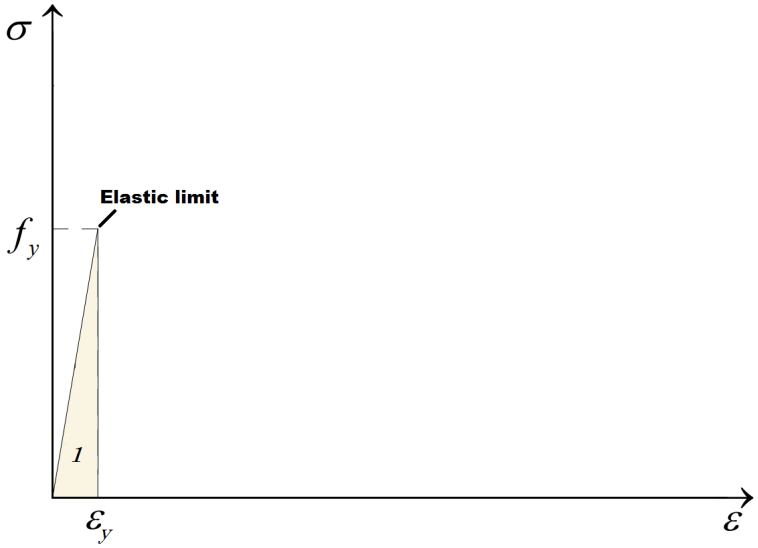

Figure 3.8: Elastic analysis

Although this is a simple and safe approach, there is quite some capacity left in the steel that is not utilized. This is demonstrated by means of a simple rectangular cross-section under the influence of a bending moment. Following the elastic analysis there is no strength left after the yield strength f_y is reached. For this reason, the strain in the outermost fibre is limited to the yield strain ϵ_y as shown in figure 3.9.

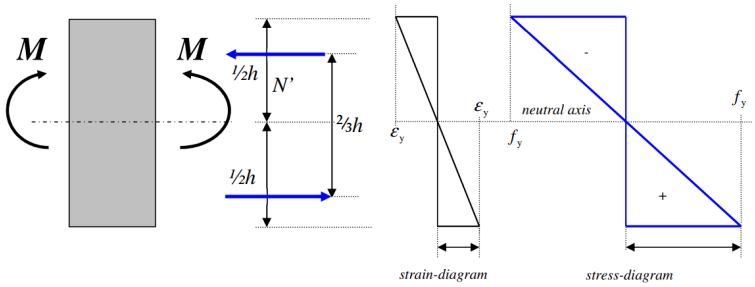

Figure 3.9: Rectengular cross-section: Elastic stress and strain diagram[2]

The maximum moment to be resisted by the indicated rectangular cross section is then given by:

$$M_e = b * \frac{h}{2} * \frac{h}{3} * f_y = \frac{bh^2}{6} f_y \tag{3.2}$$

Where b and h are the breadth and height of the cross-section respectively.

3.5.3. Plastic analysis

In the plastic analysis, the strain in the outermost fibre is not limited to the yield strain. Further increasing of the strain will result in the stress and strain distribution illustrated in 3.10.

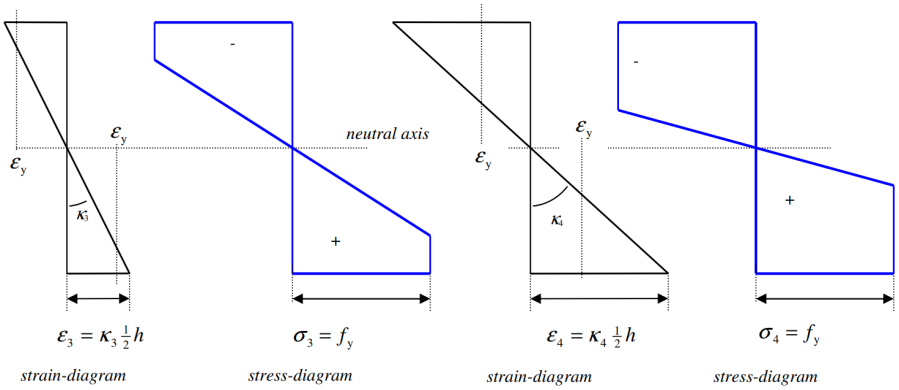

Figure 3.10: Rectangular cross-section: Increase of strain past elastic limit [2]

This continues until the full plastic capacity is reached as shown in figure 3.11.

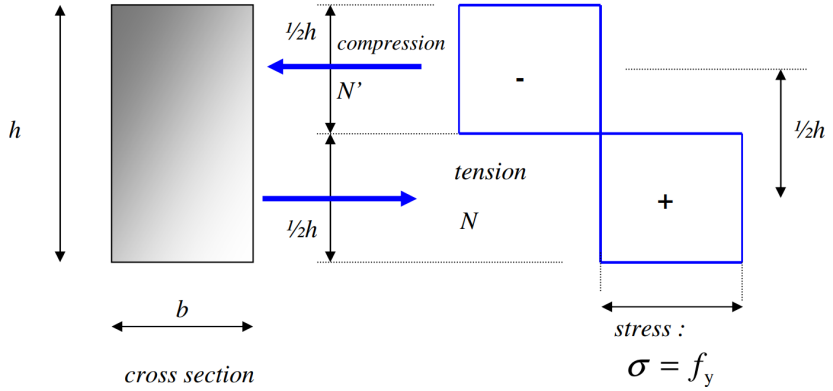

Figure 3.11: Rectangular cross-section: Plastic stress and strain diagram [2]

The maximum moment to be resisted by the indicated rectangular cross section is then given by:

$$M_p = b * \frac{h}{2} * \frac{h}{2} * f_y = \frac{bh^2}{4} f_y \tag{3.3}$$

The shape factor α is defined as the ratio of M_p over M_e.

$$\alpha = \frac{M_p}{M_e} = \frac{\frac{bh^2}{4} f_y}{\frac{bh^2}{6} f_y} = 1.5 \tag{3.4}$$

Meaning that plastic analysis results in an increase of the moment capacity by 50% for a rectangular cross-section.

3.5.4. Local buckling

For columns, buckling is an instability phenomenon that results in sudden loss of bearing capacity. This is induced by an increase of lateral deflection and going with loss of equilibrium [5]. Local buckling of plates is similar, however, it is restricted to compression members in steel structures. Plates differ from columns since they are most of the time supported along all four edges. For this reason, there is no sudden loss in bearing capacity, but some residual capacity is left due to membrane resistance.

Local buckling is illustrated for an I-profile under the influence of a bending moment shown in figure 3.12.

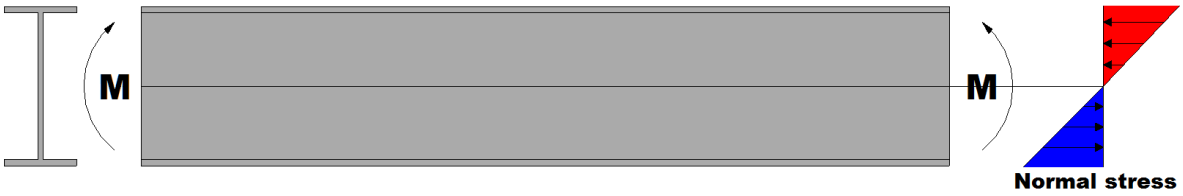

Figure 3.12: I-profile under the influence of a bending moment M

As a result of the bending moment, the bottom flange will be in tension, while the top flange is under compression. This is illustrated in figure 3.13.

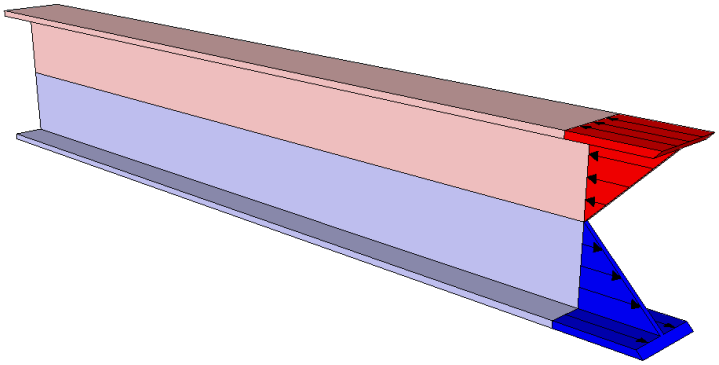

Figure 3.13: Normal stress distribution as result of a bending moment M

Because the steel member is under the influence of both tension and compression, it is referred to as a flexural member. Flexural members are classified as compact, non-compact or slender [15]. This classification depends on the slenderness of the compression member and the unbraced length. For compact flexural members, the full plastic capacity is reached before local buckling occurs. For non-compact or slender members, however, local buckling will occur before the full plastic capacity is reached. This is shown for the I-profile in figure 3.14.

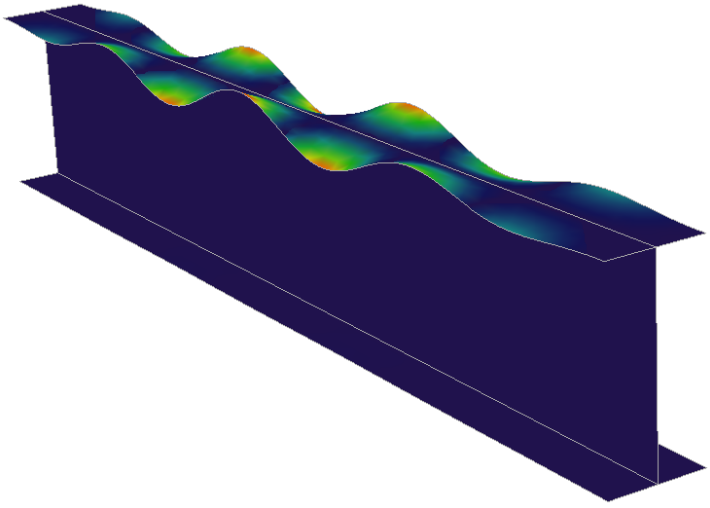

Figure 3.14: Local buckling of compression flange

3.5.5. Plastic analysis for sheet piles

The Eurocode allows for plastic calculation with respect to sheet piles, but this depends on the cross-sectional classification. The reasoning for this is that local buckling may occur before the plastic capacity is reached. Classes are related to the slenderness of the compression flange and the steel grade of the sheet pile. The following cross-sectional classes are distinguished: [17]

- Class 1 cross-sections for which a plastic analysis involving moment redistribution may be carried out, provided that they have sufficient rotation capacity
- Class 2 cross-sections for which elastic global analysis is necessary, but advantage can be taken from the plastic resistance of the cross-section
- Class 3 cross-sections which should be designed using an elastic global analysis and an elastic distribution of stresses over the cross-section, allowing yielding at the extreme fibres
- Class 4 cross-sections for which local buckling affects the cross-sectional resistance

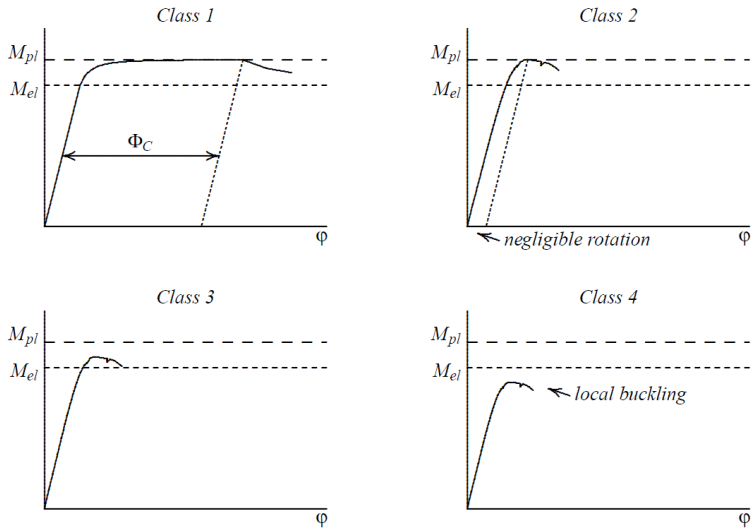

Figure 3.15: Cross-sectional classification of sheet piles [14]

Sheet piles are generally used for deep excavations. For this reason, the class is purely based upon the geometric stability of the cross-section and neglecting the effects of soil. It is expected that the behavior of a sheet pile surrounded by soil differs due to the positive effect of earth pressures. A study into the buckling resistance of sand-filled tubes(Peters et al.[7]), showed a considerable increase in rotation capacity, which is attributed to the sand-fill that prevents the tube to deform and become unstable. This is shown in figure 3.16.

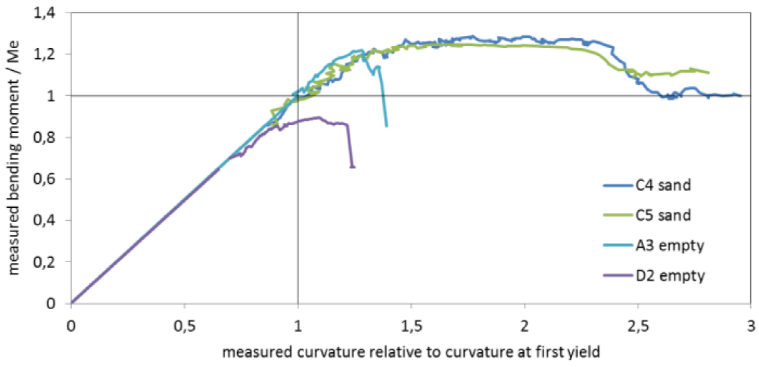

Figure 3.16: Typical measured moment –curvature diagrams of empty and sand-filled tubes

A similar influence of the soil around sheet piles could possibly result in a class shift to a class that allows for plastic calculation.

3.6. Related studies

3.6.1. Sheet pile walls in soft soils

This study (Kort [14]) was focused on filling the knowledge gaps with regards to plastic design and oblique bending that existed during the establishment of Eurocode 3, part 5. Comparison of model predictions with

full-scale test results led to great insights regarding these topics. The study demonstrated that the plastic design approach is valid and as a result, the Eurocode allows for plastic design.
The main aspects this research was focused on are:

- Performance of a sheet pile wall with a plastic hinge
- Performance of a sheet pile wall composed of double-U profiles
- Short and long term behavior of a sheet pile in soft soil

The test consisted of an excavation of 12 square meters, where two test walls were included. The test site, located in the port of Rotterdam, is shown in figure 3.17.

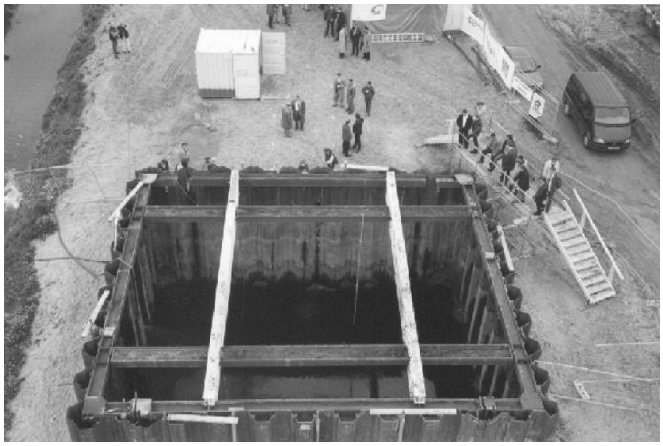

Figure 3.17: Rotterdam sheet pile wall field test (May 11, 1999)

The test walls were monitored by means of strain gauges. In order to relate the measured strains to moments, 4-point bending tests have been performed by TNO. The set-up of these tests is shown in figure 3.18.

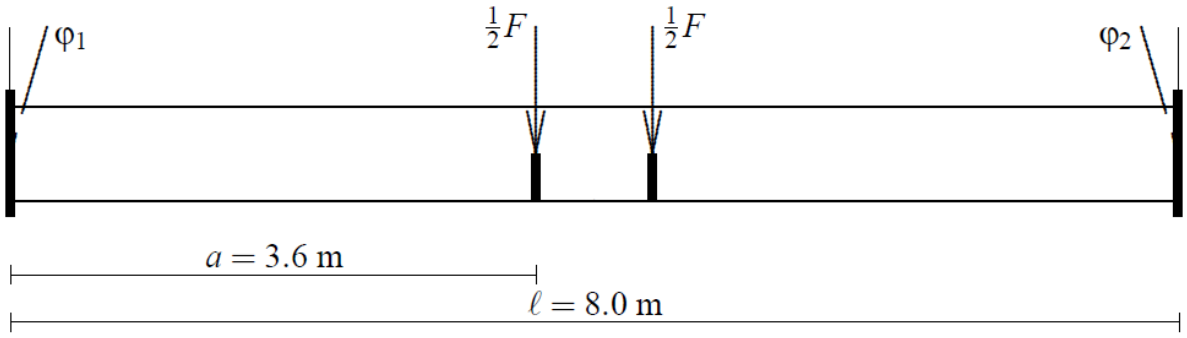

Figure 3.18: 4-points bending test set-up TNO

For the load introduction, stiff plates are used. The set-up will result in the moment-diagram shown in figure 3.19.

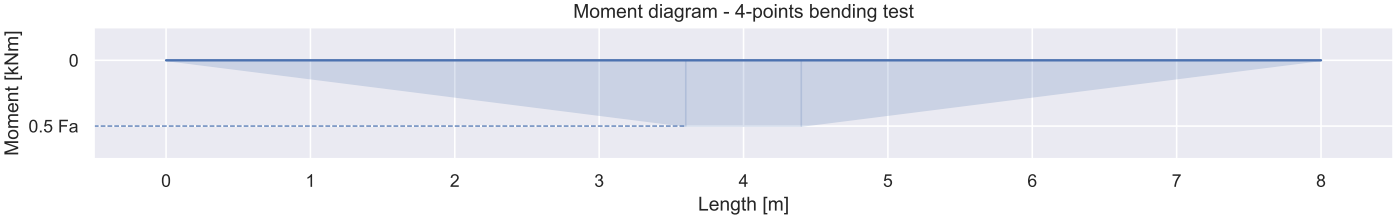

Figure 3.19: 4-points bending moment distribution

The curvature is determined as follows:

$$\kappa = \frac{\phi_1 + \phi_2}{l - a} \tag{3.5}$$

In which $l - a$ is the effective length for which multiplication with the maximum moment, results in the same area as the one under the moment-diagram. This is shown in figure 3.20.

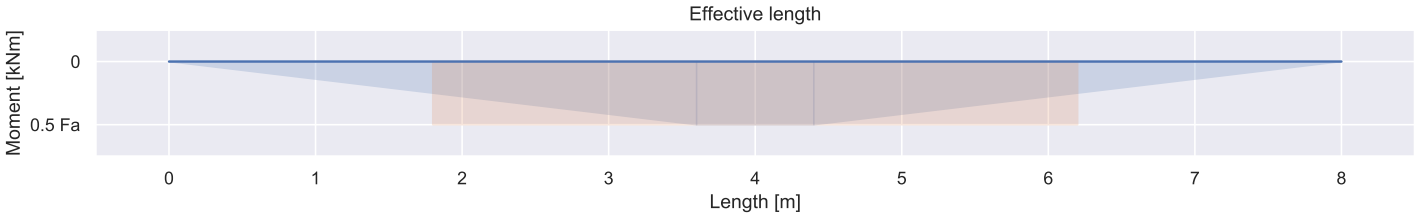

Figure 3.20: Effective length

As a result, a moment-curvature diagram can be obtained. This is done by measuring the rotation at the supports, such that the curvature can be computed. Furthermore, the moment in the middle is obtained from multiplication of the applied load by the distance to the support a. For each loading step, the combination of curvature and moment is a point on the Moment-curvature diagram. The obtained diagram for an AZ13 sheet pile is shown in 3.21.

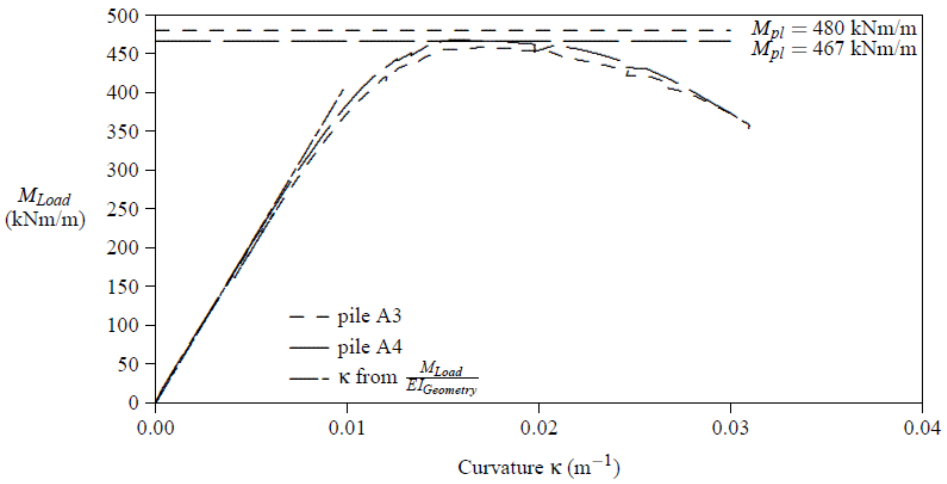

Figure 3.21: Moment-curvature diagram

With the moment-curvature diagram, the moments in the sheet pile could be calculated. Figure 3.22 indicates the moment distribution, before and after the formation of a plastic hinge.

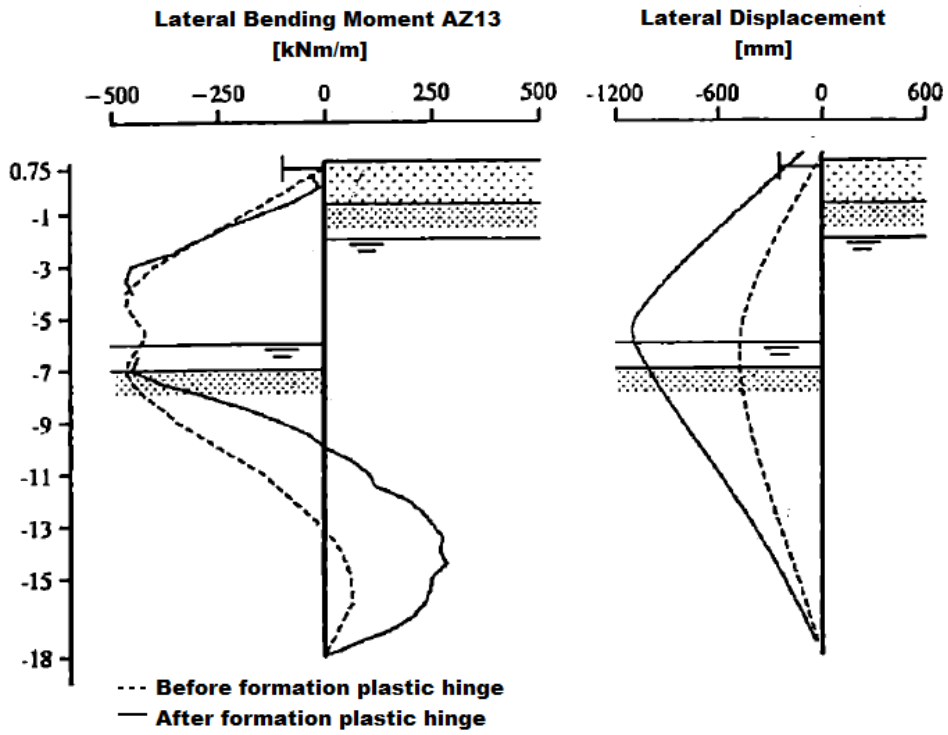

Figure 3.22: Results AZ13

It was concluded that after the formation of a plastic hinge, a new equilibrium was found in the soil. The earth pressures on the retained and excavated side were able to redistribute to develop the fixed moment, which supports the use of plastic calculation.

3.6.2. Momenten-Rotationstragfähigkeit von Spundwänden aus Z-Bohlen und U-Bohlen mit verminderter Schubkraftübertragung

In this study (Dercks [6]) the moment-rotation curves are derived for a large number of sheet pile profiles. The study provides a plastic design approach that is independent of cross-sectional classification and can be carried out for each profile.

The moment-rotation curves were derived by means of both real experiments and finite element calculations of 4-points bending tests. For this reason, the applied modeling method is considered for application in this thesis. The described aspects of the finite element model are:

- Test set-up
- Geometry

Test set-up

Set-up of the 4-points bending tests is done similar to TNO. A sheet pile length of 4m is chosen instead of 8m. The set-up is shown in figure 3.23.

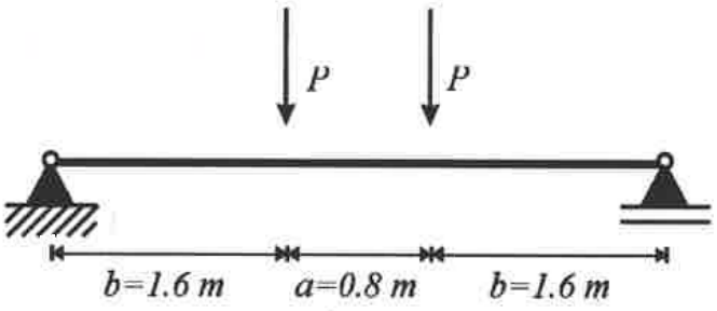

Figure 3.23: 4-points bending test set-up Dercks

Which results in the moment-diagram shown in figure 3.24

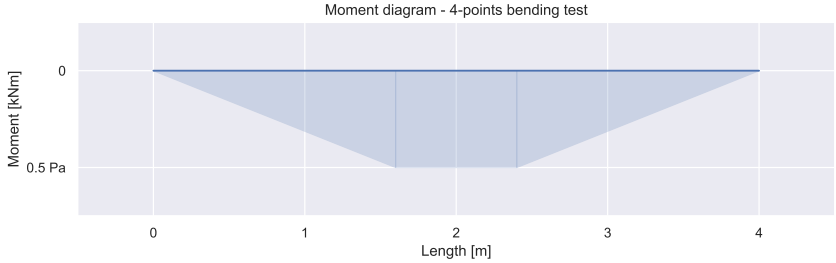

Figure 3.24: 4-points bending test moment distribution

Geometry

Dercks only describes the model geometry of U-sections, these are shown in figure 3.25.

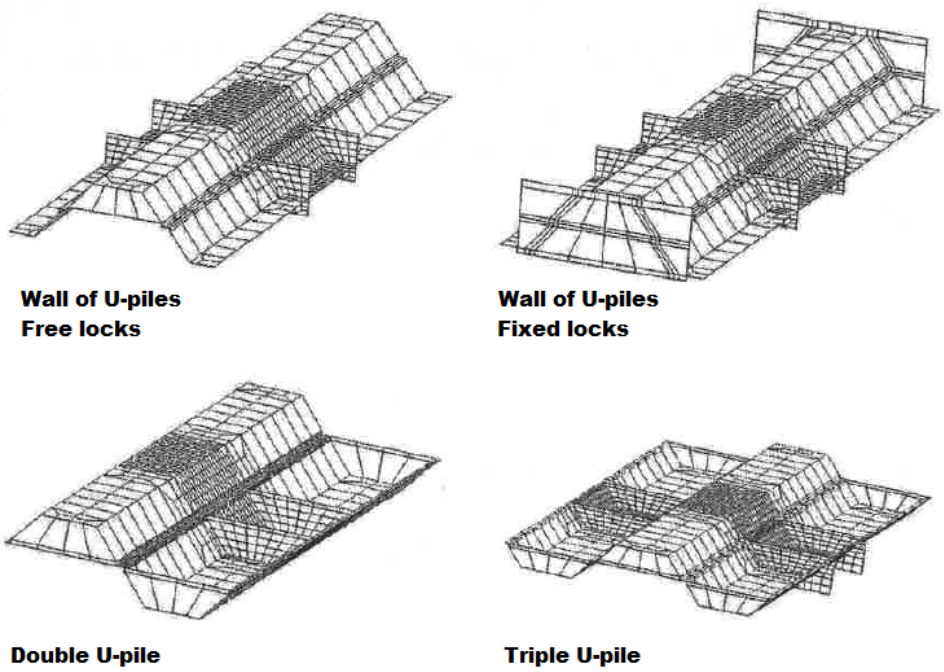

Figure 3.25: Model geometry of U-sections

From these models, it can be observed that:

- Plates are used for load introduction in the tension zone
- Continues walls are modeled as double Z-sections
- For the continues wall with fixed locks, plates are used at the supports

On the specific modeling choices is not further elaborated on by Dercks, But these will be discussed in section 3.6.3.

3.6.3. RFCS Report

Some design rules for sheet piles at the ultimate limit state in the Eurocode are based on this report (Kort et al. [11]). Finite element calculations have been carried out, for which a number of sensitivity analyses were performed. The following aspects have been investigated:

- Test set-up
- Geometry

Test set-up

A comparison is made between a 4 and a 3-points bending test. These are shown in figure 3.26.

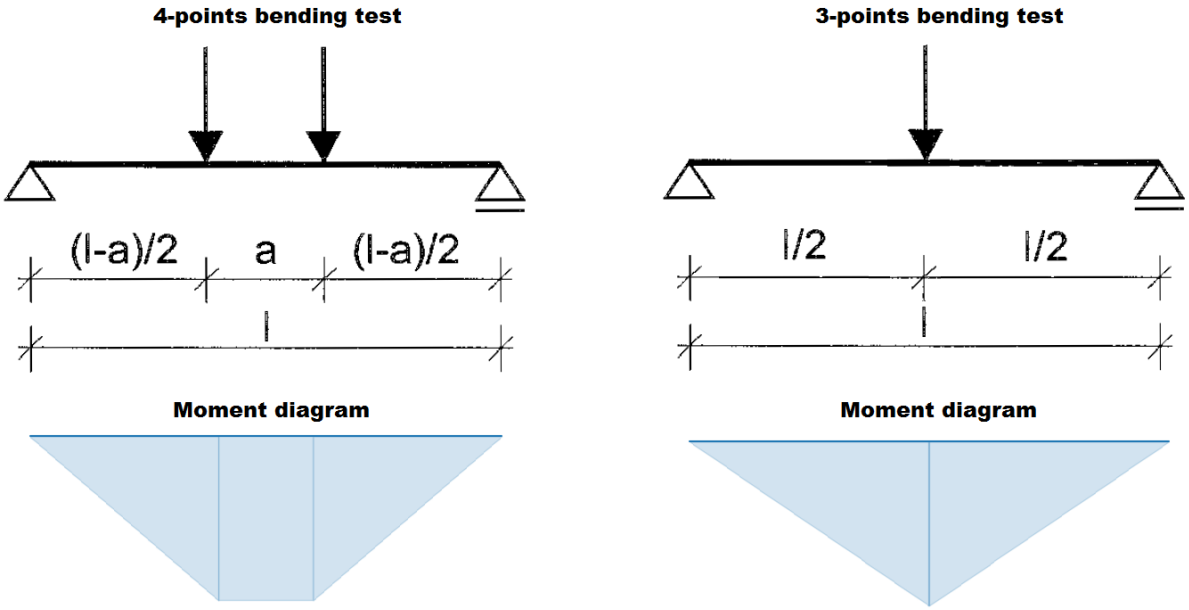

Figure 3.26: 4 and 3-points bending test

A 4-points bending test is preferred because the moment distribution is similar to a sheet pile in the field. Furthermore, the influence of load introduction plates was smaller for the 4-points bending test. To minimize the influence, the distance between the load introduction plates should be larger than two times the flange width.

Geometry

The model geometry for both U and Z-sections is described. These are shown in 3.27

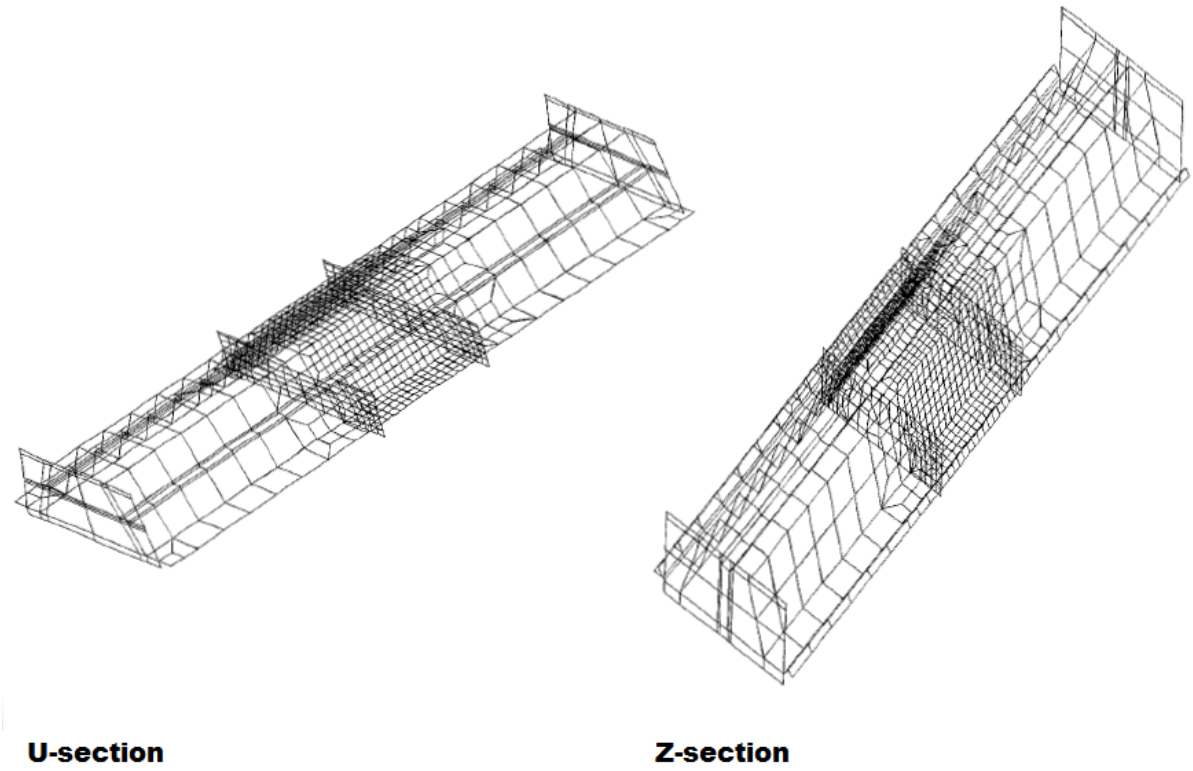

Figure 3.27: Model geometry of U and Z-sections

In order to get a moment-rotation curve that matches real test results, the following should be taken into account:

- Element size of 5 cm between and 20 cm outside of the load introduction plates.
- Interlocks are modeled as thicker shells. Cross-sectional geometry calibrated such that the error in cross-sectional area and moment of inertia is less than 1%.
- Imperfections should be used in the mid-spawn.

Furthermore, it was concluded that the differences in results are small as a result of taking symmetry into account.

4

Eemdijk Test

4.1. Introduction

4.1.1. Motivation

Within the scope of the Flood Protection Program, a cross-project exploration was formed between water boards and the national government at the end of 2014. This collaboration is called POV and the aim is to innovate dike reinforcement which will result in a better, faster and cheaper process. A separate branch of this organization, POVM, is focusing on macro-stability. Within this scope, the use of sheet pile walls in dikes has been investigated.

The currently used design guidelines are derived for specific project locations, and furthermore might be too conservative due to the lack of knowledge related to the behavior of these structures. For this reason, there is a strong demand for a more versatile and sober approach. In order to derive such an approach, a better understanding of the failure behavior is necessary. In this context two tests have been performed, namely a pull-over test (POT) and a full-scale test (FST).

4.1.2. Location

A multi-criteria analysis has been performed in order to determine a suitable project location. The results are shown in table 4.1.

Table 4.1: Multi-criteria analysis of possible project sites (translated from presentation J. Breedeveld)

Location	Retaining height [m]	Cohesive layer thickness [m]	Average cone resistance [MPa]	Saturated soil layer thickness [m]	Homogeneity [-]
Eemnes	<1.5	6.5	0.3	10	s
Gronddepot Eemdijk	4-5	5.5	0.3	5	s
Jachthaven Eemdijk	<1.5	5	-	-	-
Nieuwe sluis Terneuzen	-	9	1	20	m
Kerkdijk Veessen-Wapenveld	2-3	1-3	0.5	>>20	m
Weverdijk Veesen-Wapenveld	4-5	2-4	1	10	m
Wantijdijk	2-3	14	0.5	10	r
Crezeepolder	2-3	10	0.5	20	m
Beningerwaard	-	14	1	6	r

A successful test requires the failure of the test dike. In order for failure to occur a certain retaining height is required such that high enough water pressures can develop. Furthermore strengthening effects due to lateral earth pressures should be limited. Accordingly, Gronddepot Eemdijk was chosen as the test location.

4.2. Full-scale test

4.2.1. Test set up

The FST consisted of an arena shaped dike as shown in figure 4.1.

Figure 4.1: FST: Overview test site

One side of the dike is strengthened with a sheet pile (blue dike), while the other side consists of a regular (green dike). This set up allows for comparison in behavior. A sketch of the cross-section is shown in figure 4.2.

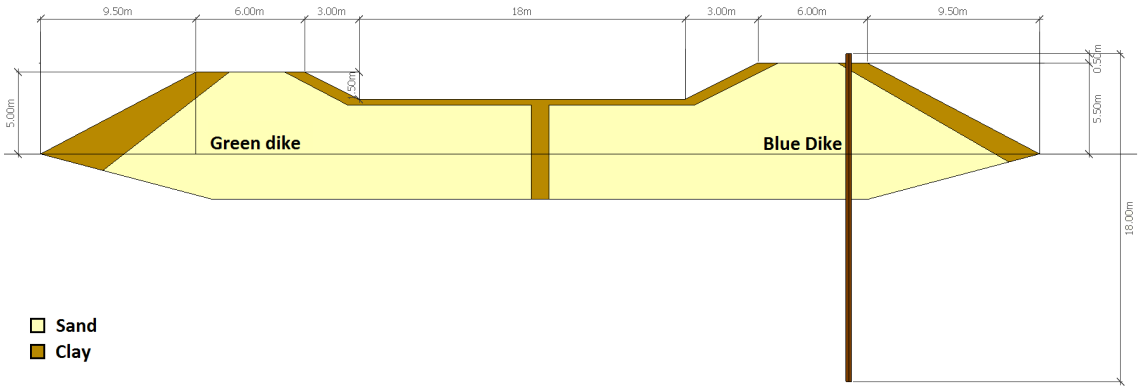

Figure 4.2: Cross-section of test dike

4.2.2. Sheet pile wall

Profile

The most commonly used sheet pile types are Z-profiles. For this reason, it was desired to use an AZ-13 profile. In order for failure to occur, the required steel grade was S240. However, the lowest available steel grade in the current production process is S355. Even with the thinnest Z-profile, an AZ-12, failure of the test

dike would be uncertain. Hence a U-profile is chosen instead, namely a triple GU8N-profile. A cross-section of the profile is shown in figure 4.3.

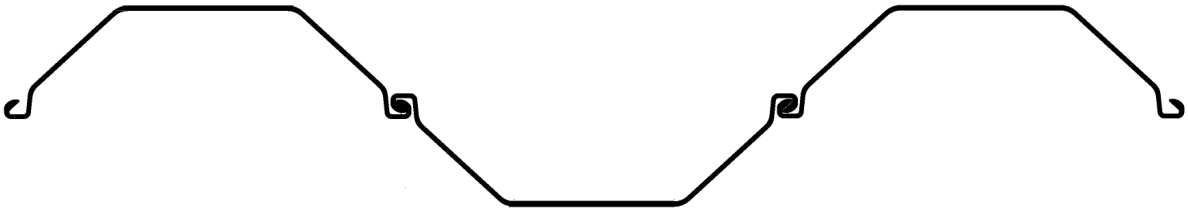

Figure 4.3: Triple GU8N profile

To guarantee failure of the dike, a staggered layout is chosen. This layout will reduce the capacity of the lower part and is illustrated in figure 4.4.

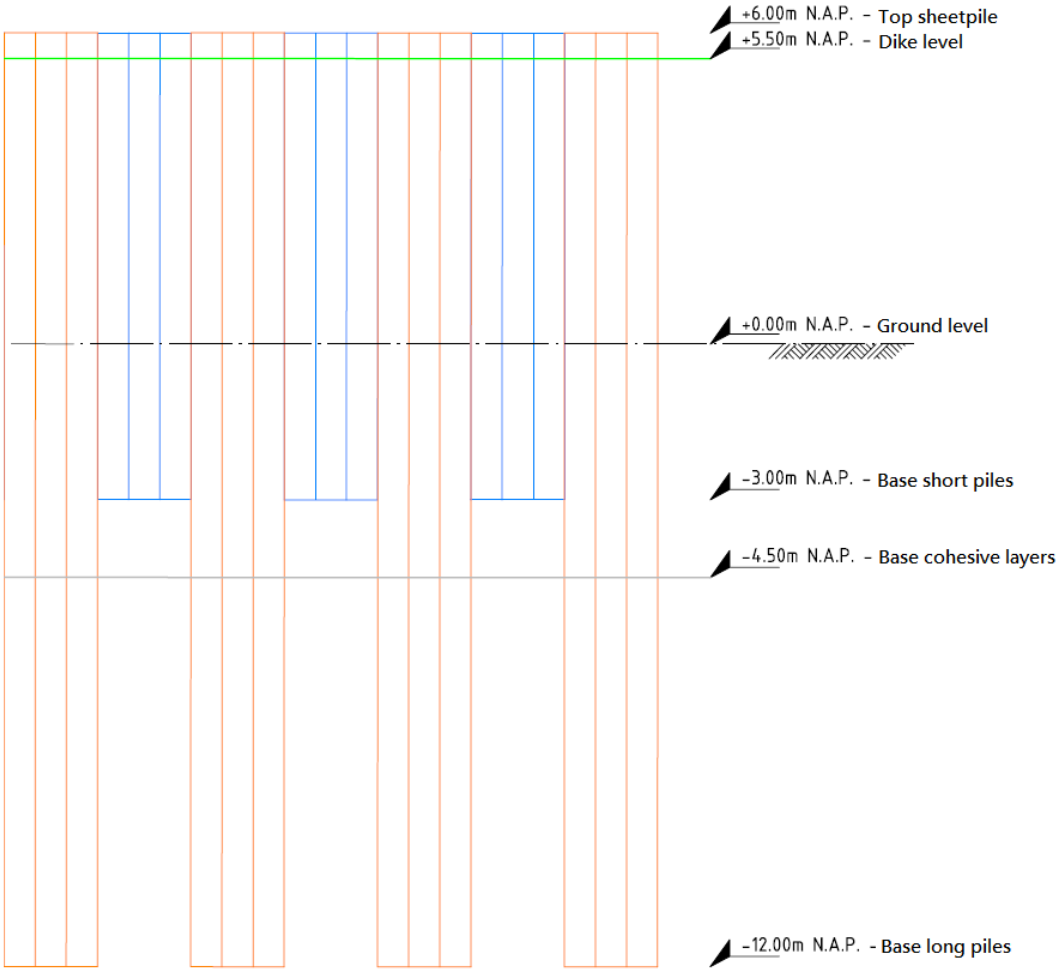

Figure 4.4: FST: Staggered layout

Triple piles are used in order to minimize losses in the moment of inertia and section modulus due to oblique bending. The installation process of sheet piles can cause an insufficient shear transmission in the interlocks to assume maximum cross-sectional resistance. The lack of shear transmission can in extreme cases lead to an alternate axis of inertia as shown by Kort: [14]

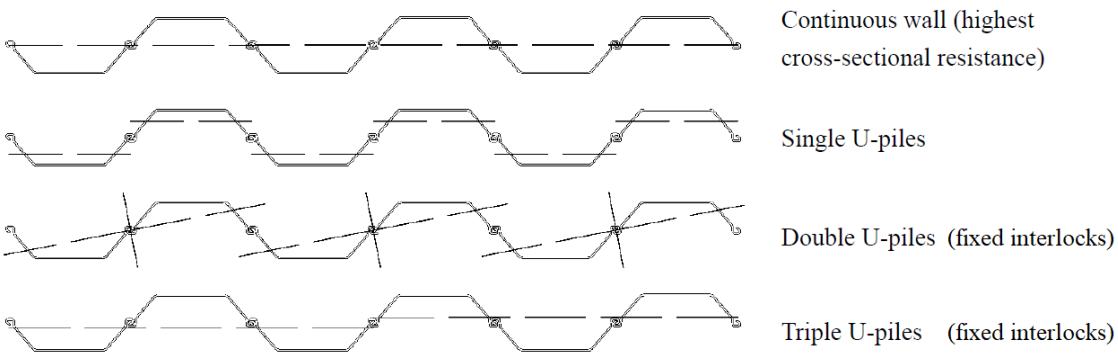

Figure 4.5: Axis of inertia (Kort)

By applying a triple profile, three sheets are connected by the manufacturer and sufficient shear transmission is ensured. In extreme cases, the reduction in the moment of inertia and section modulus is limited to 10% and 20% respectively.

Installation method

The sheet piles are installed by means of a vibratory pile driver. This method was chosen over hammering in order to protect the monitoring equipment. The installation of one of the test piles is shown in Figure 4.6.

Figure 4.6: Installing of a sheet pile equipped with monitoring devices.

4.2.3. Monitoring

With regard to studying the behavior during failure, an extensive monitoring program was set up. Out of the 32 triple piles used in the test, 4 piles have been equipped with sensors for monitoring. The monitored physical quantities consisted of:

- Displacements
- Strains
- Pressures

To accurately interpret the data, a good understanding of the devices is crucial.

Strain

The strain is monitored by FBG (fiber bragg grating) strain gauges. This is a high accuracy and precision sensor that transmits light signal with a varying spectrum related to the measured strain. An illustration of this is given in figure 4.7.

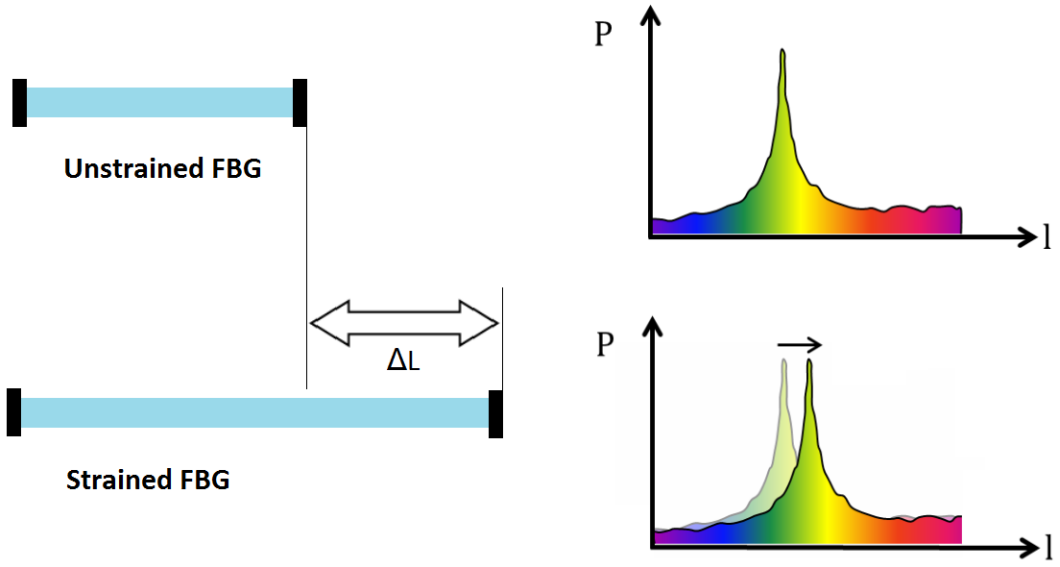

Figure 4.7: Functioning of an FBG sensor

A major advantage of this technique is that it allows for multiple light signals to travel through the same fiber (multiplexing). This results in significantly less wiring than with the use of conventional electric strain gauges and consequently less disturbance of the test specimen.
For the sheet pile, the sensor had the following requirements:

- Measure both compression and tension
- High measuring range of 20.000 micro-strain

Regular sensors have a measuring range of 5000 to 10000 micro-strain. That is why Fugro has developed a "spring-connection" in which glue guarantees pre-tensioning of the fiber. This is shown in figure 4.8.

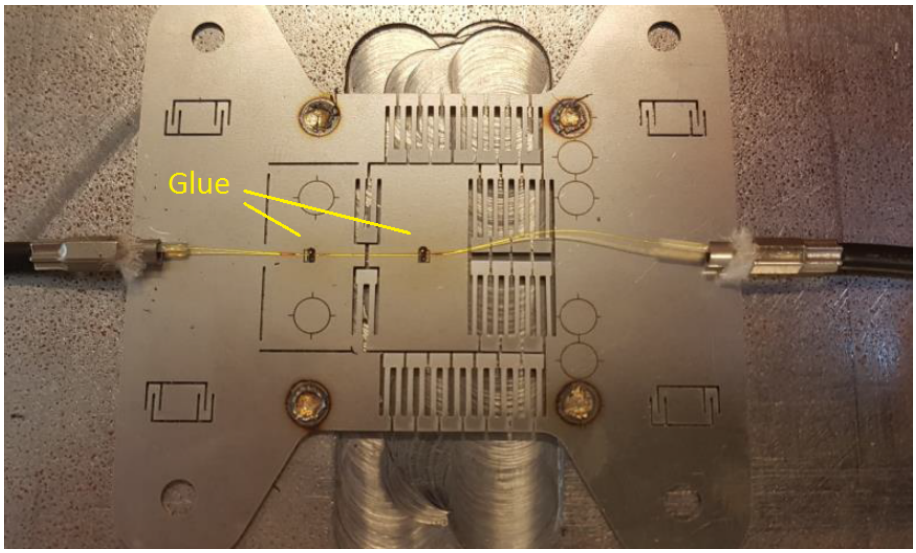

Figure 4.8: Spring connection developed by Fugro

From the four piles equipped with sensors, each was equipped with 70 FBG sensors. A detailed description of the location of each sensor can be found in Appendix A. After installation, a plate is applied to protect the sensors against moisture and preserve them during installation of the piles. This protection should be strong enough to protect the sensors, but not such that it influences the pile behavior. Figure 4.9 and 4.10 show the installed sensors before and after the protection was applied.

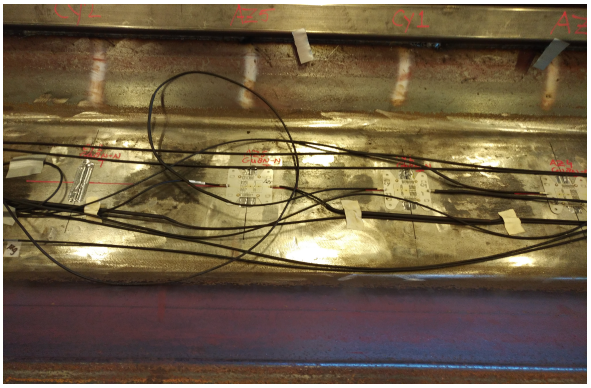

Figure 4.9: FBG sensors before protection

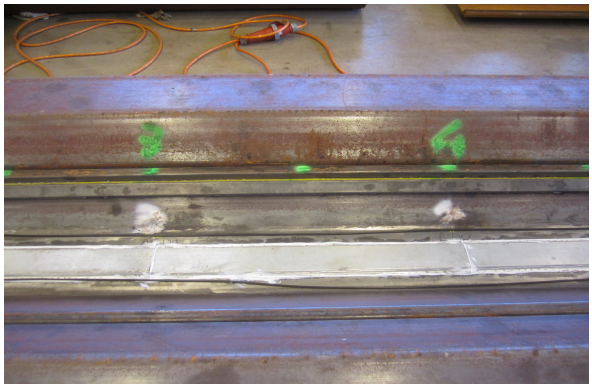

Figure 4.10: FBG sensors after protection

Deformation

Deformation is monitored using Shape Accel Array Field (SAAF) sensors. These consist of multiple segments in series. Each segment has a length of 0.5m and is equipped with a multi-dimensional accelerometer. The orientation of each segment is determined by measuring the gravity field. Deformation at the top of each segment is then calculated with respect to the bottom. The bottom end of the SAAF is fixed and functions as a reference. This process is illustrated in Figure 4.11.

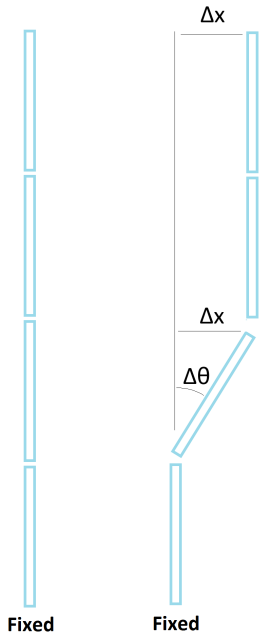

Figure 4.11: SAAF

Each of the 4 monitoring piles is equipped with a SAAF consisting of 34 elements (17m). They are installed near the locks, close to the neutral axis, to minimize strain. A detailed description of the location of each sensor can be found in Appendix A.

4.2.4. Execution

The dike will fail due to macro-instability, see section 3.2.3. The steps taken in order to instigate this mechanism are shown in figure 4.12 to 4.17.

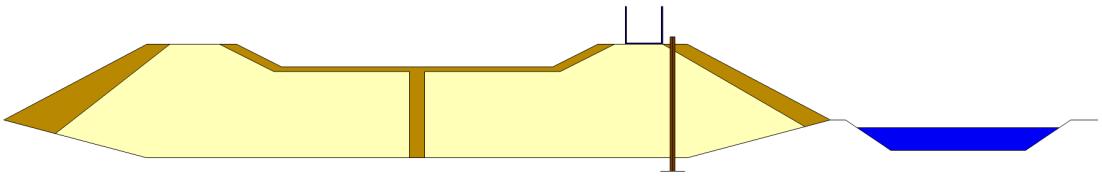

Figure 4.12: Step 1: Excavation of the soil in front of the dike to reduce factor of safety

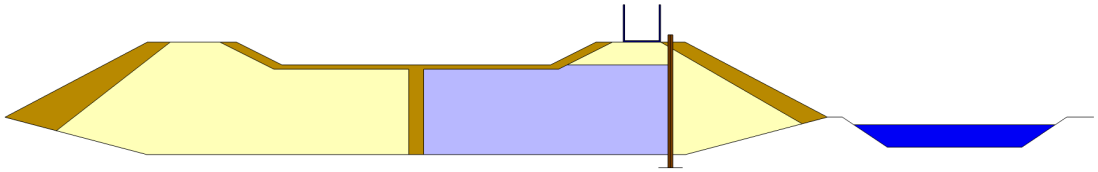

Figure 4.13: Step 2: Infiltration of the dike body to increase hydrostatic load.

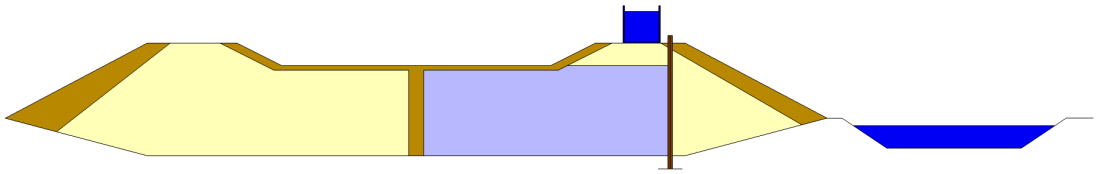

Figure 4.14: Step 3: Filling of the containers to increase the earth pressures.

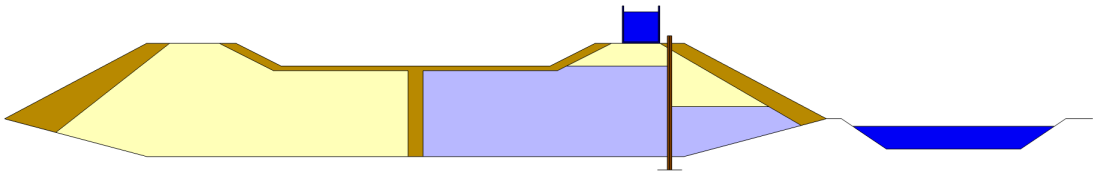

Figure 4.15: Step 4: The outer toe of the dike is infiltrated resulting in a reduction of the effective stress.

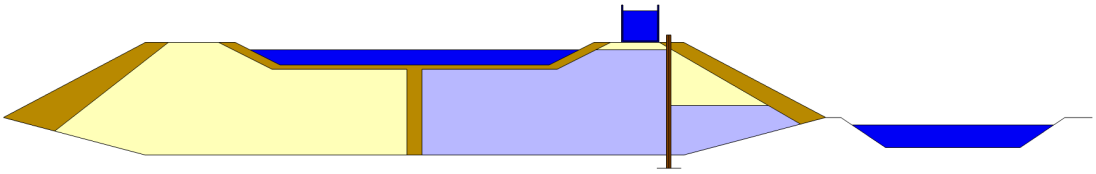

Figure 4.16: Step 5: Further increase of the hydrostatic pressure by filling the basin

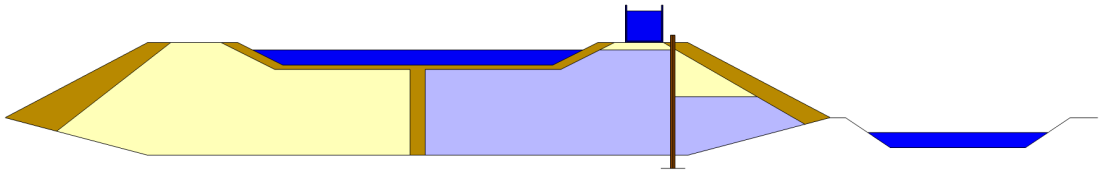

Figure 4.17: Step 6: To reduce the resisting water pressure on the sheet pile wall, the water level in the basin in front of the dike is lowered until failure occurs.

As a result, failure occurred over a circular sliding plane by means of macro-instability. This is shown in figure 4.18 and 4.19.

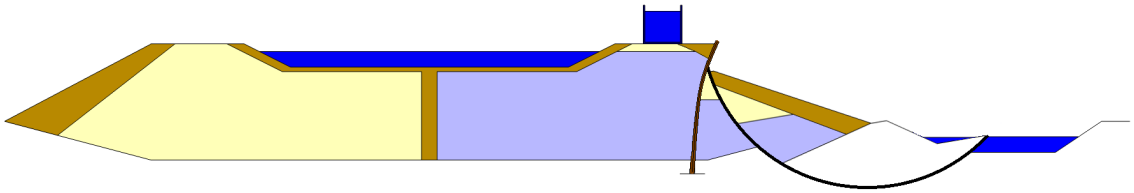

Figure 4.18: Failure of the dike (schematic)

Figure 4.19: Failure of the dike (test site)

4.3. Pull-over test

The motivation of the pull-over test was to investigate the influence of different pile configurations on the behavior. Both class 3 and class 4 piles were tested. Furthermore, the influence of a continues vs discontinues wall on the behavior was tested.

4.3.1. Test set up

Four pile configurations were tested, namely:

- Triple GU8N
- Triple GU8N-reversed (GU8R)
- 3-double AZ13-700
- 3-double AZ26

These are shown in figure 4.20.

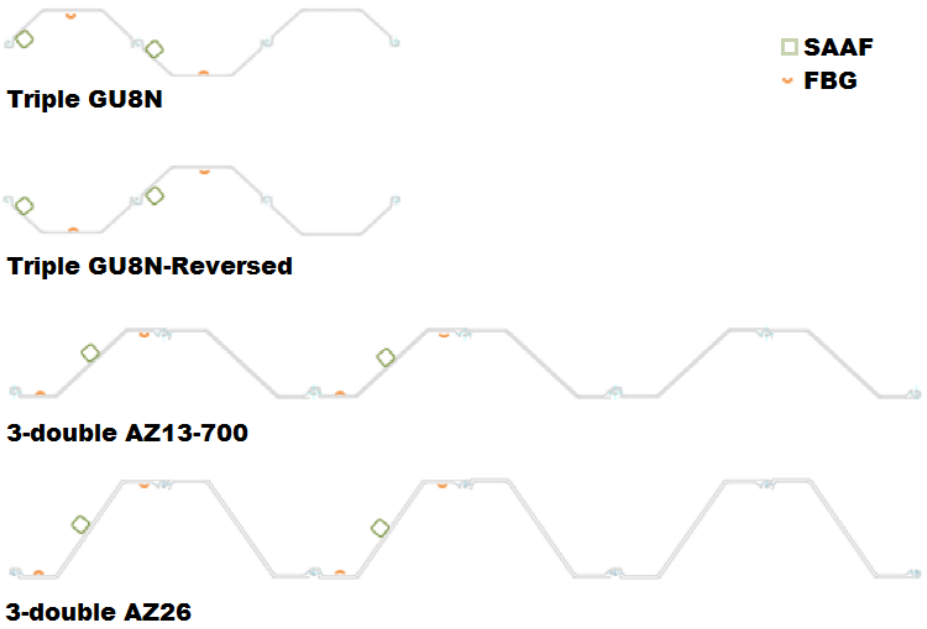

Figure 4.20: POT: Tested pile configurations

For comparison with the full-scale test, the same triple GU8N profile is tested. Triple U profiles can have either one or two compression flanges, depending on the load direction. For comparison, the test is performed in both directions. To relate to the more commonly used profiles, two AZ sections have been included in the test. The AZ26 is a class 2 profile, which is expected to reach the full plastic capacity before failure. The AZ13 is a class 3 profile, for which buckling is expected to occur before the full plastic moment is reached.

Each profile is subjected to a pulling force as shown in figure 4.21.

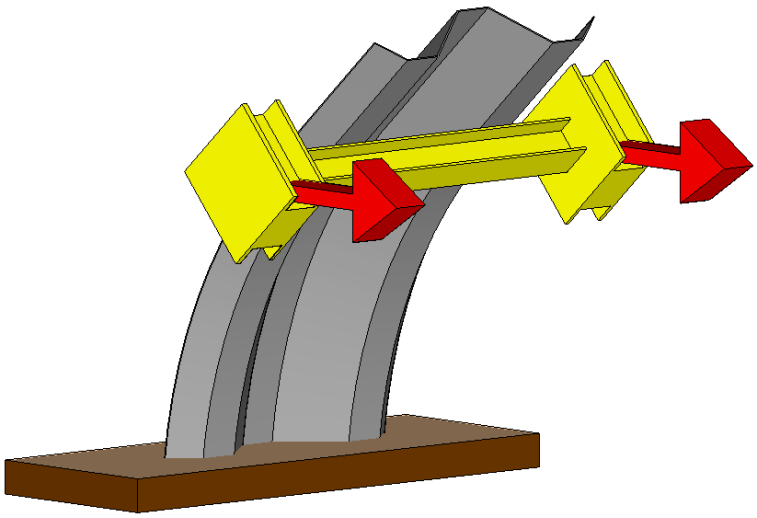

Figure 4.21: POT overview

The top view of the test is illustrated in figure 4.22.

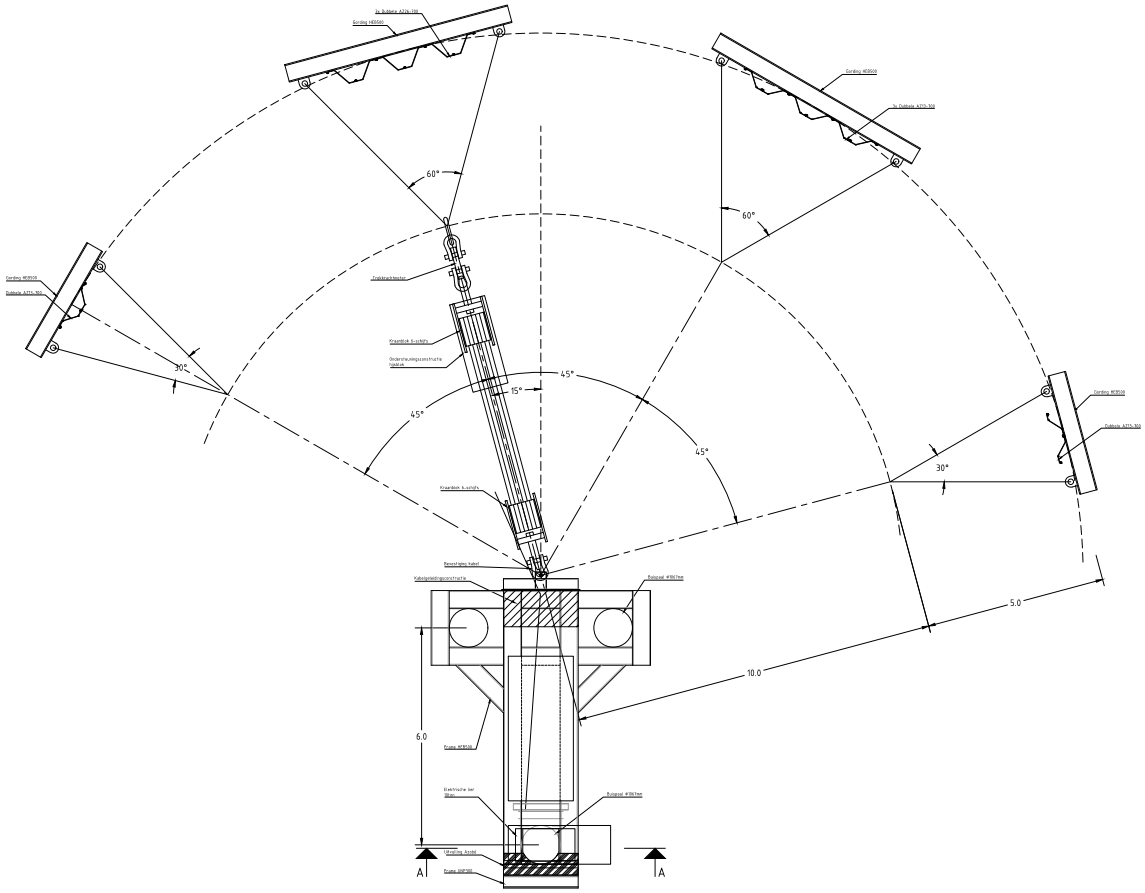

Figure 4.22: POT: Top-view test set-up (F. Sa)

4.3.2. Monitoring

With regard to studying the behavior during failure, an extensive monitoring program was set up. Out of the 21 piles used in the test, 10 piles have been equipped with sensors for monitoring. The monitored quantities are the same as in the full-scale test and include:

- Strain (FBG sensors)
- Deformation (SAAF sensors, measuring prisms)
- Reaction force (Load cell)

The sensor location for the GU8N-reversed are shown in figure 4.23. For a detailed description about the different sensors see 4.2.3. For a detailed description of the sensor locations of all tests, see Appendix A.

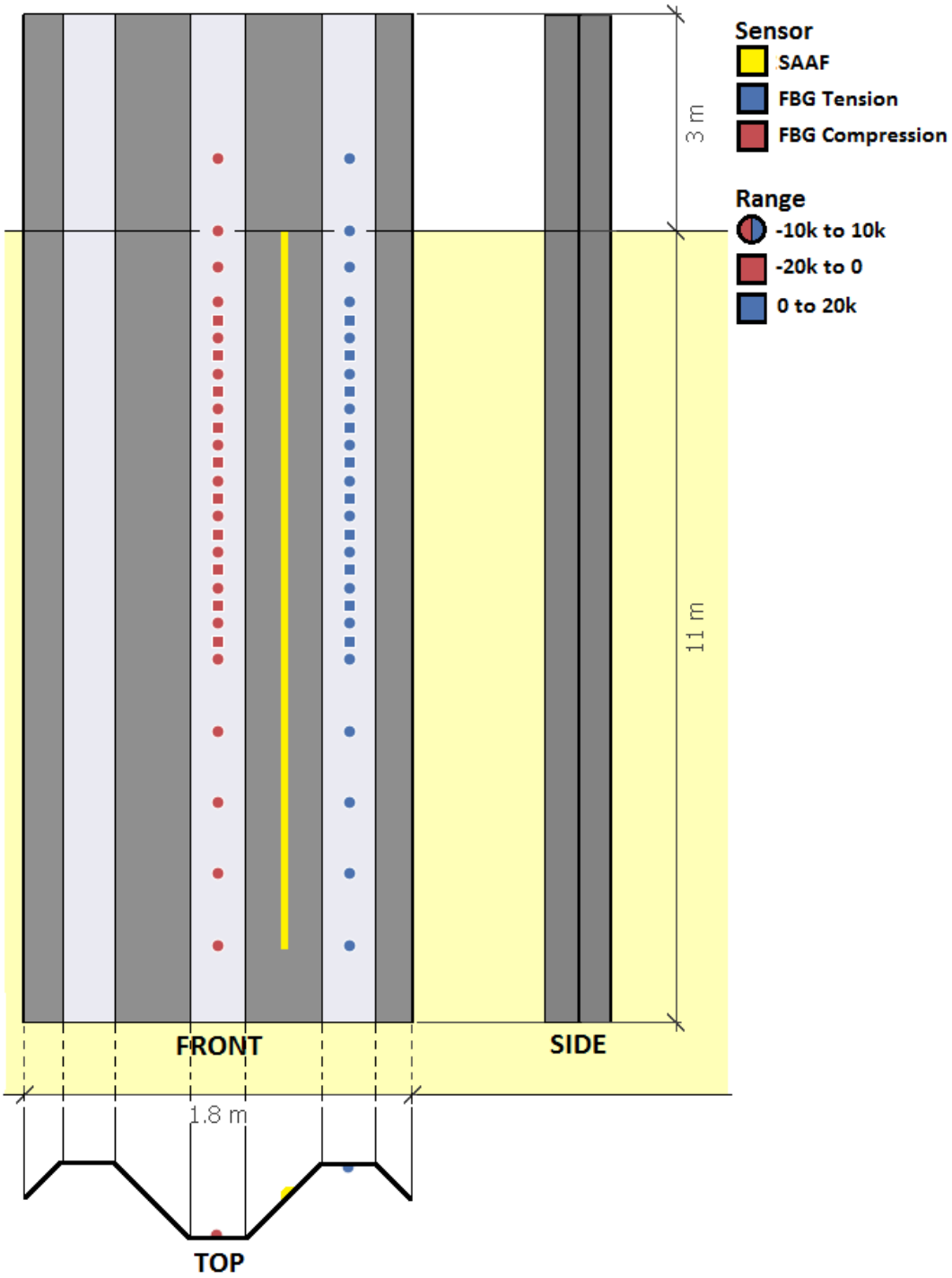

Figure 4.23: Location sensors GU8N-Reversed

FBG
The FBG sensors perform strain measurement in length direction, with an interval of one minute.

SAAF
The SAAF sensors are 10m long and measure the deformations with an interval of one minute.

Measuring prisms
The measuring prisms are installed as shown in figure 4.24.

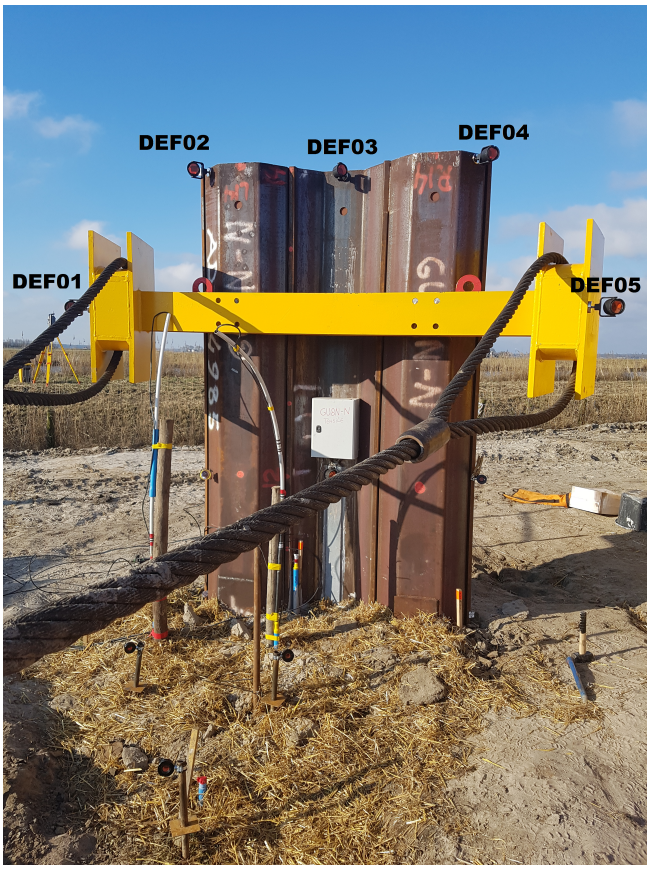

Figure 4.24: GU8N: Measuring prism set-up

Deflections of the prisms are measured by a total station every 2-5 minutes.

4.3.3. Execution
The POT tests were executed in the order as shown in table 4.2.

Table 4.2: Execution of POT tests

Profile	Date [dd-mm-yyyy]	t_{start} [hh:mm]	t_{end} [hh:mm]	T_{min} [°C]	T_{max} [°C]
AZ13-700	23-02-2018	11:00	16:30	-3.2	2.7
GU8N	27-02-2018	11:30	16:30	-8.4	0.3
GU8N-Reversed	02-03-2018	12:30	16:00	-6.2	0.8
AZ26	06-03-2018	11:00	16:30	-1.7	11.1

During the GU8N tests were performed during frost conditions. As a result, the topsoil was frozen. Accordingly, the earth pressures exerted by this layer were increased.

The test is performed displacement controlled with a rate of 1 cm/min. This is continued until one of the following stop criteria is reached:

- Horizontal displacement of 0.5 m at the top of the sheet pile.
- Horizontal displacement of 2.0 m at the hydraulic jack.
- Pulling force of 400 and 1200 kN for the U and Z-sections respectively.
- Reduction of the pulling force of 30%, which indicates sufficient reduction after the collapse.

Furthermore, the SAAF can withstand a limited amount of rotation before it will break. In order to preserve them for the other tests, they are removed when the following horizontal displacement is observed at the hydraulic jack:

- GU8N: 0.30 m
- GU8N-Reversed: 0.30 m
- AZ13-700: 0.35 m
- AZ26: 0.60 m

Figure 4.25 shows the GU8N profile after completion of the test.

Figure 4.25: POT result

5

Measurement results

5.1. Introduction

The data gathered data is analyzed in order to determine the behavior of the sheet pile wall during the tests. First, the pull-over tests are analyzed, since the acting forces and moment distributions are less complex than in the full-scale test. Afterward, the obtained methods and knowledge are applied to study the behavior of the sheet pile in the full-scale test. A flow chart of the different data streams of the POT is shown in figure 5.1.

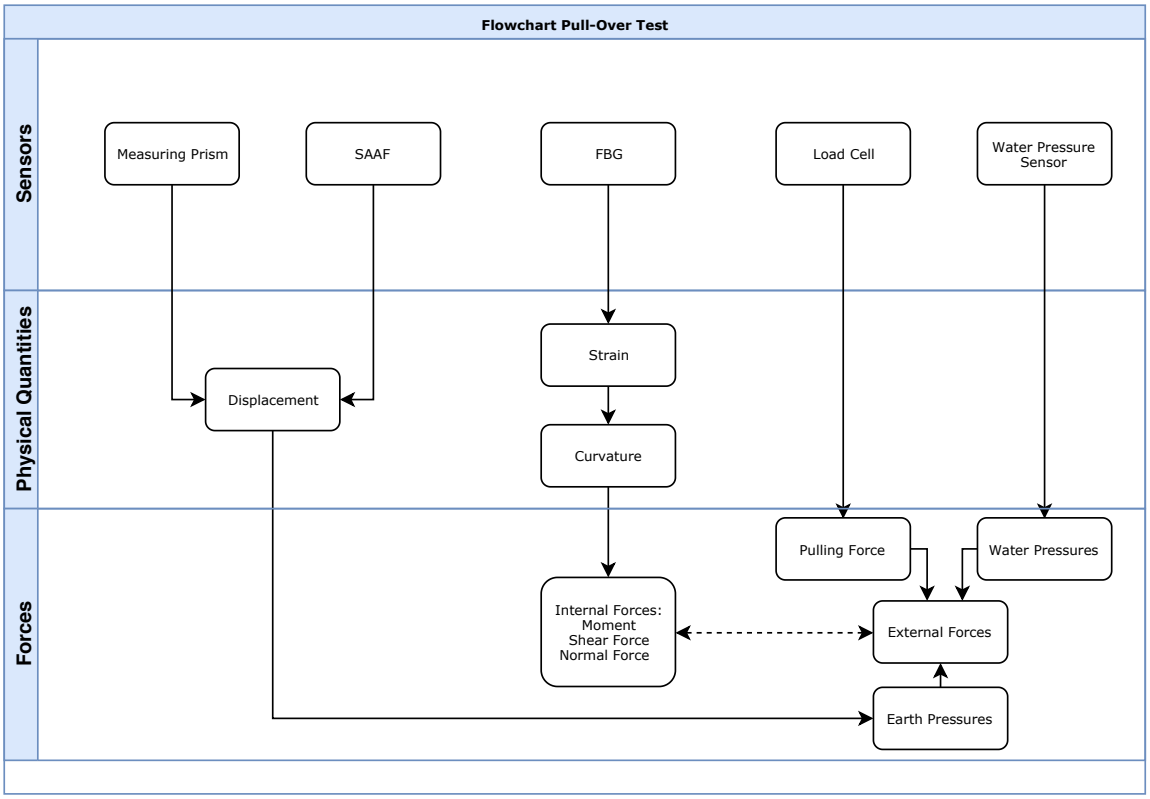

Figure 5.1: POT: Flowchart data streams

First, the load and displacements are analyzed. A prediction is made for the displacement behavior and afterward, the gathered data is checked to be in accordance with this prediction. Since both the SAAF and measuring prisms monitored the displacement, a comparison between the two is performed as a verification. Subsequently, the strain data is considered. The measured strains are compared to predictions and as a verification, a comparison is made between the strain and load data. As an extra verification step, the strains are compared with predictions from SAAF measurements.

5.2. Loads

All POT tests were performed displacement controlled. The resulting loads were monitored during the test. The measured signal for each test is shown in figure 5.2 to 5.5.

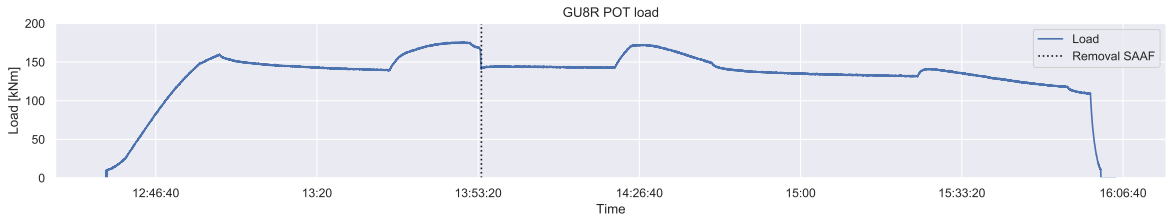

Figure 5.2: GU8R: Load signal

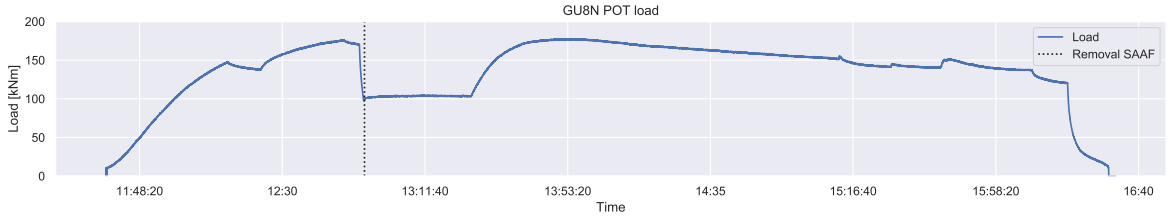

Figure 5.3: GU8N: Load signal

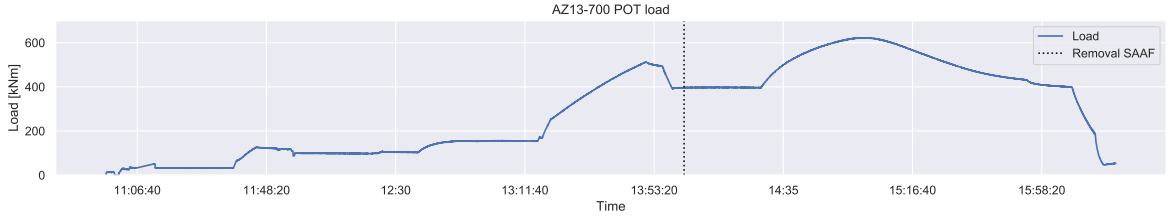

Figure 5.4: AZ13-700: Load signal

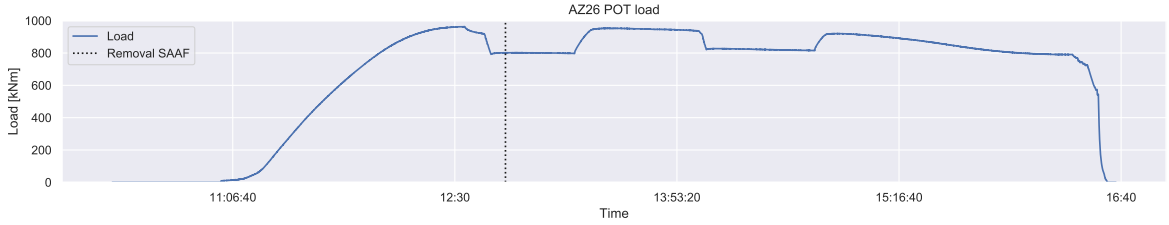

Figure 5.5: AZ26: Load signal

At a certain displacement, the load is reduced such that the SAAF sensors could be removed before they broke. The time at which this happened is indicated by the dashed line. For all tests except the AZ13-700, the maximum pulling force was reached before the SAAF was removed.

5.3. Displacements

5.3.1. Prediction

For all 4 push-over tests the sheet piles extends to NAP+3m and the pulling force is applied at NAP+2m, see 5.6.

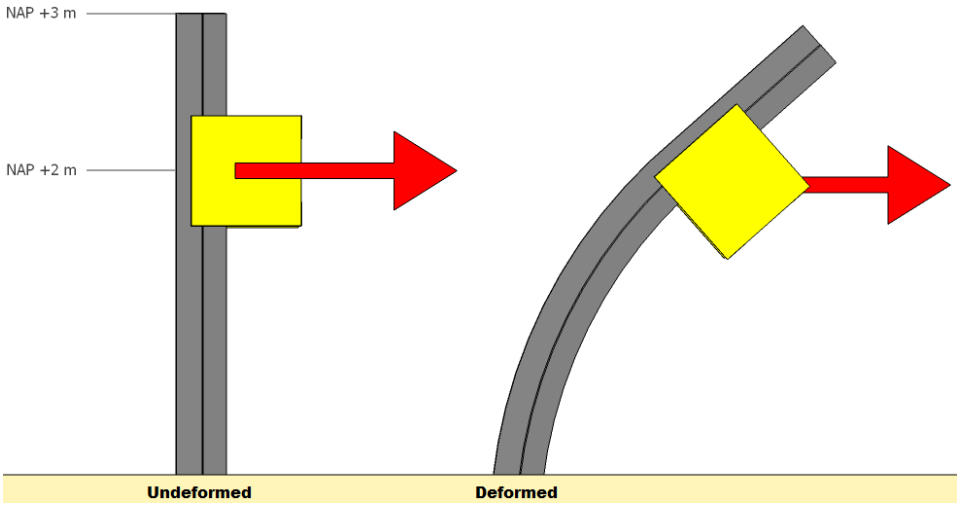

Figure 5.6: POT: Undeformed and deformed shape

The installation depth varies between NAP-13m, for the AZ26, and NAP-11m for the other profiles. With this depth, no displacements are expected at the bottom end of the sheet pile. The behaviour can be compared to a cantilever beam with the displacement proportional to the acting force. The expected displaced shape will then consist of three parts:

- Above the load application where there is no force acting and accordingly a linear development of the displacements.
- The load influence will only reach to a certain depth, below this depth the sheet pile remains vertical.
- Between these linear parts, the development of displacement is expected to be curved.

A schematization of acting forces, moments and displacements is given in figure 5.7.

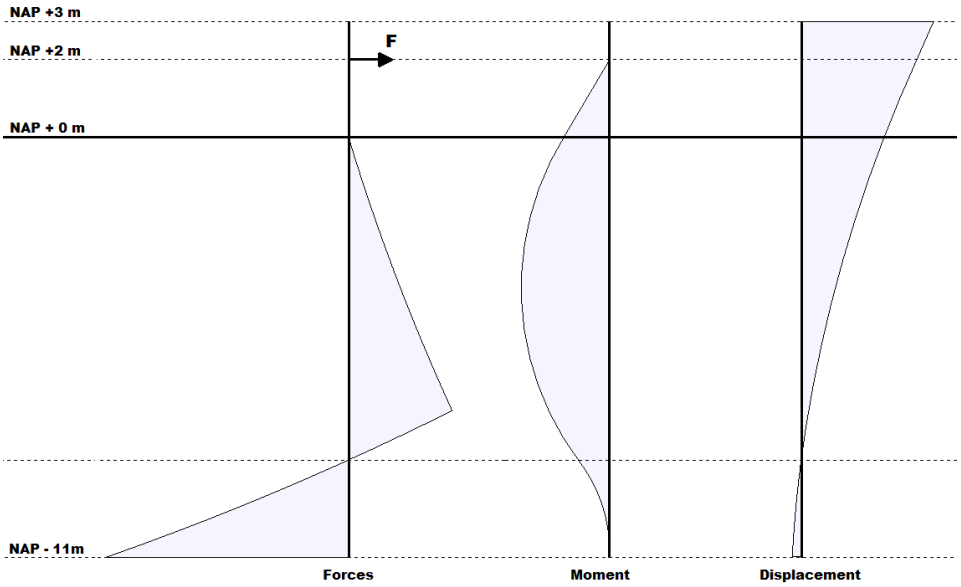

Figure 5.7: Schematisation of acting forces, and corresponding moments and displacements

5.3.2. Measuring prisms

With the measuring prisms, not only displacements but also torsion can be measured. Torsion is rotation around the length axis of the sheet pile. This will result in a deviation of the deflection, between the two sides of the pile. This rotation is indicated by ϕ in figure 5.8.

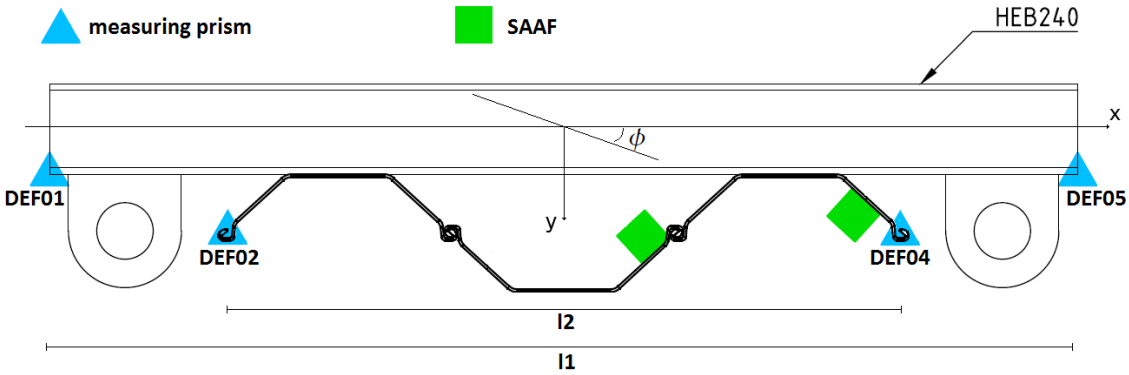

Figure 5.8: GU8N-Reversed top view: Torsion angle

A positive rotation angle ϕ, would result in a negative deflection at sensor DEF01 and a positive deflection at sensor DEF05. Accordingly, both SAAF sensors will have a positive deflection, however, the deflection for the SAAF at the side will be greater. In order to make a comparison between the two, the effect of torsion should be sufficiently small.

For all push-over tests, except for the GU8N, a positive ϕ will result in a greater deflection, and thus a greater average curvature at the side. For the GU8N, the side SAAF is placed at the opposite side. A positive ϕ will thus result in a lower average curvature since both deflections will be negative. The torsion angle ϕ is defined as shown in figure 5.9.

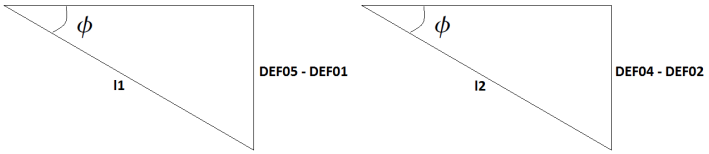

Figure 5.9: Definition of torsion angles

And is calculated as follows:

$$\phi_{1,5} = sin^{-1}(\frac{DEF05 - DEF01}{l1}) \tag{5.1}$$

$$\phi_{2,4} = sin^{-1}(\frac{DEF04 - DEF02}{l2}) \tag{5.2}$$

The displacement and torsion are shown in figures 5.10 to 5.13.

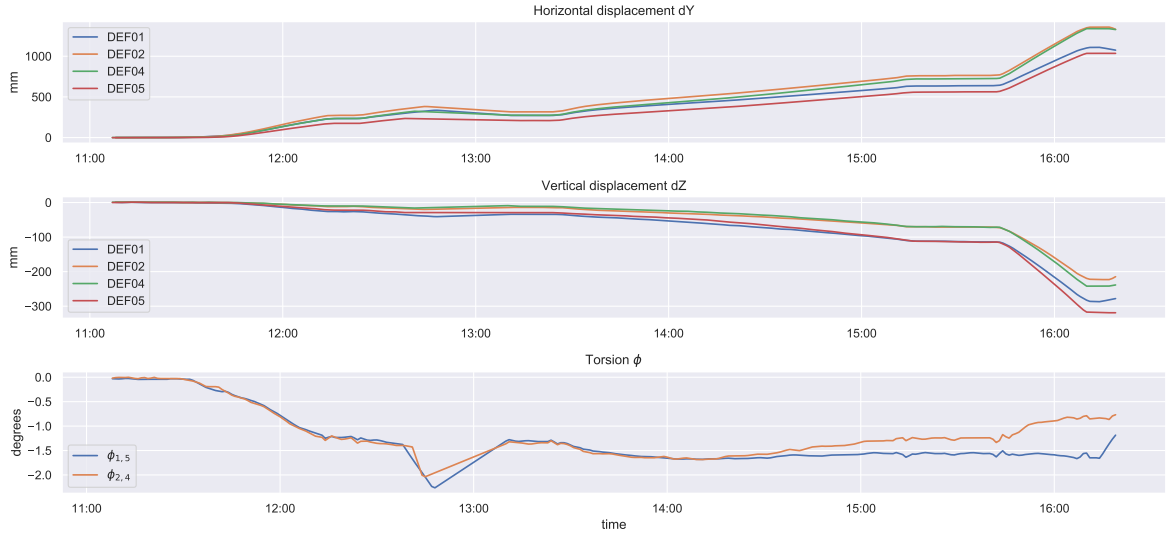

Figure 5.10: GU8N: Displacement and torsion

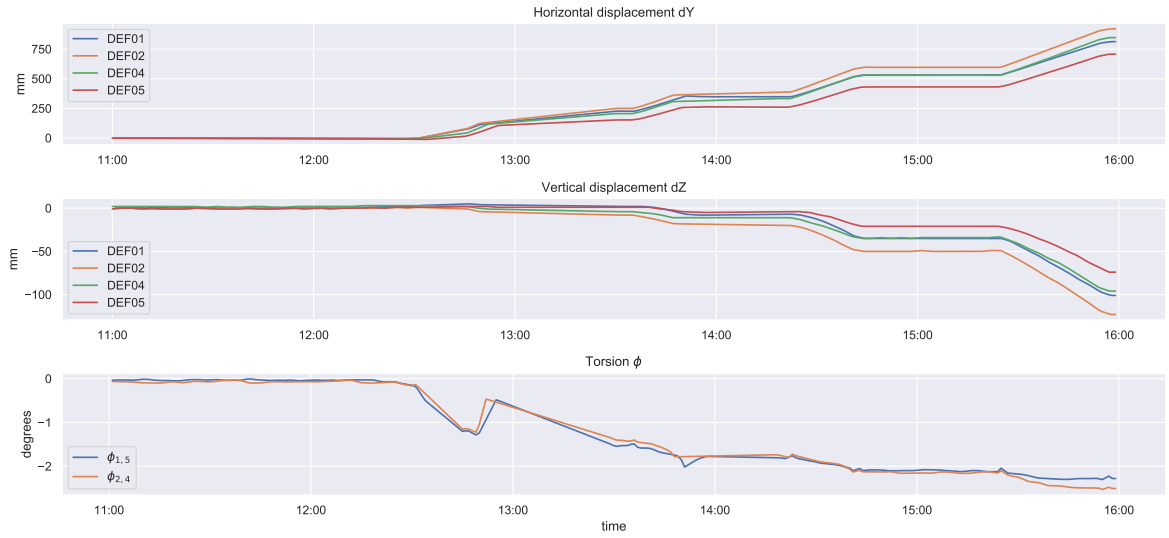

Figure 5.11: GU8N-Reversed: Displacement and torsion

Figure 5.12: AZ13-700: Displacement and torsion

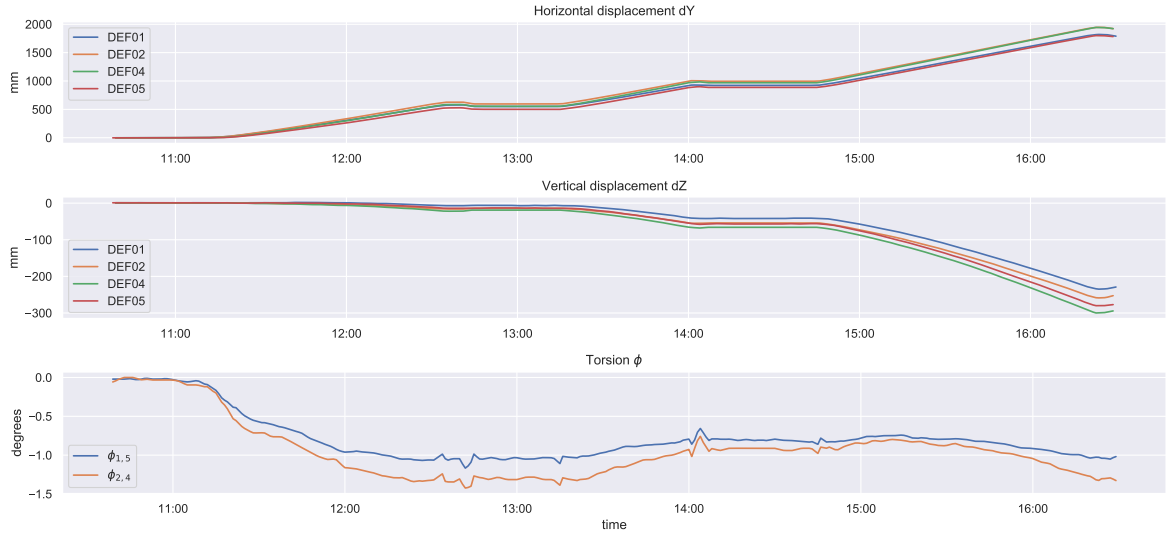

Figure 5.13: AZ26: Displacement and torsion

All the POT tests have a slightly negative torsion angle. However, the angles are small and won't have a significant influence on the tests. Furthermore, the first reading of both the DEF01 and DEF05 prism of the AZ13-700 took place after initiation of the test. For this reason it is impossible to bench mark the results and accordingly they have been excluded.

Trajectories

The measuring prisms are also used to illustrate the displacement trajectories. These are shown in figures 5.14 to 5.17.

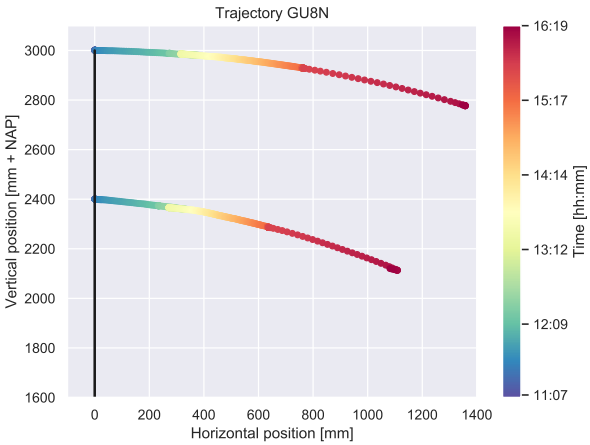

Figure 5.14: GU8N: Trajectory

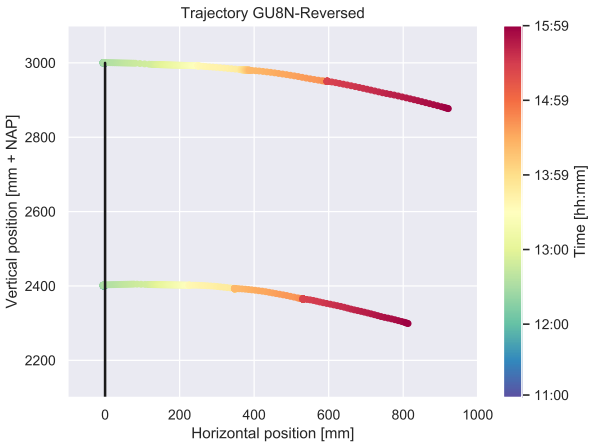

Figure 5.15: GU8N-Reversed: Trajectory

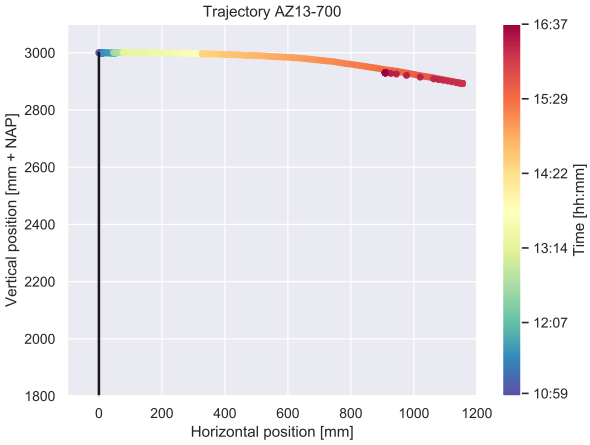

Figure 5.16: AZ13-700: Trajectory

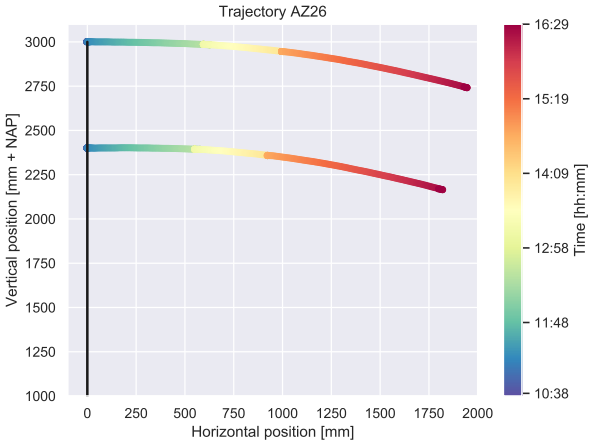

Figure 5.17: AZ26: Trajectory

There is a difference in curvature of the trajectories. The heavier sheet piles display a smaller curvature than the lighter piles. This can be explained by the distance to the plastic hinge, which is larger for heavier sheet piles. For these piles, the required pulling force is larger and this force has to be resisted by the soil. Since the soil is equal in all tests, more soil is required to resist the force and accordingly, the plastic hinge develops deeper. As a result, the radius over which the sheet pile rotates is larger.

Force-displacement curves

The displacements of the top of the sheet piles are plotted against the exerted force in figures 5.18 to 5.21. The displacements are obtained from the middle prisms (DEF03), see figure 4.24.

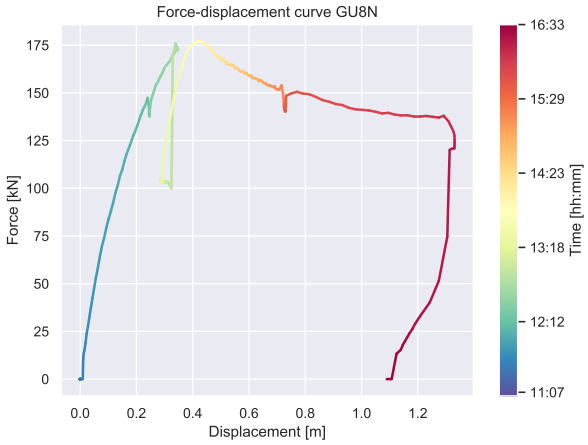

Figure 5.18: GU8N: Force-displacement curve

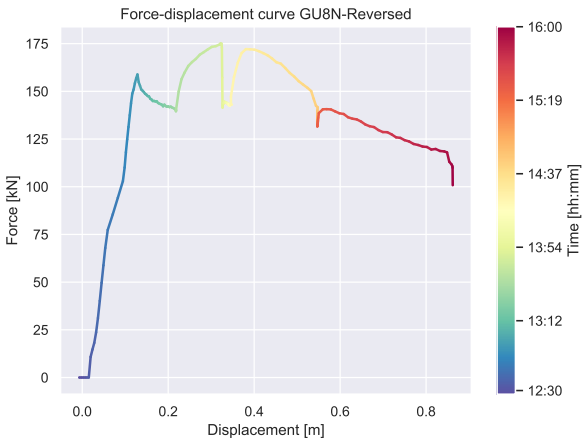

Figure 5.19: GU8N-Reversed: Force-displacement curve

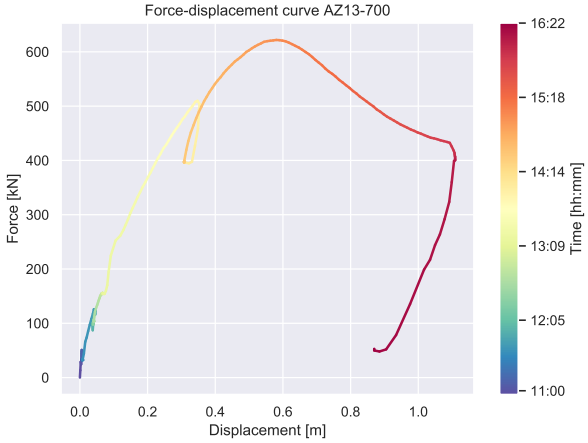

Figure 5.20: AZ13-700: Force-displacement curve

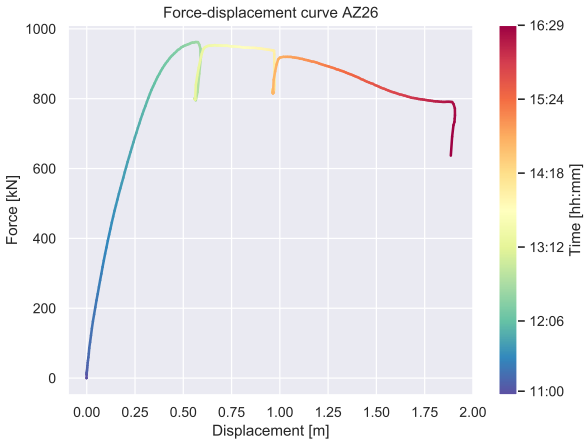

Figure 5.21: AZ26: Force-displacement curve

The first tested pile was the AZ13-700. There were some difficulties with controlling the deformation rate. This is visible at the start of this test.

The same difficulties led to a too high deformation rate at the start of the GU8N-Reversed test. As a result, the total station was not able to read the deformations of the measuring prisms and the test was interrupted for 30 minutes. This explains the drop in force, however, the increase of displacement during a decreasing force is not expected. This might be a result of pore pressures. The rapid deformation resulted in over-pressures in the soil, as a result, the soil could not further compact. During the interruption of the test, these over-pressures could dissipate and allow the soil to further compact.

Around 0.3m displacement, all profiles except the AZ26 show a drop in the exerted force. This drop is related to the removal of the SAAF as discussed in section 4.3.3. For the AZ26 this took place at a displacement of 0.6m as the plastic hinge is located at a larger distance from the top.

5.3.3. SAAF

The displacements measured by the SAAF, in the middle and at the side of the sheet pile, are shown in figure 5.22.

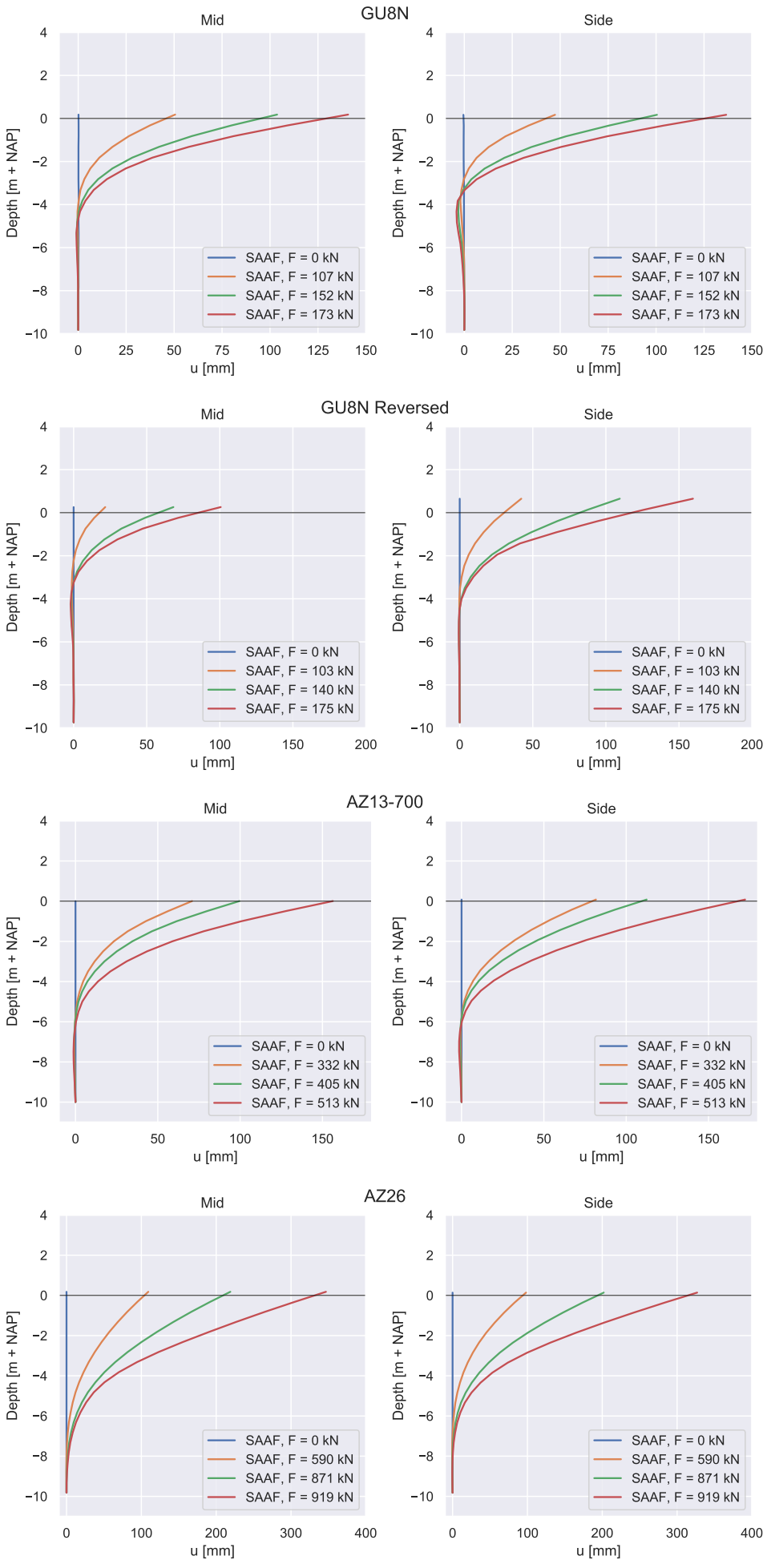

Figure 5.22: POT SAAF: Horizontal displacements

The measured displacements are in accordance with the predictions. All tests except the GU8N reversed demonstrate slightly smaller displacements at the side. This is caused by the larger earth pressures at the side, which are a result of more soil mobilization. For the GU8N reversed, however, larger displacements are observed at the side, which is questionable. In order to verify the measurements, a comparison is made with the measuring prisms.

5.3.4. Verification

The SAAF data is verified by means of comparison with prism measurements. If both sensors indicate the same deformed shape the data can be assumed accurate. In figure 5.23 to 5.26 the prism measurements are added for comparison.

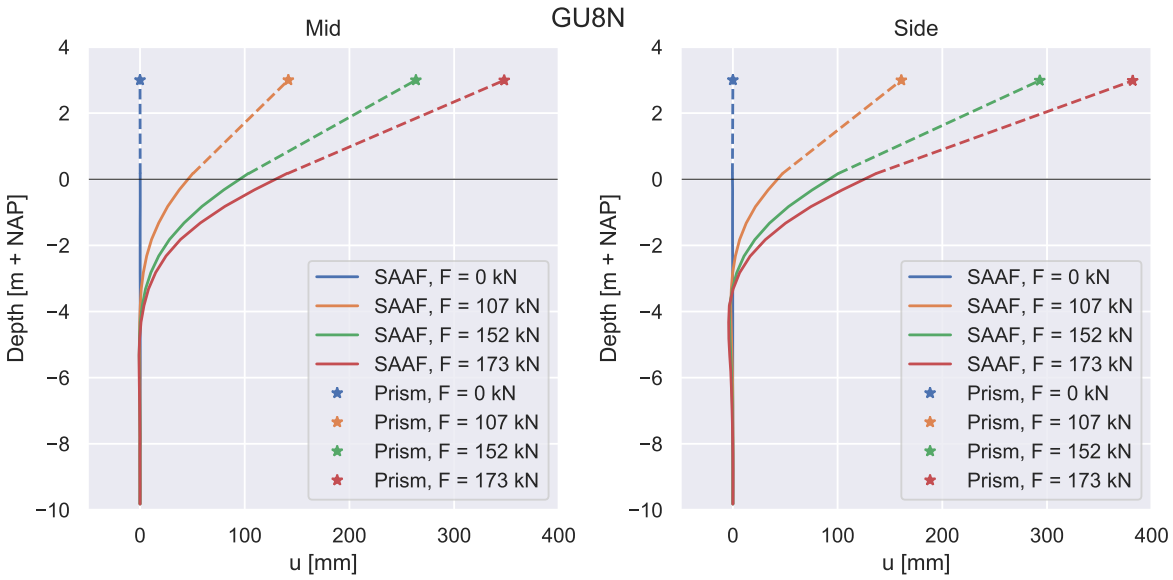

Figure 5.23: Comparison between SAAF and prism GU8N

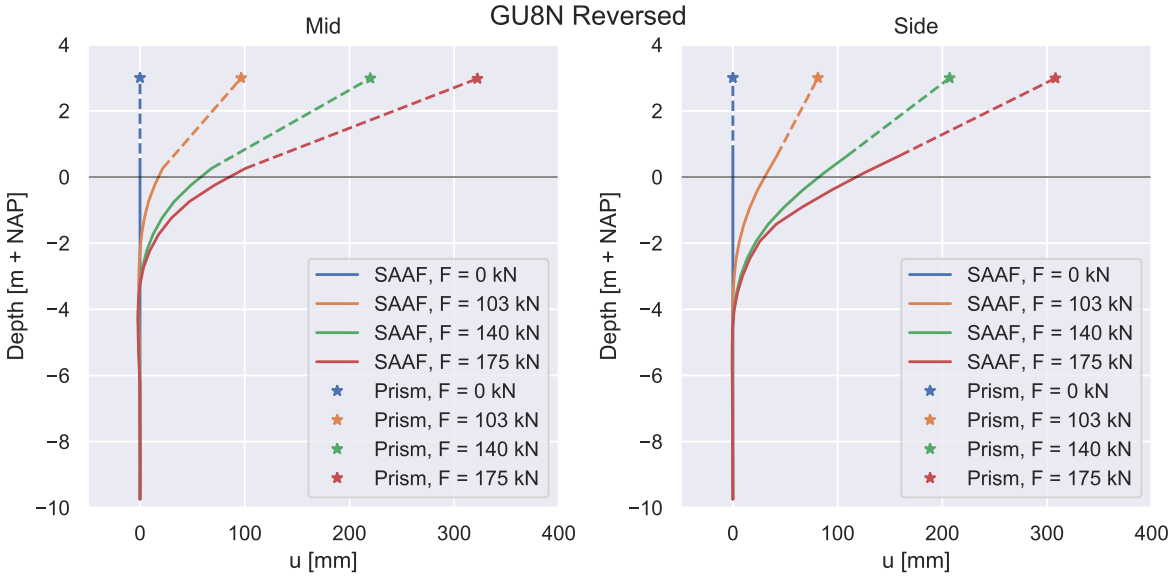

Figure 5.24: Comparison between SAAF and prism GU8N-reversed

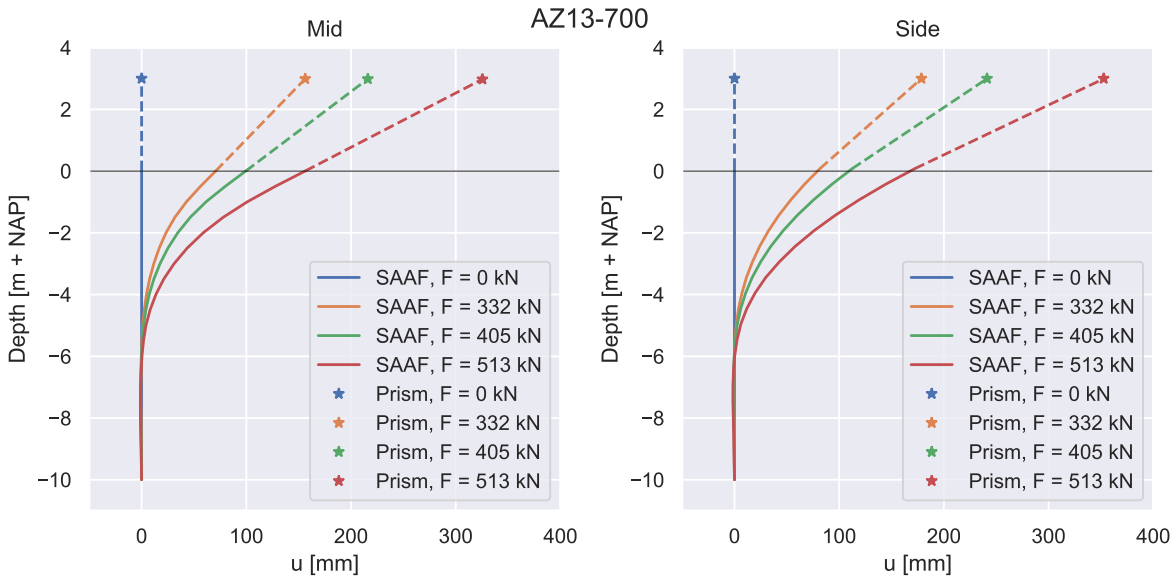

Figure 5.25: Comparison between SAAF and prism AZ13-700

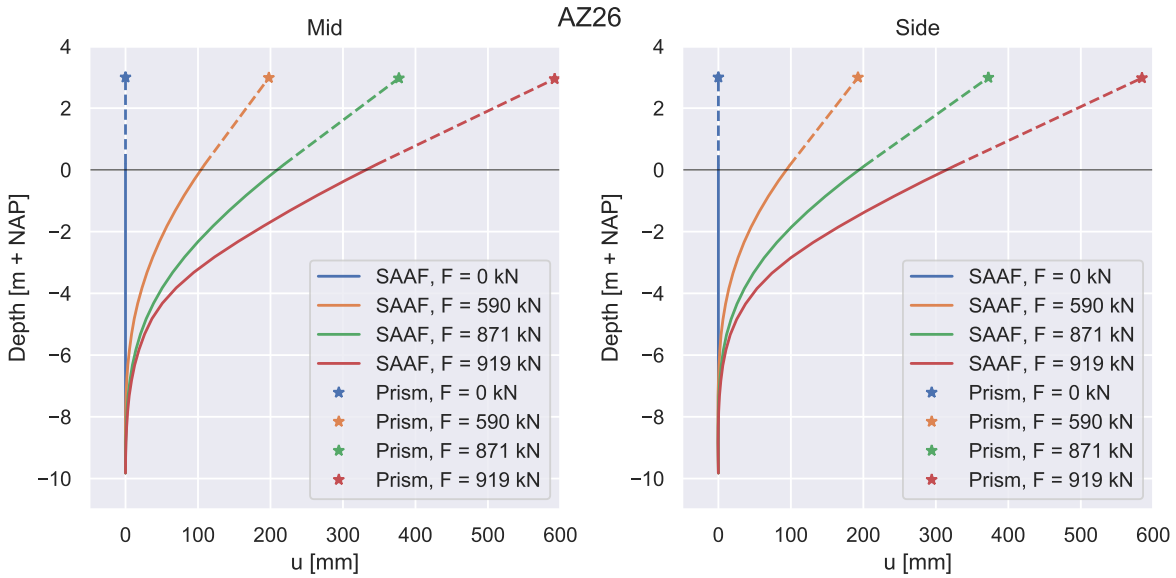

Figure 5.26: Comparison between SAAF and prism AZ26

For all tests except the GU8N-reversed, the SAAF and prism measurements are in accordance. For the GU8N-reversed, the side prism indicates a smaller deflection than the SAAF. For this reason, the reliability of the SAAF cannot be verified. Furthermore, the measurement results are in contradiction with the prediction and other measurement results. Accordingly, the side SAAF of the GU8N-reversed is excluded from further analyses.

5.4. Strains

5.4.1. Prediction

Strain ϵ is related to the curvature κ by:

$$\epsilon(x,y) = \epsilon + x\kappa_x + y\kappa_y \tag{5.3}$$

And for the elastic part, the moment can be expressed as:

$$M_y = EI_{yy} * \kappa_y \tag{5.4}$$

For this reason, the strain distribution is expected to have a similar shape as the moment distribution in figure 5.7.

5.4.2. Results

The strain analysis is rather comprehensive and the results for different tests are similar. For this reason, only the analysis is of the GU8N-Reversed profile is treated in the main report. Detailed analysis of the other profiles can be found in Appendix B. The stain development for the GU8N profile is shown in figure 5.27.

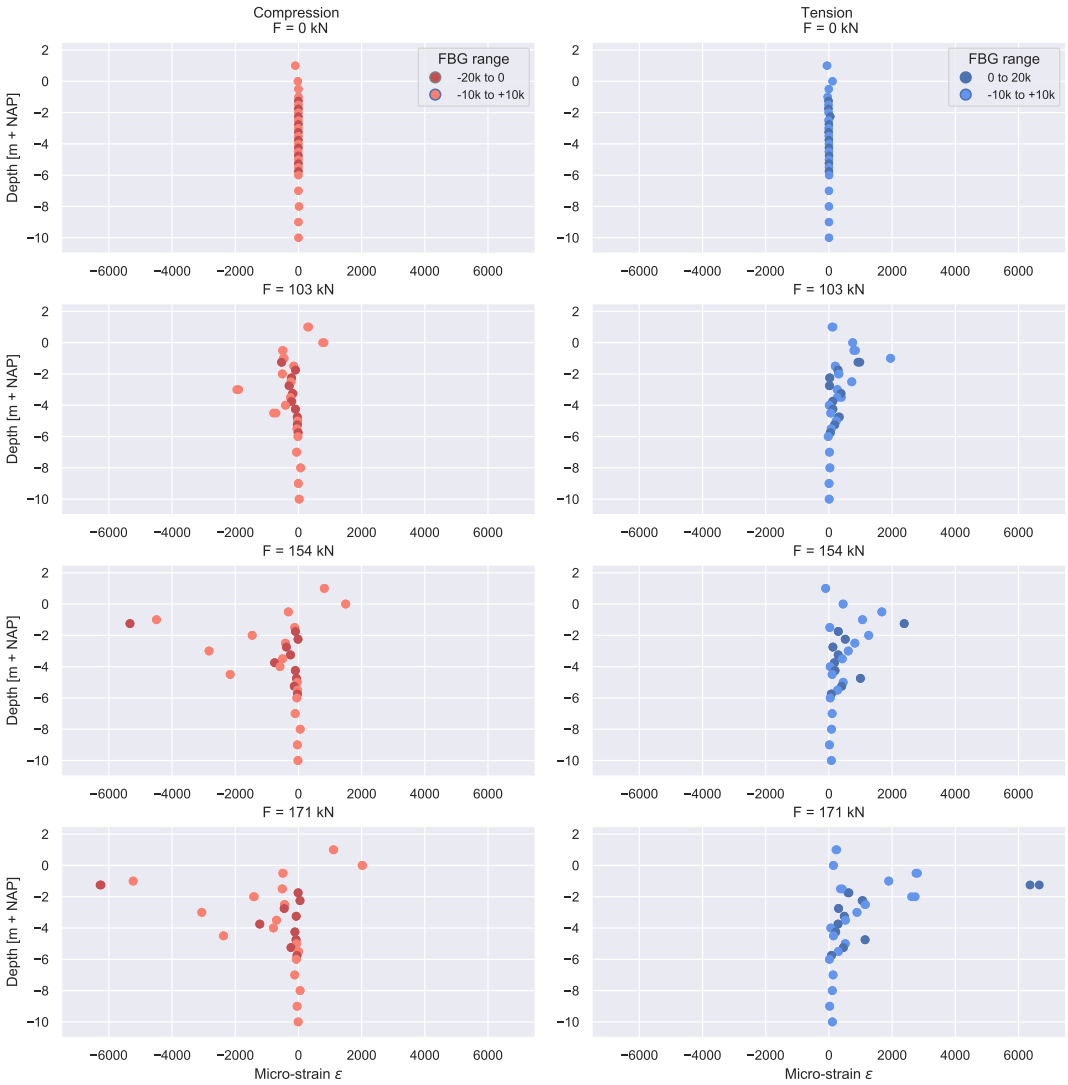

Figure 5.27: Strain development GU8N-Reversed

The following conclusions can be drawn with regards to the measured strains:

- No clear strain trajectory can be obtained from the measurements.
- A significant part of the sensors does not respond to the applied force. This includes sensors in the range where the most strain is expected (NAP-4m - NAP+0m).
- There is a large scatter between measurements. This is not in accordance with the high accuracy of the used sensors.

This behavior was observed for all tests. To identify any problems with the sensors, visual inspection of the excavated test piles was performed.

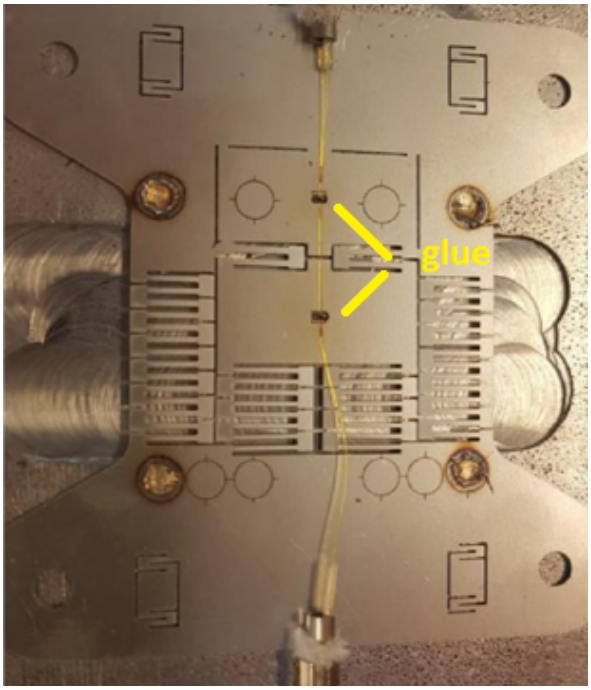

Figure 5.28: FBG sensor before test

Figure 5.29: FBG sensor after test

The glue that guarantees pre-tensioning of the fiber was not present anymore after the test. Without glue, the fiber can move freely and this allows for slip-induced errors in the measurements. However, it is not clear at what point the glue connection has failed. This could be either before, during or after the test. Part of the measurements could still be correct, but to identify which part a verification method is required, which is not available.

With the use of an innovative sensor, a back-up system should have been in place. Without a back-up system, this sensor should not have been used for all experiments. In that case, it would have been a better practice to limit the innovative sensor to one pull-over test.

5.5. Verification by the load signal

Two verification methods have been constructed in order to verify the data. In the first verification, the measured strain in each sensor is compared with the load signal. Good working sensors should have the following characteristics:

- Development of the strain and load signal should be in agreement.
- No strains should be left after load reduces to zero (no slip).

Both load and strain have been normalized for comparison. Each sensor is then assigned to one of the following classes as shown in figure 5.30 to 5.33, where the flange at which the sensor is located is indicated.

- Class 1: Good correlation with load throughout the test, no slip

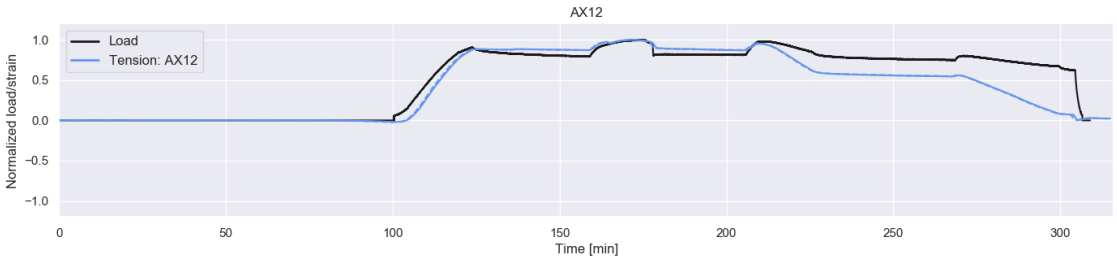

Figure 5.30: Class 1 by load verification

- Class 2: Good correlation with load throughout the test, but with residual strain (slip)

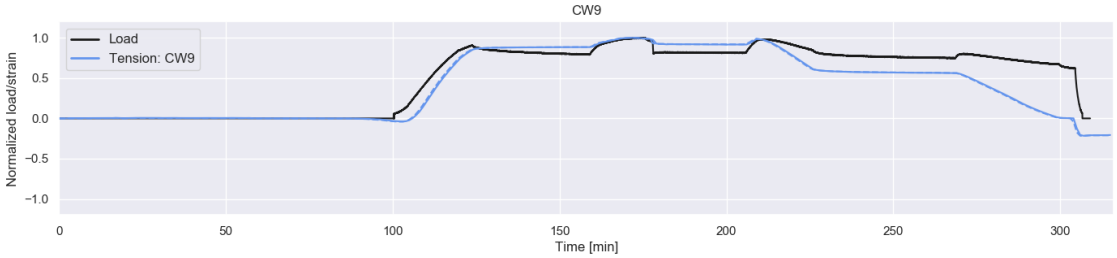

Figure 5.31: Class 2 by load verification

- Class 3: Good correlation with load during incremental loading

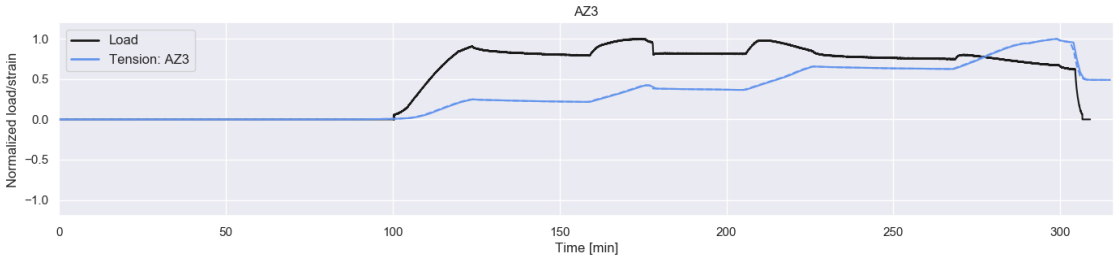

Figure 5.32: Class 3 by load verification

- Class 4: Bad correlation with load

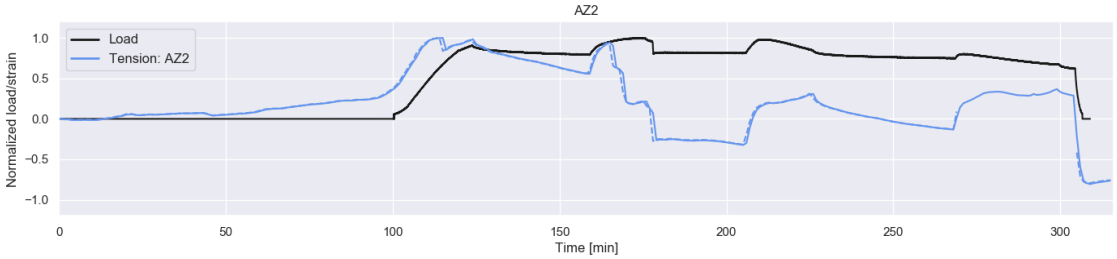

Figure 5.33: Class 4 by load verification

This resulted in the class distribution shown in 5.34.

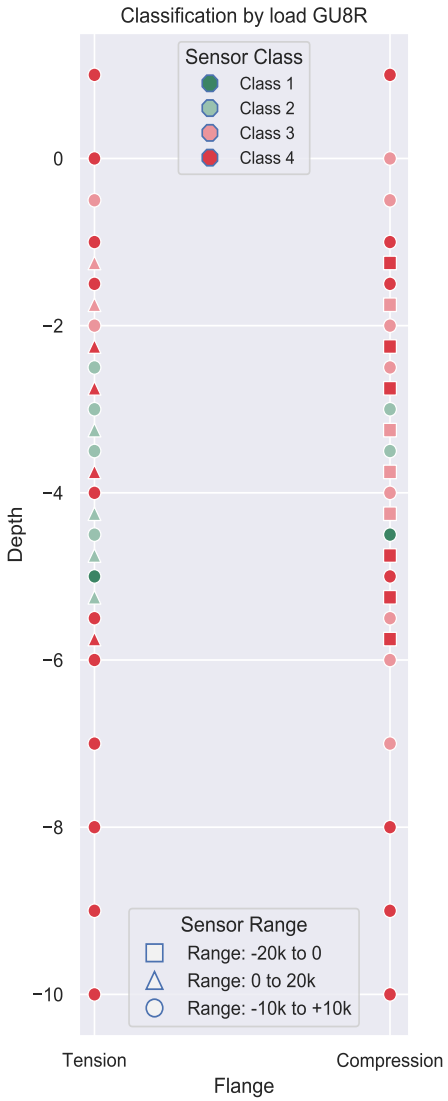

(a) Overview sensor class and measurement range

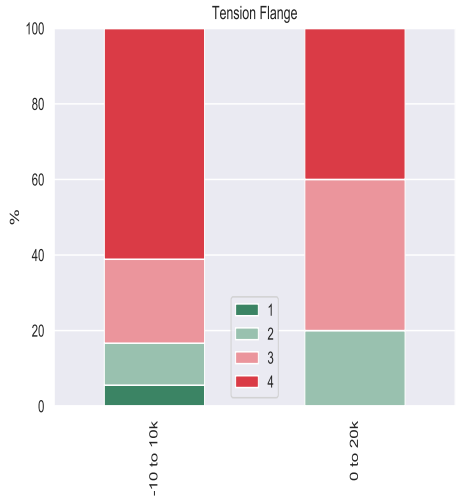

(b) Class distribution tension flange

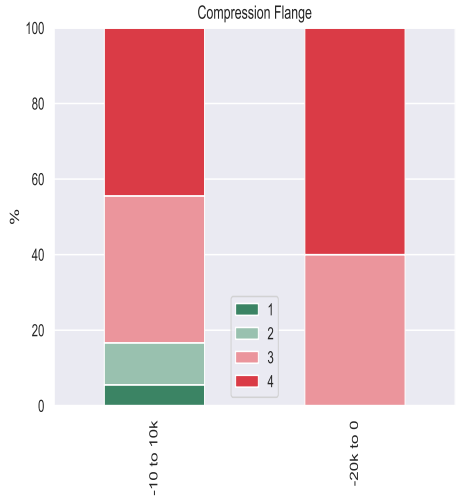

(c) Class distribution compression flange

Figure 5.34: GU8R: FBG classification by load

From the classification, it follows that a large part of the sensors failed before the test. A possible explanation might be the friction-induced heat during the installation process. Possibly the used glue was not sufficiently heat resistant. Although a large part of the sensors failed, a small part of the sensors has a good correlation with the applied load and might have produced valid data.

5.6. Verification by strain estimation

5.6.1. Method

As a second verification step, the strain is estimated from displacements measured with the SAAF sensors. The strain can be expressed as:

$$\epsilon(x,y) = \epsilon + x\kappa_x + y\kappa_y \tag{5.5}$$

In which ϵ is the strain induced by normal force, κ_x and κ_y are the curvatures parallel and perpendicular to the dike respectively. κ_x is negligible compared to κ_y. Furthermore, there are no vertical forces acting on the sheet pile wall and thus no strains due to normal forces. Equation 5.5 can, therefore, be simplified into:

$$\epsilon(z) = y\kappa_y \tag{5.6}$$

The curvature κ can be related to the deflection u by:

$$\kappa_y = -\frac{\mathrm{d}^2 u_y}{\mathrm{d}z^2} \tag{5.7}$$

This second order derivative is estimated by the following numerical scheme:

$$\frac{\mathrm{d}^2 u_y}{\mathrm{d}z^2} = \frac{u_y(z+h) - 2u_y(z) + u_y(z-h)}{h^2} + \mathcal{O}(h^2) \tag{5.8}$$

In which the step-size h is equal to the SAAF element length of 0.5m.
To determine the strain at the location of the sensor, the obtained curvature is multiplied with the y-coordinate of the sensor as shown in 5.35

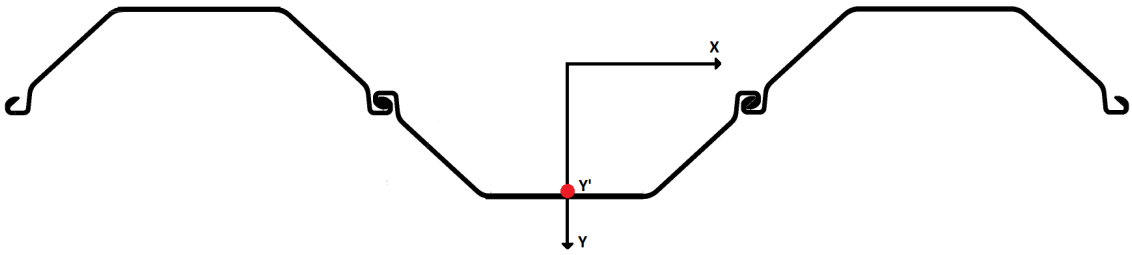

Figure 5.35: Y coordinate of FBG sensor

5.6.2. Errors

Several errors are taken into account:

- The error related to the sensor accuracy
- The error introduced by the numerical scheme in order to calculate the second derivative

Measurement error

The accuracy for a SAAF sensor with a length of 32m is 1.5mm [16]. The influence of the total length is illustrated in figure 5.36.

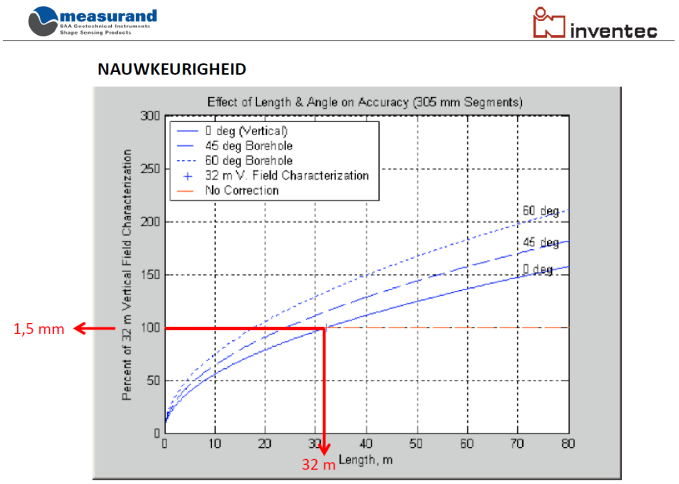

Figure 5.36: Accuracy SAAF

The error doe not vary linearly, but with the square root of the length. The length over which the curvature is determined is equal to 1m. The maximum error of this length is given by:

$$\epsilon_{1m} = \frac{1.5}{\sqrt{\frac{32}{1}}} = 0.27mm \tag{5.9}$$

This error is taken into account in the numerical scheme as shown in 5.37.

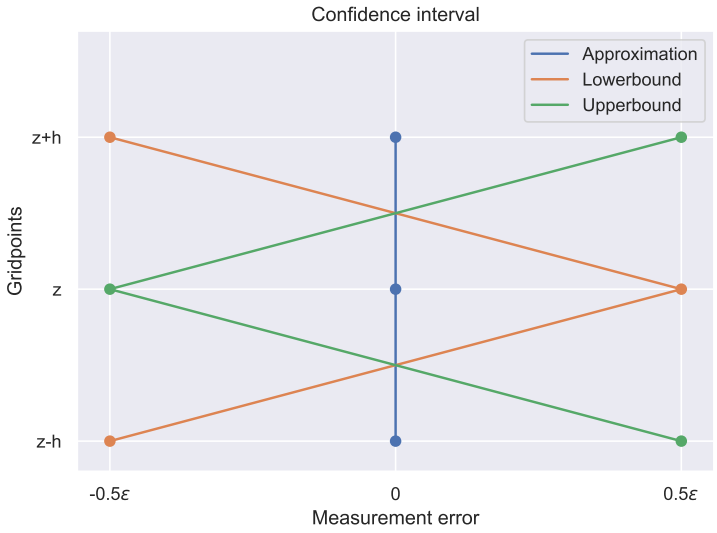

Figure 5.37: Confidence interval numerical approximation

Numerical error

Furthermore, the error introduced by the numerical scheme has to be taken into account. The second derivative is calculated by means of central differences which is second-order accurate, $\mathcal{O}(h^2)$. This means that the error isn't exactly known, but it can be estimated by:

$$c * h^2 \tag{5.10}$$

In which c is an unknown constant. However an approximation can be done by means of Richardson extrapolation. The same calculation is done with a step-size of 2h. This will result in the following set of equations:

$$\kappa_{y,h} = \frac{\mathrm{d}^2 u}{\mathrm{d}z^2} = \frac{u(z+h) - 2u(z) + u(z-h)}{h^2} + c * h^2 \tag{5.11}$$

$$\kappa_{y,2h} = \frac{\mathrm{d}^2 u}{\mathrm{d}z^2} = \frac{u(z+2h) - 2u(z) + u(z-2h)}{(2h)^2} + c * (2h)^2 \tag{5.12}$$

An approximation of the constant c can now be obtained by:

$$c = \frac{\kappa_{y,h} - \kappa_{y,2h}}{(2^2 - 1)h^2} \tag{5.13}$$

This is an estimation of the error between step-sizes of 0.5m and 1m. Since 0.5m is already too coarse to capture local variations at a plastic hinge, this estimate is an underestimation of the real error. This is indicated in 5.38

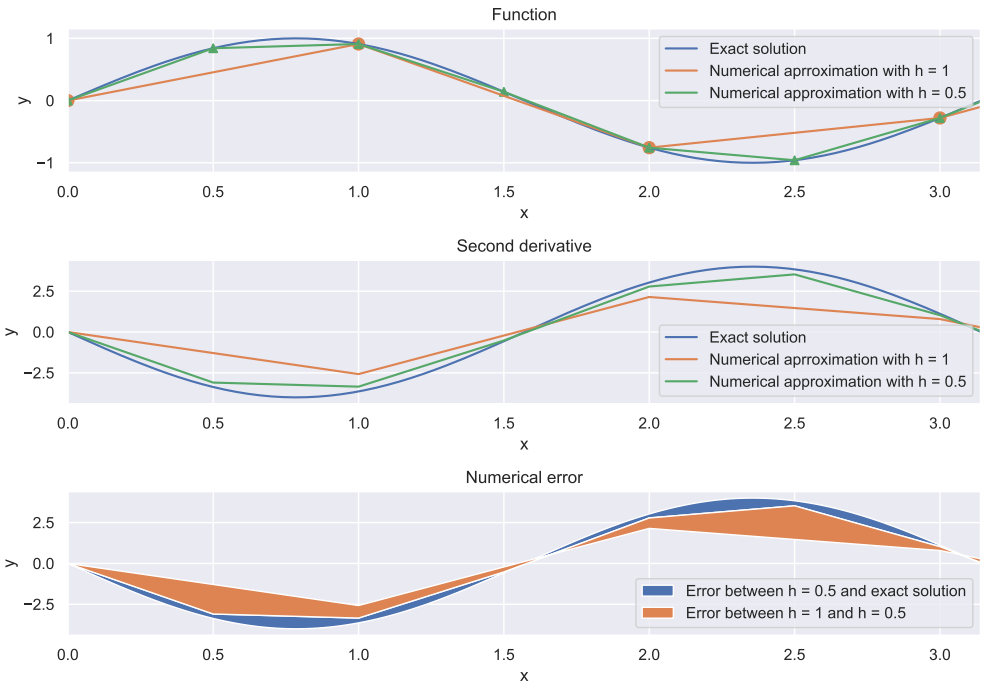

Figure 5.38: Numerical error underestimation

Since there is an underestimation of the numerical error, a multiplication is performed with a certain factor. This factor is determined such that the development of the curvature is in accordance with the expectations, i.e. without wiggles. A sensitivity analysis of this factor is shown in 5.39

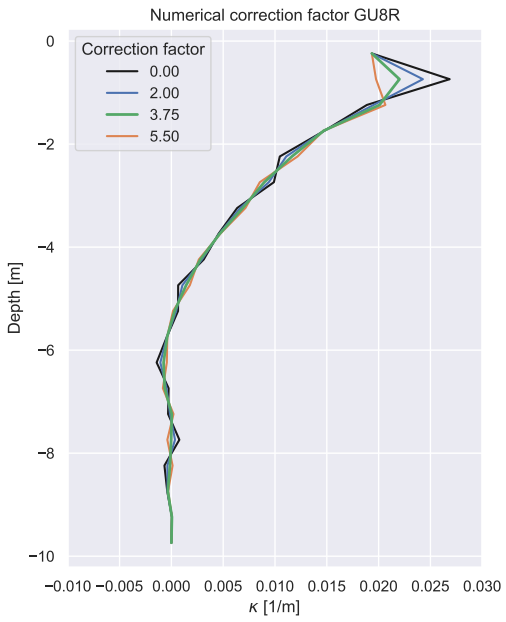

Figure 5.39: Determination of numerical factor GU8R

This resulted in a correction factor of 3.75 for the GU8R profile.

5.6.3. Strain estimation

Following the procedure and taking into account the errors described in this chapter, the strain distribution shown in 5.40 is obtained.

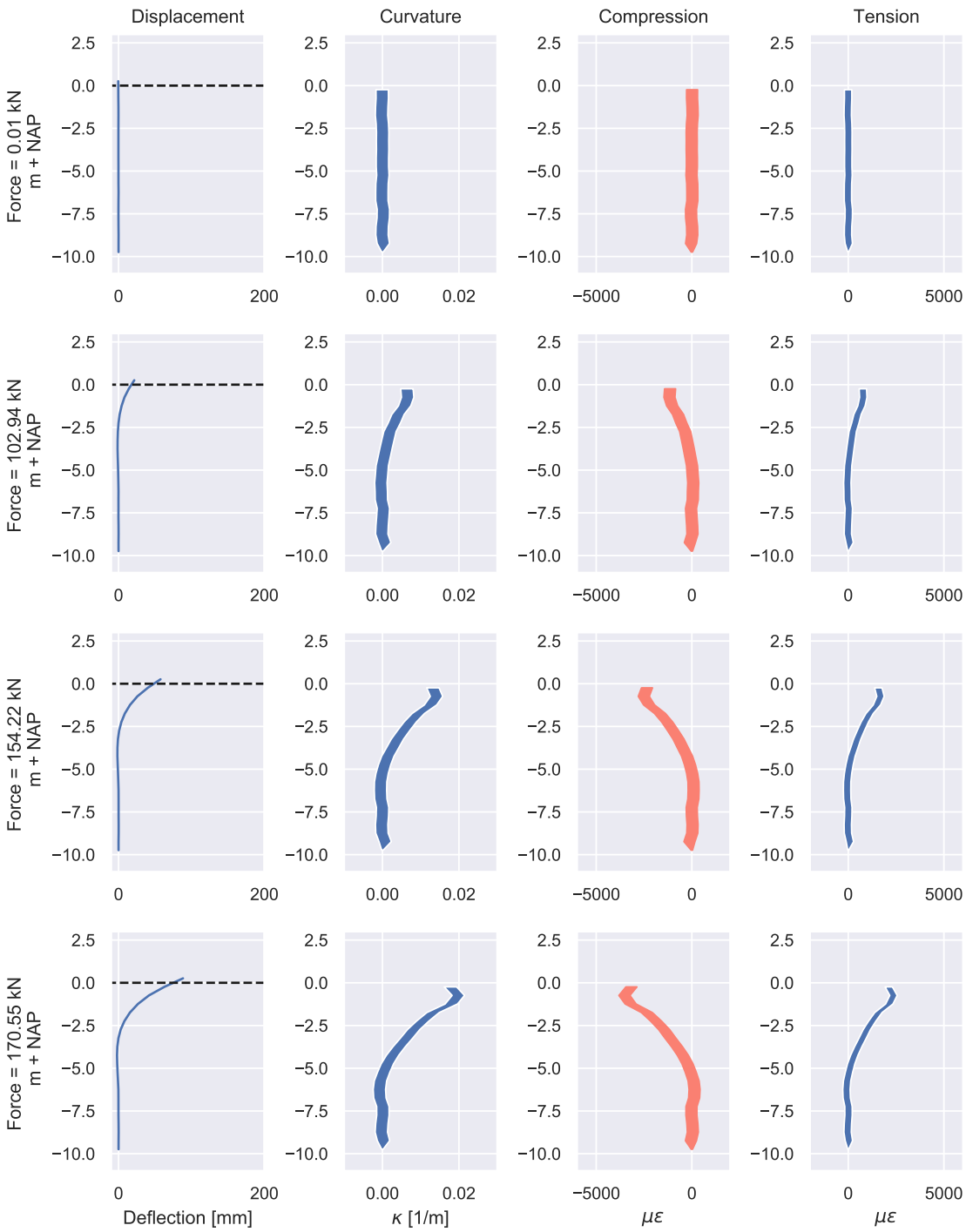

Figure 5.40: Strain estimation from SAAF measurements

5.6.4. Strain verification

In order to verify the FBG sensors, the obtained strain estimation is compared with the measured strains. Subsequently, each sensor is assigned to one of the following classes:

- Class 1: Sensor remains within the estimated confidence interval during the entire test.
- Class 2: Maximum error < 500 $\mu\epsilon$
- Class 3: Maximum error between 500 - 1000 $\mu\epsilon$
- Class 4: Maximum error > 1000 $\mu\epsilon$

The course of the verification is shown in figures 5.41 to 5.44.

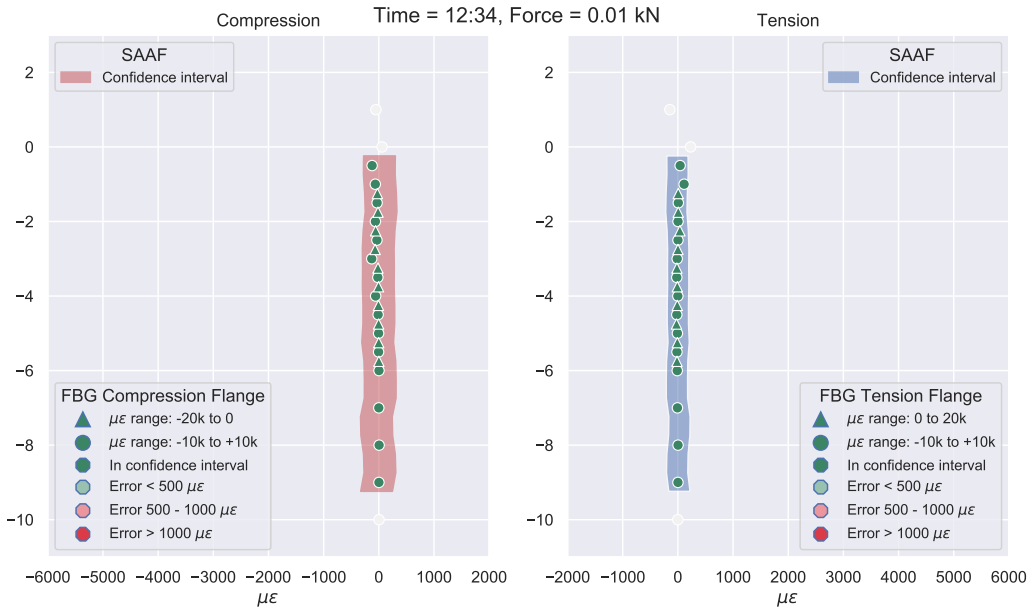

Figure 5.41: Strain verification, F = 0 kN

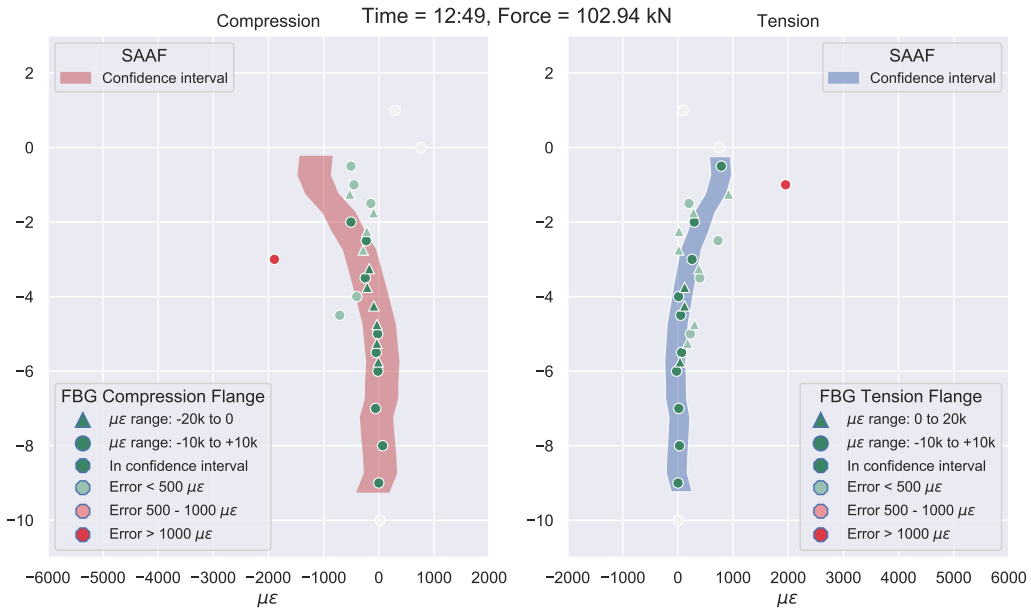

Figure 5.42: Strain verification, F = 103 kN

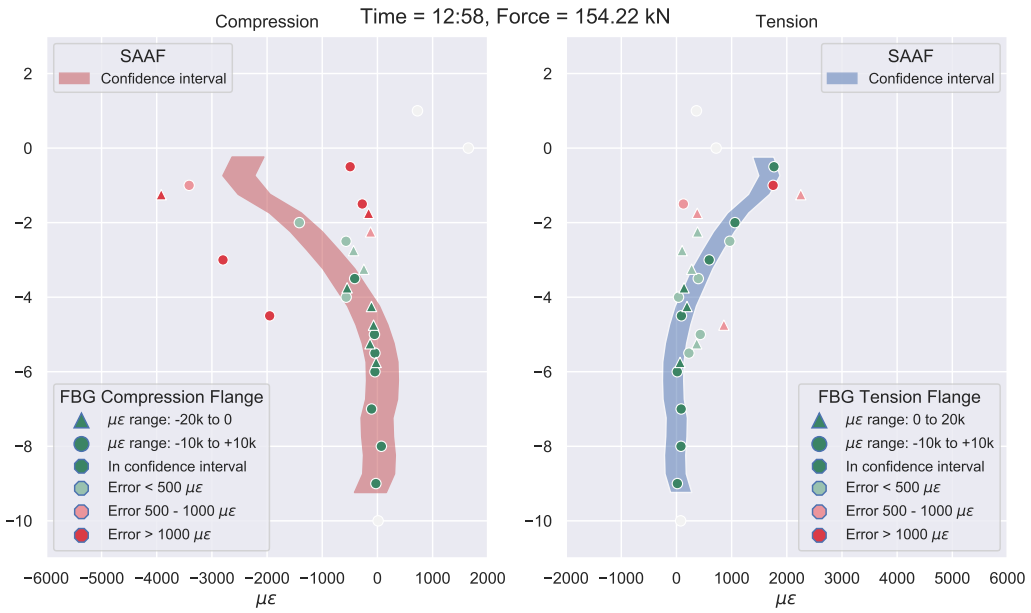

Figure 5.43: Strain verification, F = 154 kN

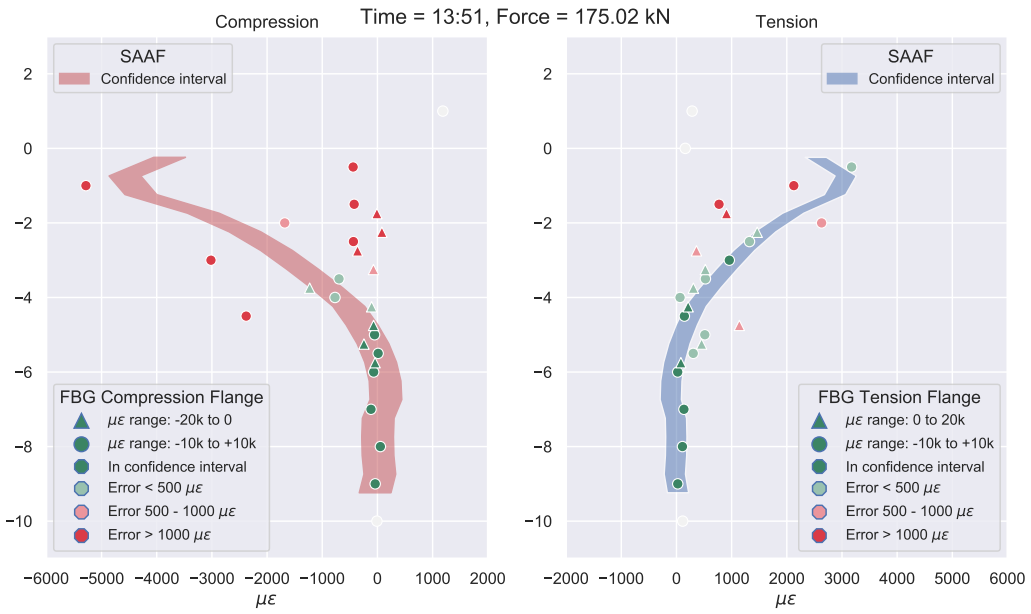

Figure 5.44: Strain verification, F = 175 kN

An overview of the results is given in figure 5.45.

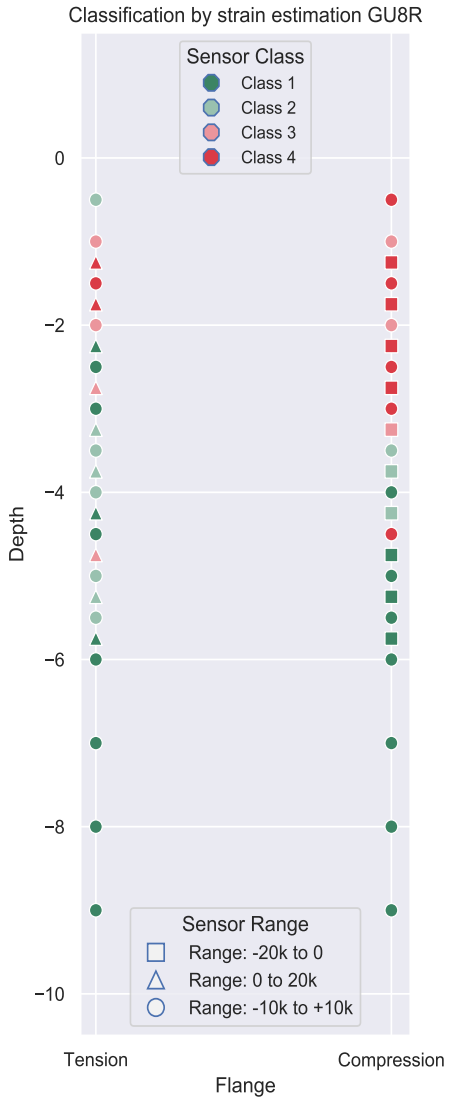

(a) Overview sensor class and measurement range

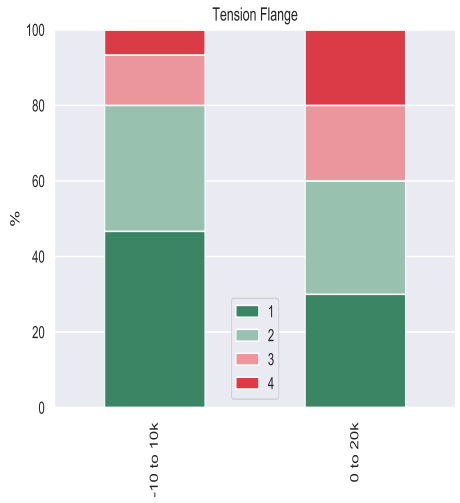

(b) Class distribution tension flange

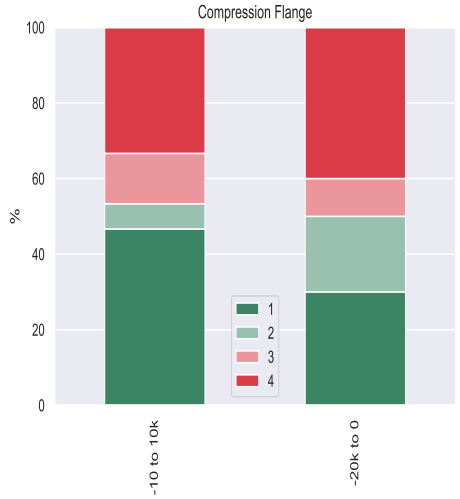

(c) Class distribution compression flange

Figure 5.45: GU8R: FBG classification by strain estimation

5.7. Results

5.7.1. Results POT

The two verification methods described in this chapter have been performed on all the POT tests. Detailed documentation of these tests can be found in Appendix B. The results are shown in figure 5.46.

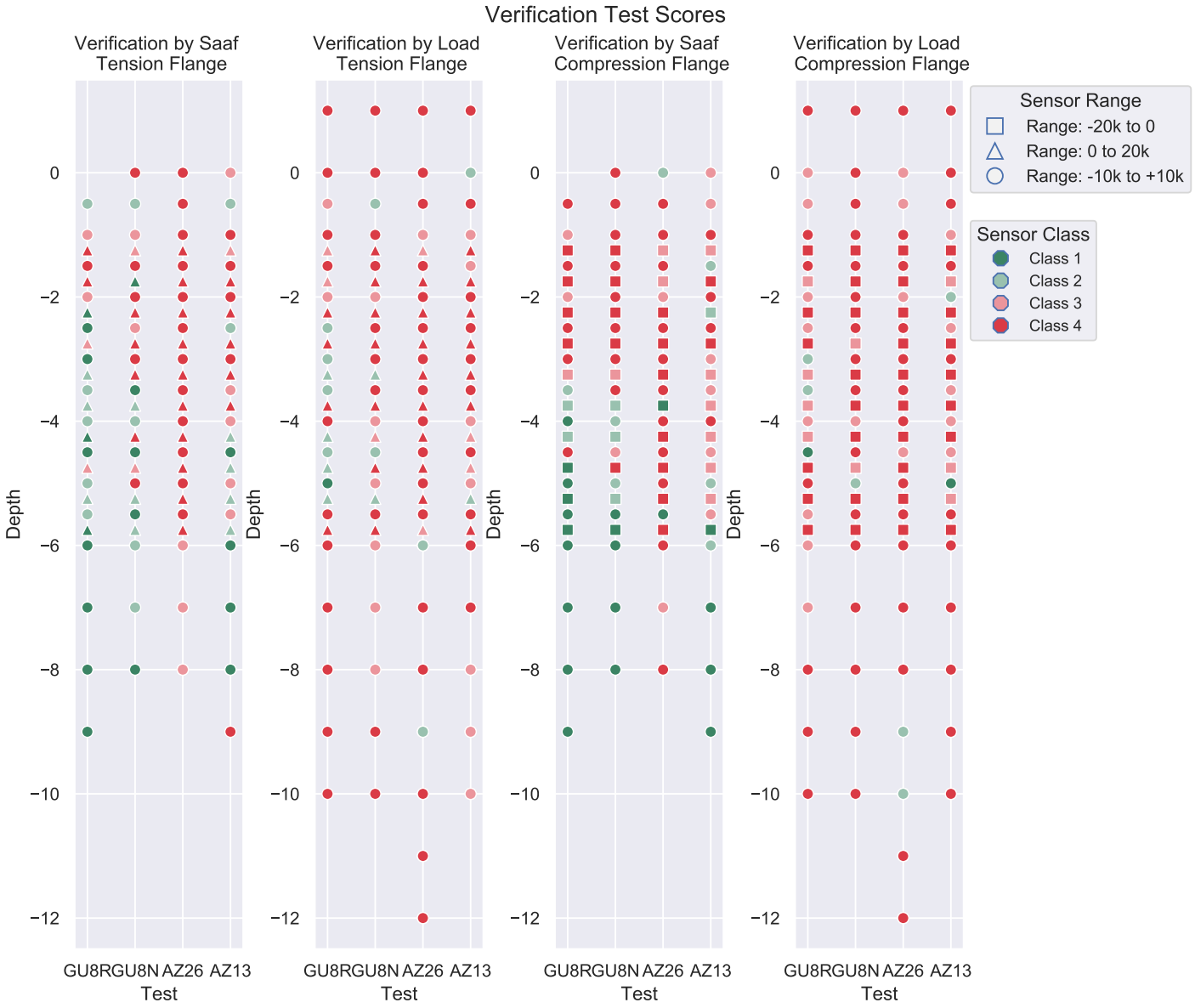

Figure 5.46: POT: Overview verification test results

It is clear that the majority of the sensors did not function properly. The distribution of the results and the correlation between the verification tests are shown in figure 5.47 and table 5.1 respectively.

Figure 5.47: POT: Verification test scores

Table 5.1: POT: Correlation between verification methods

Sensor type	Correlation
-20k to 0	0.998961
-10k to 10k	0.946382
0 - 20k	0.962060

The distribution indicates that the sensors performed better in the SAAF verification test. However, this method requires some strains in order to verify the measurements. At lower depths these strains are insufficient and thus some sensors may incorrectly obtain a higher class as a result. For a fair comparison, only the sensors are considered where the strains were sufficient for verification. This is the case for sensors with a maximum depth of 4m and the distribution of results is shown in 5.48.

Figure 5.48: POT: Verification test scores, depth > NAP - 4m

The correlation between the verification tests is shown in table 5.2.

Table 5.2: POT: Correlation between verification methods, depth > NAP - 4m

Sensor type	Correlation
-20k to 0	0.967903
-10k to 10k	0.997363
0 - 20k	0.996831

From the test performance, it can be concluded that the vast majority of the FBG sensors did not work properly in the POT. Since the correlation between the tests is close to 1, being completely correlated, the results can be assumed reliable.

5.7.2. Results FST

For the FST there is no pulling force and for this reason, only the SAAF verification is performed. The results are shown in 5.49 and the corresponding class distribution is shown 5.50.

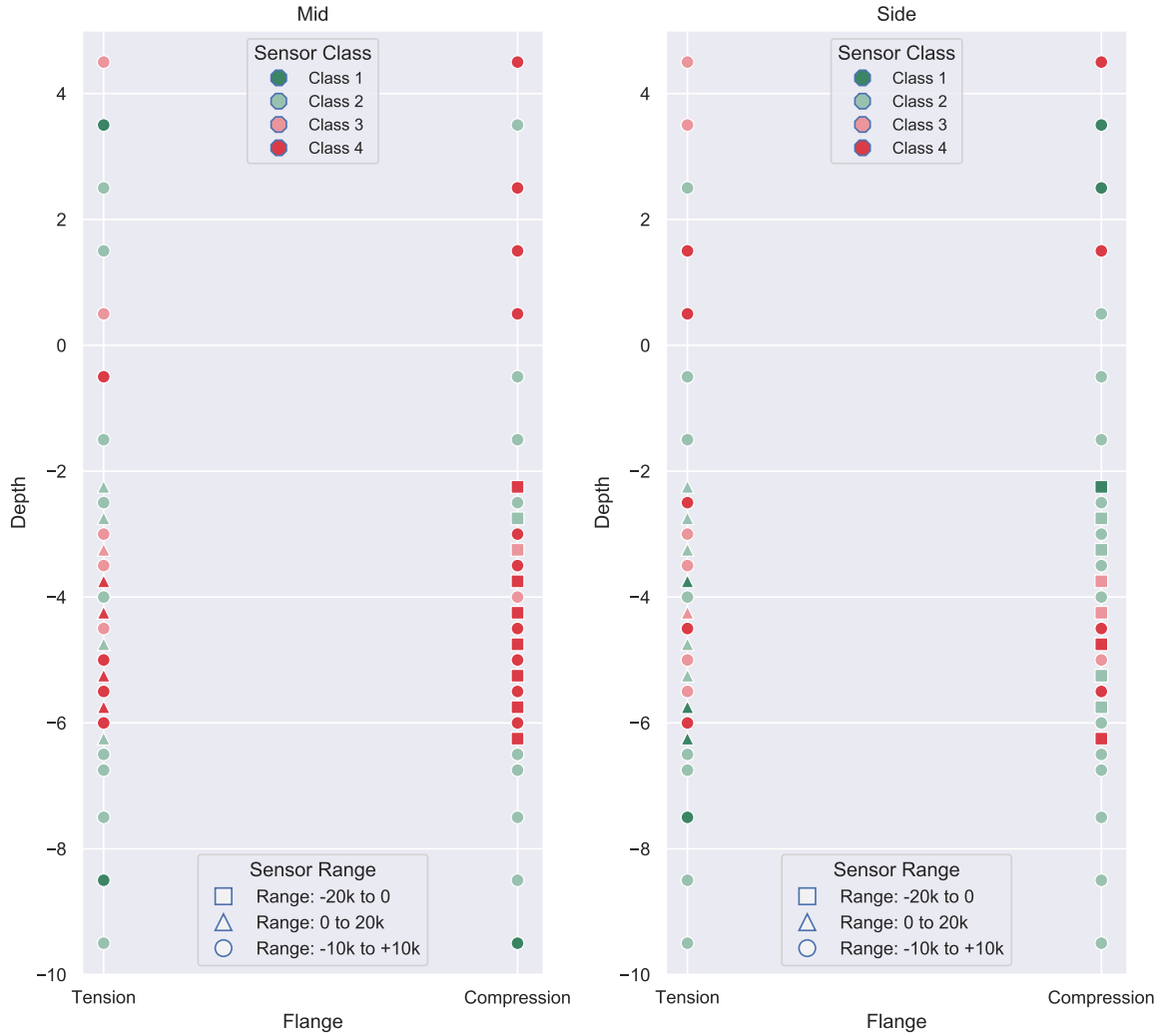

Figure 5.49: FST: Overview verification test results

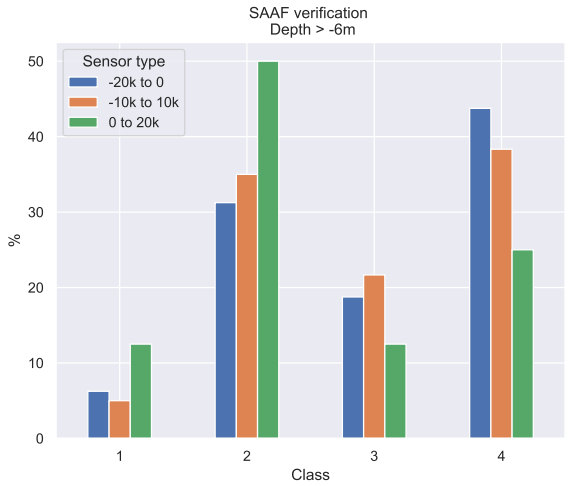

Figure 5.50: FST: Verification test scores, depth > NAP - 6m

The sensors in the FST performed much better than in the POT. However, in the section where local buckling occurred, between -5 m and -2.5 m, only a few sensors performed well. With only a few points it is hard to construct a reliable strain distribution from these measurements. Nevertheless, the verification by SAAF resulted in an alternative method to approximate this distribution. Accordingly, this method will be used in order to determine the curvature distribution in the next chapter.

6 Curvature

6.1. Introduction

Since the FBG sensors have been found unreliable, the curvature will be determined from the SAAF measurements, for which the same method is used as described in section 5.6. This results in a change of the flow chart presented in figure 5.1. The new flow chart is illustrated in figure 6.1.

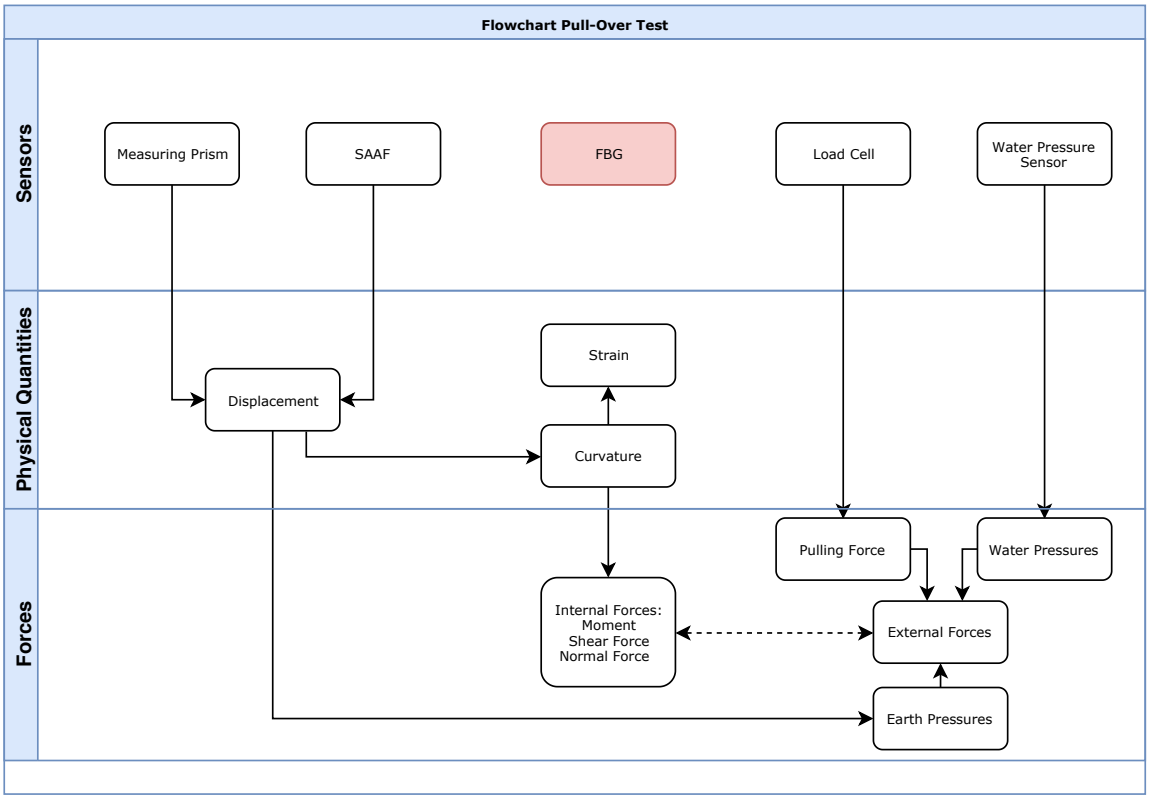

Figure 6.1: POT: Updated flowchart data streams

For the pull-over tests, graphs are shown for several load steps up to the maximum pulling force measured, before the SAAF was removed. For the FST, the graph illustrates the last 24 hours before the collapse of the test dike. Furthermore, to determine if there is an edge effect as discussed in 2.7, a comparison is made between curvatures in the middle and side of the push-over tests.

6.2. AZ26

The displacement and curvature are shown in figure 6.2.

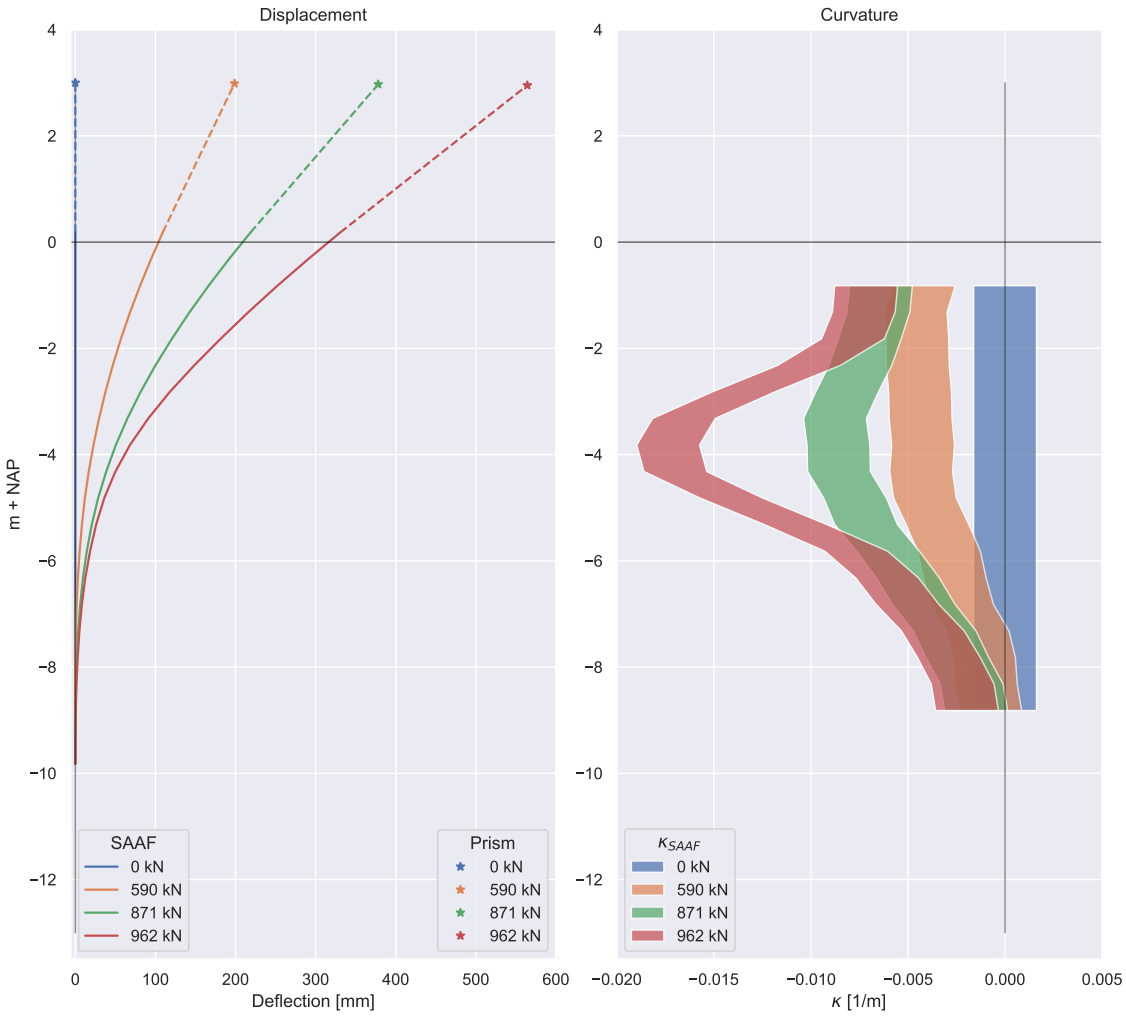

Figure 6.2: AZ26: Displacement and curvature

The maximum curvature is found at NAP-4 m, which indicates the location of the plastic hinge.

6.3. AZ13-700

The displacement and curvature are shown in figure 6.3.

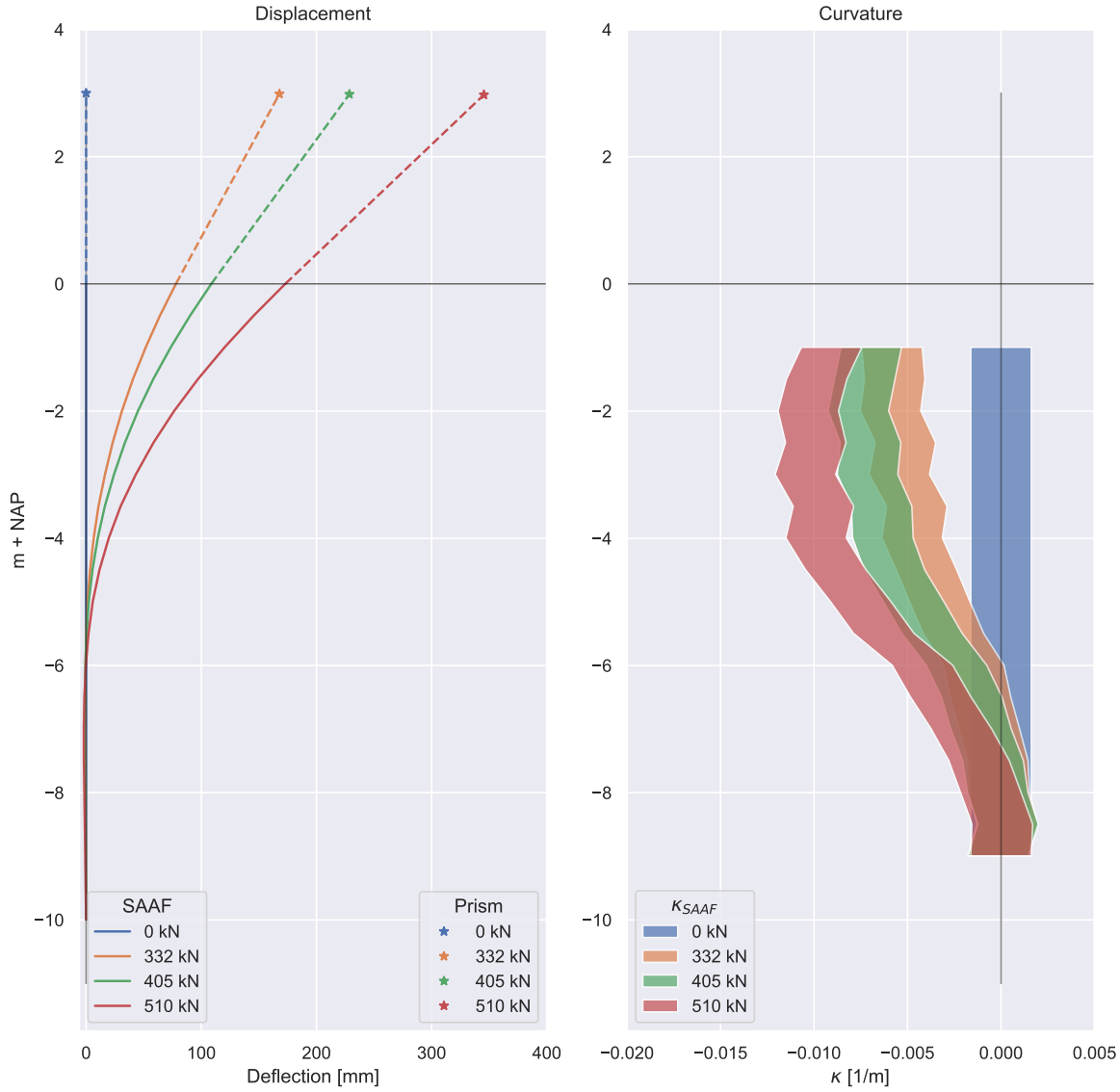

Figure 6.3: AZ13-700: Displacement and curvature

The maximum curvature is found at NAP-3 m, which indicates the location of the plastic hinge.

6.4. GU8N

The displacement and curvature are shown in figure 6.4.

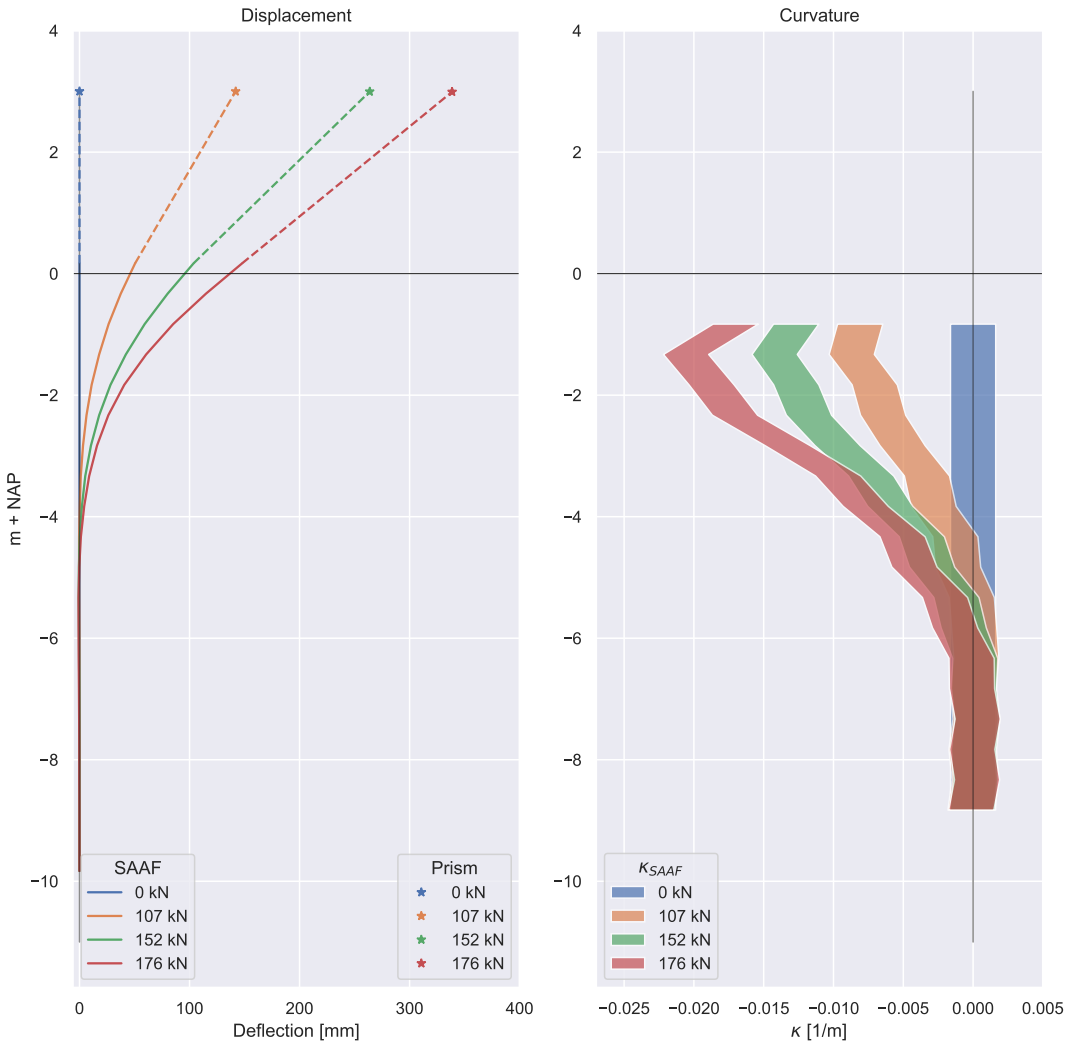

Figure 6.4: GU8N: Displacement and curvature

The maximum curvature is found at NAP-1.5 m, which indicates the location of the plastic hinge.

6.5. GU8N-Reversed

The displacement and curvature are shown in figure 6.5.

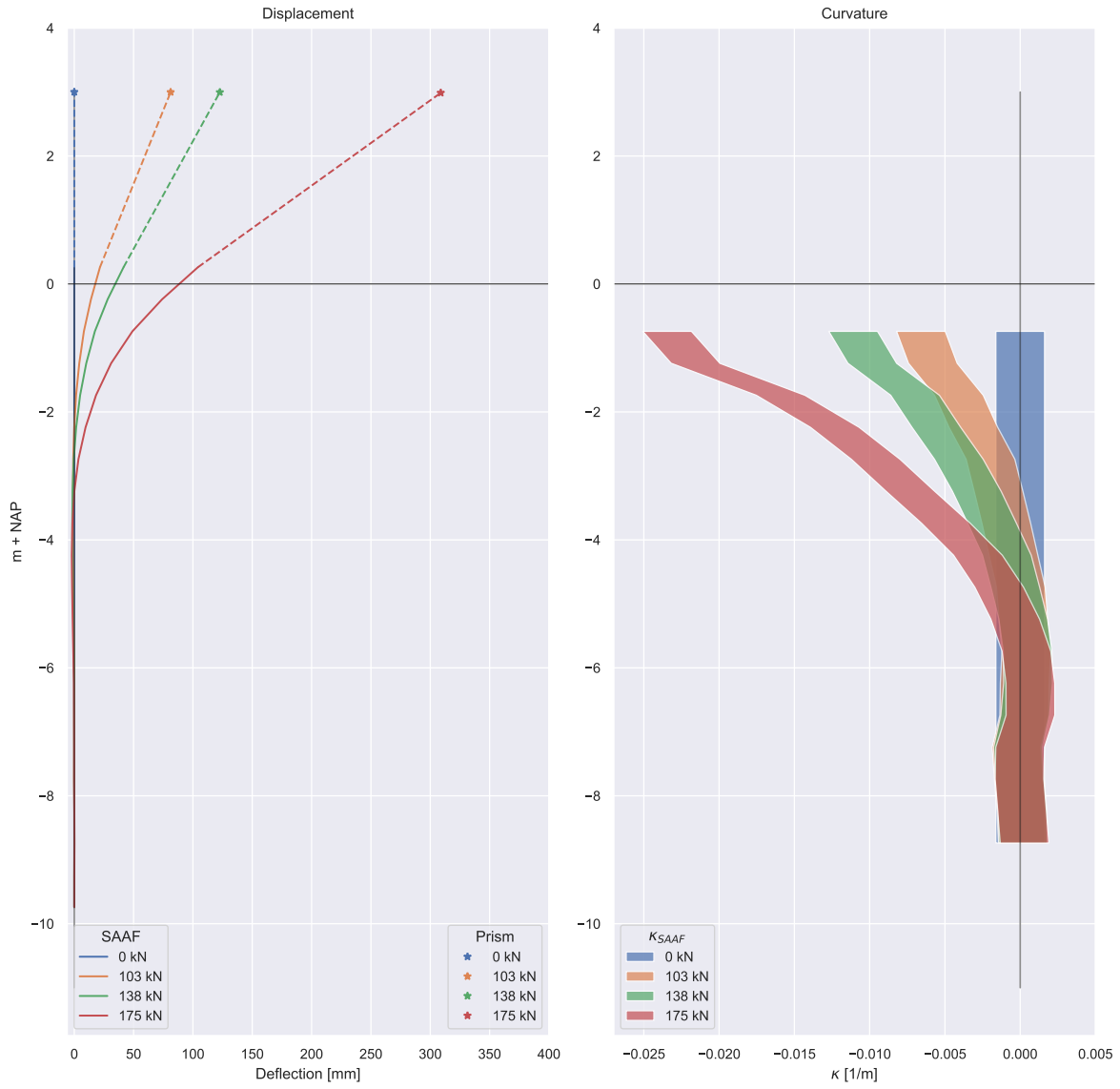

Figure 6.5: GU8N-Reversed: Displacement and curvature

The maximum curvature is found at NAP-1 m, which indicates the location of the plastic hinge. Compared to the other tests, there is a considerable curvature for the last time-step. As the SAAF for the side has been found unreliable, no edge effect analysis has been performed.

6.6. GU8N-FST

The displacement and curvature are shown in figure 6.6.

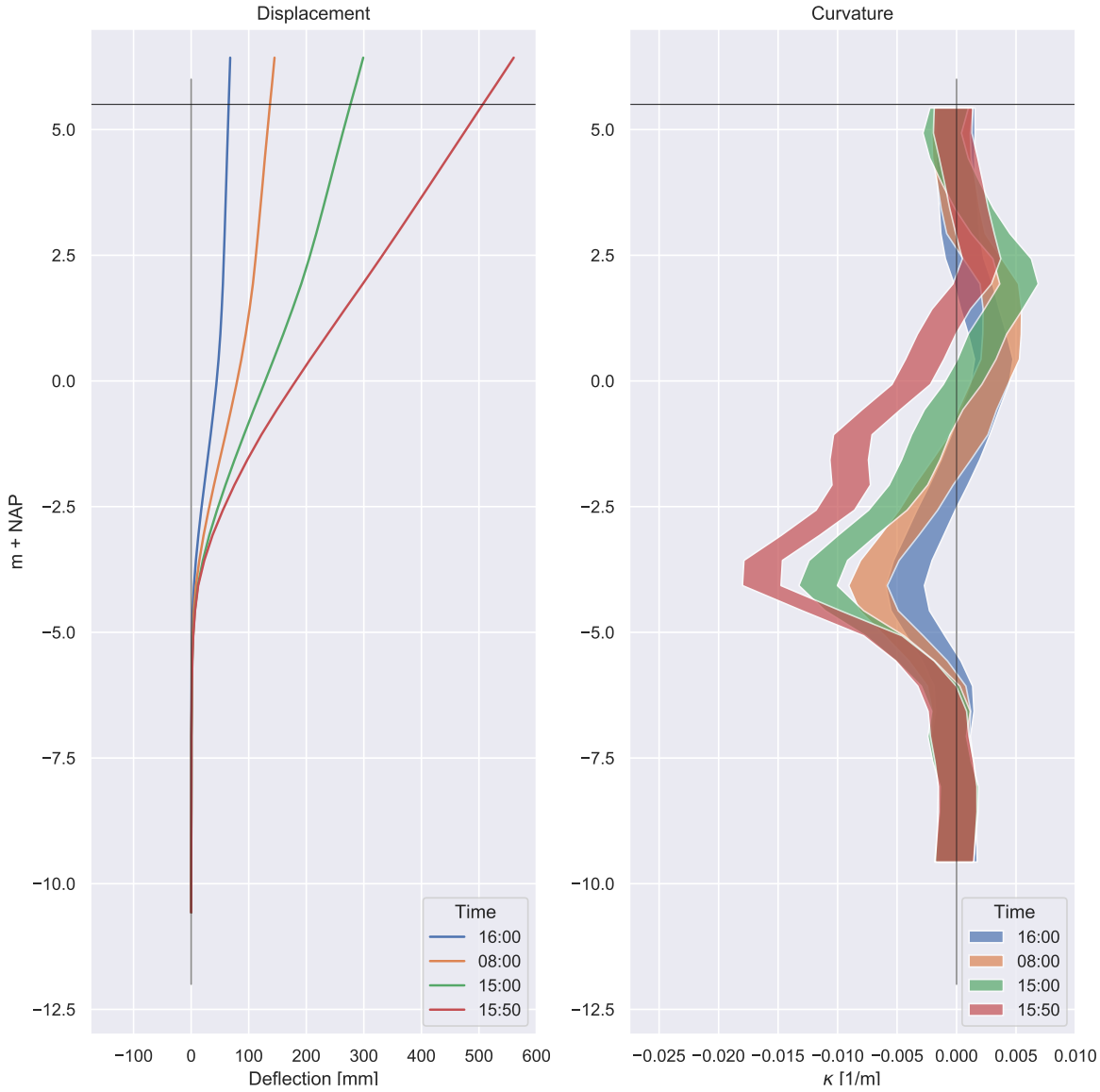

Figure 6.6: GU8N-FST: Displacement and curvature

The maximum curvature is found at NAP-3.75 m, which indicates the location of the plastic hinge. The sheet pile in this test had a staggered layout shown in figure 4.4. The transition between continuous and staggered is located at NAP-3.5 m. As expected, the plastic hinge has developed just below this transition.

7

Moment-curvature diagrams

7.1. Introduction

In this chapter, the relation between the curvature distribution as derived in the previous chapter and the moment distribution will be determined. In order to do so, a moment-curvature diagram is required, which relates curvatures to moments in the sheet pile. First, an elaboration is given on the method. Subsequently, the chosen model is calibrated by means of reproducing the measurement results of three real documented 4-point bending tests. Finally, the model is applied to the sheet pile profiles used in the Eemdijk test.

7.2. Method

An M-κ diagram is usually obtained by means of a 4-point bending test. Since this test was not performed, the required M-κ diagrams are obtained by finite element calculations.

7.2.1. 4-points bending test

The 4-points bending test is designed such as was described by Kort for the Rotterdam sheet pile wall field test [14]. The setup of this test is shown in figure 7.1.

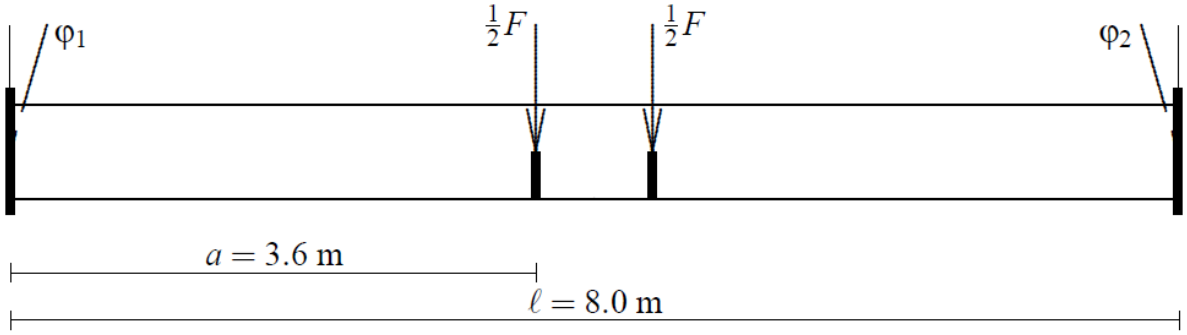

Figure 7.1: 4 points bending test setup

This setup results in the moment-diagram shown in in figure 7.2.

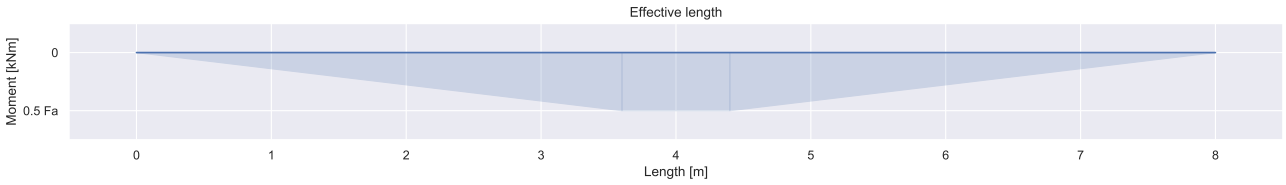

Figure 7.2: 4-points bending moment distribution

The load is increased gradually and for each load-step, the curvature and moment are calculated. The average curvature can be obtained by dividing the summation of angles at the supports by the effective length l_{eff}:

$$\kappa = \frac{\phi_1 + \phi_2}{l_{eff}} \tag{7.1}$$

l_{eff} is the length for which multiplication with the maximum moment, results in the same area as the area under the moment-diagram shown in 7.2. This length can be obtained by subtracting the distance to the load a from the total length l:

$$l_{eff} = l - a \tag{7.2}$$

This is indicated in figure 7.3.

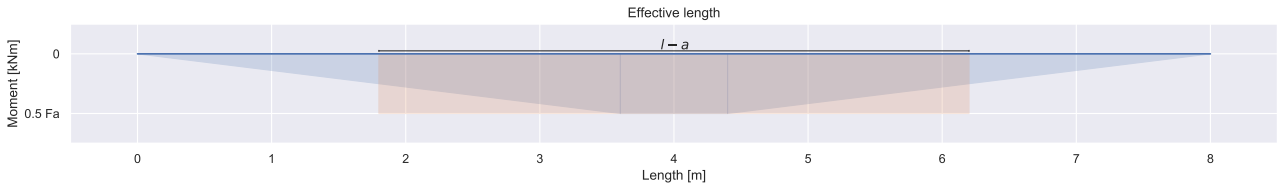

Figure 7.3: Effective length

For each load step κ and the corresponding moment represents a point on the M-κ diagram.

7.2.2. Finite element model

The test is simulated in DIANA, a finite element software package. In order to get a good result, the following elements have to be addressed thoroughly:

- Cross-section
- End supports
- Load introduction
- Mesh
- Element type
- Non-linear behaviour
- Geometrical imperfections
- Stress-strain behaviour

Cross-section

The cross-section is modeled by shell elements. The locks are modeled using thicker shell elements. This is illustrated in figure 7.4.

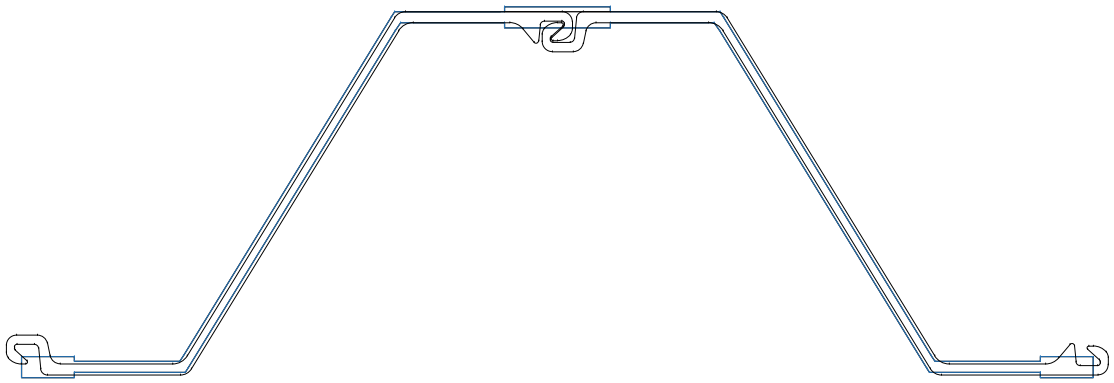

Figure 7.4: Cross-section: AZ26 model

The cross-sectional geometry was calibrated such that the cross-sectional area and moment of inertia deviates less than 1% [11].

End supports

In order to allow for rotations and to prevent clamping moments, the end supports are modeled as stiff plates. These plates are simply supported with a pinned and roller support as shown in figure 7.5.

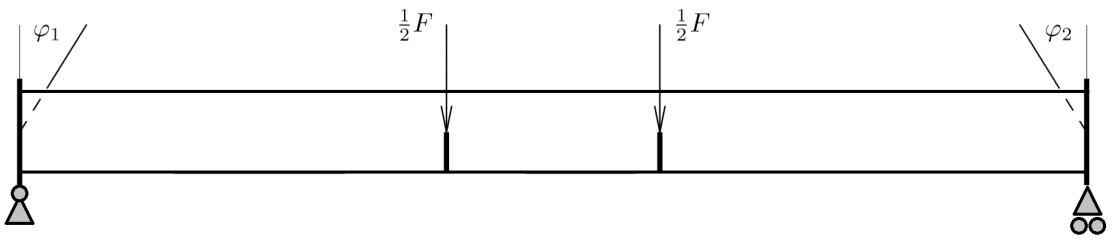

Figure 7.5: End supports FEM model

Load introduction

The test can be performed either force or displacement controlled. Force-controlled allows for deformation of the cross-section, but will only result in an M-κ diagram up to the maximum moment. There cannot be found a solution for a moment higher than this maximum. However, there is still some capacity left in the profile after this maximum moment is reached. By means of a displacement controlled simulation, a solution will be found for a lower moment after the maximum is reached, this is illustrated in figure 7.6.

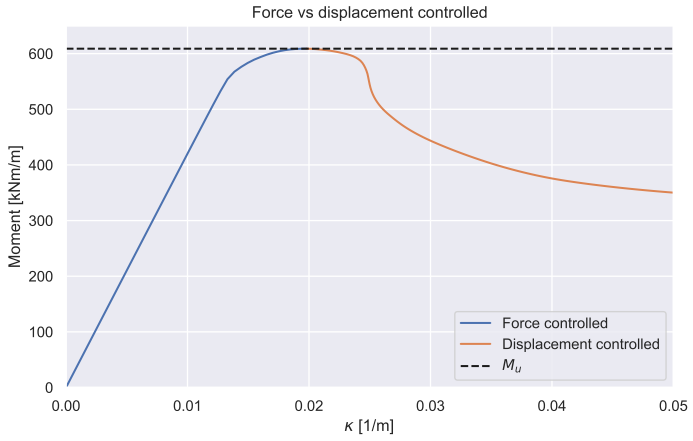

Figure 7.6: Force vs. displacement controlled simulation

Accordingly, a displacement controlled approach is taken. However, this doesn't allow for relative deformations at the section where the deformation is applied, since the same deformation is applied over the entire section. To prevent this restriction from influencing the capacity, the displacement is only applied in the tension zone. Failure due to buckling appears in the compression zone and thus this approach will minimize any disturbances in the simulation. Furthermore, a double sheet pile profile is tested. In order to simulate the behavior of a continuous wall, horizontal support is required. This achieved by applying stiff plates for the load introduction. These plates will provide the horizontal support similar to the horizontal support of a double profile as part of a continuous wall. The plates slightly increase the strength, however, this effect is minimal for a distance between the plates, which is greater than two times the flange width [11]. Accordingly, a distance between the plates of 0.8 m is chosen.

Mesh

As discussed in section 3.6.3, the mesh size between the load introduction plates should be 5 by 5 cm in order to match real test results. For this reason, an equidistant grid of 5 by 5 cm is chosen for all meshes. For the AZ26, the grid is shown in figure 7.7.

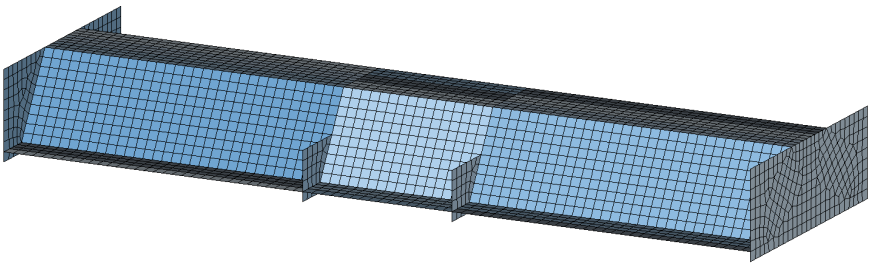

Figure 7.7: Mesh AZ26

Element type

The used element type is CQ40S. This is quadrilateral isoparametric curved shell element with eight nodes. This element has three integration points over the thickness and is shown in figure 7.8.

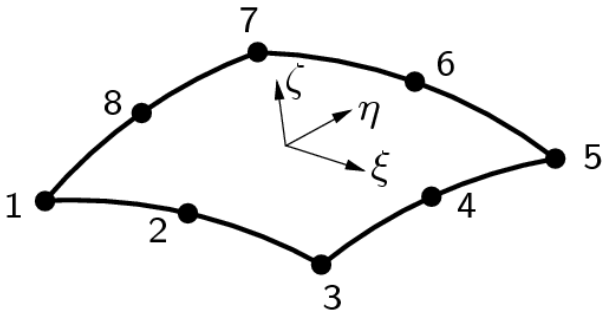

Figure 7.8: Regular curved shell element

Non-linear behavior

Plasticity and buckling are taking into account by physical and geometrically non-linear calculation (Total Lagrange).

Geometrical imperfections

For each test, a buckling analysis is performed. Subsequently, imperfections have been taking into account in same buckling modes as were observed in the field test.

Stress-strain behavior

Tensile tests have been performed, which resulted in the yield strengths shown in table 7.1.

Table 7.1: Tensile test results

Profile	f_{yield} $[N/mm^2]$	E $[N/mm^2]$
GU8N	S380.5	$2.1 \cdot 10^5$
GU8N-Reversed	S380.5	$2.1 \cdot 10^5$
AZ13-700	S406.0	$2.1 \cdot 10^5$
AZ26	S327.0	$2.1 \cdot 10^5$

The idealized stress strain-behavior of steel is shown in figure 7.9. In accordance with the Eurocode, the material behavior is modeled elastic-plastic, with linear strain hardening. This is shown in figure 7.10.

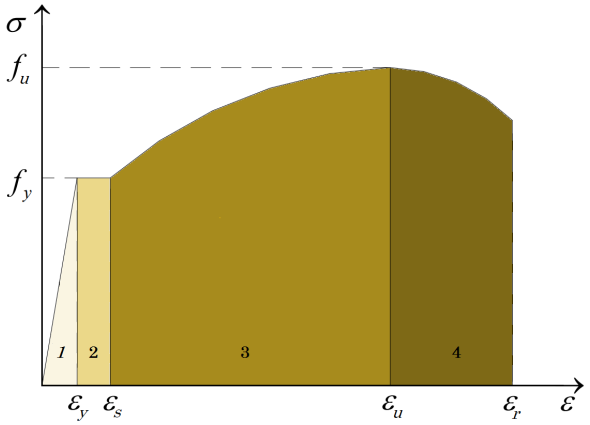

Figure 7.9: Idealized stress-strain diagram for steel

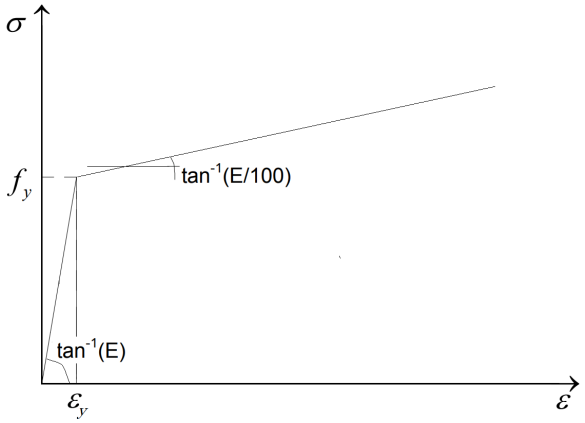

Figure 7.10: Stress-strain model Eurocode

The Eurocode prescribes linear hardening with 1% of the Young's modulus E. In the next section a sensitivity analysis will be performed, with several values for strain hardening.

7.3. Model calibration

The finite element method offers a wide variety of input parameters and calculation schemes. This freedom also results in a widespread in calculation results depending on the made choices. For this reason, the model is first calibrated. The calibration is performed by reproducing the measurement results of three real documented 4-points bending tests, namely:

- Class 3: Z-profile AZ13
- Class 3: U-profile PU8
- Class 2: Z-profile AZ26

7.3.1. AZ13

The AZ13 the calibration is based upon results concerning two PhD dissertations from Kort (TU Delft) [14] and Dercks (RWTH Aachen) [6]. Their results are shown in 7.11

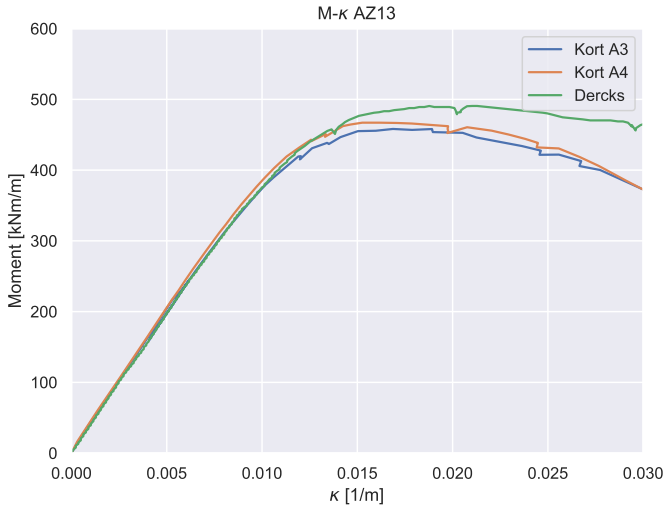

Figure 7.11: M-κ AZ13 Kort, Dercks

Cross-section

The modeling of the locks results in a slightly higher moment of inertia for Z-sections. To be in agreement with the real moment of inertia, the model height is slightly decreased. The real and modeled cross-section is shown in 7.12.

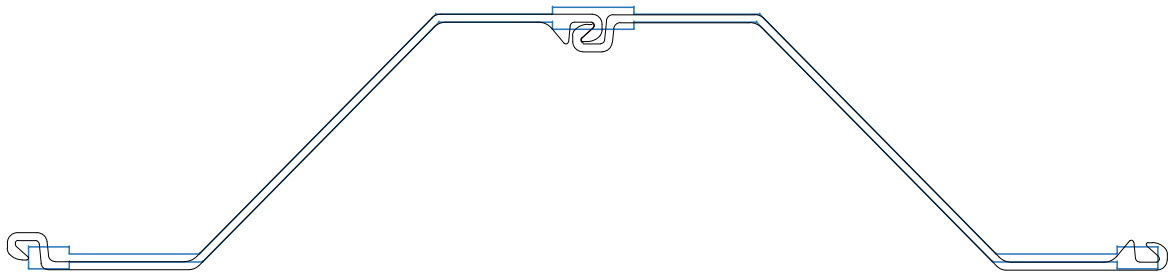

Figure 7.12: Cross-section: AZ13 model

The cross-sectional properties given by the manufacturer and the modeled ones are shown in table 7.2.

Table 7.2: Cross-sectional properties: AZ13 model

	Area $[cm^2]$	Moment of inertia $[cm^4]$
Brochure	183.00	26400
Model	181.77	26545
Δ%	-0.67	0.55

Buckling analysis

A buckling analysis was performed. A typical buckling shape for a 4-point bending test of a Z-section is shown in figure 7.13. This corresponds to the 4th mode found in DIANA, see figure 7.14.

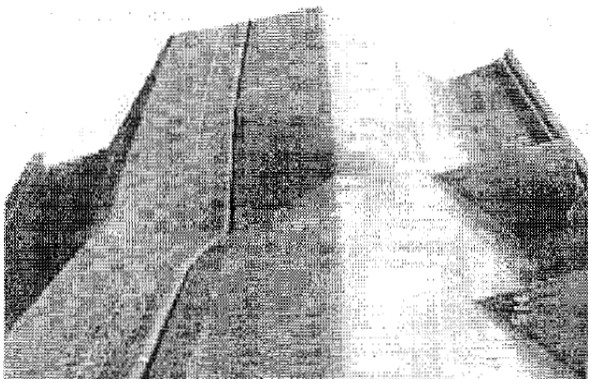

Figure 7.13: Typical buckling shape for Z-sections [11]

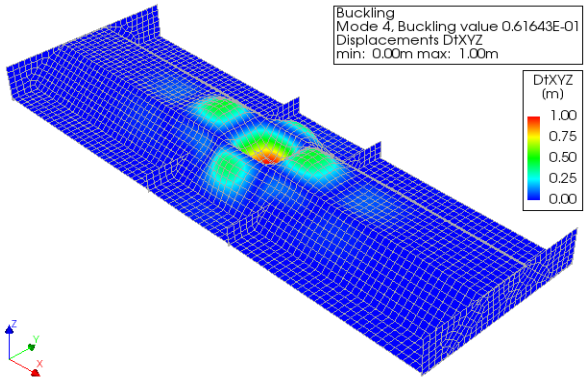

Figure 7.14: 4th buckling mode DIANA

The first three buckling modes are shown in figure 7.15.

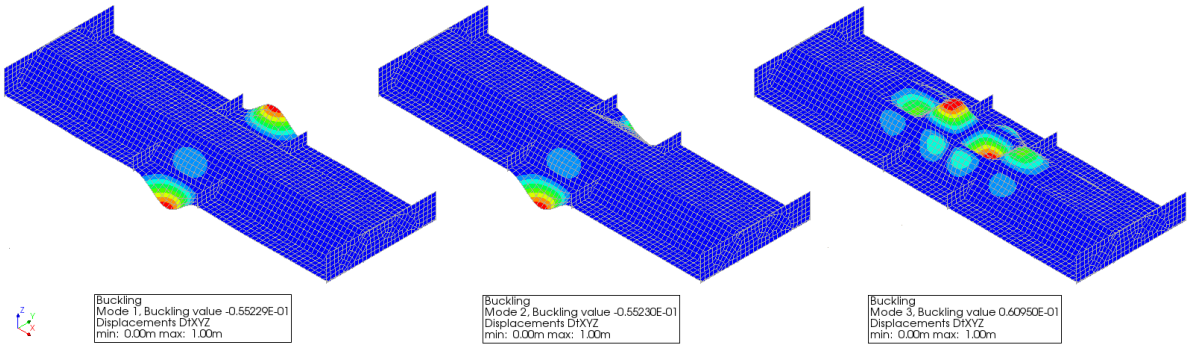

Figure 7.15: AZ13: Buckling modes 1,2 and 3

Sensitivity analysis

Subsequently, a sensitivity analysis was performed with regards to imperfections in the 4th buckling mode and different models of stress-strain behavior. The findings are presented in figure 7.16.

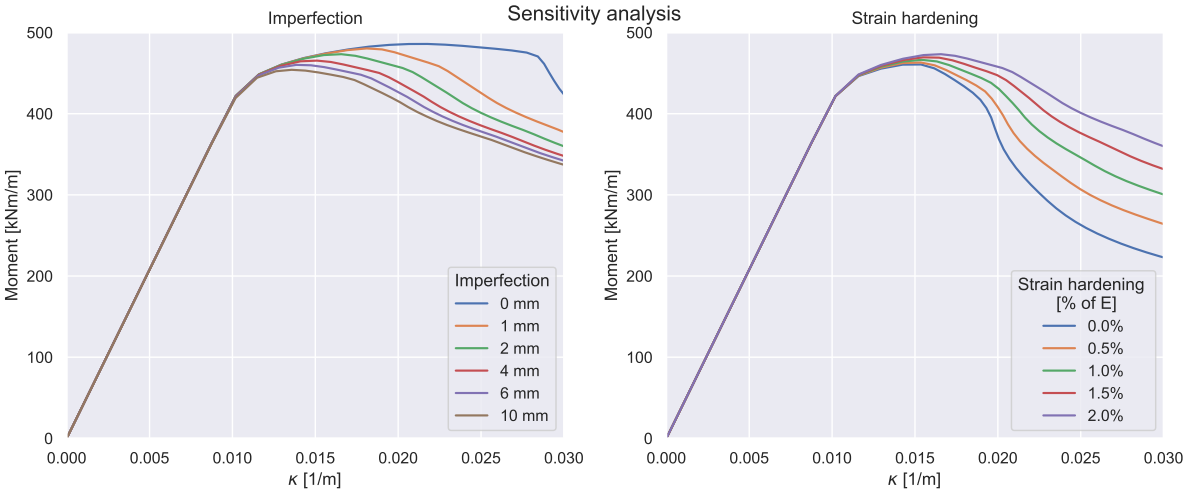

Figure 7.16: Sensitivity analysis AZ13

Imperfections influence the moment capacity, while strain hardening influences both moment and rotation capacity.

Result

The best fit has been found for an imperfection of 2 mm combined with a strain hardening of 2%. The deformed shape of the model and the obtained diagram are shown in figure 7.17 and 7.18 respectively.

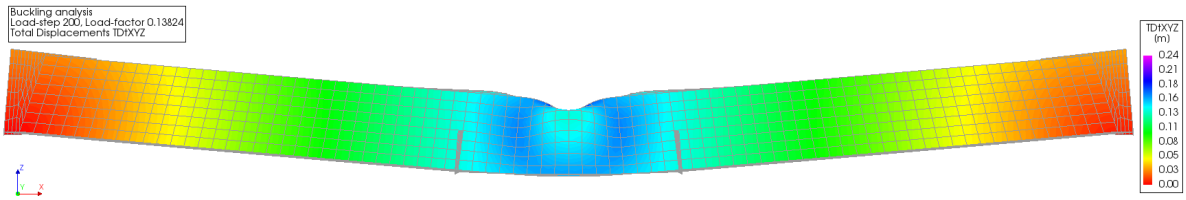

Figure 7.17: Deformed shape AZ13

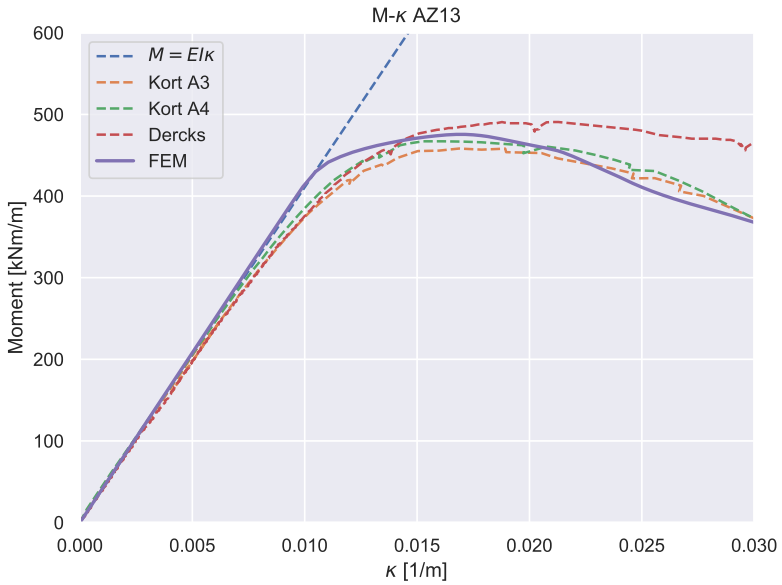

Figure 7.18: M-κ AZ13

7.3.2. PU8

In order to verify if the found parameters are also applicable for class 3 U-profiles, a check was performed on a PU8 profile. This verification is based on a real 4-points bending test done by Dercks [6].

Cross-section

To perform the same method as used for the AZ13 profile, the cross-section is modeled as shown in figure 7.19.

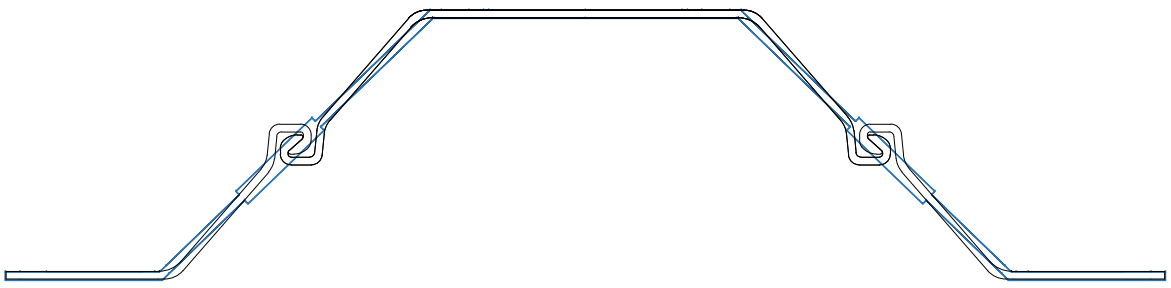

Figure 7.19: Cross-section: PU8 model

The cross-sectional properties given by the manufacturer and the modeled ones are shown in table 7.3.

Table 7.3: Cross-sectional properties: PU8 model

	Area $[cm^2]$	Moment of inertia $[cm^4]$
Brochure	139.00	13940
Model	138.92	14031
Δ%	-0.06	0.65

Buckling analysis

A buckling analysis was performed. A typical buckling shape for a 4-point bending test of a U-section is shown in figure 7.20. This corresponds to the 6th mode found in DIANA, see figure 7.21.

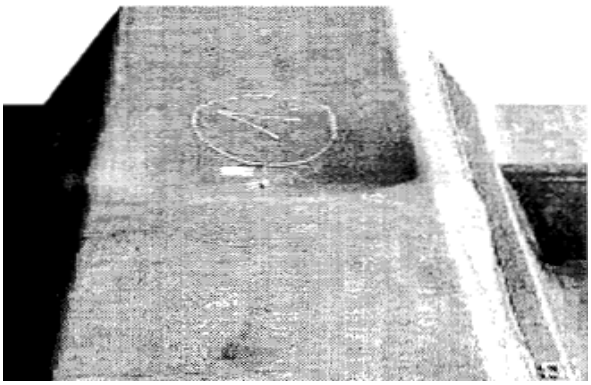

Figure 7.20: Typical buckling shape for U-sections [11]

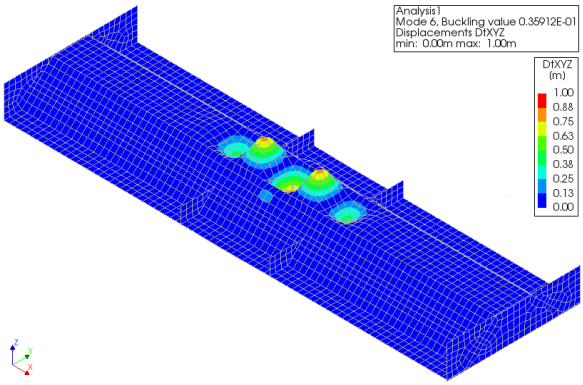

Figure 7.21: 6th buckling mode DIANA

A top-view of the first 5 buckling modes are shown in figures 7.22 to 7.26.

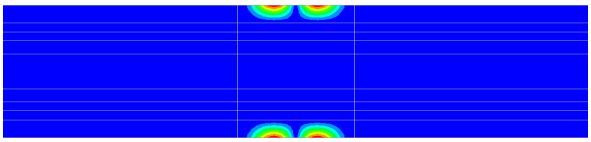

Figure 7.22: 1st mode

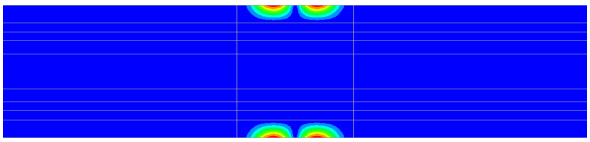

Figure 7.23: 2nd mode

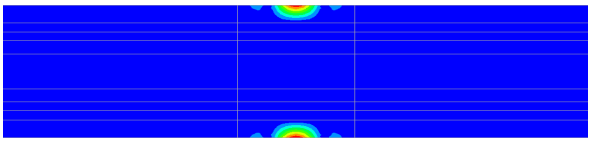

Figure 7.24: 3rd mode

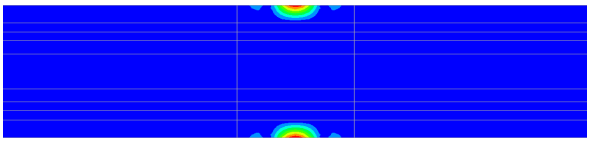

Figure 7.25: 4th mode

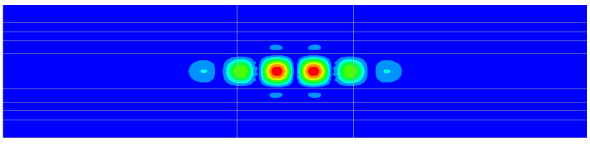

Figure 7.26: 5th mode

Result

Imperfections with a maximum of 2 mm have been applied in the 6th buckling mode. Furthermore, a strain hardening of 2% is taken into account. The deformed shape of the model and the obtained diagram are shown in figure 7.27 and 7.28 respectively.

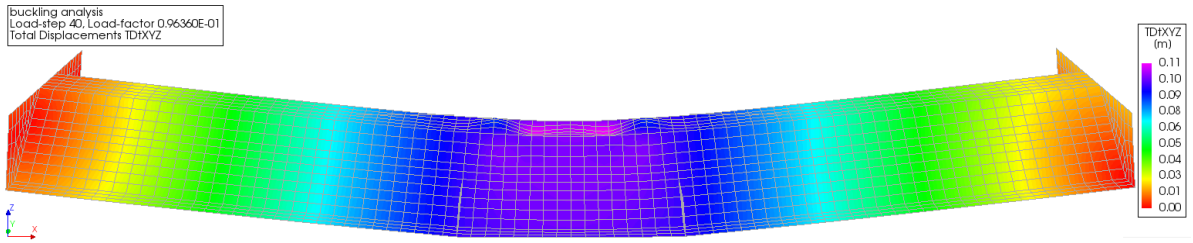

Figure 7.27: Deformed shape PU8

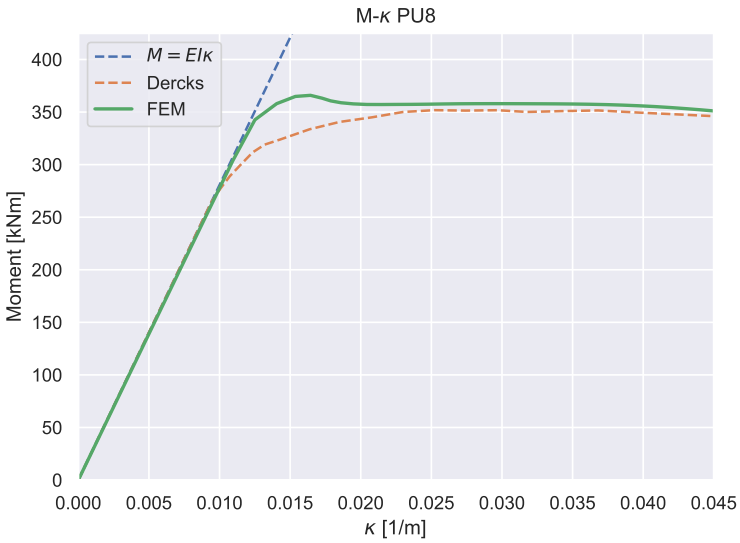

Figure 7.28: M-κ PU8

Since there is a good resemblance between the model and real test, it is concluded that the derived parameters also hold for class 3 U-sections.

7.3.3. AZ26

The AZ26 is a class 2 profile. A separate set of parameters is derived in a similar manner. This verification is based on a real 4-points bending test done by Dercks [6].

Cross-section

The cross-section is modeled as shown in figure 7.29.

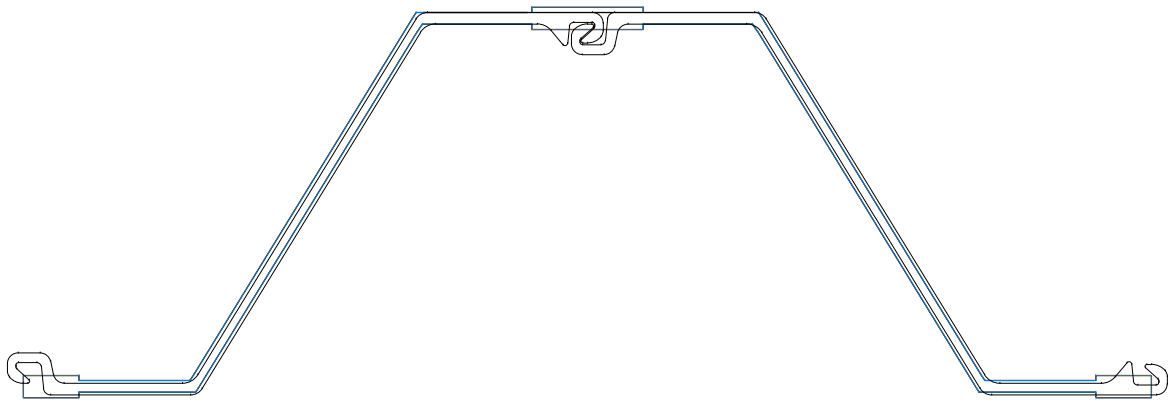

Figure 7.29: Cross-section: AZ26 model

The cross-sectional properties given by the manufacturer and the modeled ones are shown in table 7.4.

Table 7.4: Cross-sectional properties: AZ26 model

	Area $[cm^2]$	Moment of inertia $[cm^4]$
Brochure	249.20	69940
Model	244.88	70380
Δ%	-1.73	0.63

Buckling analysis

A buckling analysis was performed. A typical buckling shape for a 4-point bending test of a Z-section is shown in figure 7.30. This corresponds to the 4th mode found in DIANA, see figure 7.31.

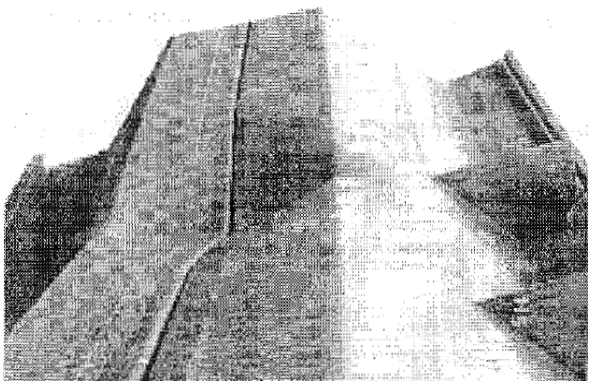

Figure 7.30: Typical buckling shape for Z-sections [11]

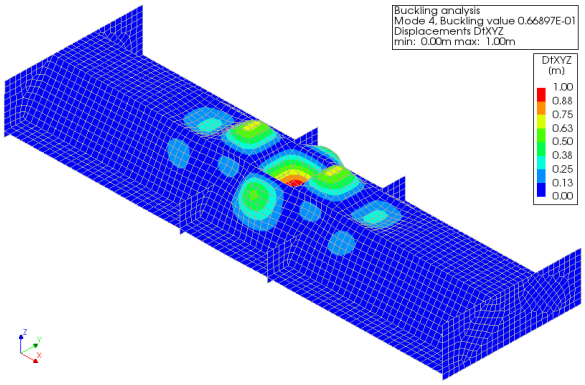

Figure 7.31: 4th buckling mode DIANA

The first three buckling modes are shown in figure 7.32.

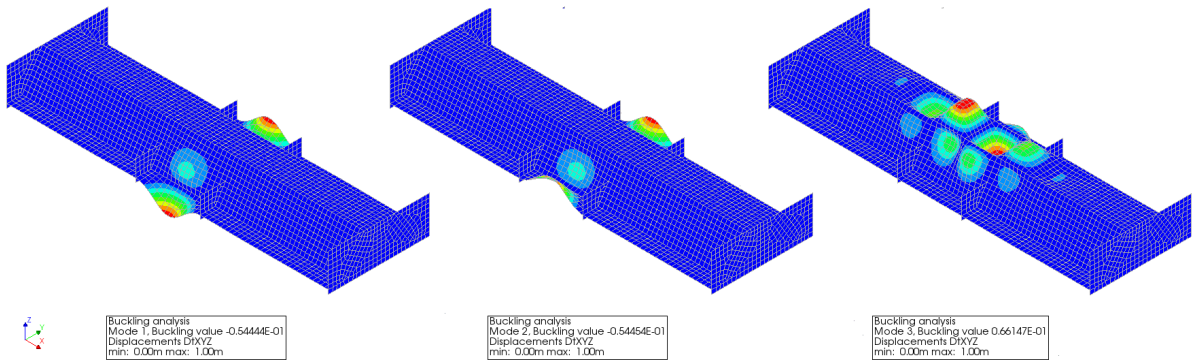

Figure 7.32: AZ26: Buckling modes 1,2 and 3

Result

Imperfections with a maximum of 2 mm combined with a strain hardening of 0.5% resulted in the best fit. The deformed shape of the model and the obtained diagram are shown in figure 7.33 and 7.34 respectively.

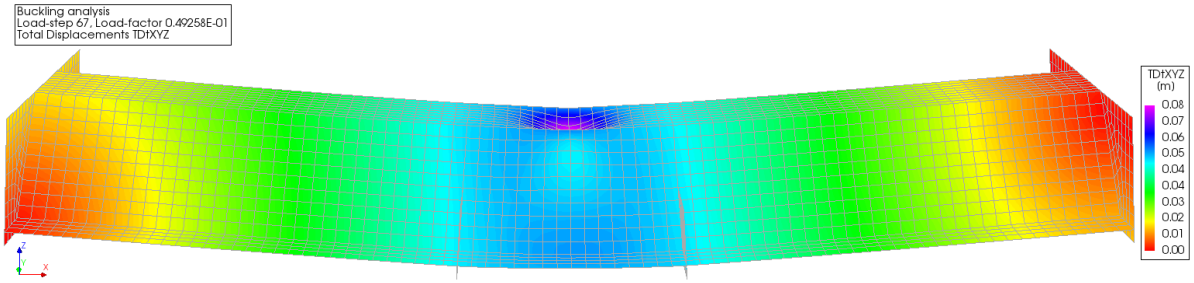

Figure 7.33: Deformed shape AZ26

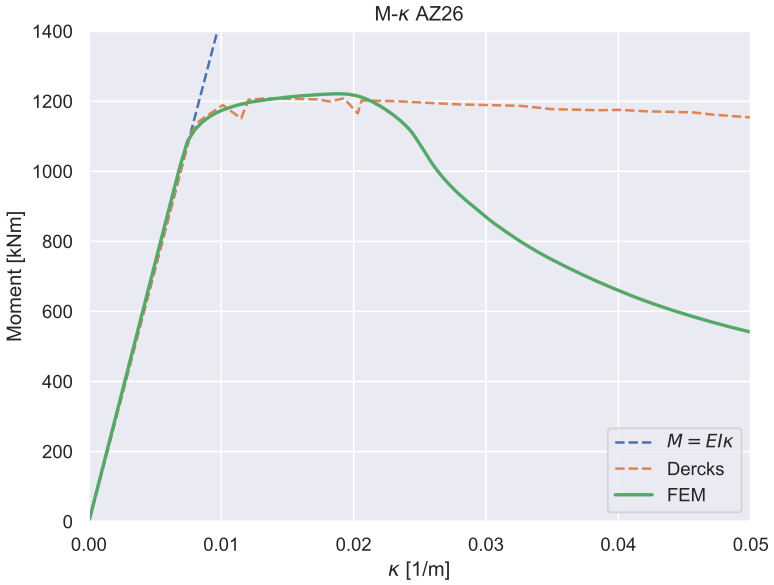

Figure 7.34: M-κ AZ26

The model has a good resemblance to the strength found in the real test. The sheet pile in the real test, however, does not seem to fail. This is strange since a decrease in capacity is expected after the occurrence of local buckling. Since this holds for all other curves derived by Dercks, it might be a result of the measurement set-up.

7.3.4. Soil-structure interaction

The curves derived in sections 7.3.1 to 7.3.3 are based on experiments in the lab, where there is no soil surrounding the sheet pile. To clarify if this approach is reasonable for the behavior of a sheet pile in the field, the influence of soil pressures on local buckling is investigated in DIANA. In order to do so, the soil should be included in the model. However, the moment diagram is shown in 7.35 will no longer valid as a result of earth pressures.

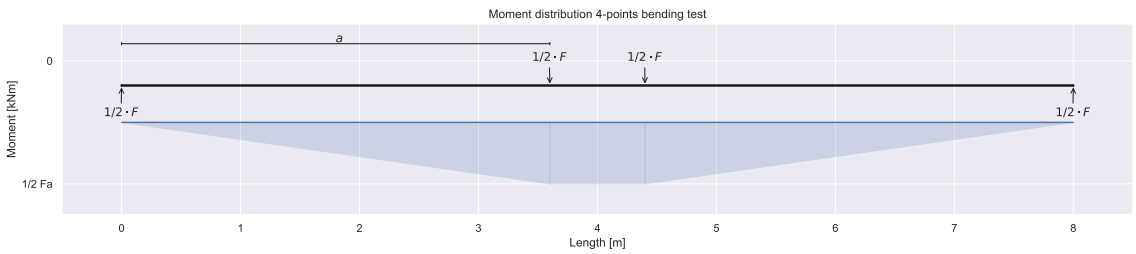

Figure 7.35: Moment diagram of a 4 points bending test without soil

As a result of deflection induced earth pressures, the applied force will partly be carried by the soil. The moment distribution is then shown in 7.36.

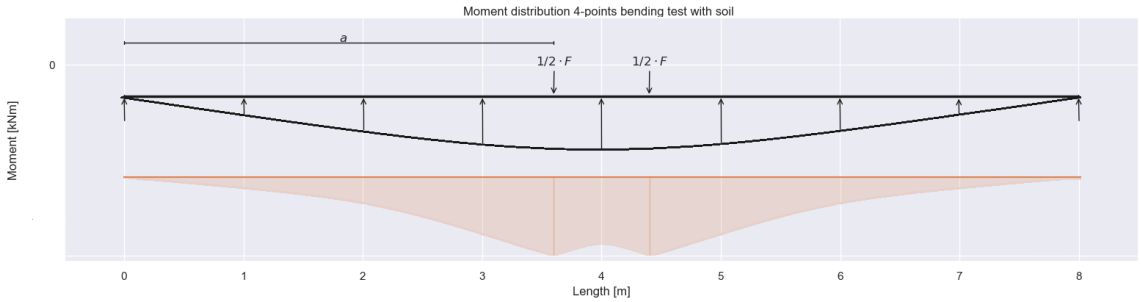

Figure 7.36: Moment diagram of a 4 points bending test with soil

Accordingly, a different approach is required in order to derive the M-κ diagram, which complicates the comparison between the two models. For this reason, a different approach is taken. A model is constructed, which filters out earth pressures as a result of the deflection, but includes earth pressures as a result of local buckling. This is achieved by the addition of a beam in the original 4-points bending model. The beam has the same bending stiffness EI and is modeled exactly above the 4-points bending model. This is shown in figure 7.37.

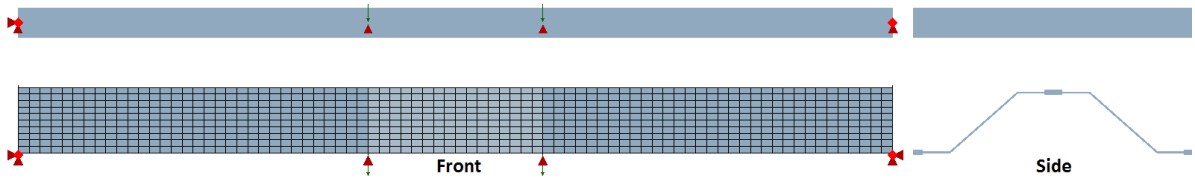

Figure 7.37: Soil-structure model

This beam is displaced in the same manner as the sheet pile wall and due to the corresponding bending stiffnesses, both models will bend alike. In the beam, there are no slender plate members and thus the beam will not be susceptible to local buckling. As a result, the vertical distance between the two models will only vary when the sheet pile buckles. This is illustrated in figure 7.38.

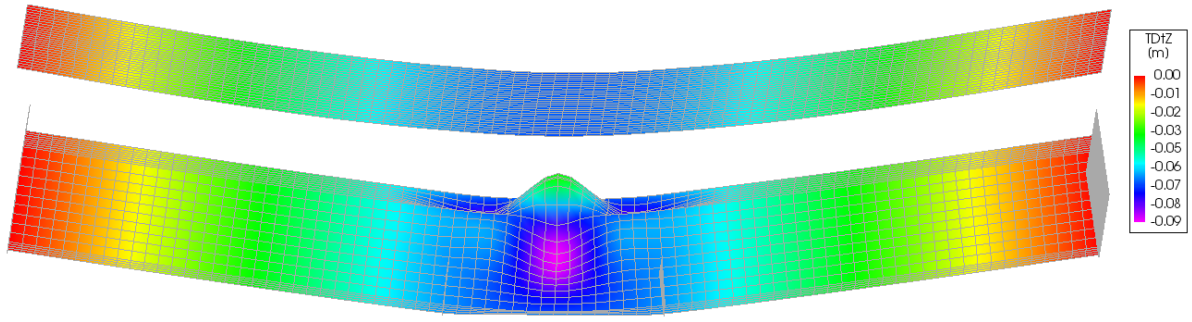

Figure 7.38: Displaced soil-structure model

To model the soil, an interface is created between the two models. This interface is modeled as smeared out vertical springs that connect the compression flange of the sheet pile to the beam. Q24IF elements are used as the interface. This element is serving as an interface between two planes in a three-dimensional configuration and is shown in figure 7.39.

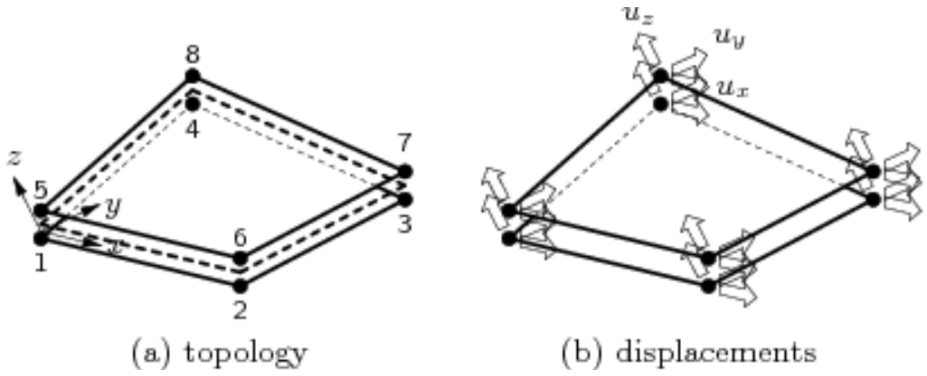

Figure 7.39: Q24IF interface element [1]

The model with springs is shown in 7.40.

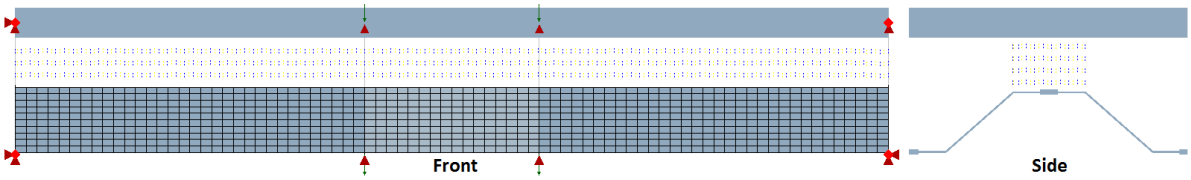

Figure 7.40: Interface soil-structure model

To verify whether the springs work as intended, the spring forces are compared with the vertical displacements in the compression flange. These are represented in figure 7.41 respectively.

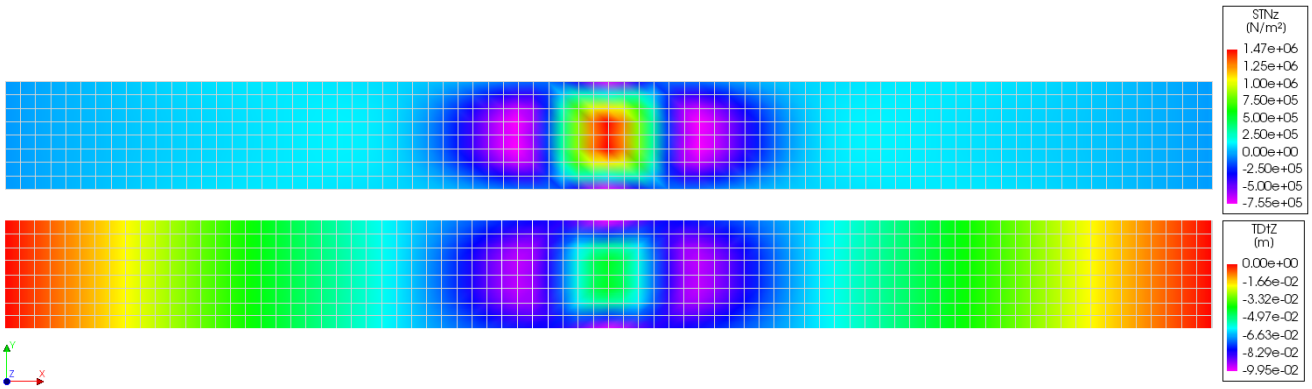

Figure 7.41: Upper: Spring force exerted on compression flange, Lower: Vertical displacement compression flange

It can be concluded that the springs work as intended and the spring force is only acting on the buckled part of the compression flange. To investigate the influence of different types of soil, the stiffness of the springs is adjusted to the modulus of subgrade reaction of various soil types [4]. These values are shown in table 7.5.

Table 7.5: Spring stiffness, modulus of subgrade reaction

Soil type	Spring stiffness k $[kN/m^3]$
Peat	2000
Clay	4000
Sand	40000

The M-κ curve has been calculated for the different soil types, the result is shown in figure 7.42.
The following conclusions with respect to the soil-structure behavior can be drawn:

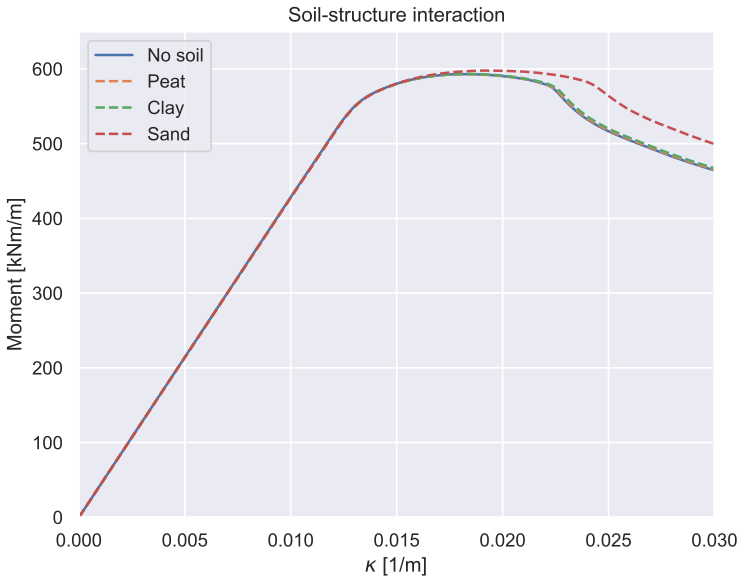

Figure 7.42: Soil-structure interaction

- Influence from peat and clay is negligible
- Sand increases the rotation capacity, influence on strength is negligible

For all tests, the plastic hinges were formed in weak layers, i.e., peat or clay. Accordingly, the M-κ curves can be calculated without taking into account of the soil.

7.3.5. Model parameters

Calibration of the model resulted in the parameters shown in table 7.6.

Table 7.6: FEM model parameters

Class profile	Strain-hardening $[\%of E]$	Imperfections $[mm]$
Class 2	0.5	2
Class 3	2	2

Accordingly, these values will be used for the determination of the M-κ diagrams of the tested profiles.

7.4. M-κ diagrams

7.4.1. AZ26

The AZ26 profile used in the Eemdijk experiment was geometric identical to the one used to calibrate the model. For this reason, both the cross-section and buckling modes are the same as in section 7.3.3. The profile does have a different yield strength and thus results in a different $M-\kappa$ diagram. This is illustrated in 7.43.

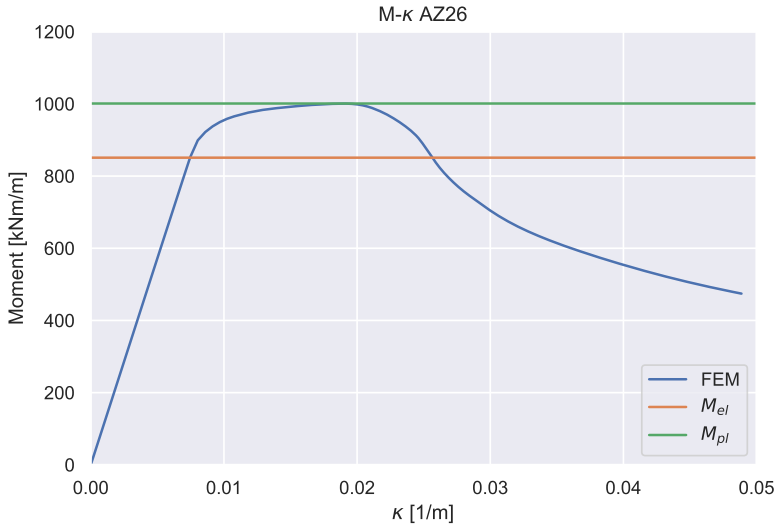

Figure 7.43: M-κ AZ26 POT

7.4.2. AZ13-700

Cross-section

The cross-section is modeled as shown in figure 7.44. The cross-sectional properties of the model relative to

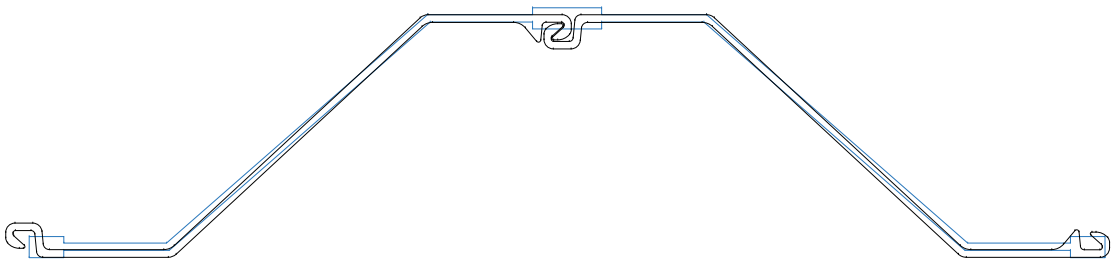

Figure 7.44: Cross-section: AZ13-700 model

the properties of the manufacturer are shown in table 7.7.

Table 7.7: Cross-sectional properties: AZ13-700 model

	Area $[cm^2]$	Moment of inertia $[cm^4]$
Brochure	188.50	28750
Model	186.42	28603
Δ%	-1.10	-0.51

Buckling analysis

A buckling analysis was performed. The mode from the excavated sheet pile is shown in figure 7.45 This corresponds to the 4th mode found in DIANA, see figure 7.46.

Figure 7.45: Excavated AZ13-700

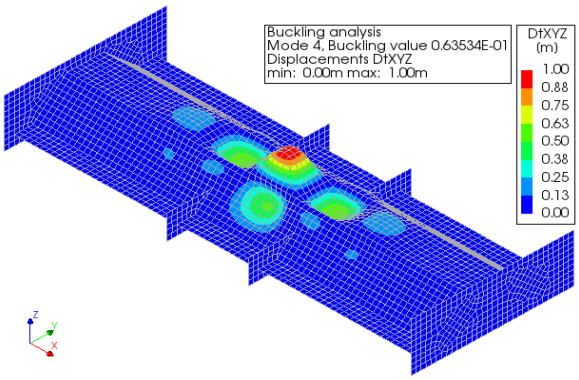

Figure 7.46: 4th buckling mode DIANA

The first three buckling modes are shown in figure 7.47.

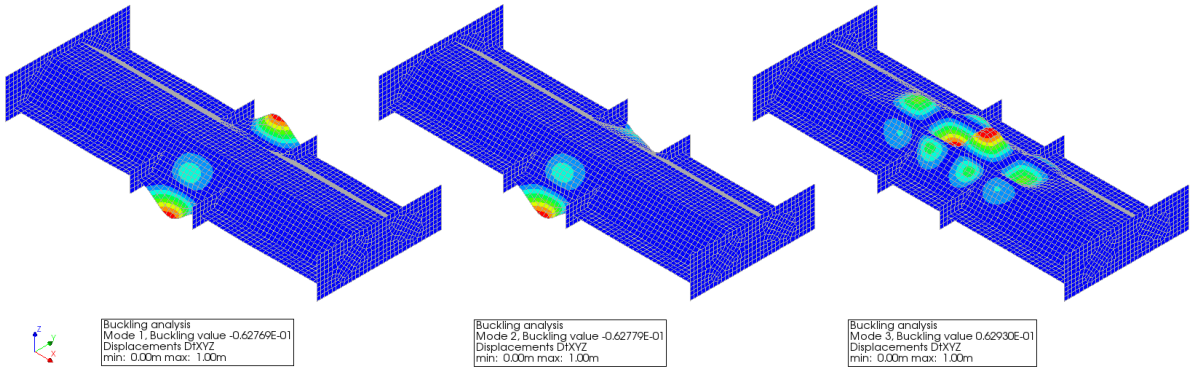

Figure 7.47: AZ13-700: Buckling modes 1,2 and 3

Result

The deformed shape of the profile is illustrated in figure 7.48.

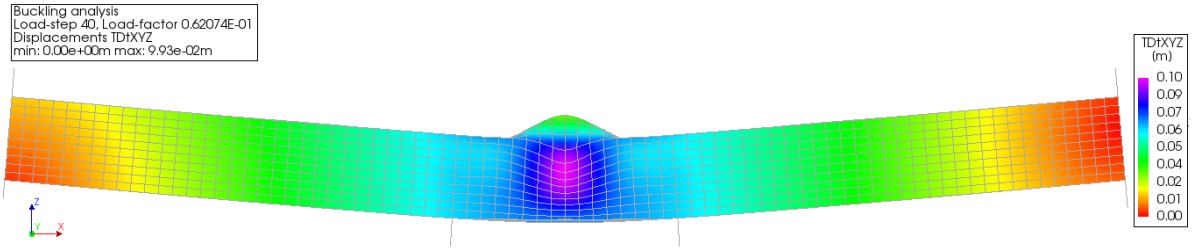

Figure 7.48: Deformed shape AZ13-700

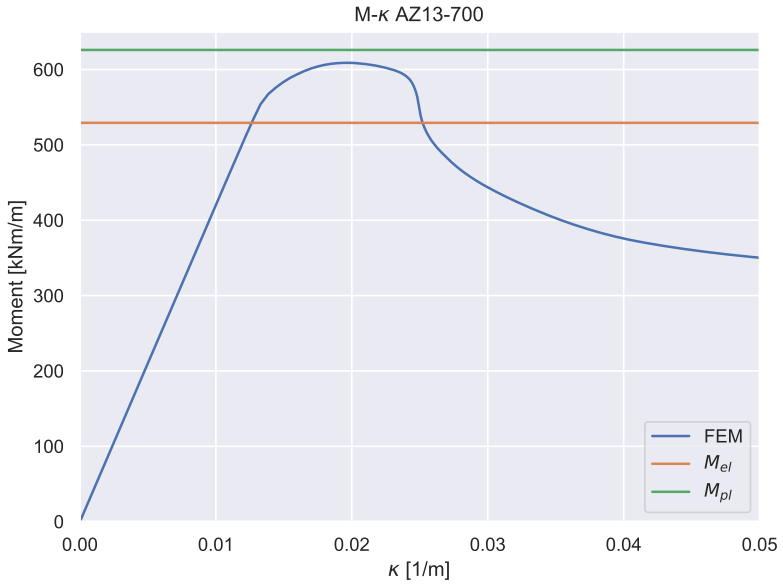

Figure 7.49: M-κ AZ13-700

7.4.3. GU8N FST

Cross-section

The triple profile used in the full-scale test is part of a continuous wall and accordingly can be modeled as a double profile as shown in figure 7.50.

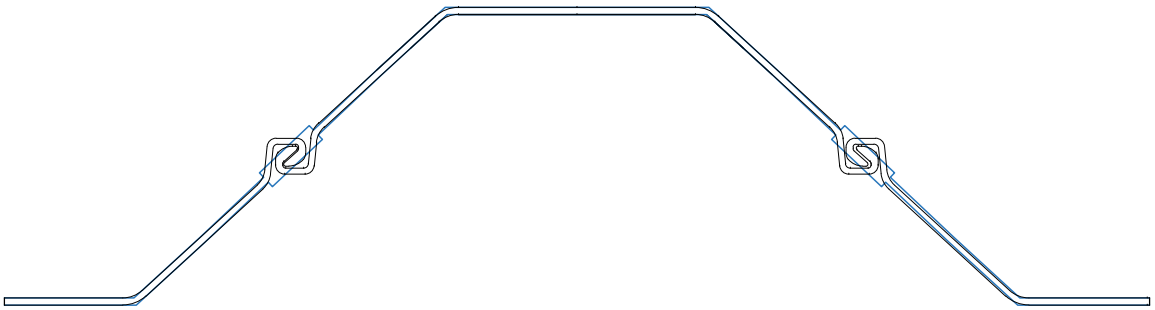

Figure 7.50: Cross-section: GU8N-double model

The cross-sectional properties given by the manufacturer and the modeled ones are shown in table 7.8.

Table 7.8: Cross-sectional properties: GU8N-FST model

	Area $[cm^2]$	Moment of inertia $[cm^4]$
Brochure	123.70	14420
Model	124.05	14598
Δ%	0.28	1.23

Buckling analysis

A buckling analysis was performed. The mode from the excavated sheet pile is shown in figure 7.51 This corresponds to the 18th mode found in DIANA, see figure 7.52.

Figure 7.51: Excavated GU8N FST

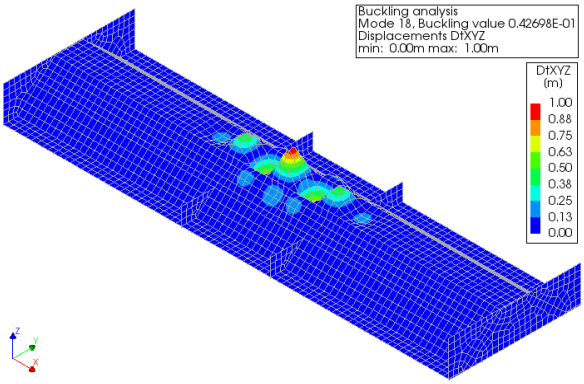

Figure 7.52: 18th buckling mode DIANA

The first 17 buckling modes are shown in figures 7.53 to 7.69.

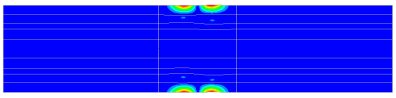

Figure 7.53: 1st mode

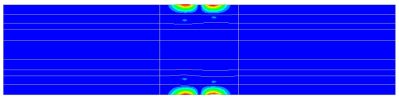

Figure 7.54: 2nd mode

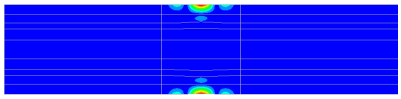

Figure 7.55: 3rd mode

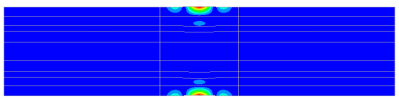

Figure 7.56: 4th mode

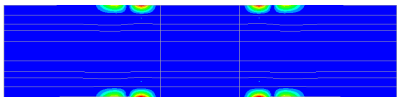

Figure 7.57: 5th mode

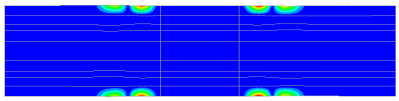

Figure 7.58: 6th mode

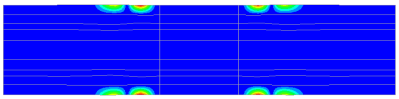

Figure 7.59: 7th mode

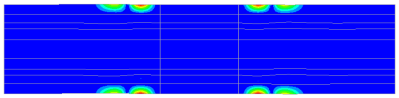

Figure 7.60: 8th mode

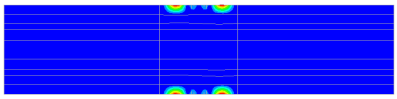

Figure 7.61: 9th mode

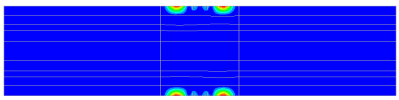

Figure 7.62: 10th mode

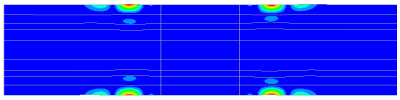

Figure 7.63: 11th mode

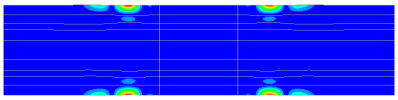

Figure 7.64: 12th mode

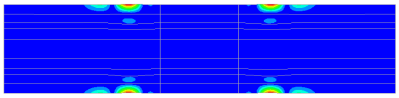

Figure 7.65: 13th mode

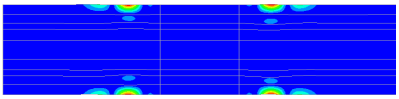

Figure 7.66: 14th mode

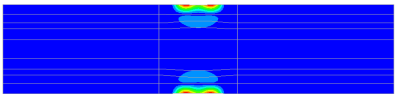

Figure 7.67: 15th mode

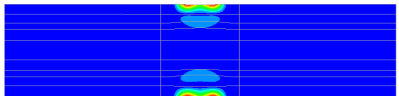

Figure 7.68: 16th mode

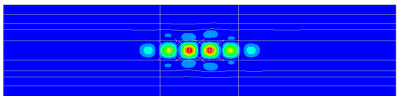

Figure 7.69: 17th mode

Result

The deformed shape of the model and the obtained diagram are shown in figure 7.70 and 7.71 respectively.

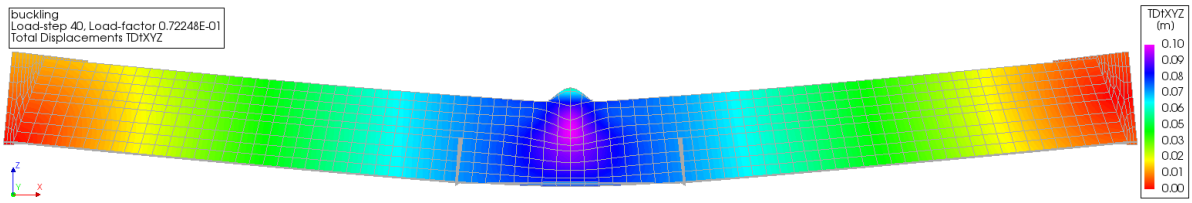

Figure 7.70: Deformed shape GU8N FST

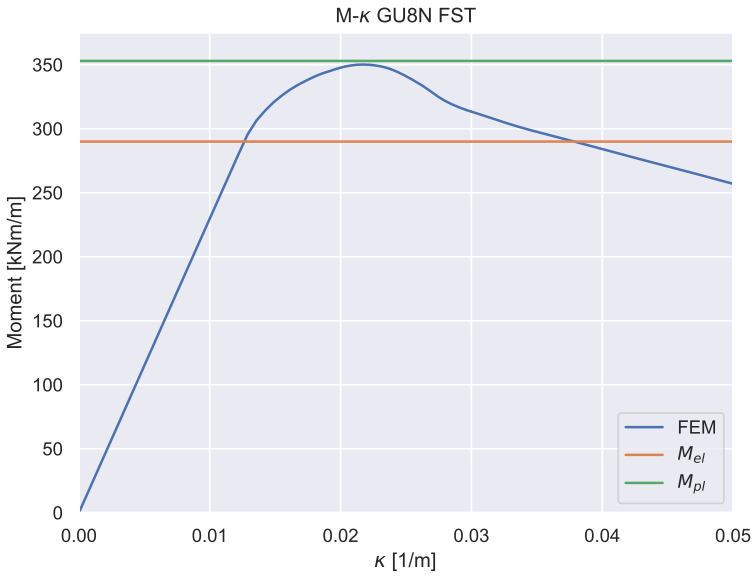

Figure 7.71: M-κ GU8N FST

7.4.4. GU8N POT

In contrary to the other tests, the GU8N POT test is performed on a triple profile, which isn't part of a continuous wall. Applying the same approach to derive the M-κ diagram would, therefore, result in an overestimation of the capacity. To obtain a reliable diagram, deformation of the cross-section should not be restricted and thus a load controlled test is required. However, as discussed in section 7.2.2 this approach will only be able to solve part of the diagram. Furthermore, since there is no horizontal support as with a continuous wall, no plates are modeled for the load introduction. Accordingly, folding out of the sheet pile is not restricted, leading to a reduction in moment of inertia.

Cross-section

The cross-section is modeled as shown in figure 7.72.

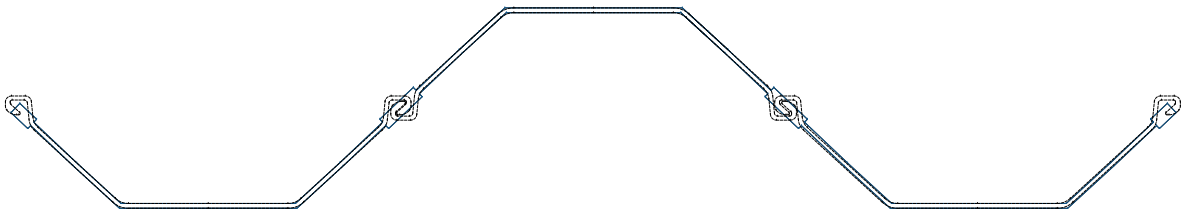

Figure 7.72: Cross-section: GU8N-triple model

The cross-sectional properties given by the manufacturer and the modeled ones are shown in table 7.9.

Table 7.9: Cross-sectional properties: GU8N-POT model

	Area $[cm^2]$	Moment of inertia $[cm^4]$
Brochure	185.50	20030
Model	184.62	20022
Δ%	-0.47	-0.04

Buckling analysis

A buckling analysis was performed. The mode from the excavated sheet pile is shown in figure 7.73 This corresponds to the 18th mode found in DIANA, see figure 7.73.

Figure 7.73: Excavated GU8N POT

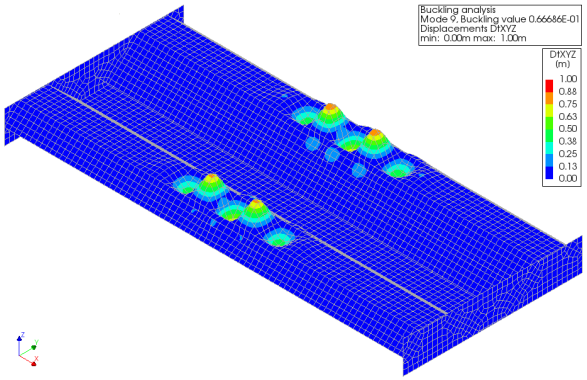

Figure 7.74: 9th buckling mode DIANA

A top-view of the first 8 buckling modes are shown in figures 7.75 to 7.82.

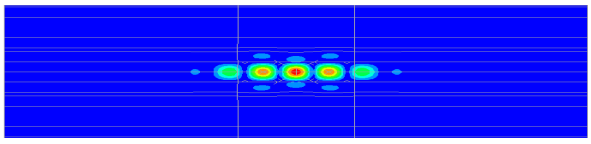

Figure 7.75: 1st mode

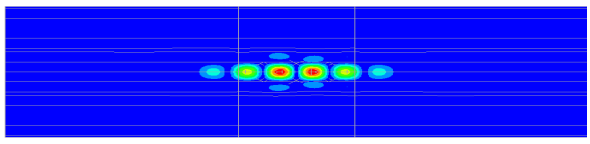

Figure 7.76: 2nd mode

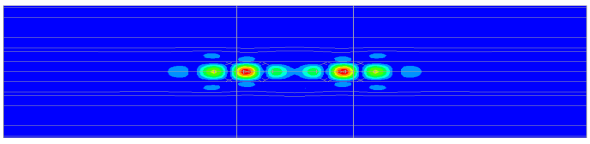

Figure 7.77: 3rd mode

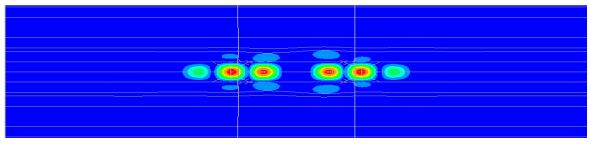

Figure 7.78: 4th mode

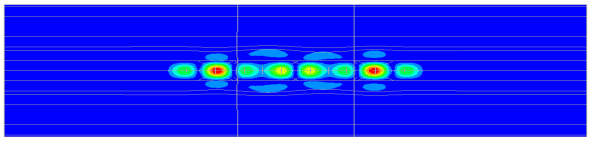

Figure 7.79: 5th mode

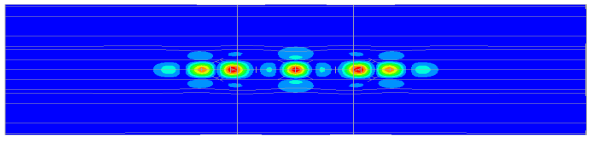

Figure 7.80: 6th mode

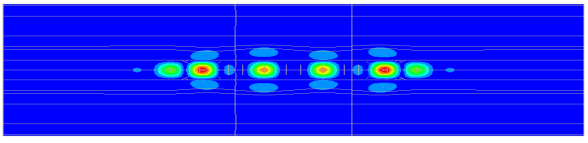

Figure 7.81: 7th mode

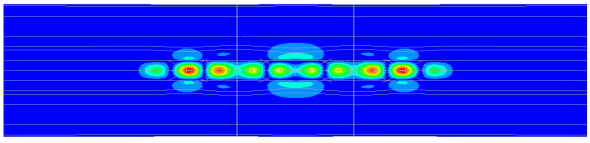

Figure 7.82: 8th mode

Result GU8N

The deformed shape of the model and the obtained diagram are shown in figure 7.83 and 7.84 respectively.

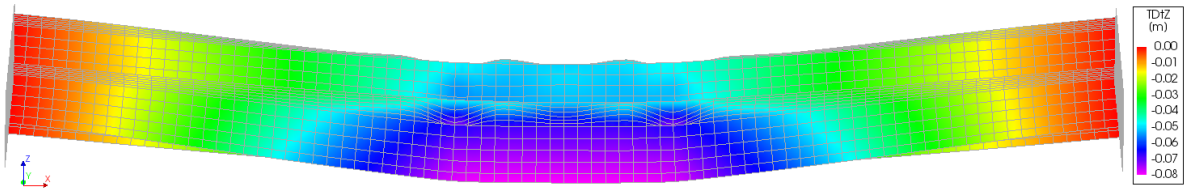

Figure 7.83: Deformed shape GU8N

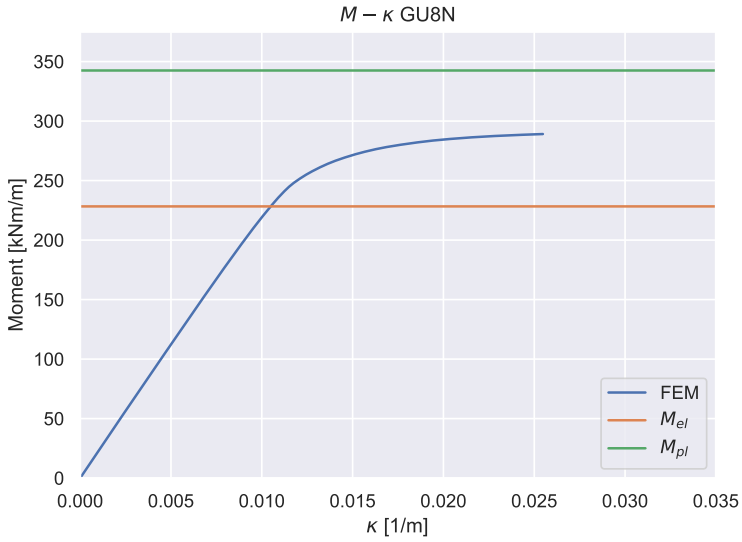

Figure 7.84: M-κ GU8N

Due to the unconstrained edges, large deformations are visible in the web, which results in more material closer to the neutral axis. As a result, the moment of inertia decreases, while the shape factor increases. Because of the decreased moment of inertia and the eccentricity of the neutral axis, the moment capacity is lower compared to the continuous wall. However, the rotation capacity increases, due to the larger shape factor.

Result GU8R

The buckling mode for the reversed profile corresponds to the first mode found in DIANA, see figure 7.75. The deformed shape of the model and the obtained diagram are shown in figure 7.85 and 7.86 respectively.

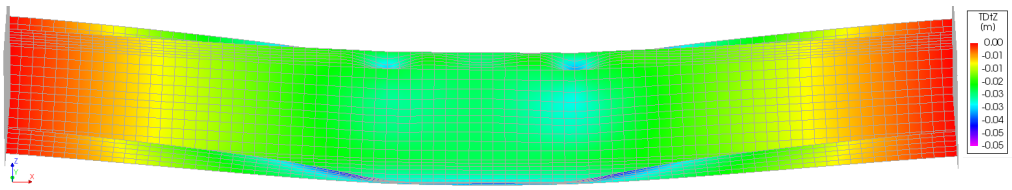

Figure 7.85: Deformed shape GU8R

Due to the unconstrained edges, large deformations are visible on the web. Here, the material is displaced towards the outer fiber, which results in a higher moment of inertia and a lower shape factor. However, due to the limited material in the compression zone, local buckling occurs much earlier than for the continuous wall.

Figure 7.86: M-κ GU8R

Rotation capacity

Three curves have been obtained for the GU8N profile:

- GU8N as a continuous wall, 1/2 flanges as compression flange
- GU8N as a triple profile, 2/3 flanges as compression flange
- GU8R as a triple profile, 1/3 flanges as compression flange

Figure 7.87 indicates that the moment capacity is positively correlated with the ratio of compression flanges.

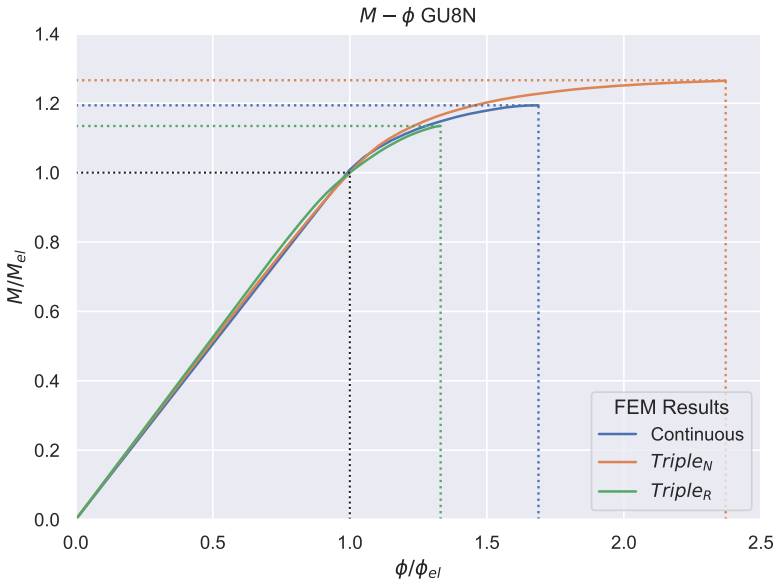

Figure 7.87: Comparison M-ϕ GU8N

So, the unconstrained edges of U-piles influence the rotation capacity by a deformation induced change of the shape factor, while the ratio of material in the compression members determines the rate M/M_{el} at which local buckling occurs.

8

Moment distribution

8.1. Introduction

With the derived M-κ curves, the moment distribution is obtained. This internal moment distribution should be in equilibrium with the external moment distribution. Accordingly, a verification is performed by comparing the two. Above the surface, there are no earth or water pressures acting on the sheet pile. As a result, the external moments above the surface are solely depending on the pulling force. This is indicated in figure 8.1.

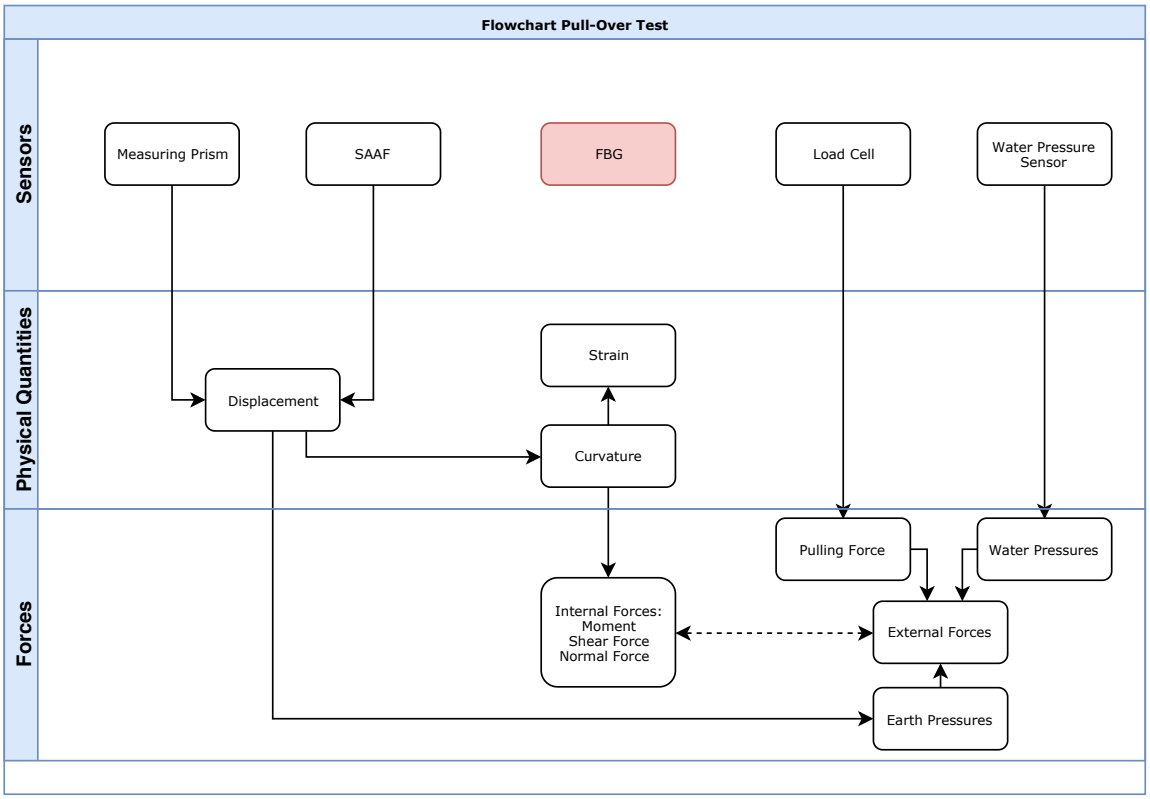

Figure 8.1: POT: Flowchart data streams

For the pull-over tests, graphs are shown for several load steps up to the maximum pulling force measured, before the SAAF was removed. For the FST, the graph illustrates the last 24 hours before the collapse of the test dike.

8.2. AZ26

The displacement, curvature and moment are shown in figure 8.2.

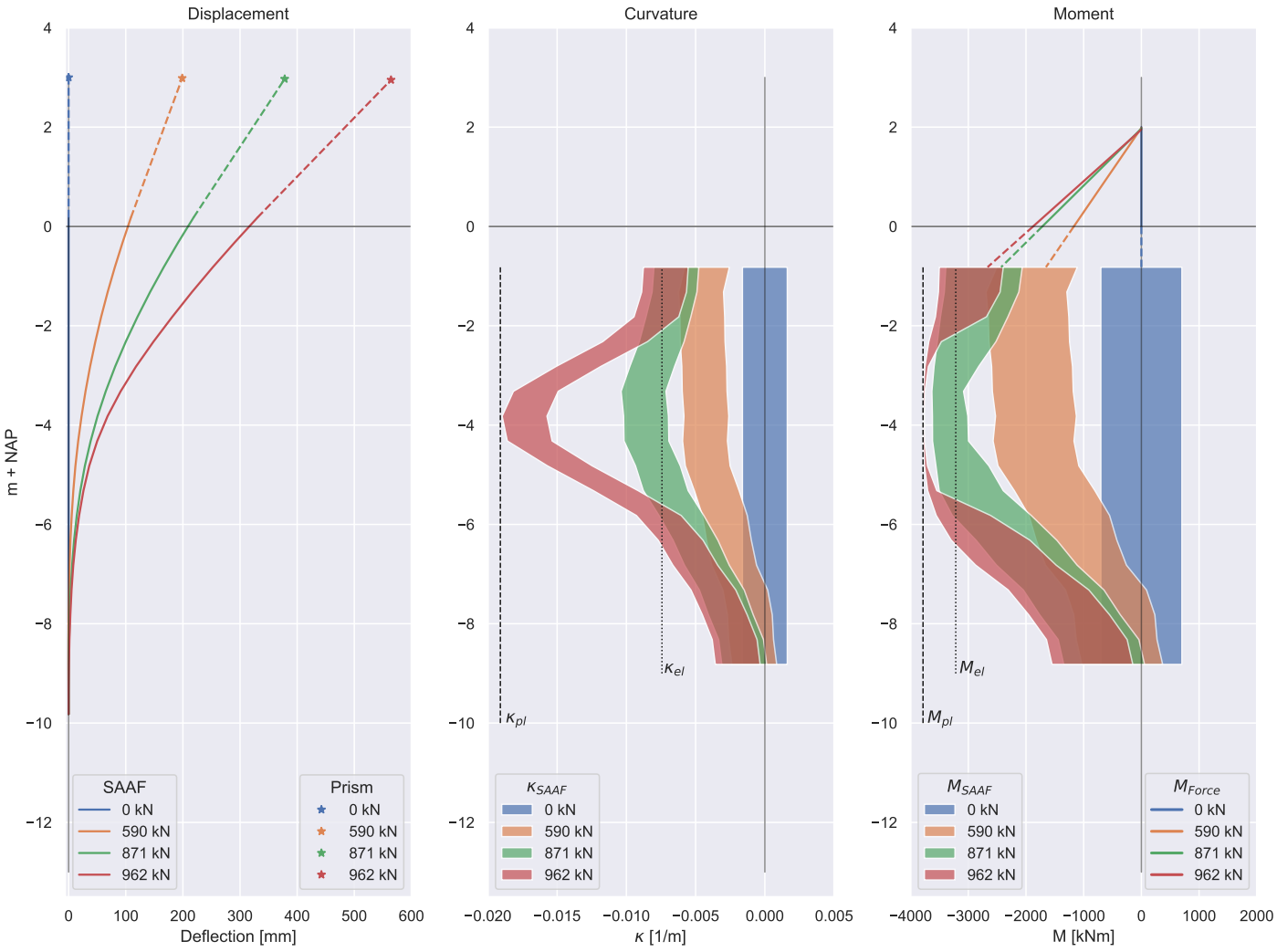

Figure 8.2: AZ26: Displacement, curvature and moment

The obtained moment distribution corresponds well to the moment estimated from the acting force. Furthermore, two limits are indicated, namely M_{el} and M_{pl}. These correspond to the elastic and plastic moment capacity, respectively. The same limits are indicated for the curvatures corresponding to these moments, κ_{el} and κ_{pl} and are derived from the $M-\kappa$ diagram. The AZ26 S327 is a class 2 profile according to the Eurocode. As a result, advantage may be taken from the plastic resistance. The obtained moment distribution confirms this since the full plastic moment is reached before failure occurred. Although a clear edge effect was observed, this did not result in premature failure of the sheet pile.

8.3. AZ13-700

The displacement, curvature and moment are shown in figure 8.3.

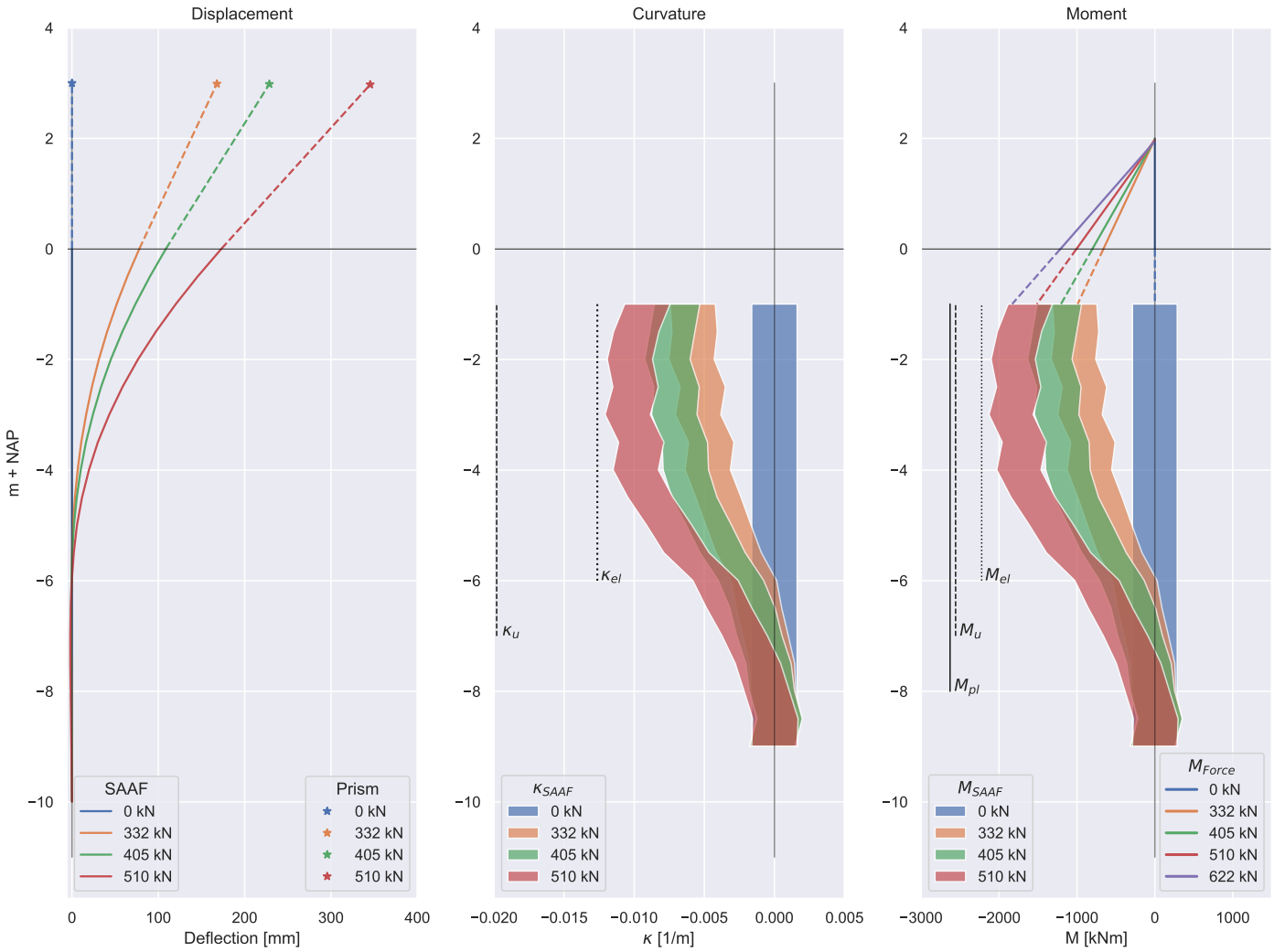

Figure 8.3: AZ13-700: Displacement, curvature and moment

The obtained moment distribution corresponds well to the moment estimated from the acting force. The AZ13 S406 is a class 3 profile and is expected to buckle before the full plastic moment is reached. As a result, the plastic moment M_{pl} is only theoretical and the corresponding κ_{pl} does not exist. For this reason, the ultimate moment from the $M-\kappa$ diagram is included, at which the profile is expected to fail. Furthermore, the corresponding κ values have been included. Regarding the Eurocode, the elastic capacity may be used. Unfortunately, the SAAF was removed before the full capacity was reached as is shown in figure 5.4. However, it is very likely that the elastic capacity was exceeded after the SAAF was removed. As an indication, the moment corresponding to the maximum pulling force is indicated in purple.

8.4. GU8N POT

The displacement, curvature and moment are shown in figure 8.4.

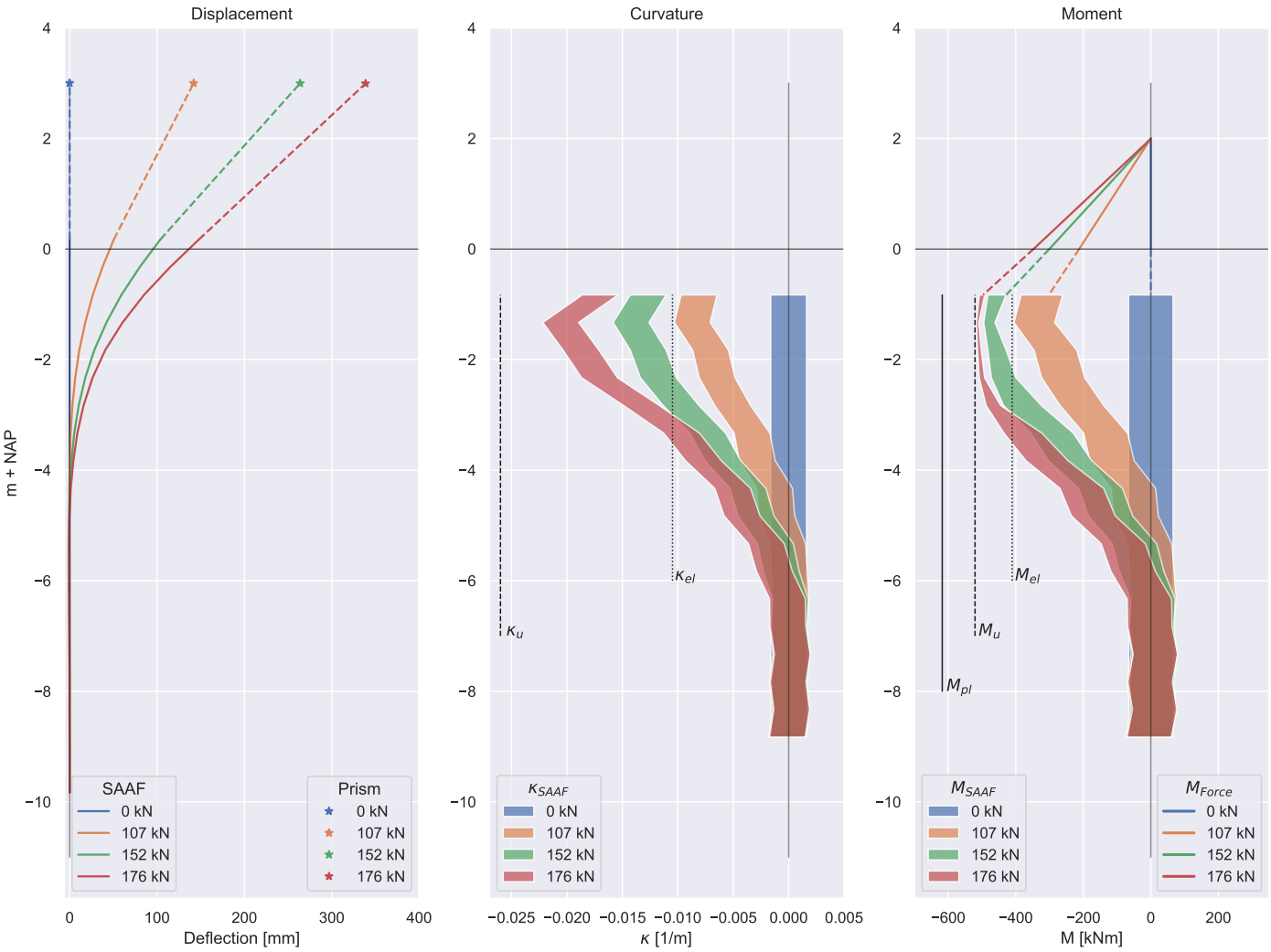

Figure 8.4: GU8N-t: Displacement, curvature and moment

The obtained moment distribution corresponds well to the moment estimated from the load acting on the sheet pile. The GU8N S380.5 is also a class 3 profile and thus the ultimate moment M_u is included. Both SAAF and force indicate this moment reached. Conform Eurocode, the elastic capacity may be used. However, the measurements indicate that there is quite some capacity left past the elastic limit.

8.5. GU8R POT

The displacement, curvature and moment are shown in figure 8.5.

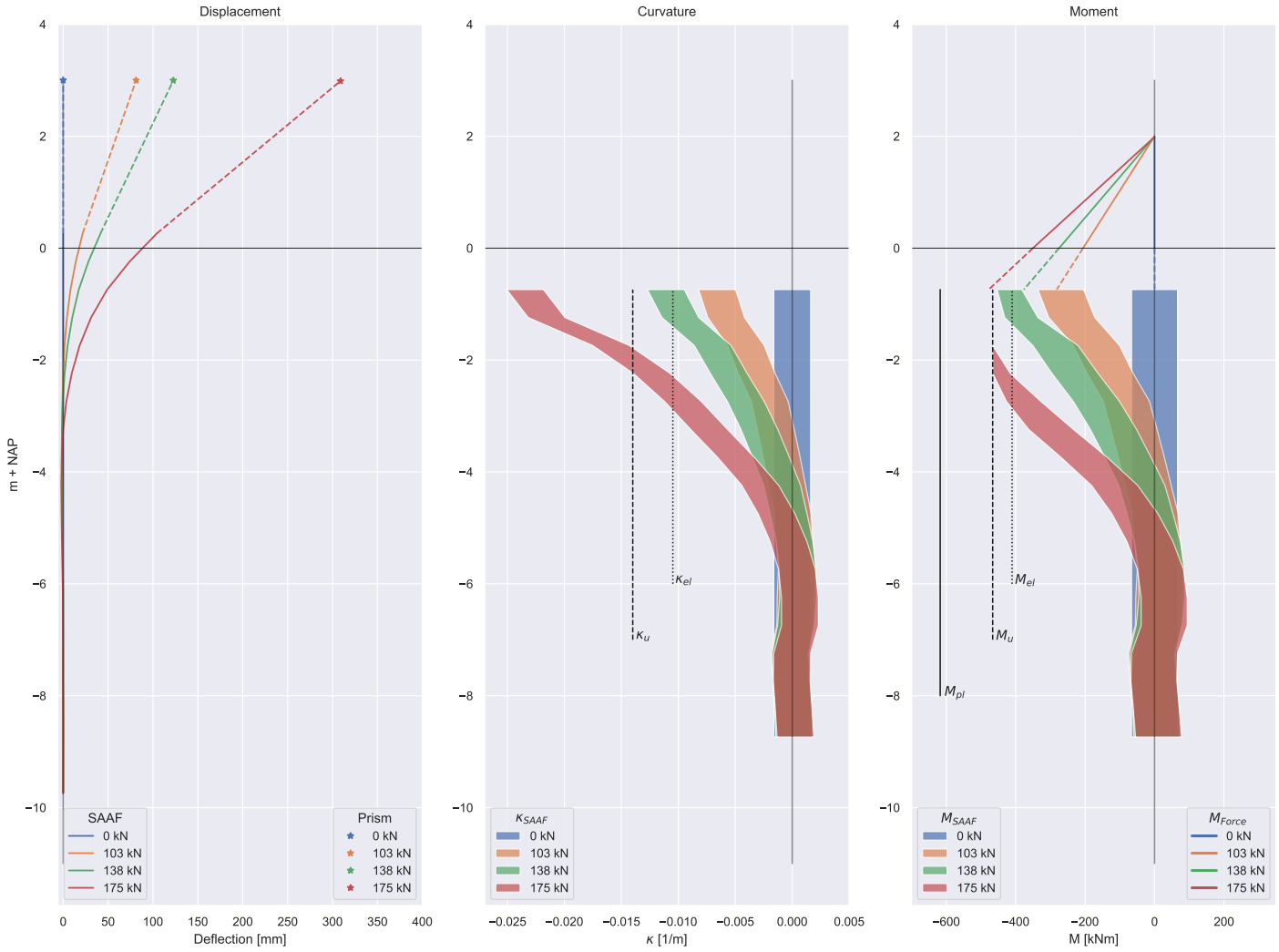

Figure 8.5: GU8R-t: Displacement, curvature and moment

The obtained moment distribution corresponds well to the moment estimated from the load acting on the sheet pile. But for the largest measured force, the curvatures were larger than expected. As shown in figure 7.86, the rotation-capacity of the reversed profile is limited. Based upon this, the profile was expected to fail earlier and accordingly a lower reaction force was expected. However, both SAAF and force indicate that the ultimate moment M_u was exceeded. A possible explanation might be related to the weather conditions. Temperatures dropped to -8°C during the night prior to the GU8R POT, which resulted in frozen topsoil. As a consequence, there might be some additional capacity and thus larger reaction forces than expected.

8.6. GU8N FST

For the FST, the last 24 hours before collapse are shown in figure 8.6.

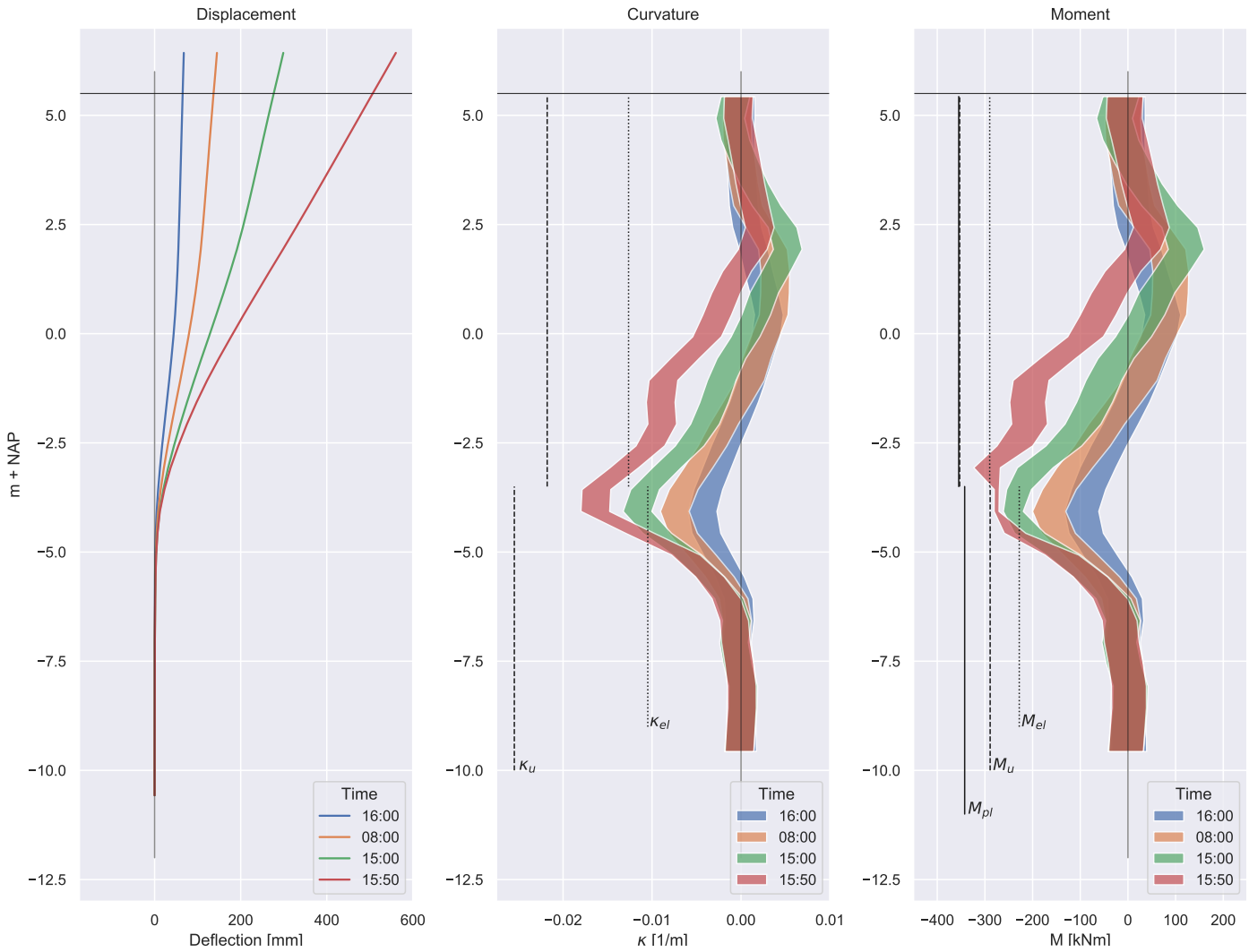

Figure 8.6: FST: Displacement, curvature and moment

As a result of the staggered layout shown in figure 4.4, the distribution is split into two parts. The top part corresponds to the continuous wall as discussed in section 7.4.3, while the bottom part corresponds with a discontinuous GU8N profile as discussed in section 7.4.4.

The last estimated moment already shows significant capacity past the elastic limit M_{el} and almost reaches the ultimate moment M_u in the staggered part. However, the failure of the dike occurred at 15:59, while the last SAAF measurement was at 15:50. For this reason, it is expected that M_u is reached.

Furthermore, the moment curve illustrates an alternating moment. This is surprising since this means that the slope of a failing dike still supports the sheet pile close to the surface. This support holds up to failure and results in a smaller deflection at the crest of the dike. Accordingly, with a deflection at the crest of the dike of 0.5 m, the ultimate moment capacity is reached.

The sheet pile finally collapsed just below the transition of continuous to a staggered pile. According to the Eurocode, the elastic capacity may be used since it is a class 3 profile, but also in this test, there is still quite some capacity left after the elastic moment is reached.

9

Edge effect

9.1. Introduction

For sheet piles implemented as panels, a distinction has to be made between mid and side piles. With respect to mid piles, side piles endure two additional effects, namely:

- Mobilization of more soil as a result of arching
- Less restriction against cross-sectional deformation due to one of the sides being unconstrained

For this reason, the OSPW states that a factor of 1.1 on forces and moments should be applied to the entire panel. To verify if this factor is adequate, a comparison is performed between the behavior of mid and side piles of the pull-over tests.

9.2. Background

The factor is explained by a rotation of the side pile of up to 5°, due to the unrestricted edge [3]. This is indicated in figure 9.1.

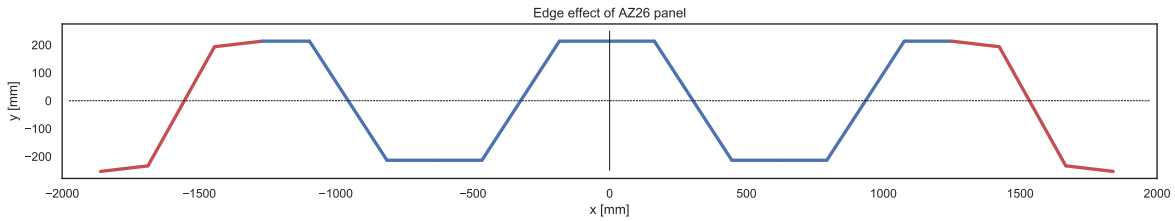

Figure 9.1: AZ26: Deformation outer flange in tension

As a result of the rotation, the stiffness increases. Since stiffer parts carry more load, this will lead to an increase of total stresses between 5 and 10%. However, this assumes that the neutral axis does not shift.

9.3. Test results

Four panels have been tested in the pull-over test. For the AZ13-700 the SAAF was removed before the elastic capacity was reached, while for the GU8N-reversed the side SAAF has been found unreliable. Accordingly, the edge effect is investigated for the AZ26 and GU8N-normal test.

9.3.1. AZ26

The influence of the edge effect on displacement and curvature is illustrated in 9.2.

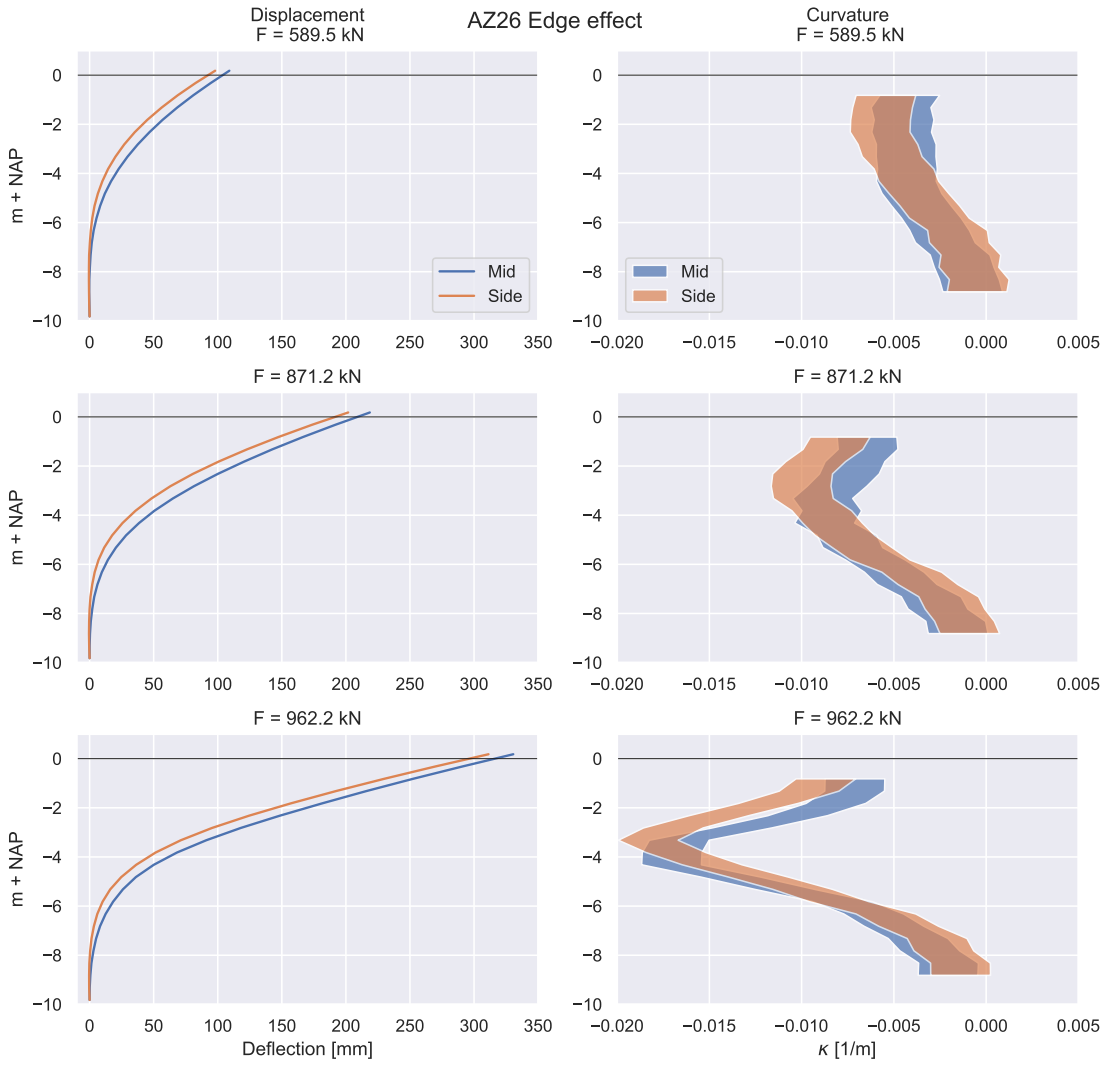

Figure 9.2: AZ26: Edge effect

As a result of more soil mobilization at the edge, the side pile has less horizontal displacements deeper in the soil. At the point of load introduction, however, both piles have the same displacements. For this reason, larger curvatures are required in the side pile. Furthermore, it can be observed that the transition point is located at the plastic hinge. Below this point, the curvatures in the middle are dominant, while above this point, the side curvatures are dominant. In figure 9.3, the maximum curvature of the middle and side pile are shown as a function of time.

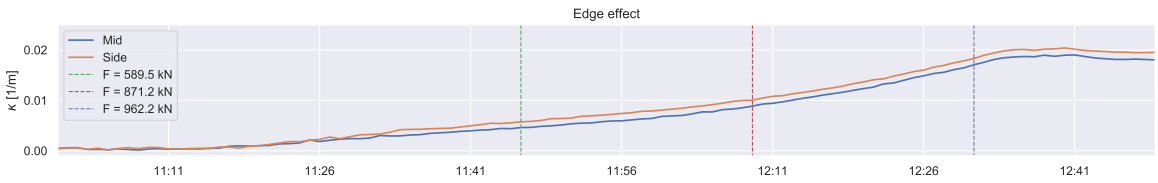

Figure 9.3: AZ26: Edge effect over time

For the last 50 measurements before the SAAF was removed, curvature for the edge pile is on average 14.5% larger than for the mid pile.

With the derived moment distribution and the measured curvature at the side, the $M-\kappa$-diagram for the side is computed. The diagrams for the mid and side pile at depth of the plastic hinge are illustrated in figure 9.4.

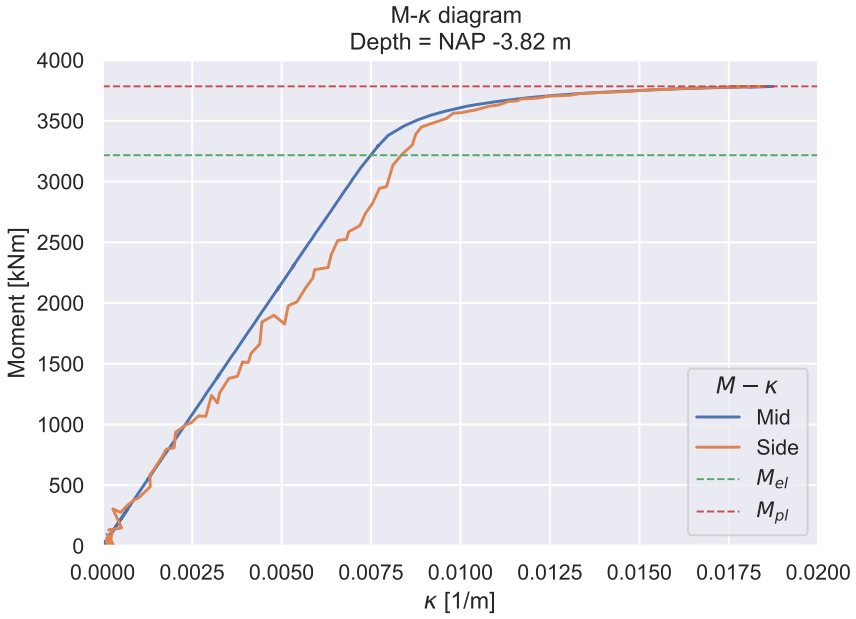

Figure 9.4: AZ26: $M-\kappa$ diagram of middle and side

The graph indicates that at the depth of local buckling, the side pile actually has a lower stiffness than the mid-pile. From this it can be concluded that the neutral axis actually shifts at the edge of the panel, resulting in a lower moment of inertia and thus lower total stresses. This is in contradiction with the reasoning of the OSPW, which states that the total stresses will be up to 10% larger as a result of increased stiffness.

9.3.2. GU8N

The derivation of the edge factor is based on a panel of Z-sections. However, the design approach does not make a distinction for U-sections. Following the same approach as for the AZ26, the deformed shape of the GU8N section is illustrated in figure 9.5.

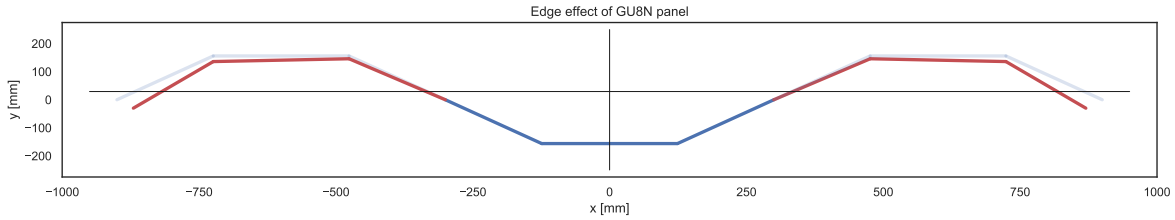

Figure 9.5: GU8N: Edge effect U-section

For triple U-sections, the neutral axis is slightly eccentric due to asymmetry. Deformation of the outer piles will result in a reduction of the stiffness since the outer flanges displace towards the neutral axis. The influence of the edge effect on displacement and curvature is shown in figure 9.6.

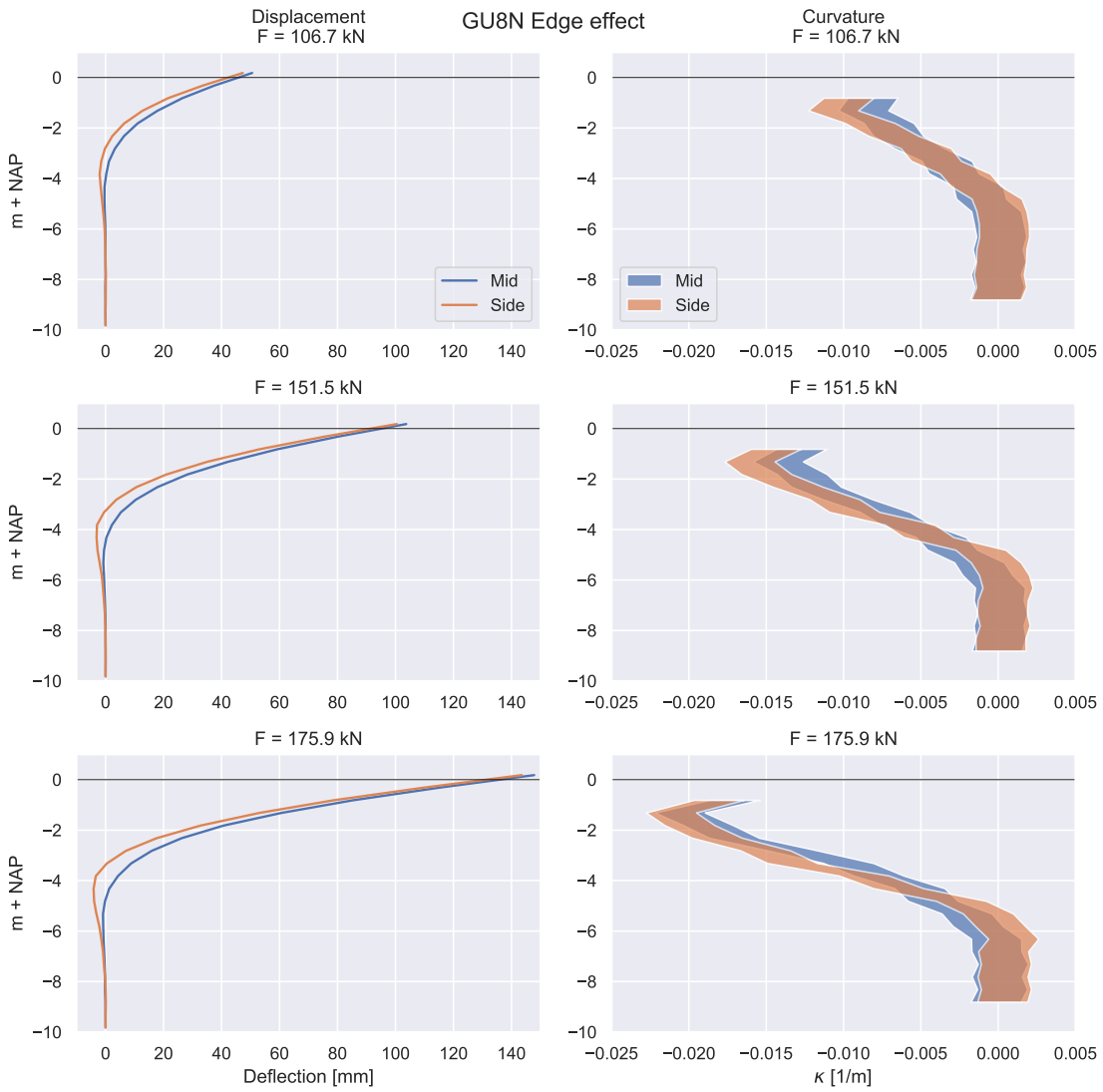

Figure 9.6: GU8N: Edge effect

The edge effect is clearly visible. However, the differences between mid and side are smaller than with the Z-sections. This can be explained by the dimensions of the panel, see figure 4.20. The distance between mid and side is much smaller for the U-sections. As a result, the influence of the edge effect is also smaller. In figure 9.7, the maximum curvature of the mid and side pile are shown as a function of time.

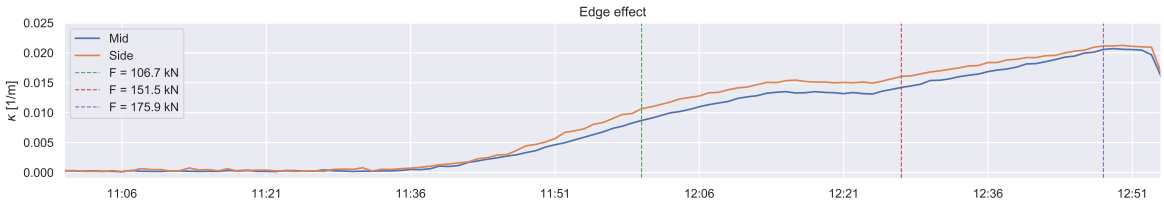

Figure 9.7: GU8N: Edge effect over time

For the last 50 measurements before the SAAF was removed, curvature for the edge pile is on average 11.3% larger than for the mid pile.

With the derived moment distribution and the measured curvature at the side, the $M-\kappa$-diagram for the side is computed. The diagrams for the mid and side pile at depth of the plastic hinge are illustrated in figure 9.8.

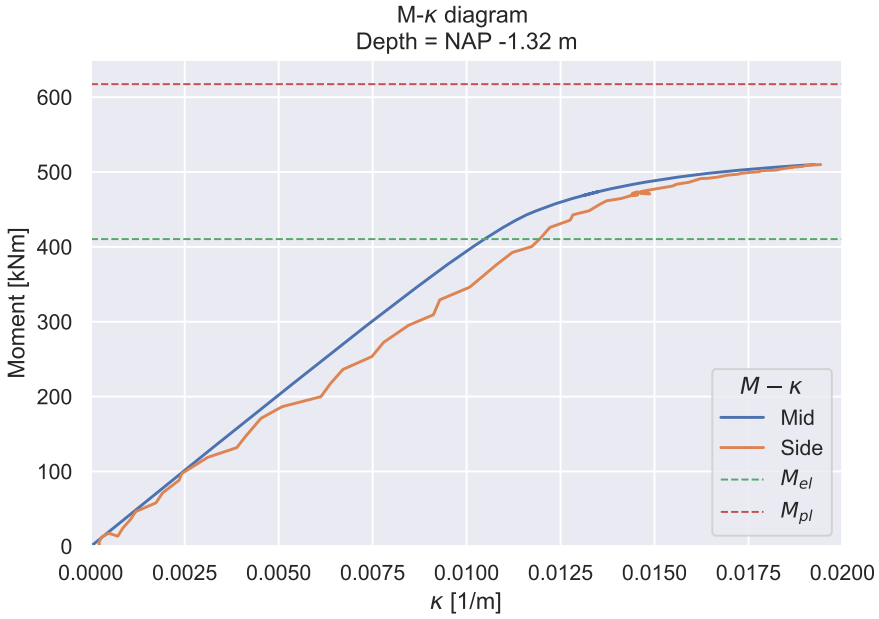

Figure 9.8: GU8N: $M-\kappa$ diagram of middle and side

Similar as for the Z-section, the side pile actually has a lower stiffness than the mid pile at the location of local buckling. Accordingly, the side has a lower moment of inertia and thus lower total stresses. This is in contradiction with the reasoning of the OSPW, which states that the total stresses will be up to 10% larger as a result of increased stiffness.

10

Conclusions and recommendations

10.1. Conclusions

10.1.1. Introduction

The global objective of this study was to obtain a good understanding of the structural behavior of sheet pile walls in the soil. This understanding is obtained by means of analyzing the results of two full-scale tests. The findings are used to see if the current design standards are adequate, or if there is room for improvement.

10.1.2. Research questions

Within this scope, the following research questions have been answered:

1. *What is the current design approach?*

   The current design guideline is the OSPW. Two aspects that are addressed by this thesis are:

   - In contradiction to the Eurocode [10], it is not allowed to take into account the plastic capacity of structural elements.
   - When the opening between structural elements is larger than the width (in length direction of the dike), a model factor of 1.1 should be applied on the calculated forces and moments.

2. *How are the curvatures and moments in the sheet pile distributed during the tests?*

   The moment-distributions are given in chapter 8. In all tests, the elastic capacity was exceeded. For the AZ26, the full plastic moment capacity was reached.

3. *What conclusions can be drawn with regards to the design approach based on this?*

   #### Plastic design of sheet piles

   Steel is a plastic material and plastic design has been around for some time now. It has been adopted by most design guidelines, including the Eurocode. For the design of dike stability screens in the Netherlands, however, it is still not allowed. The Eemdijk tests support the Eurocode since all the tests exceeded the elastic limit before failure occurred.

   - The AZ26 S327 is a class 2 profile according to the Eurocode. As a result, advantage may be taken from the plastic resistance. This is in accordance with the derived moment-curvature diagram, which reaches the full plastic capacity in combination with a high rotations capacity. The obtained moment distribution of the test also confirms this, since the full plastic moment is reached before failure occurred.
   - The AZ13-700 S406 is a class 3 profile according to the Eurocode. Accordingly, the elastic capacity may be used. Unfortunately, the SAAF was removed before the full capacity was reached, this is shown in figure 5.4. However, after removal of the SAAF, the applied force reached a significantly higher value. For this reason, it is very likely that the elastic capacity was exceeded after the SAAF was removed. The moment-curvature diagram indicates that the ultimate moment is close to the full plastic moment, however, the utilized rotation capacity is limited.

- The GU8N S380.5 is a class 3 profile conform the Eurocode. Thus, the elastic capacity may be used. Both the POT and the FST indicate that there is quite some moment capacity left past the elastic limit. Furthermore, in both tests, the ultimate moment is reached before geotechnical failure. The moment-curvature diagram indicates that the ultimate moment is close to the full plastic moment, however, the rotation capacity is limited.

Accordingly, it should be allowed to take advantage of the plastic resistance, depending on the profile class:

- Class 2 profiles should be allowed to take advantage of the plastic resistance.
- Class 3 profiles buckle before the full plastic capacity is reached. For this reason, it is not allowed to take advantage of plastic resistance. Although both AZ13-700 and GU8N sections had an ultimate moment M_u that is close to the full plastic moment, the rotation capacity is limited.

Edge effect

For sheet piles implemented as panels, a distinction has to be made between mid and side piles. With respect to mid piles, side piles endure two additional effects, namely:

- Mobilization of more soil as a result of arching
- Less restriction against cross-sectional deformation due to one of the sides being unconstrained

For this reason, the OSPW states that a factor of 1.1 on forces and moments should be applied to the entire panel. The factor is explained by a rotation of the side pile of up to 5°, due to the unrestricted edge [3]. As a result of rotation, the stiffness increases. Since stiffer parts carry more load, this will lead to an increase of total stresses between 5 and 10%. However, this assumes that the neutral axis does not shift.

To verify if this factor is adequate, a comparison is made between the behavior of mid and side piles of two pull-over tests. Both tests indicate that at the depth of local buckling, the side pile actually has a lower stiffness than the mid-pile. As a result, the moment of inertia and the total stresses are lower. This is in contradiction with the reasoning of the OSPW.

The total stresses in the side pile are actually lower. Furthermore, since there is a good fit between external and internal moments for the mid pile, the mid pile does not carry a significantly higher load. Accordingly, a factor of 1.1 on forces and moments has been found conservative.

Result of utilizing the extra capacity

Implementing both purposed changes into the current design approach will lead to considerable savings in the required steel. This is quantified in table 10.1.

Table 10.1: Reduction in required steel

Panel	Class 2	Class 3
Yes	24%	9%
No	15%	0%

The reduction in steel will not only result in cheaper dikes but also in lighter sheet piles, requiring smaller machinery. Since the sheet pile solution is often applied at locations, where space is limited, this greatly increases the applicability.

4. *Is it possible to relate curvature to moments by means of a finite element calculation?*

   With a finite element model, it was possible to reproduce the results of multiple documented 4-point bending tests, which were performed in the lab. The same approach was subsequently used to simulate 4-point bending tests upon sheet piles used in the Eemdijk test. As a verification, results were compared with moments estimated from the applied force in the pull-over tests. For all the tests, the moment estimated from SAAF measurements and the moment estimated from the applied force are in agreement.

In order to get a moment-curvature diagram that continues after buckling occurs, however, the 4-point bending test has to be performed displacement controlled. The displacement is introduced in the tension zone of the sheet pile and as a result, the displacement is equal throughout this section. This prohibits cross-sectional deformation and results in a slight overestimation of the capacity. Furthermore, the actual stress-strain behavior of the sheet pile has to be obtained by means of a tensile test. Since this test was not performed, the stress-strain behavior is modeled by a bi-linear model with nominal yield.

In order to deal with these uncertainties, a sensitivity analysis was performed. Both the post-yield stiffness and the imperfections were adjusted in order to fit the results of two real tests.

5. *What conclusions can be drawn with regards to the applied monitoring program?*

FBG

An extensive verification process was performed in order to verify if the FBG strain gauges were reliable. This verification process consisted of two independent methods, namely:

- Verification by the load signal
- Verification by strain estimation (SAAF)

In both verification tests the FBG sensors performed poorly and, accordingly, are found unreliable.

SAAF

The SAAF sensors were used as an alternative for strain gauges since it was possible to estimate the strains. However, there are some limitations of using this sensor to monitor steel strains. There is some uncertainty in de estimation due to the accuracy and the large step-size related to the dimensions of the sensor. These uncertainties lead to a spread in calculated curvatures and strains and as a result, translate to an uncertainty in the moment. Heavier sheet piles have a steep M-κ diagram. Accordingly, uncertainty in the curvature will result in a large uncertainty in moments for these profiles. This is clearly visible in figure 8.2.

6. *Does the embedment of the sheet pile delay the onset of local buckling?*

   In contradiction to a sheet pile in the field, a 4-point bending test is performed without the presence of soil. For this reason, the effect of soil on local buckling is investigated. A significant increase in the profiles rotation capacity was found, due to an embedment in sand. The effect of weak layers such as peat and clay, however, was negligible.

   It should be noted that the applied model only took into account soil around the compression flange, while the buckling shape also includes the web. For this reason, the increase in rotation capacity is probably underestimated.

10.2. Recommendations

10.2.1. Monitoring

FBG

The applied strain gauges in the Eemdijk test were recently developed in order to measure a wide range of strains. The experience with this specific sensor, however, was limited. For future tests, it is not recommended to apply sensors of which the reliability is not properly tested. It would be a better practice to be applied as secondary strain instrumentation or at a small part of the test as a pilot, such that the reliability could be tested.

SAAF

The SAAF sensors used in the test had a length of 50 cm and are also available in 30.5 or 20 cm. The use of these dimensions would result in a much smaller numerical error. As a result, this solution will be applicable to obtain the moment distributions for a wider range of sheet piles. Accordingly, SAAF could be an attractive alternative to FBG sensors for deriving moments, since they are much cheaper and easier to install. However, from the curvature, it is only possible to obtain the difference in strain between the compression and tension

side. So for determination of the normal force distribution, strain gauges are still required. Furthermore, the SAAF instrument is usually not used for measuring high curvatures and strains during collapse, as it is retracted before that phase.

10.2.2. Soil-structure interaction

A more thorough look into this behavior in future research could lead to valuable insights. Instead of only taking into account soil around the compression flange of the FEM model, also the web should be included.

Bibliography

[1] *DIANA User's Manual – Release 9.5*.

[2] J.W. Welleman C. Hartsuijker. *Non-symmetrical and inhomogeneous cross sections*. 2017.

[3] Concretio. Memo pim schipper ontwerp damwand met openingspercentage 20151214. Technical report, ingenieursbureau concretio zwijndrecht, 2015.

[4] CUR. Cur-publication 166, sheet pile structures. Technical report, 2008.

[5] R. Abspoel P.A. de Vries F.S.K. Bijlaard. *Lecture Notes CTB2220 Concrete and Steel structures*. 2013.

[6] Dercks. *Momenten-Rotationstragfähigkeit von Spundwänden aus Z-Bohlen und U-Bohlen mit verminderter Schubkraftübertragung*. PhD thesis, RWTH Aachen, 2004.

[7] A.M. Gresnigt S.H.J. van Es D.J. Peters, E.J. Broos. Local buckling resistance of sand-filled spirally welded tubes. Technical report, ISOPE, 2015.

[8] Bureau Coördinatie en Organisatie. Rapport overstromingsramp in tuindorp-oostzaan te amsterdam-noord. Technical report, 1960.

[9] H.L. Bakker H. Schelfhout M.T. van der Meer E.O.F. Calle, J.A.M. Teunissen. Stabiliteits- en sterktecriteria bij lange damwanden in dijken ten behoeve van & begeleidingscommissie dijkversterkingen krimpenerwaard. Technical report, Deltares, 2003.

[10] European Committee for Standardization. Eurocode 3: Design of steel structures - part 5: Piling. Technical report, 2007.

[11] F.van Tol A. Kort A. Schmitt M. Meyrer G. Sedlacek, R.Hartmann-Linden. Development of unified design rules for steel sheet piles for introduction into eurocode 3, part 5. Technical report, 2001.

[12] J. Breedeveld H. Larsen, P. Lubking. Ontwerp stabiliteitsschermen (type ii) in primaire waterkeringen (groene versie). Technical report, Deltares, 2013.

[13] Hans Teunissen Henk Bakker, Joost Breedeveld. Analyse macrostabiliteit dijken met de eindige elementen methode. Technical report, Rijkswaterstaat, 2010.

[14] D.A. Kort. *Steel sheet pile walls in soft soils*. PhD thesis, Technische Universiteit Delft, 2002.

[15] James S. Davidson Mahendrakumar Madhavan. Theoretical evaluation of flange local bucklingfor horizontally curved i-girders. Technical report, 2009.

[16] Measurand. *SAA Description & Installation Revision 5*. Measurand Inc., 2015.

[17] NEN. Eurocode 3: Design of steel structures - part 5: Piling. Technical report, 2007.

[18] T. Schweckendiek J.P. van den Bos S.N. Jonkman, R.E. Jorissen. *Lecture notes CIE5314: Flood defences*. Delft University of Technology, April 2018.

[19] TAW/ENW. Leidraad voor het ontwerpen van rivierdijken deel 2 - benedenrivierengebied. Technical report, 1989.

[20] TAW/ENW. Leidraad kunstwerken. Technical report, 2003.

[21] Ministerie van Infrastructuur en Milieu. Deltaprogramma. Technical report, 2015.

[22] A. Verruijt. *SOIL MECHANICS*. Delft University of Technology, 2012.

A

Monitoring

A.1. FST

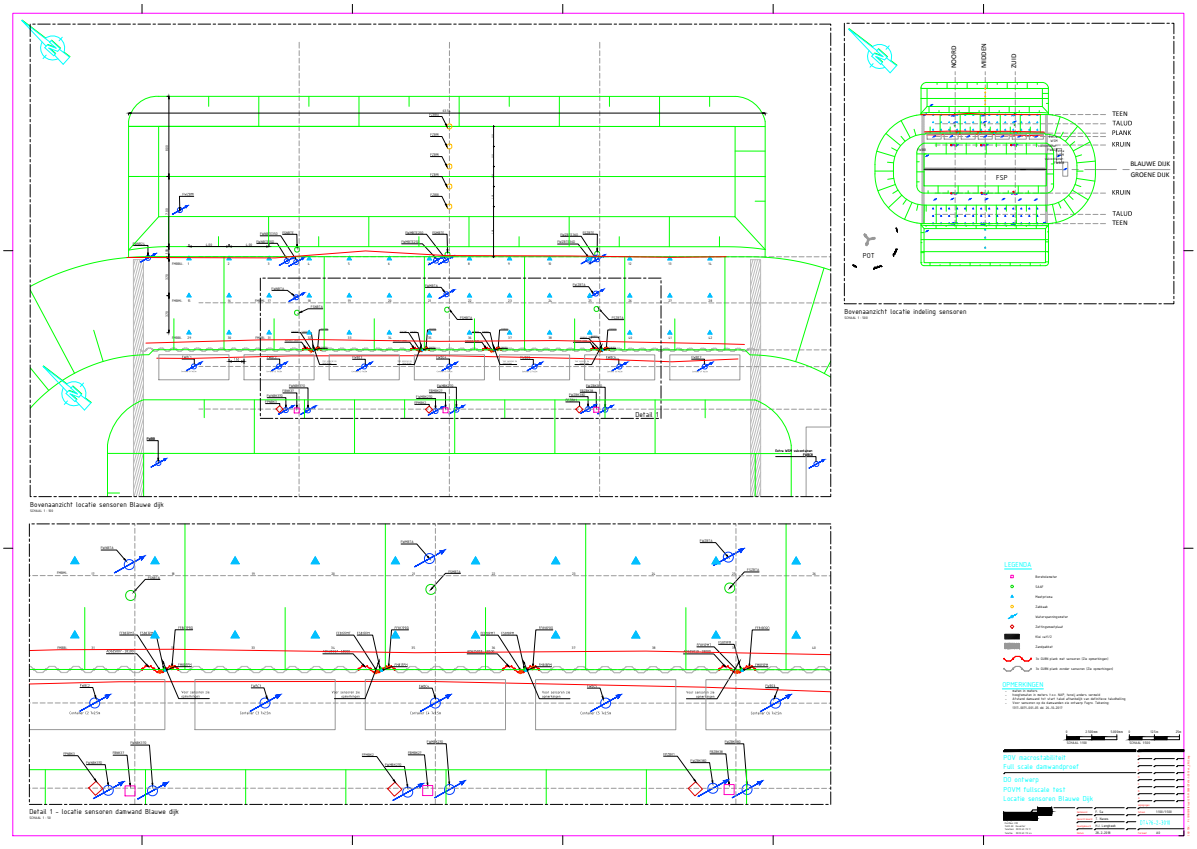

A.2. POT

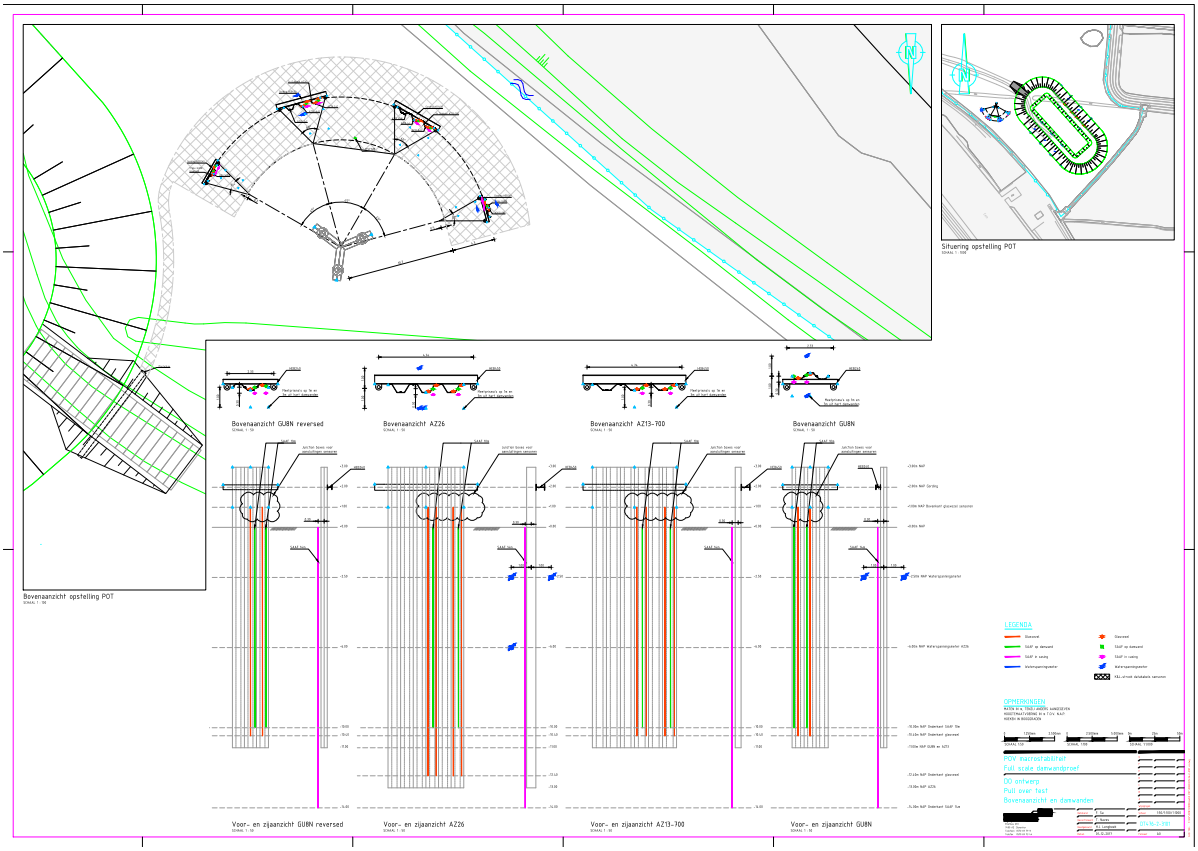
Situering opstelling POT
Bovenaanzicht opstelling POT
Bovenaanzicht GUBN reversed
Bovenaanzicht AZ26
Bovenaanzicht AZ13-700
Bovenaanzicht GUBN
Voor- en zijaanzicht GUBN reversed
Voor- en zijaanzicht AZ26
Voor- en zijaanzicht AZ13-700
Voor- en zijaanzicht GUBN
LEGENDA
OPMERKINGEN
POV macrostabiliteit
Pull over test
OD ontwerp
Bovenaanzicht en dwarsnaden

B

FBG verification

B.1. AZ26

B.1.1. Install configuration mid

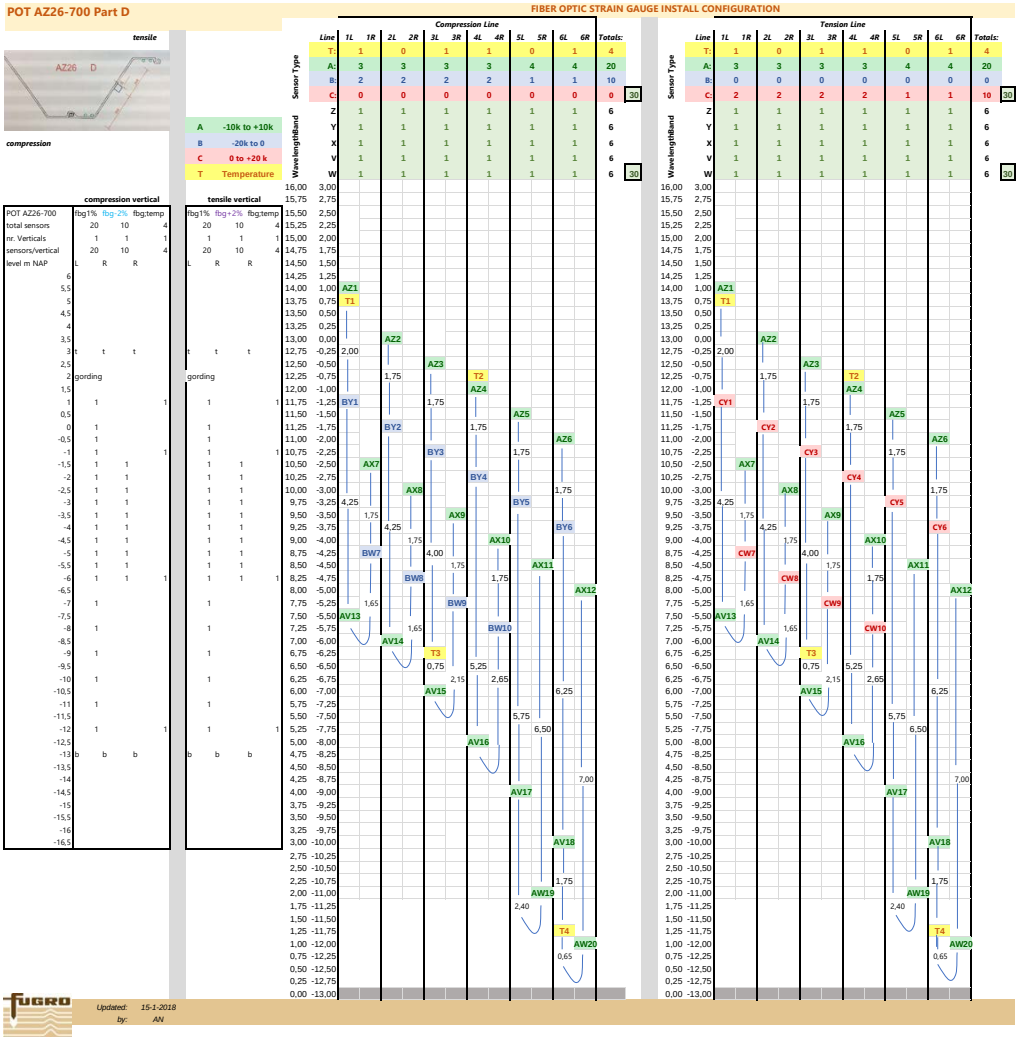

B.1.2. Load verification mid

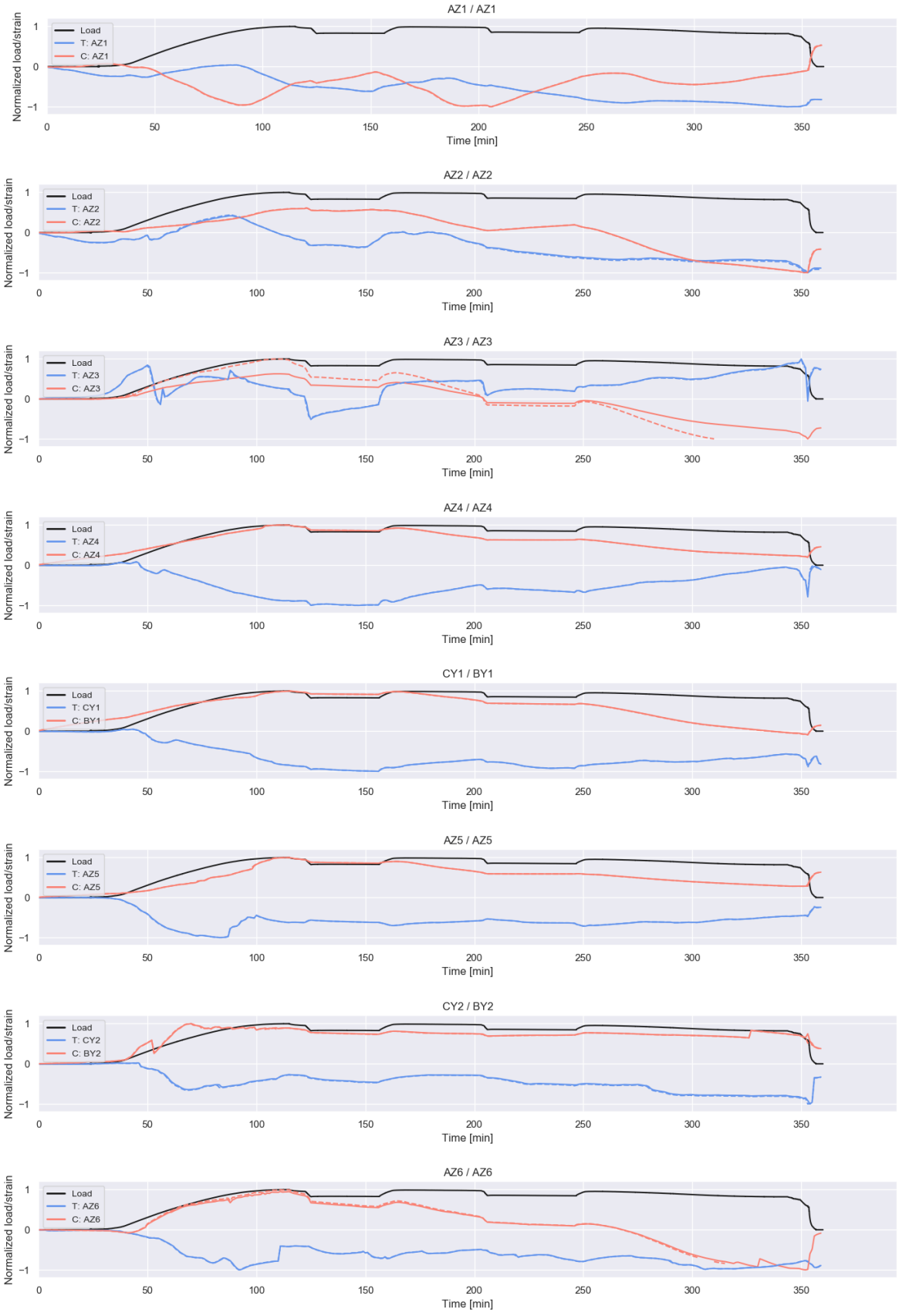

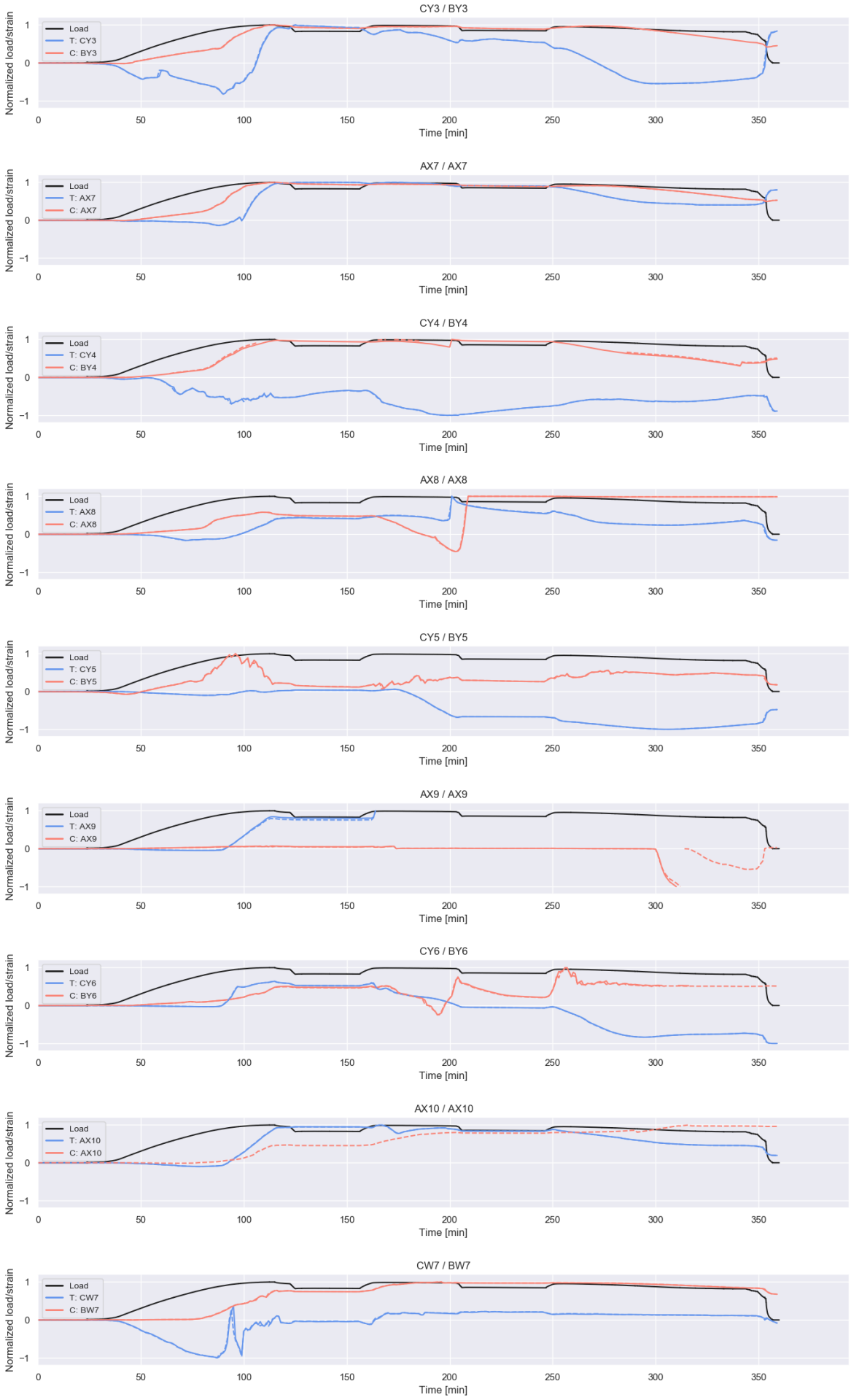
CY3 / BY3
Load
T: CY3
C: BY3
AX7 / AX7
Load
T: AX7
C: AX7
CY4 / BY4
Load
T: CY4
C: BY4
AX8 / AX8
Load
T: AX8
C: AX8
CY5 / BY5
Load
T: CY5
C: BY5
AX9 / AX9
Load
T: AX9
C: AX9
CY6 / BY6
Load
T: CY6
C: BY6
AX10 / AX10
Load
T: AX10
C: AX10
CW7 / BW7
Load
T: CW7
C: BW7
Normalized load/strain
Time [min]

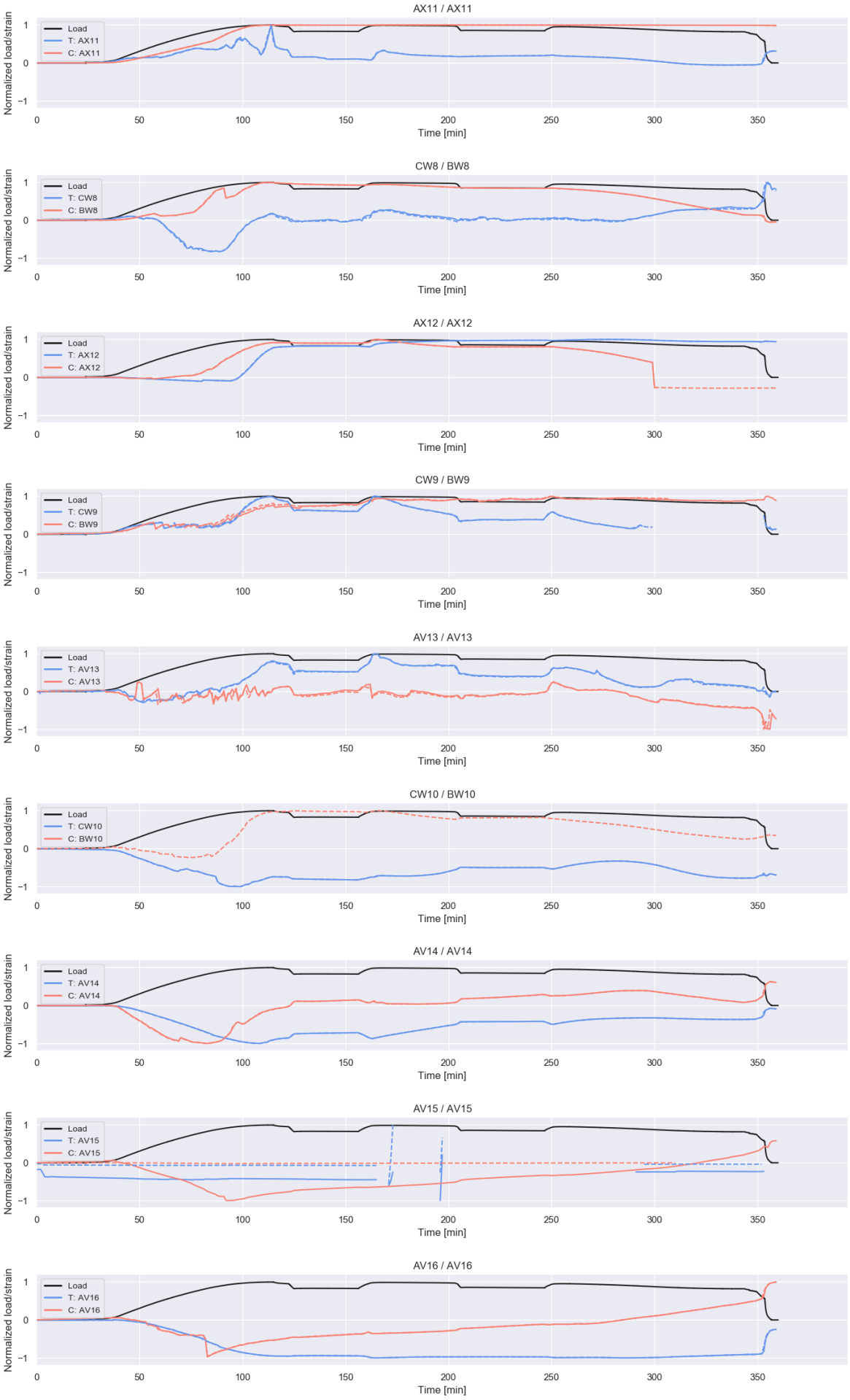
AX11 / AX11
Load
T: AX11
C: AX11
CW8 / BW8
Load
T: CW8
C: BW8
AX12 / AX12
Load
T: AX12
C: AX12
CW9 / BW9
Load
T: CW9
C: BW9
AV13 / AV13
Load
T: AV13
C: AV13
CW10 / BW10
Load
T: CW10
C: BW10
AV14 / AV14
Load
T: AV14
C: AV14
AV15 / AV15
Load
T: AV15
C: AV15
AV16 / AV16
Load
T: AV16
C: AV16
Normalized load/strain
Time [min]

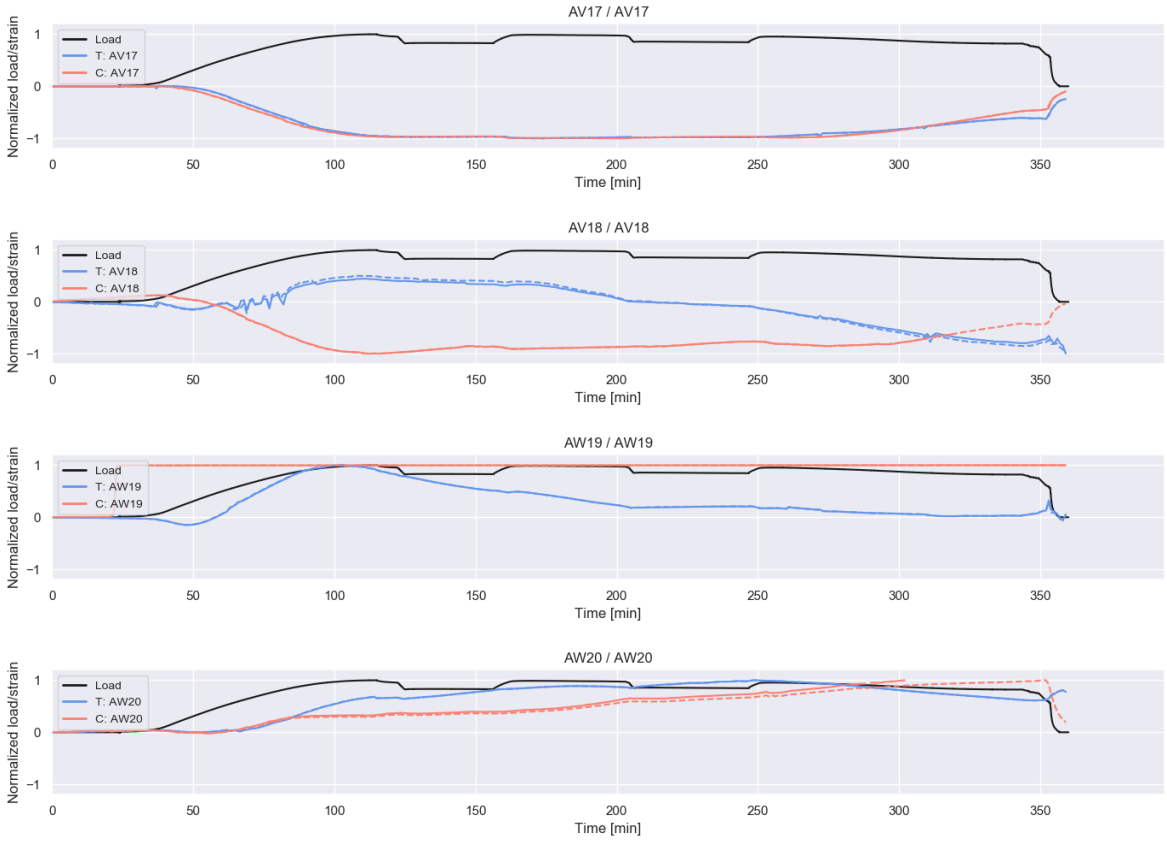
AV17 / AV17
Load
T: AV17
C: AV17
Normalized load/strain
Time [min]
AV18 / AV18
Load
T: AV18
C: AV18
Normalized load/strain
Time [min]
AW19 / AW19
Load
T: AW19
C: AW19
Normalized load/strain
Time [min]
AW20 / AW20
Load
T: AW20
C: AW20
Normalized load/strain
Time [min]

B.1.3. SAAF verifciation mid

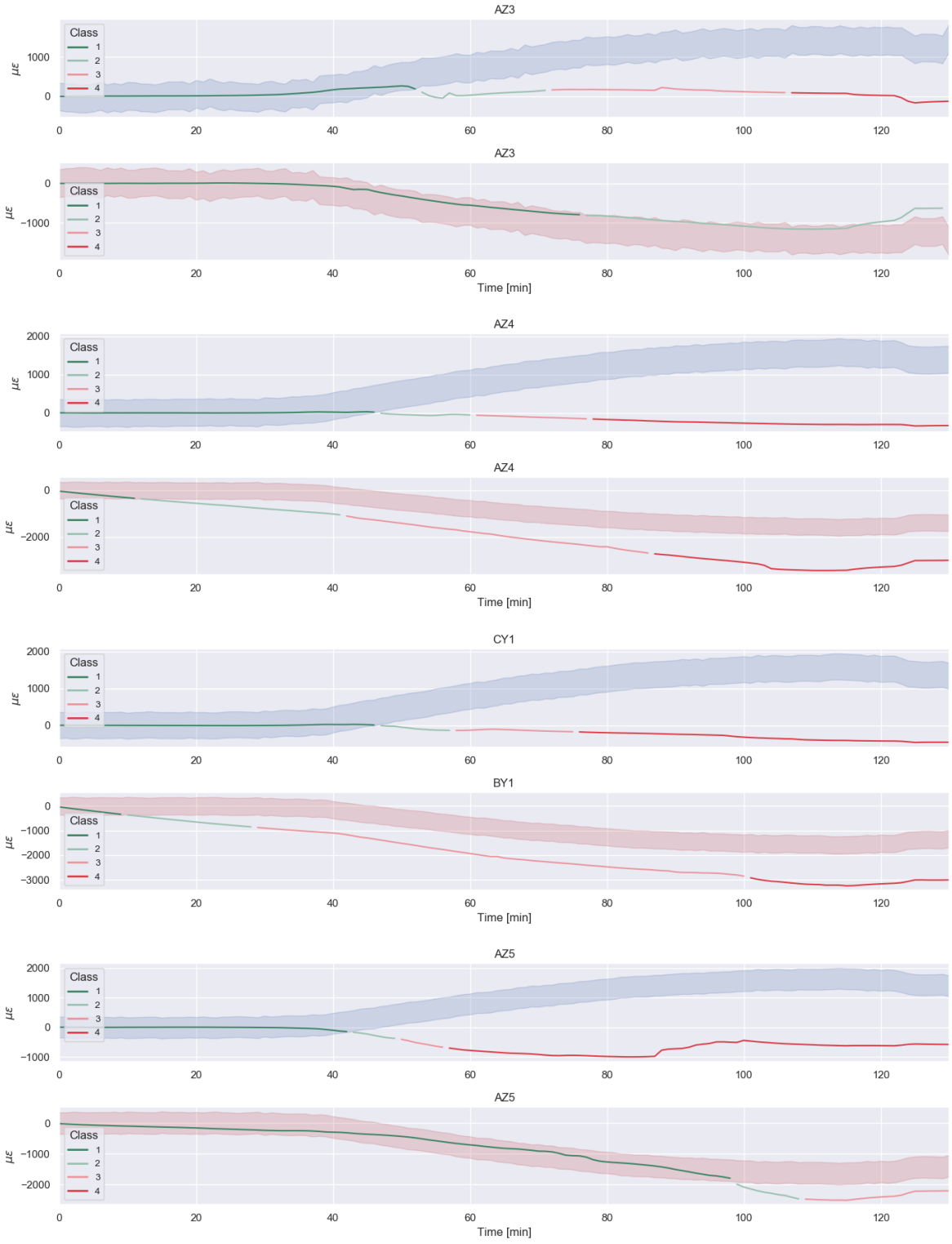

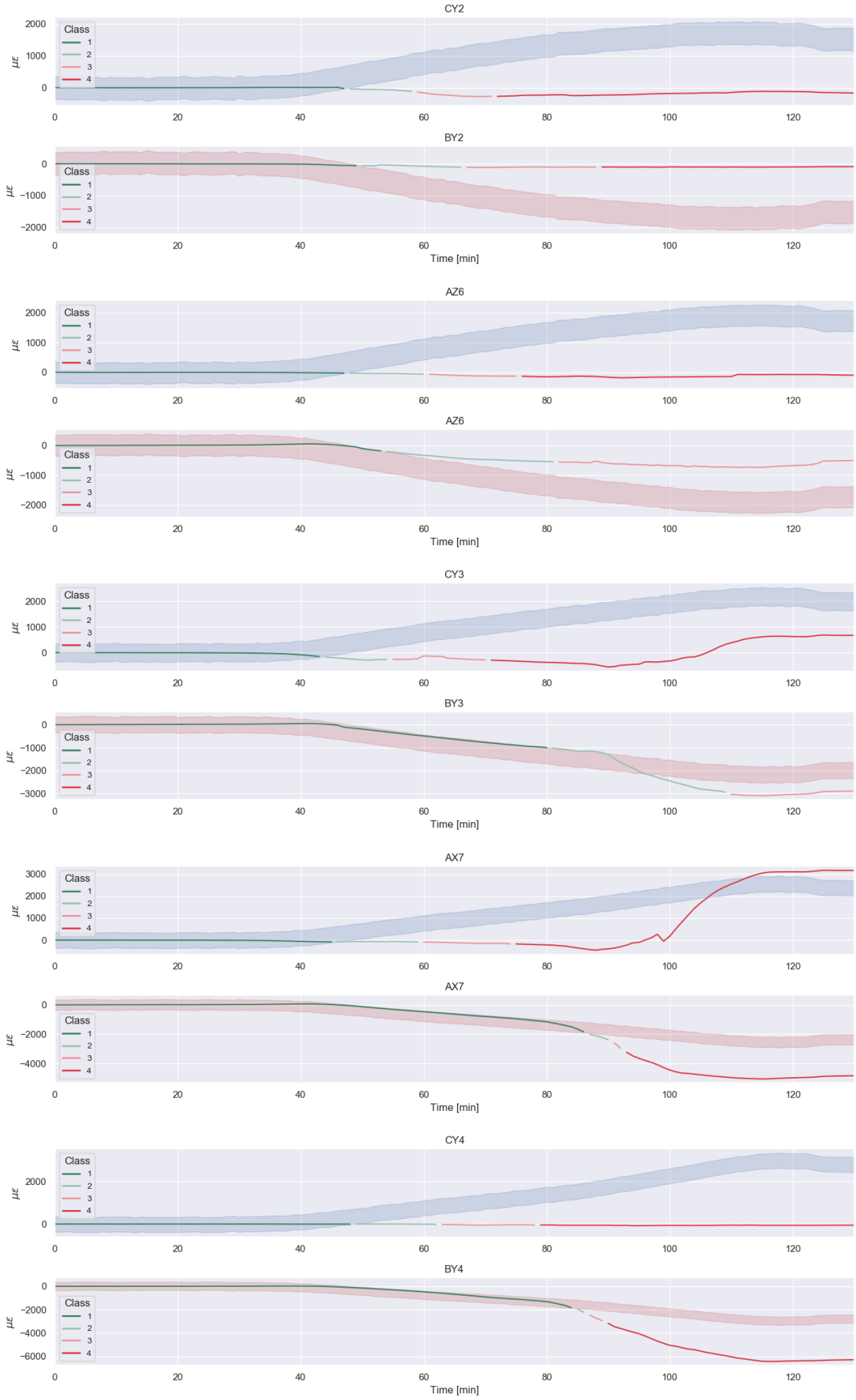
CY2
BY2
AZ6
AZ6
CY3
BY3
AX7
AX7
CY4
BY4
Class
1
2
3
4
με
Time [min]

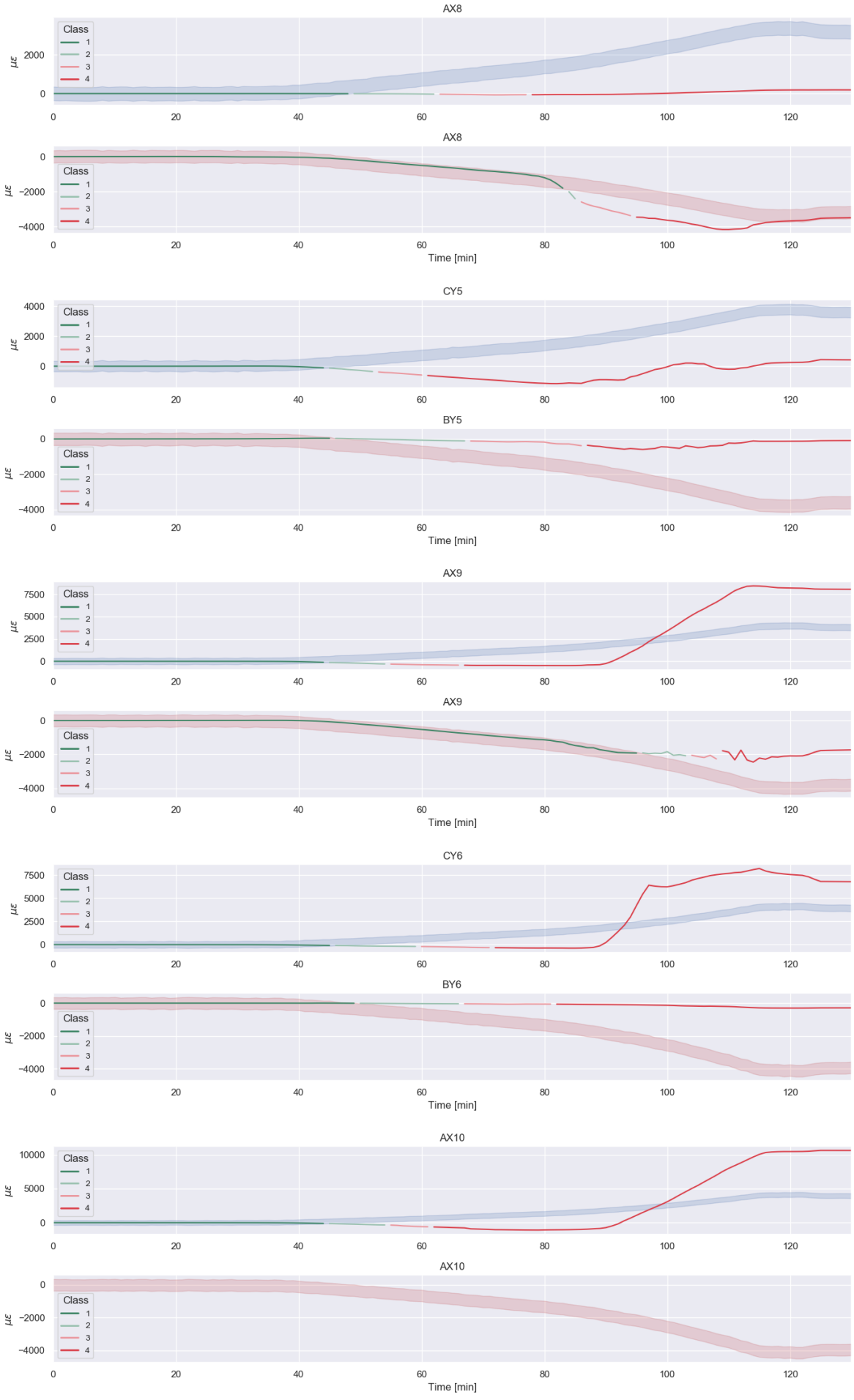
AX8
Class
1
2
3
4
με
2000
0
0
20
40
60
80
100
120
AX8
0
−2000
−4000
Time [min]
CY5
4000
BY5
AX9
7500
5000
2500
CY6
BY6
AX10

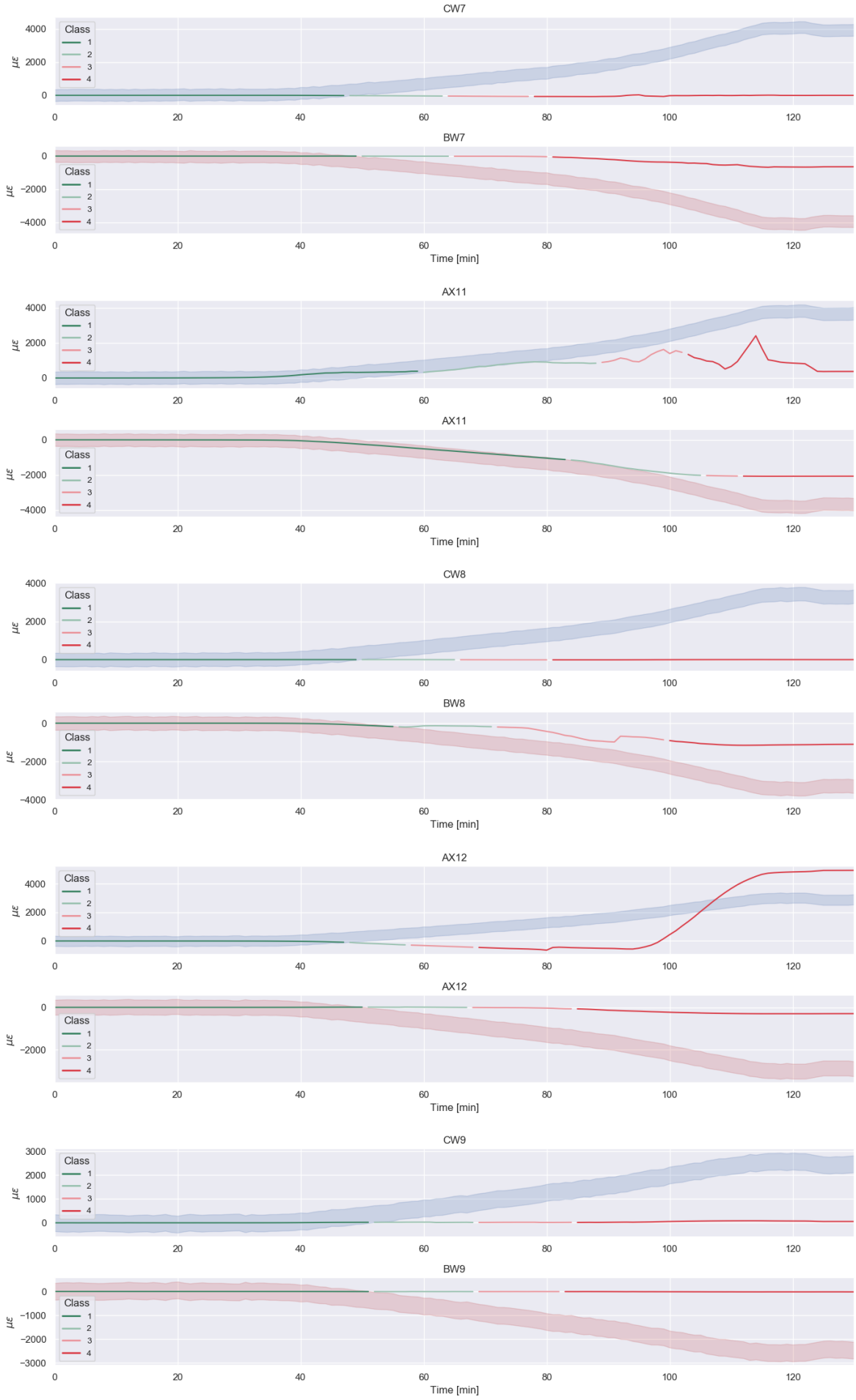
CW7
BW7
AX11
AX11
CW8
BW8
AX12
AX12
CW9
BW9
Class
1
2
3
4
με
Time [min]

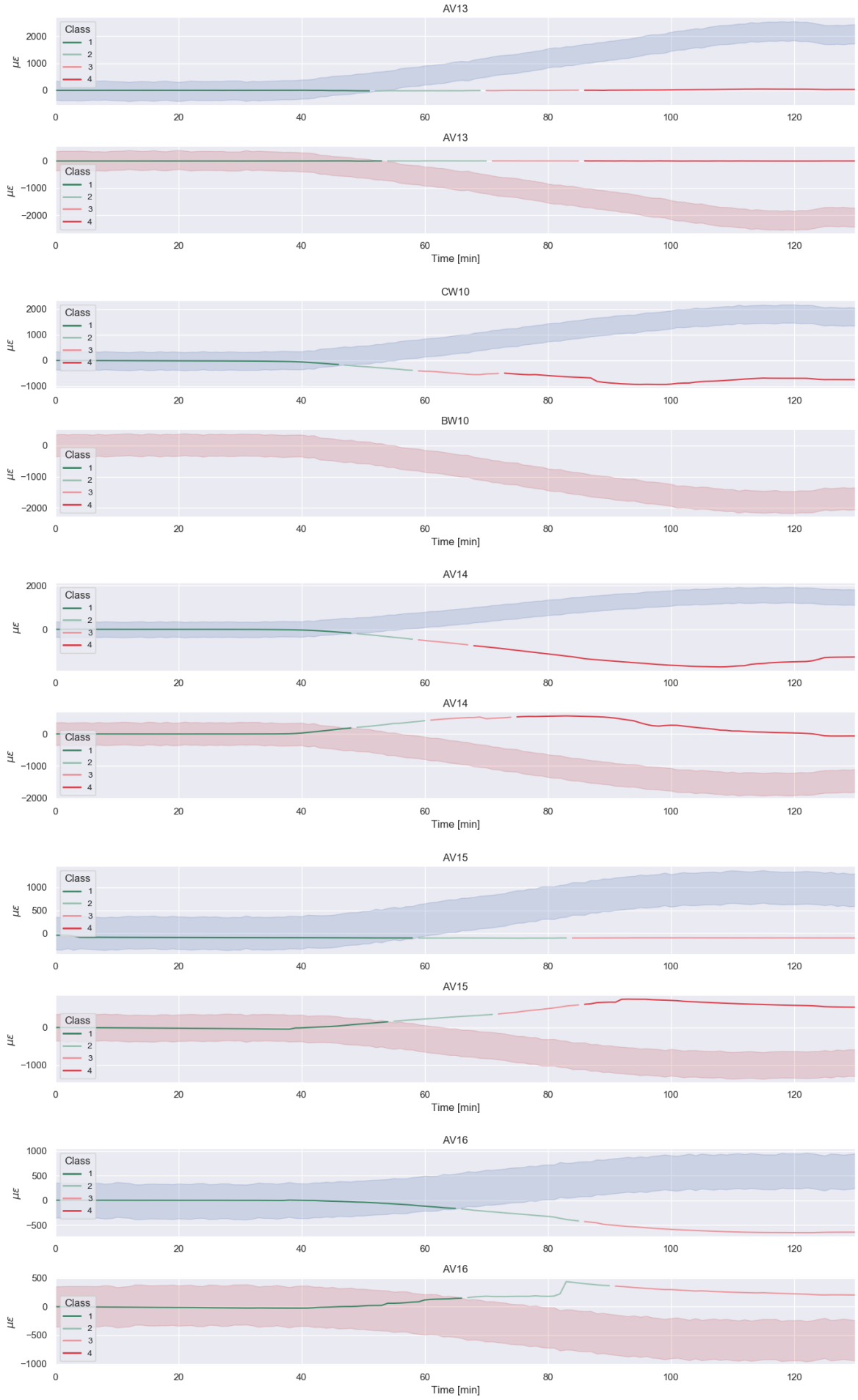
AV13
Class
1
2
3
4
με
2000
1000
0
0
20
40
60
80
100
120
AV13
Class
1
2
3
4
με
0
−1000
−2000
Time [min]
CW10
Class
1
2
3
4
με
2000
1000
0
−1000
BW10
Class
1
2
3
4
με
0
−1000
−2000
Time [min]
AV14
Class
1
2
3
4
με
2000
0
AV14
Class
1
2
3
4
με
0
−1000
−2000
Time [min]
AV15
Class
1
2
3
4
με
1000
500
0
AV15
Class
1
2
3
4
με
0
−1000
Time [min]
AV16
Class
1
2
3
4
με
1000
500
0
−500
AV16
Class
1
2
3
4
με
500
0
−500
−1000
Time [min]

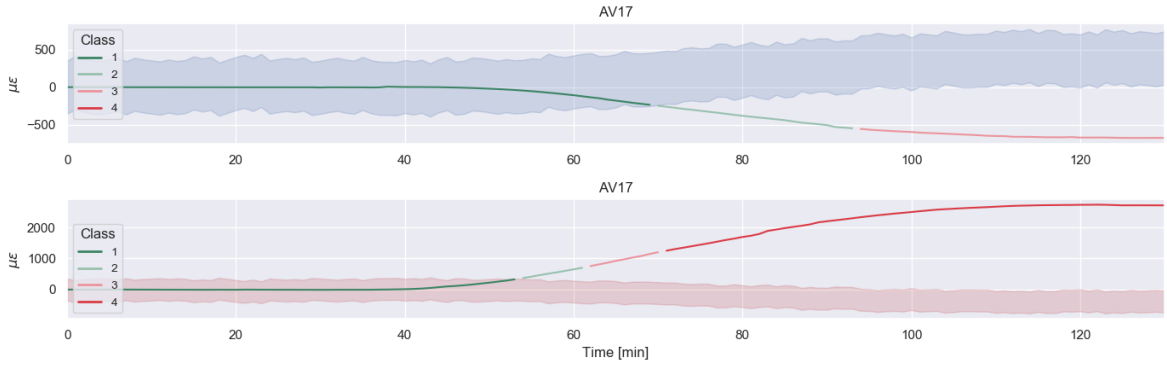
AV17
Class
1
2
3
4
500
0
−500
με
0
20
40
60
80
100
120
AV17
Class
1
2
3
4
2000
1000
0
με
0
20
40
60
80
100
120
Time [min]

B.1.4. Install configuration side

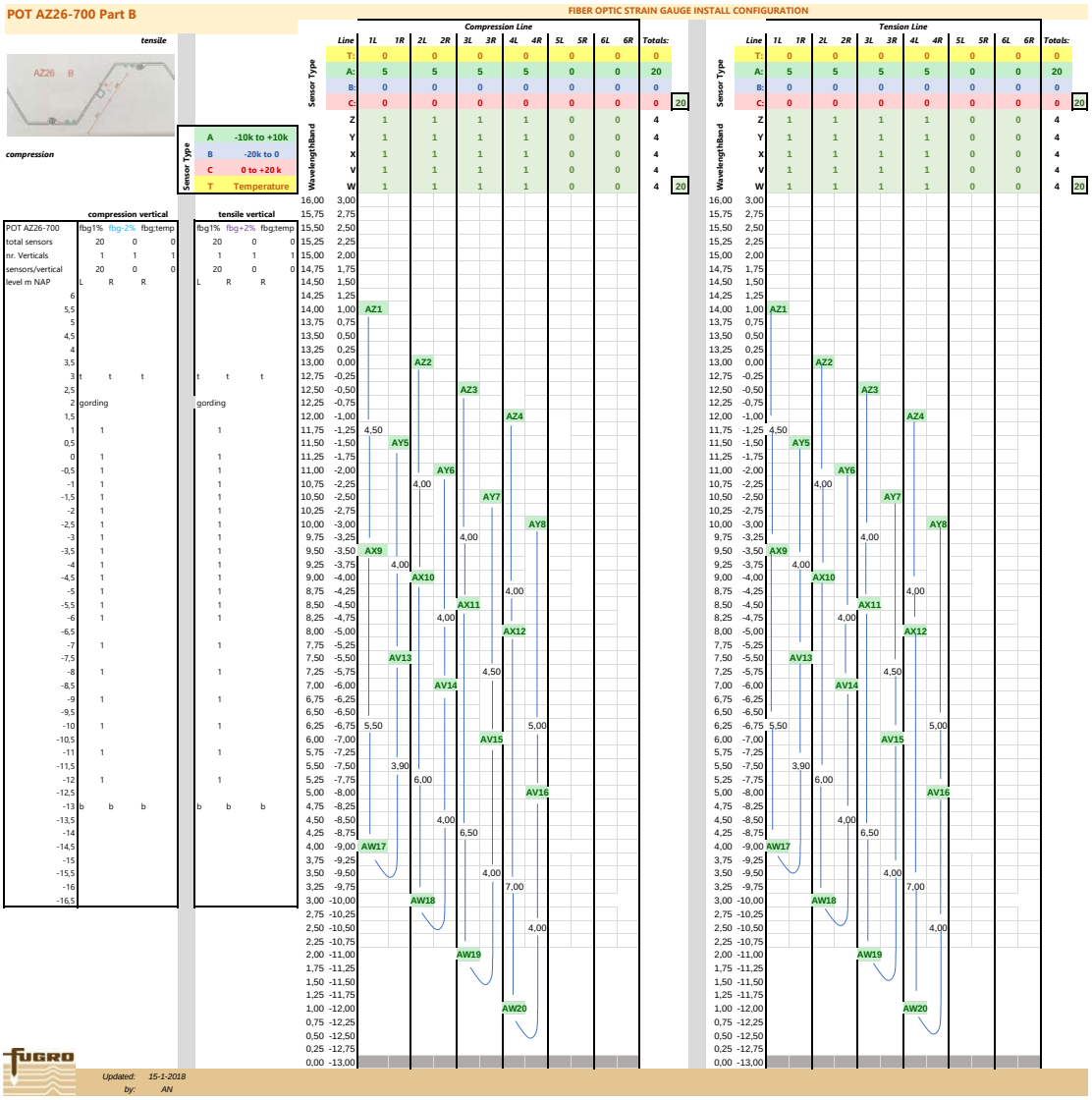

B.1.5. Load verification side

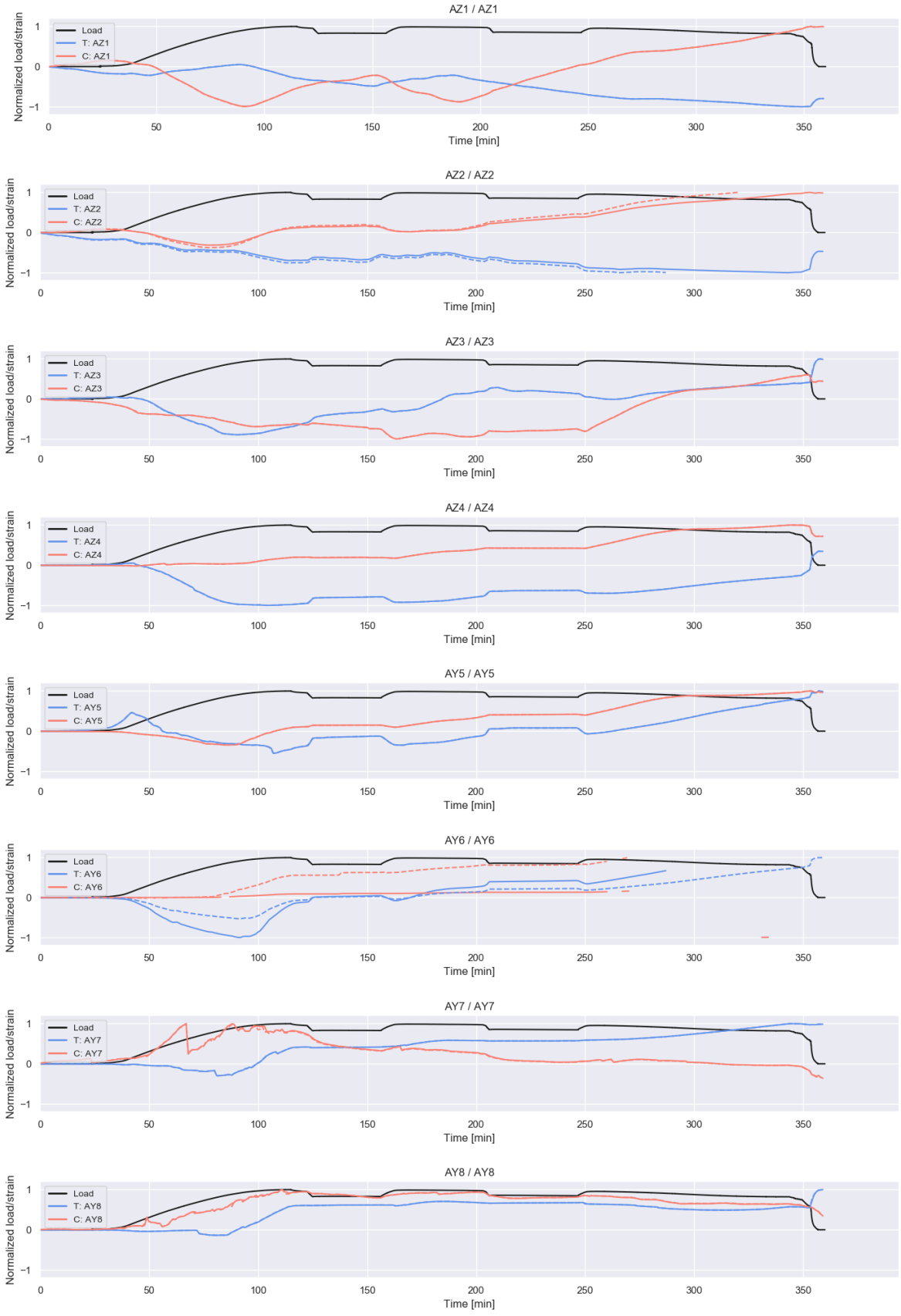

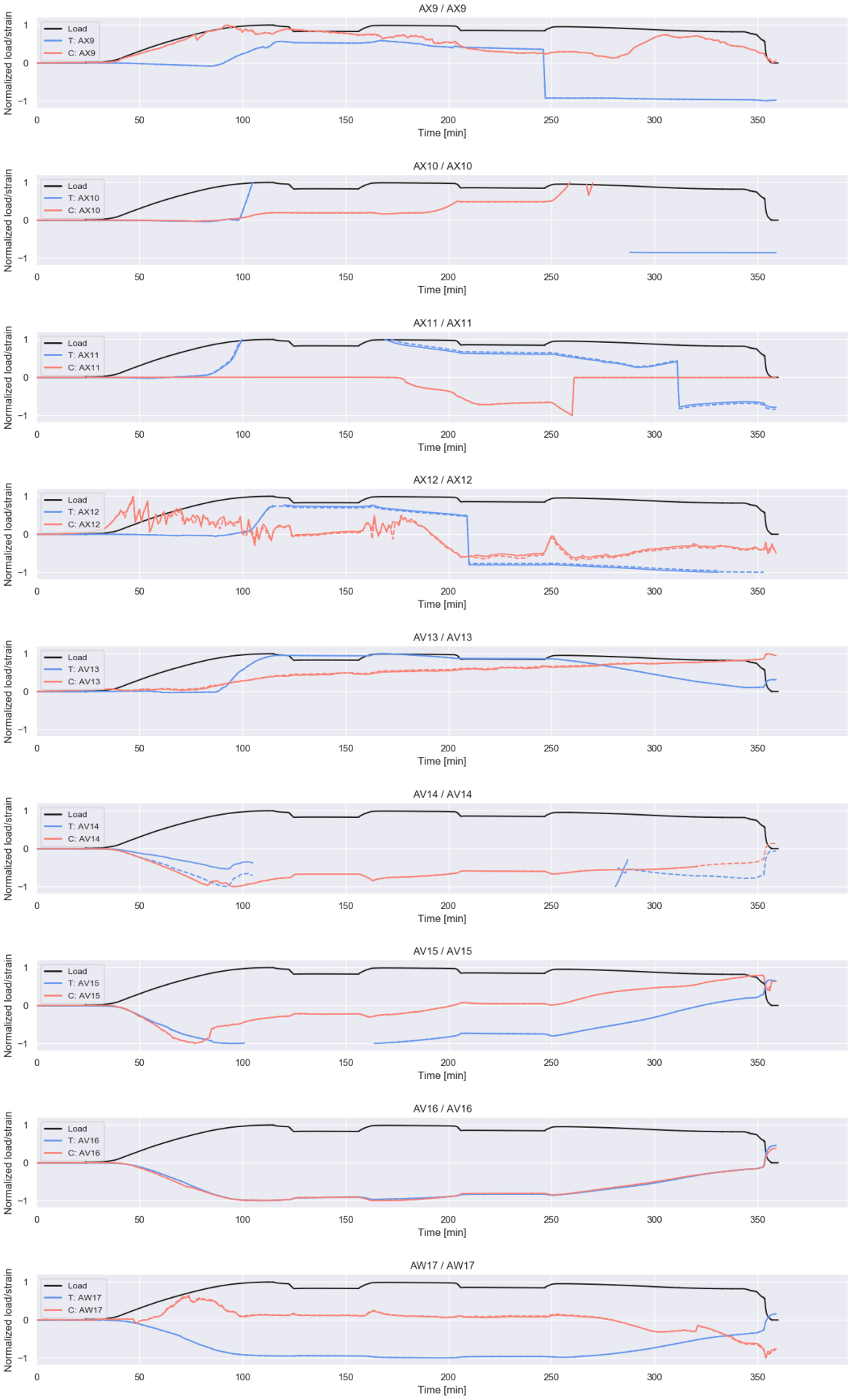
AX9 / AX9
Load
T: AX9
C: AX9
AX10 / AX10
Load
T: AX10
C: AX10
AX11 / AX11
Load
T: AX11
C: AX11
AX12 / AX12
Load
T: AX12
C: AX12
AV13 / AV13
Load
T: AV13
C: AV13
AV14 / AV14
Load
T: AV14
C: AV14
AV15 / AV15
Load
T: AV15
C: AV15
AV16 / AV16
Load
T: AV16
C: AV16
AW17 / AW17
Load
T: AW17
C: AW17
Normalized load/strain
Time [min]

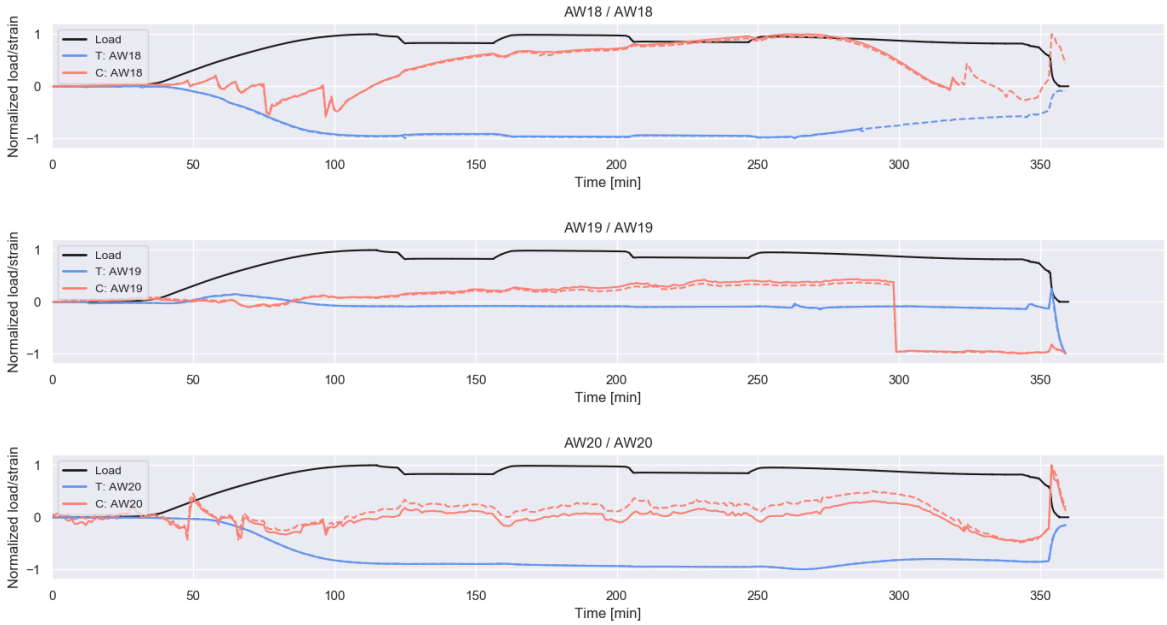
AW18 / AW18
Load
T: AW18
C: AW18
Normalized load/strain
Time [min]
AW19 / AW19
Load
T: AW19
C: AW19
Normalized load/strain
Time [min]
AW20 / AW20
Load
T: AW20
C: AW20
Normalized load/strain
Time [min]

B.1.6. SAAF verifciation side

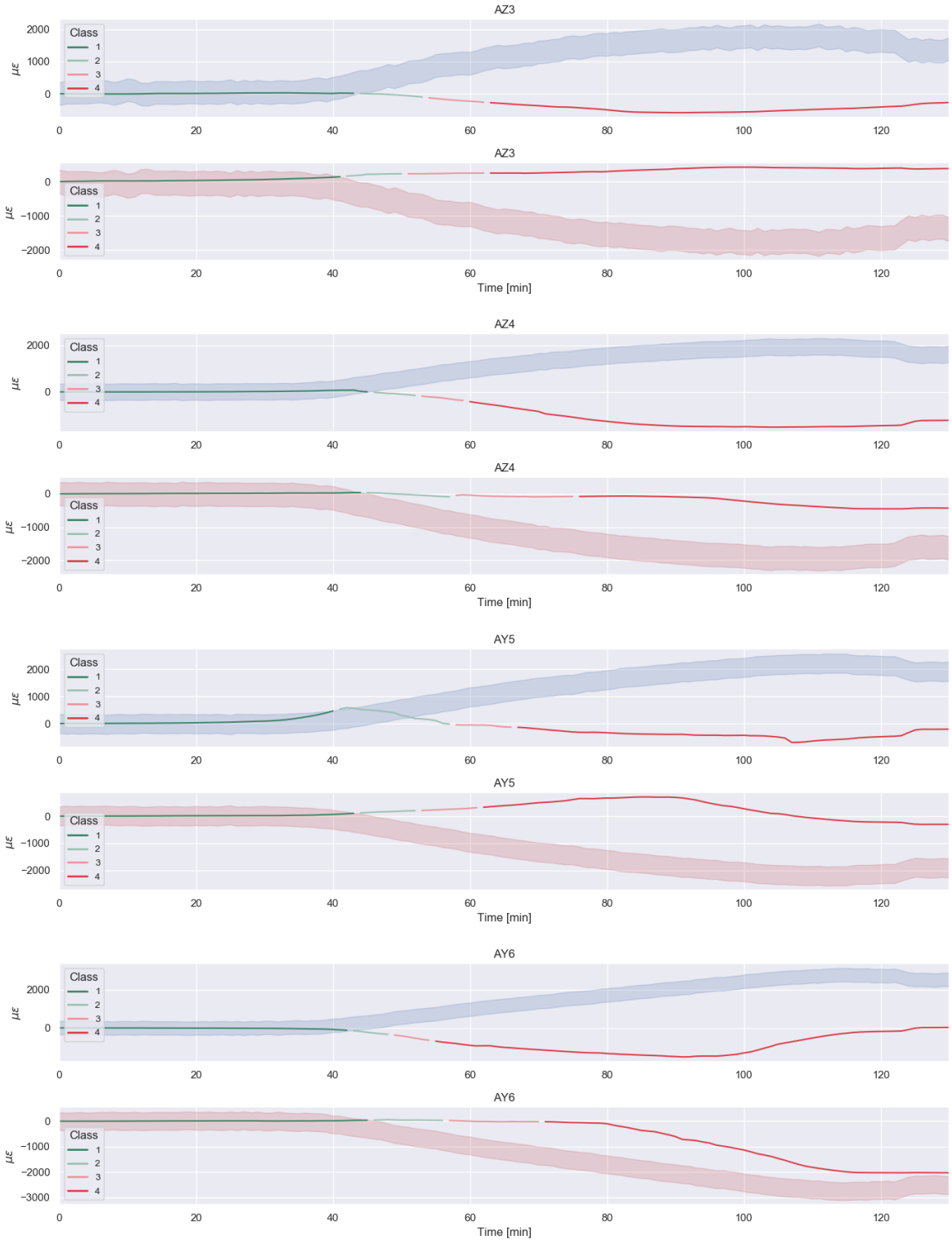

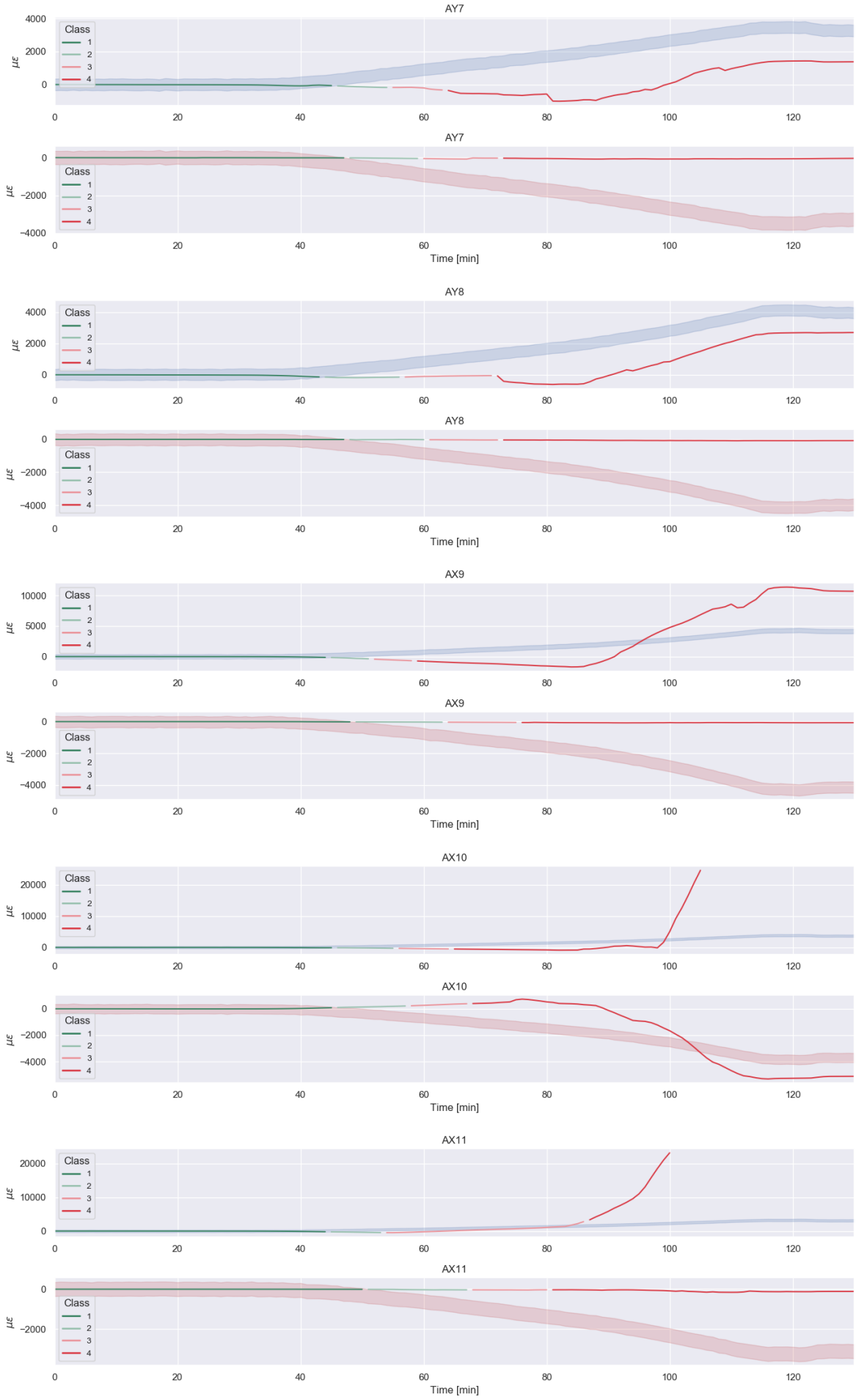
AY7
AY7
AY8
AY8
AX9
AX9
AX10
AX10
AX11
AX11
Class
1
2
3
4
$\mu\varepsilon$
Time [min]

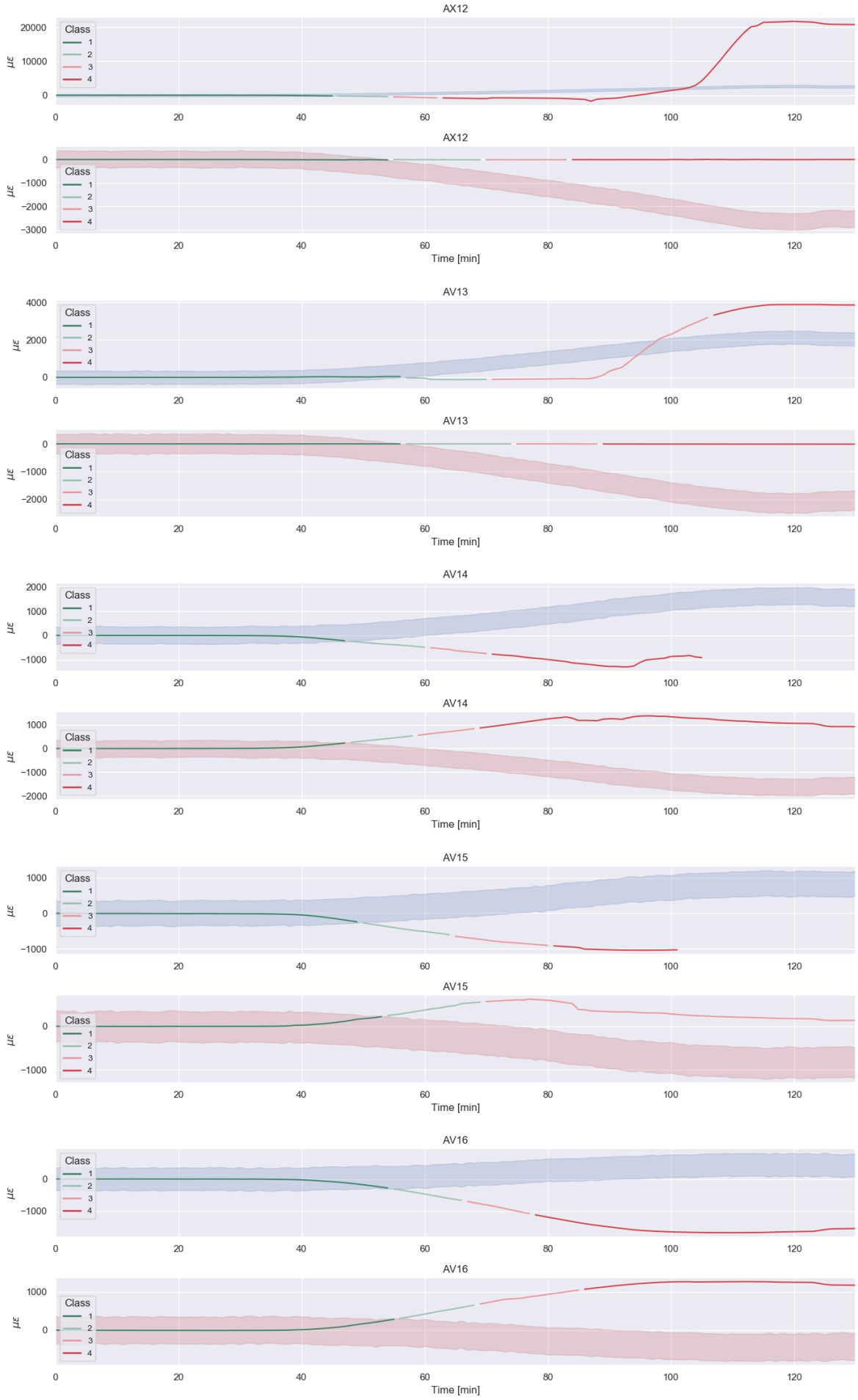
AX12
AX12
AV13
AV13
AV14
AV14
AV15
AV15
AV16
AV16
Class
1
2
3
4
με
Time [min]

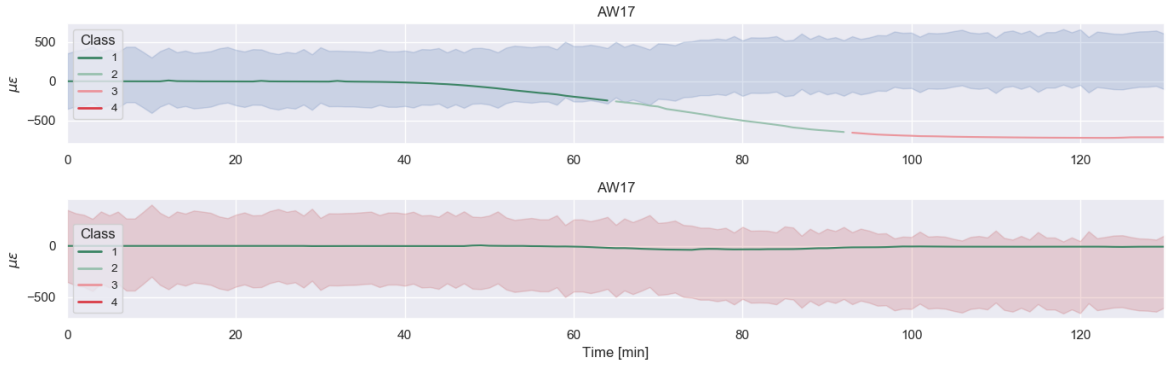
AW17
Class
1
2
3
4
500
0
−500
με
0
20
40
60
80
100
120
AW17
Class
1
2
3
4
0
−500
με
0
20
40
60
80
100
120
Time [min]

B.2. AZ13-700

B.2.1. Install configuration mid

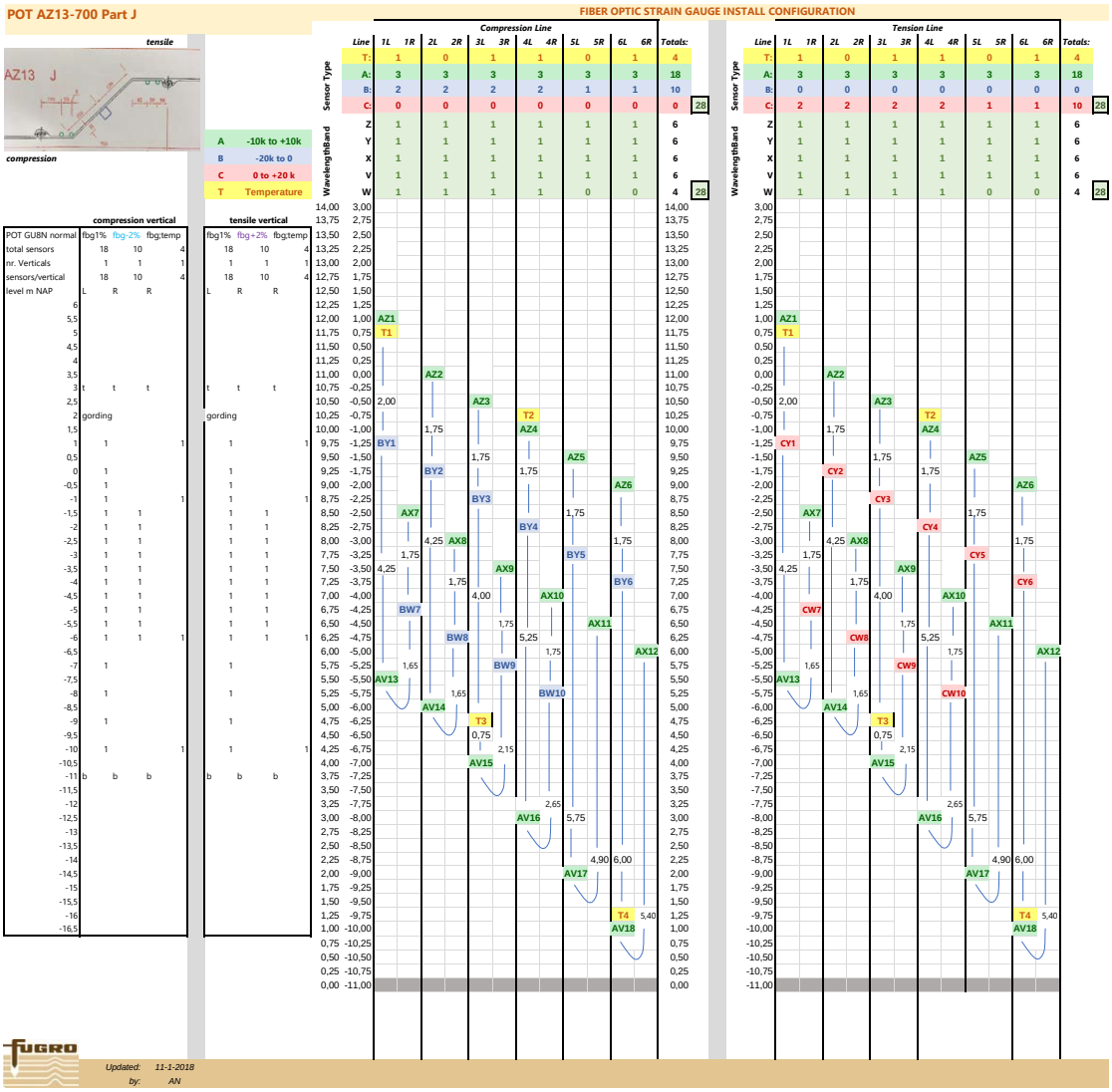

B.2.2. Load verification mid

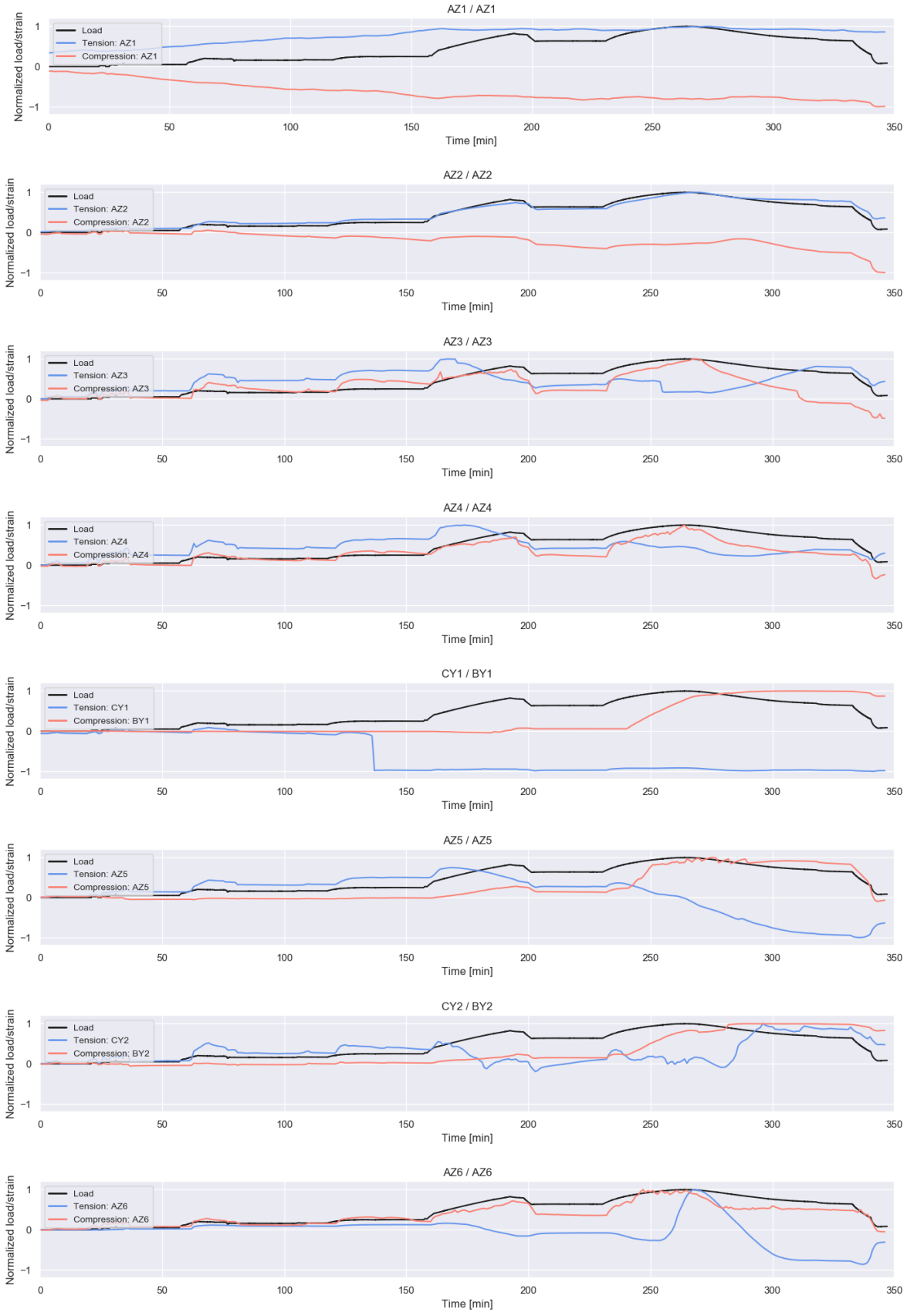

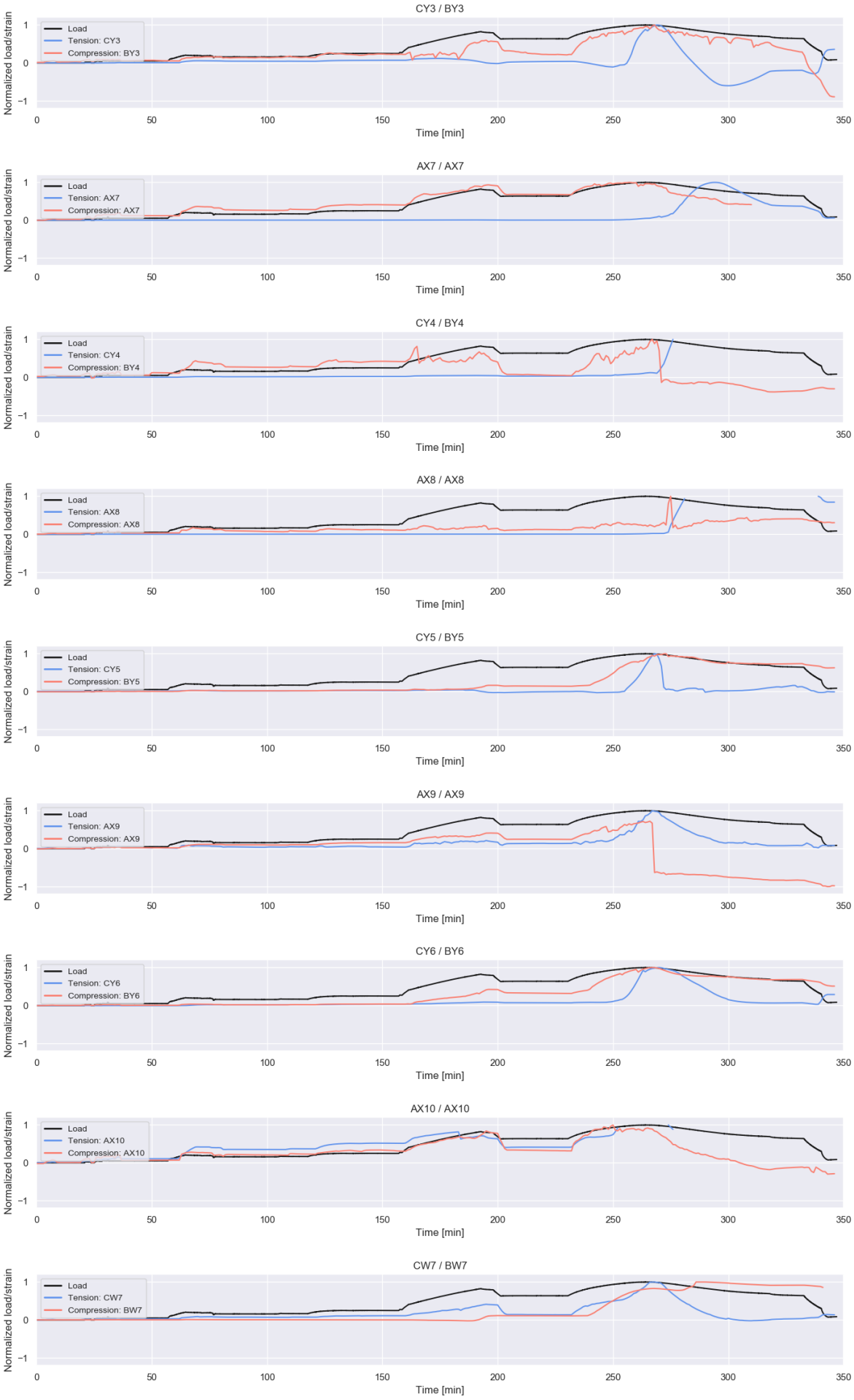
CY3 / BY3
Load
Tension: CY3
Compression: BY3
AX7 / AX7
Load
Tension: AX7
Compression: AX7
CY4 / BY4
Load
Tension: CY4
Compression: BY4
AX8 / AX8
Load
Tension: AX8
Compression: AX8
CY5 / BY5
Load
Tension: CY5
Compression: BY5
AX9 / AX9
Load
Tension: AX9
Compression: AX9
CY6 / BY6
Load
Tension: CY6
Compression: BY6
AX10 / AX10
Load
Tension: AX10
Compression: AX10
CW7 / BW7
Load
Tension: CW7
Compression: BW7
Normalized load/strain
Time [min]

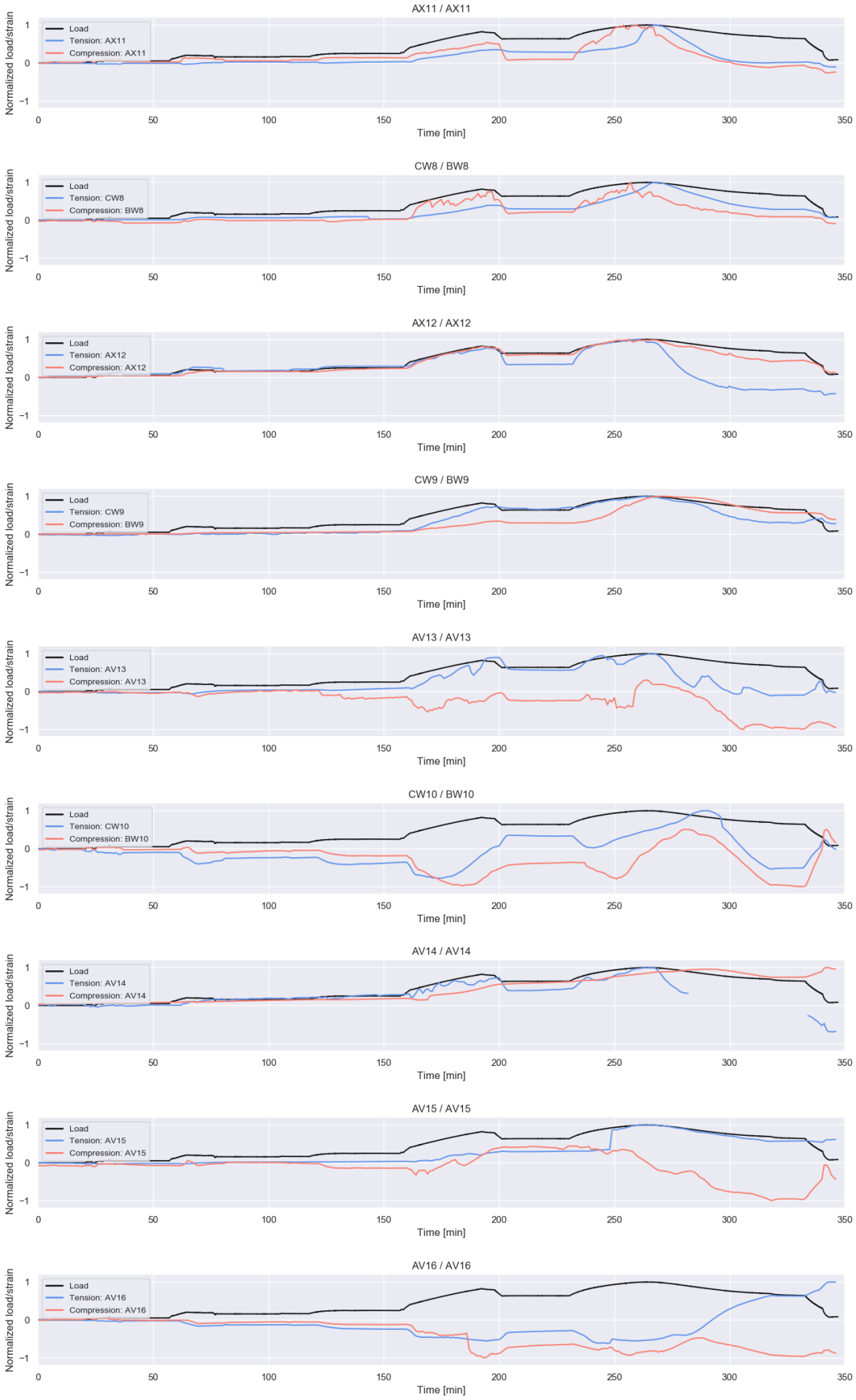
AX11 / AX11
Load
Tension: AX11
Compression: AX11
CW8 / BW8
Load
Tension: CW8
Compression: BW8
AX12 / AX12
Load
Tension: AX12
Compression: AX12
CW9 / BW9
Load
Tension: CW9
Compression: BW9
AV13 / AV13
Load
Tension: AV13
Compression: AV13
CW10 / BW10
Load
Tension: CW10
Compression: BW10
AV14 / AV14
Load
Tension: AV14
Compression: AV14
AV15 / AV15
Load
Tension: AV15
Compression: AV15
AV16 / AV16
Load
Tension: AV16
Compression: AV16
Normalized load/strain
Time [min]

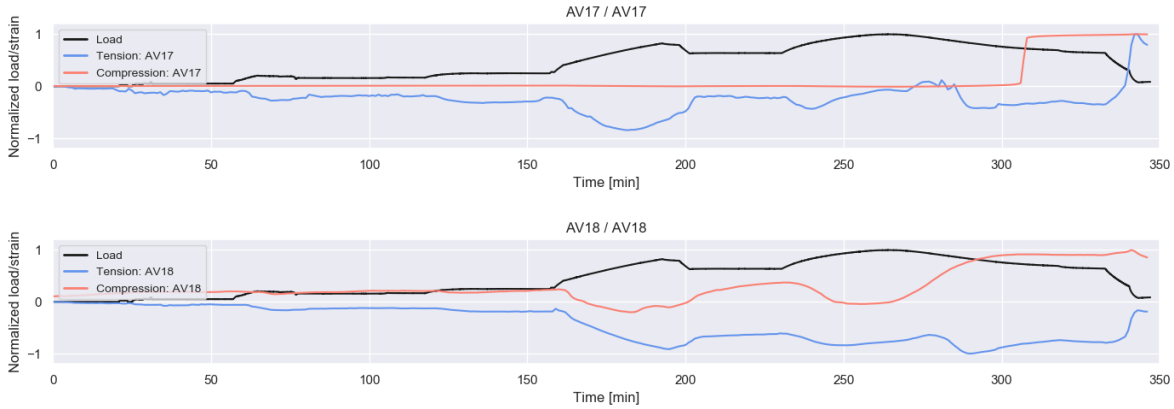
AV17 / AV17
Load
Tension: AV17
Compression: AV17
Normalized load/strain
Time [min]
AV18 / AV18
Load
Tension: AV18
Compression: AV18
Normalized load/strain
Time [min]

B.2.3. SAAF verifciation mid

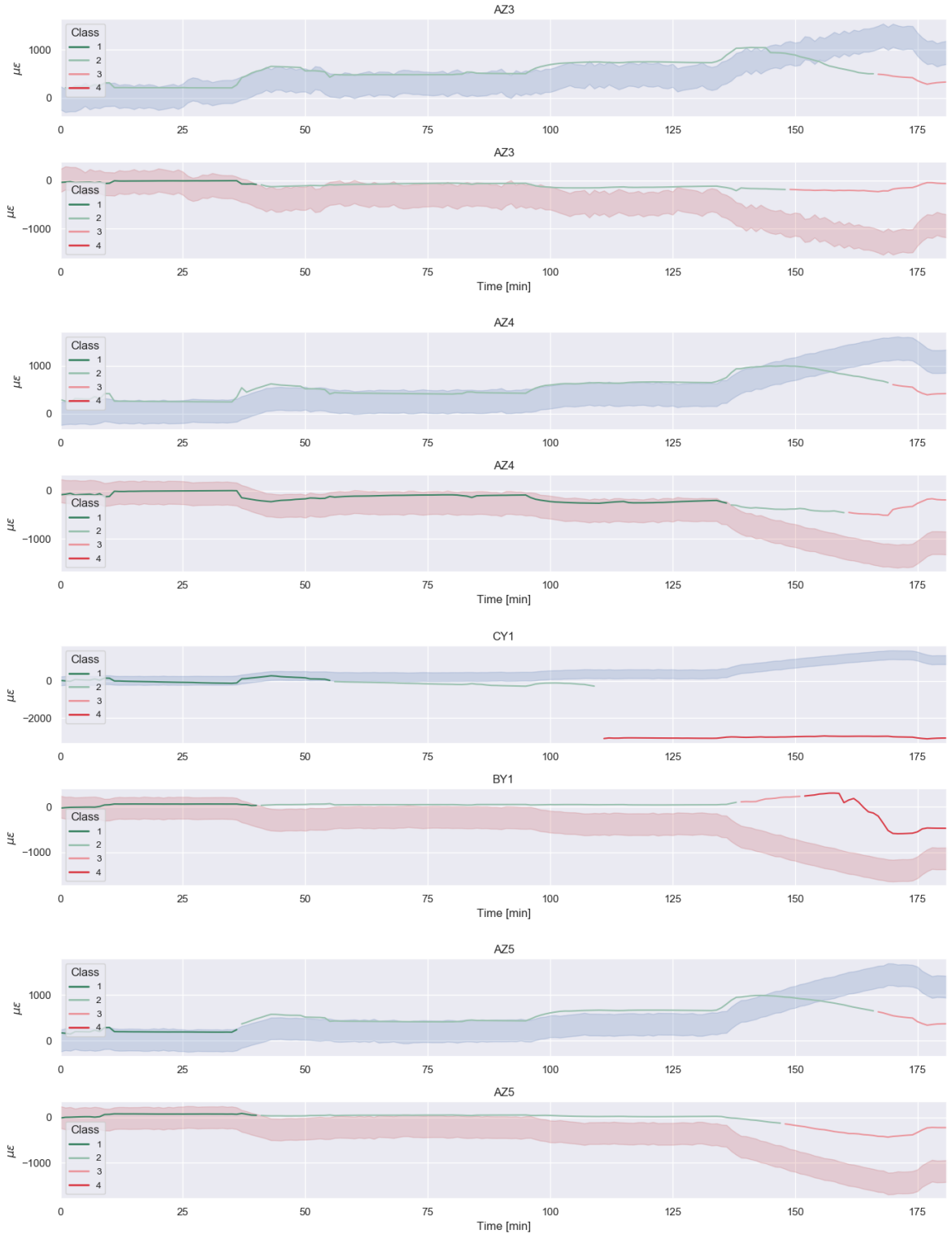

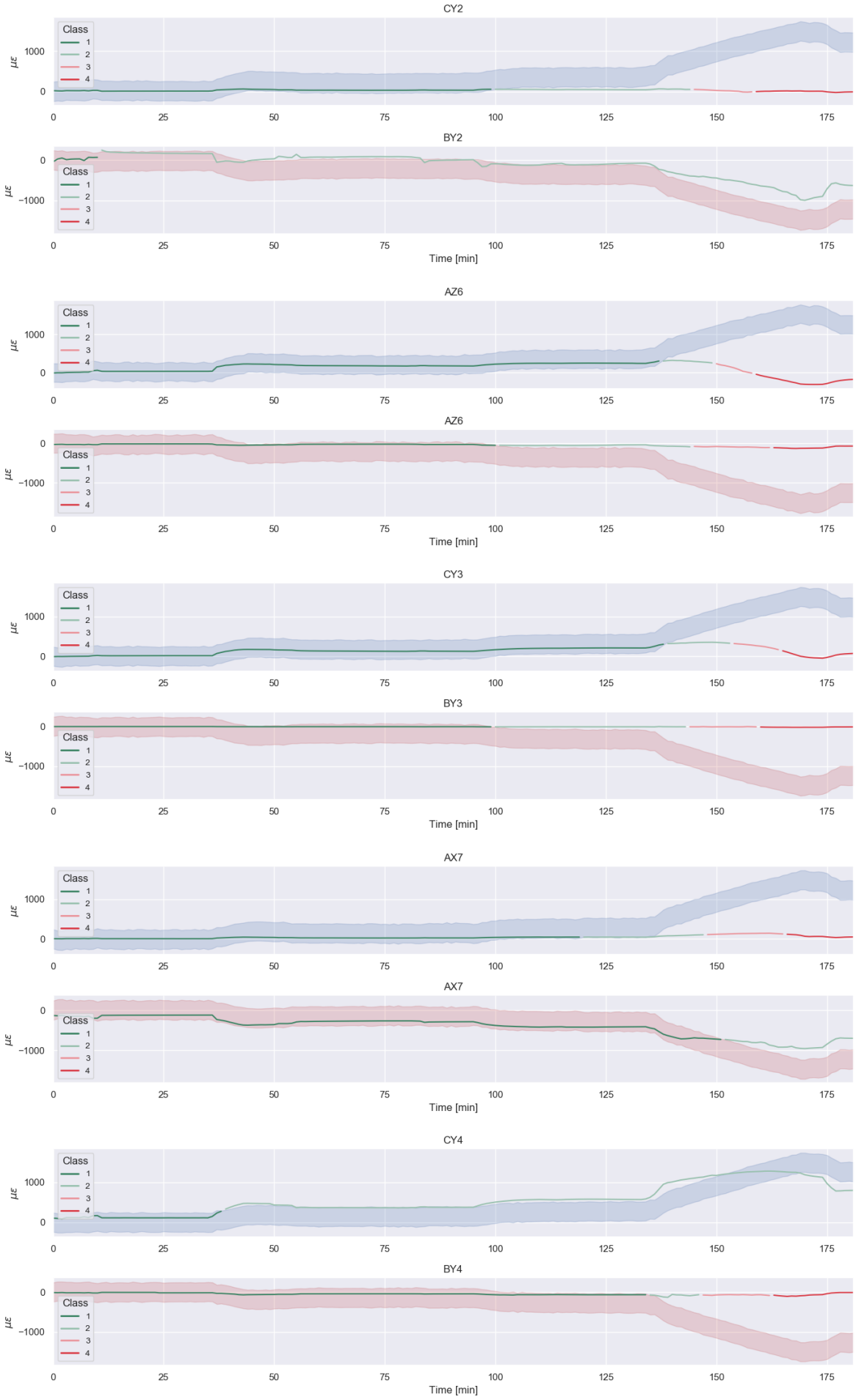
CY2
BY2
AZ6
AZ6
CY3
BY3
AX7
AX7
CY4
BY4
Class
1
2
3
4
με
1000
0
−1000
0
25
50
75
100
125
150
175
Time [min]

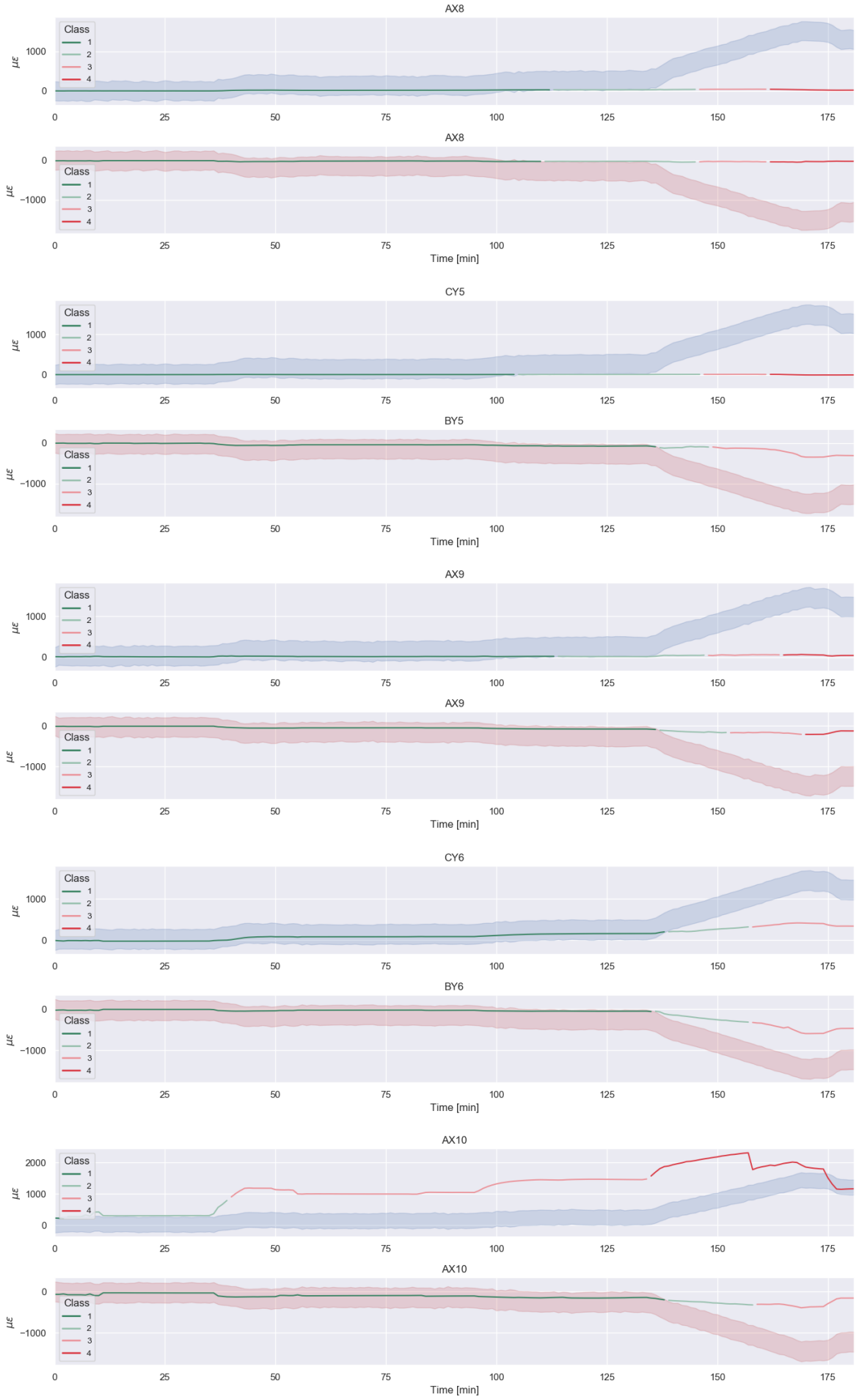
AX8
Class
1
2
3
4
1000
0
με
0
25
50
75
100
125
150
175
AX8
0
−1000
Time [min]
CY5
BY5
AX9
CY6
BY6
AX10
2000

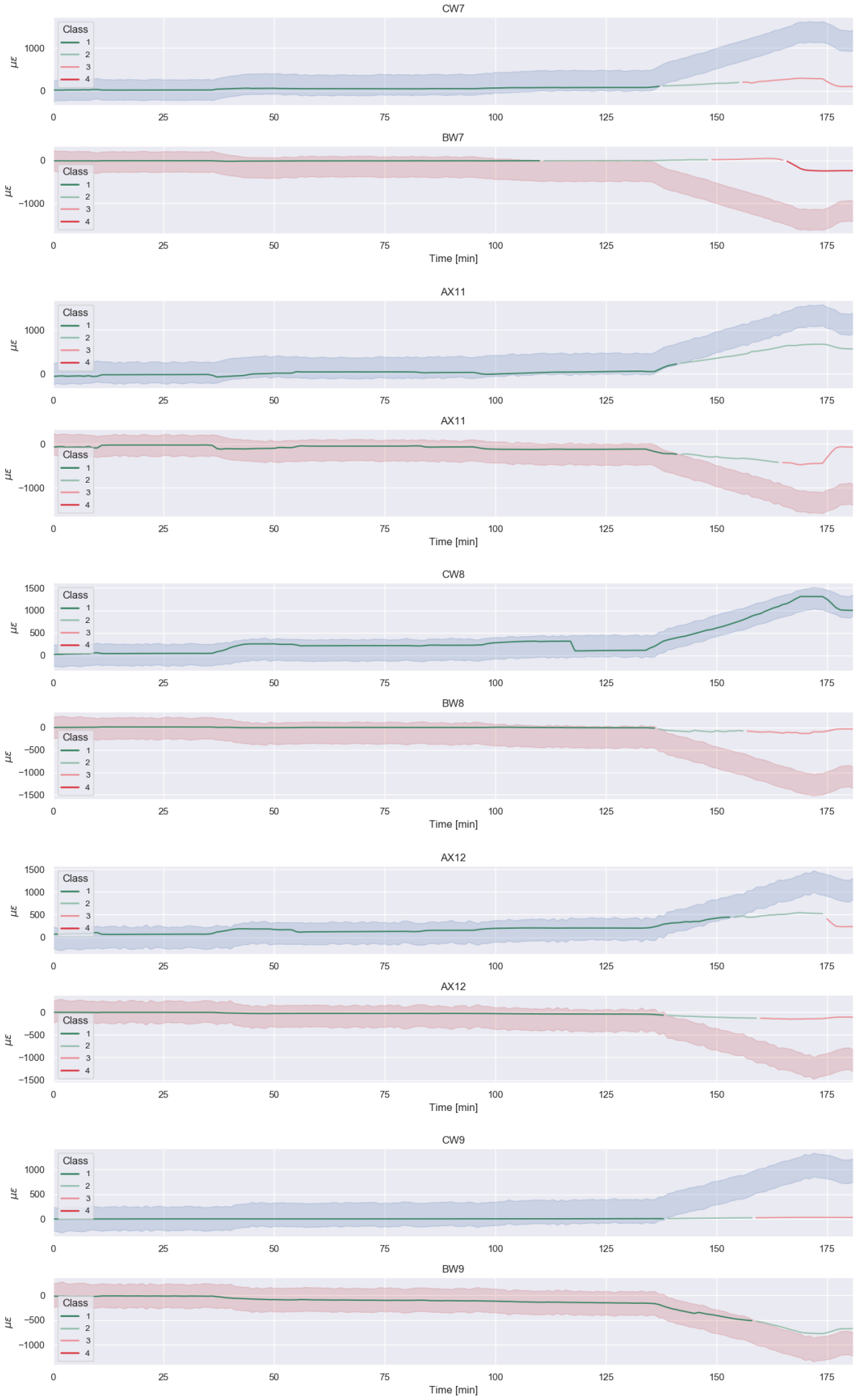
CW7
BW7
AX11
AX11
CW8
BW8
AX12
AX12
CW9
BW9
Class
1
2
3
4
με
Time [min]

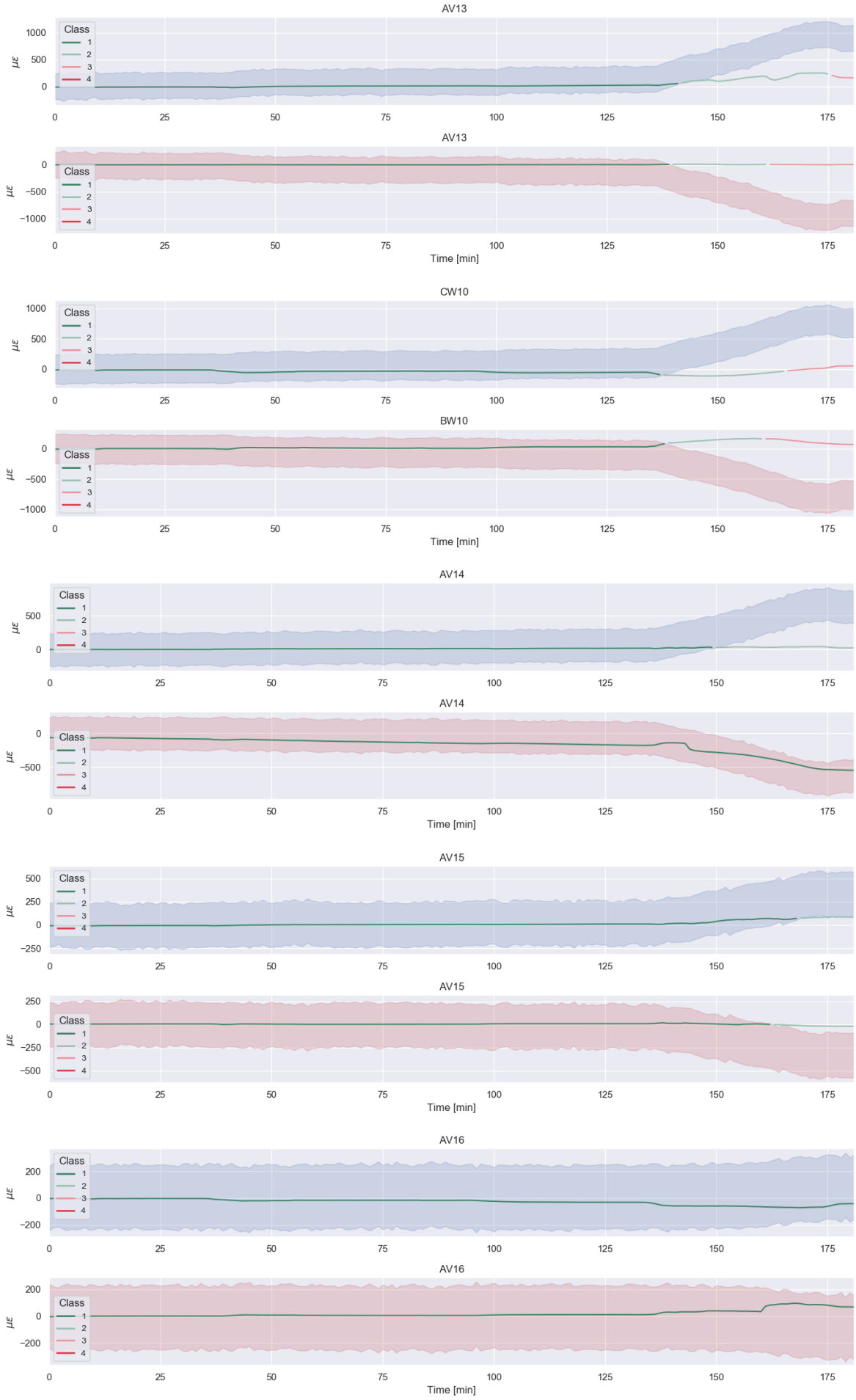
AV13
Class
1
2
3
4
με
1000
500
0
0
25
50
75
100
125
150
175
AV13
Class
1
2
3
4
με
0
−500
−1000
Time [min]
CW10
Class
1
2
3
4
με
1000
500
0
BW10
Class
1
2
3
4
με
0
−500
−1000
Time [min]
AV14
Class
1
2
3
4
με
500
0
AV14
Class
1
2
3
4
με
0
−500
Time [min]
AV15
Class
1
2
3
4
με
500
250
0
−250
AV15
Class
1
2
3
4
με
250
0
−250
−500
Time [min]
AV16
Class
1
2
3
4
με
200
0
−200
AV16
Class
1
2
3
4
με
200
0
−200
Time [min]

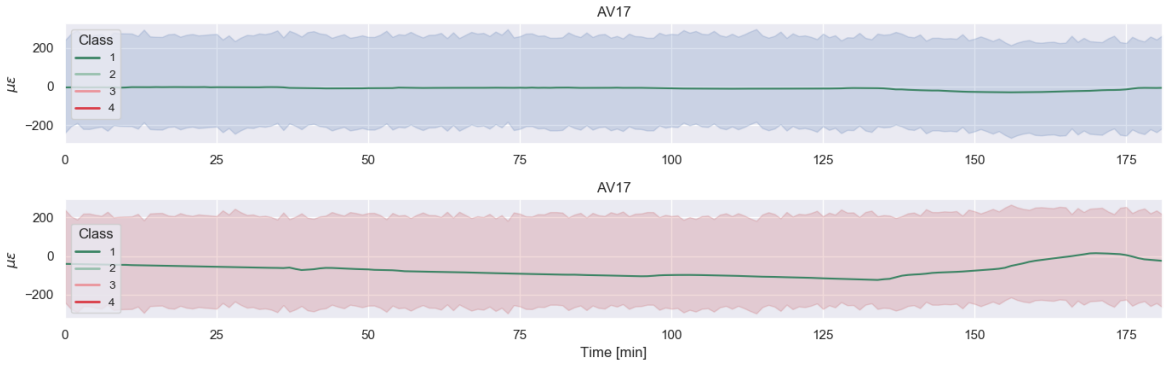
AV17
Class
1
2
3
4
200
0
−200
με
0
25
50
75
100
125
150
175
AV17
Class
1
2
3
4
200
0
−200
με
0
25
50
75
100
125
150
175
Time [min]

B.2.4. Install configuration side

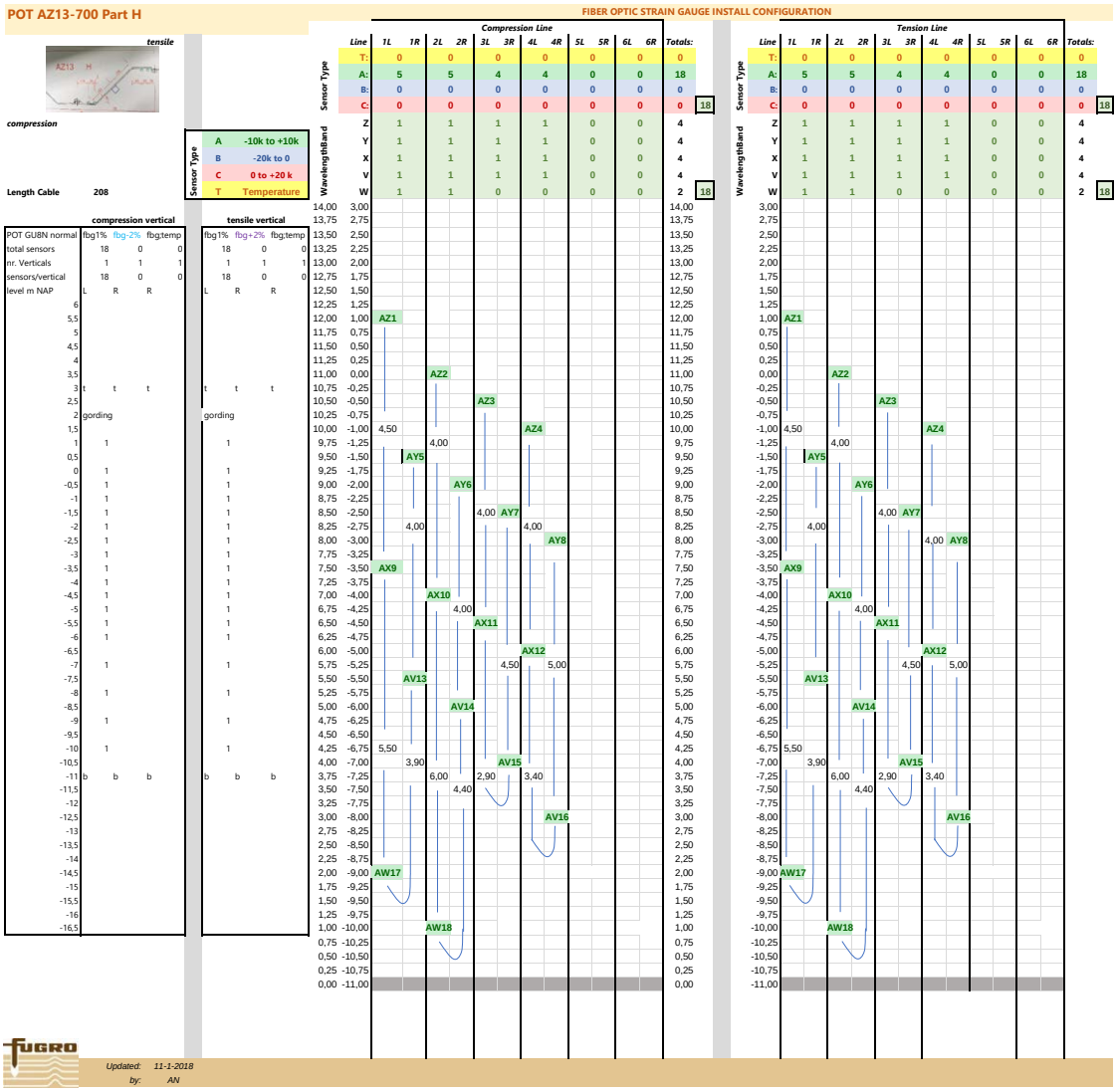

B.2.5. Load verification side

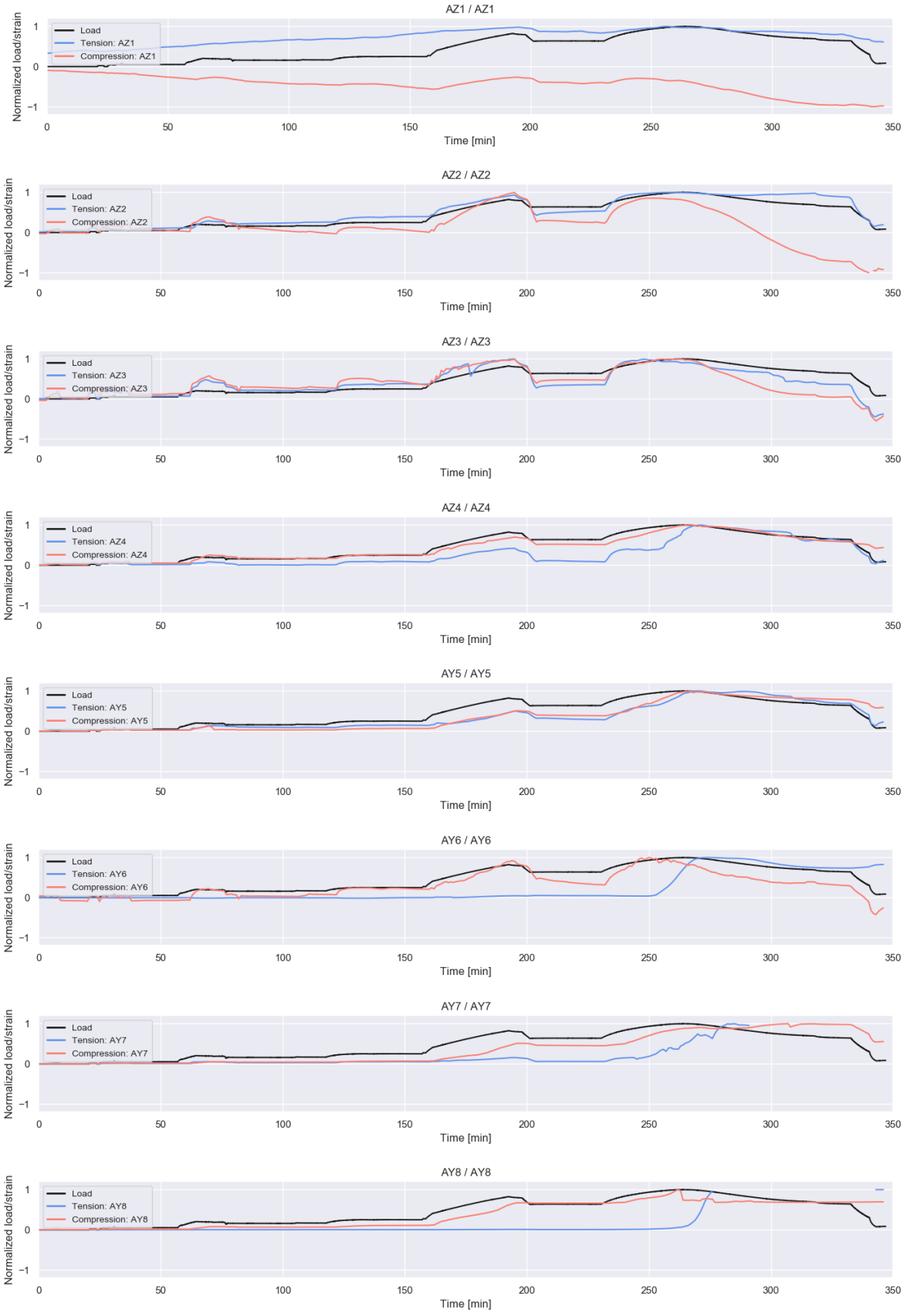

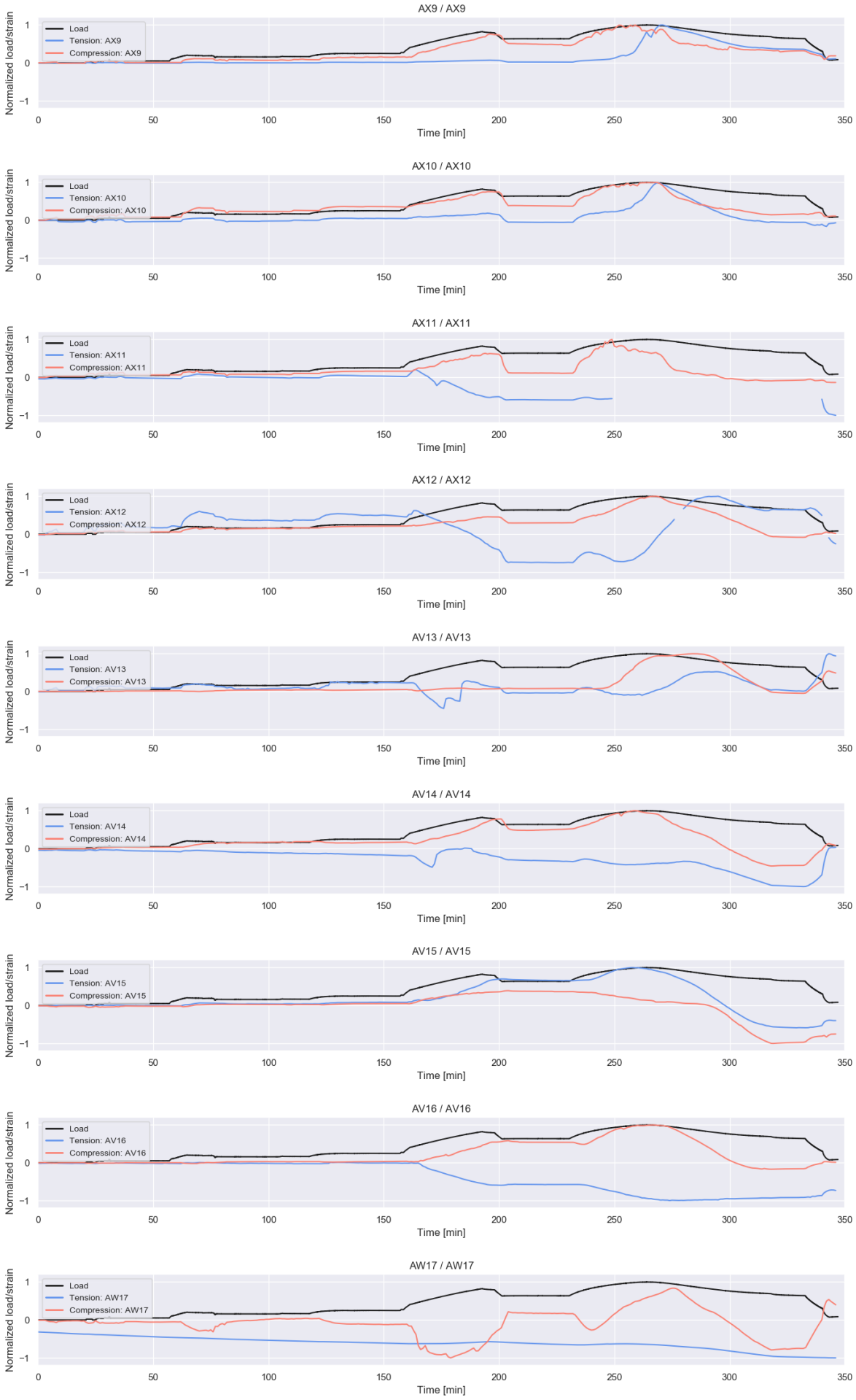
AX9 / AX9
Load
Tension: AX9
Compression: AX9
AX10 / AX10
Load
Tension: AX10
Compression: AX10
AX11 / AX11
Load
Tension: AX11
Compression: AX11
AX12 / AX12
Load
Tension: AX12
Compression: AX12
AV13 / AV13
Load
Tension: AV13
Compression: AV13
AV14 / AV14
Load
Tension: AV14
Compression: AV14
AV15 / AV15
Load
Tension: AV15
Compression: AV15
AV16 / AV16
Load
Tension: AV16
Compression: AV16
AW17 / AW17
Load
Tension: AW17
Compression: AW17
Normalized load/strain
Time [min]

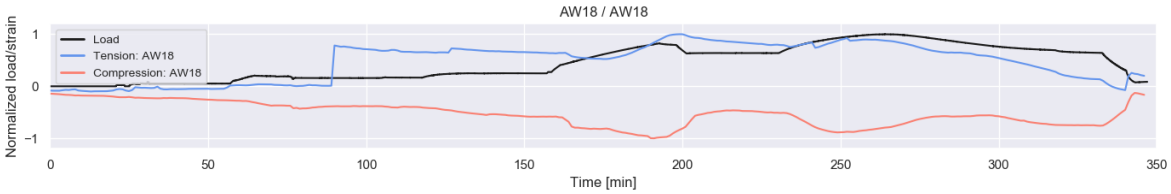
AW18 / AW18
Load
Tension: AW18
Compression: AW18
Normalized load/strain
1
0
−1
0
50
100
150
200
250
300
350
Time [min]

B.2.6. SAAF verifciation side

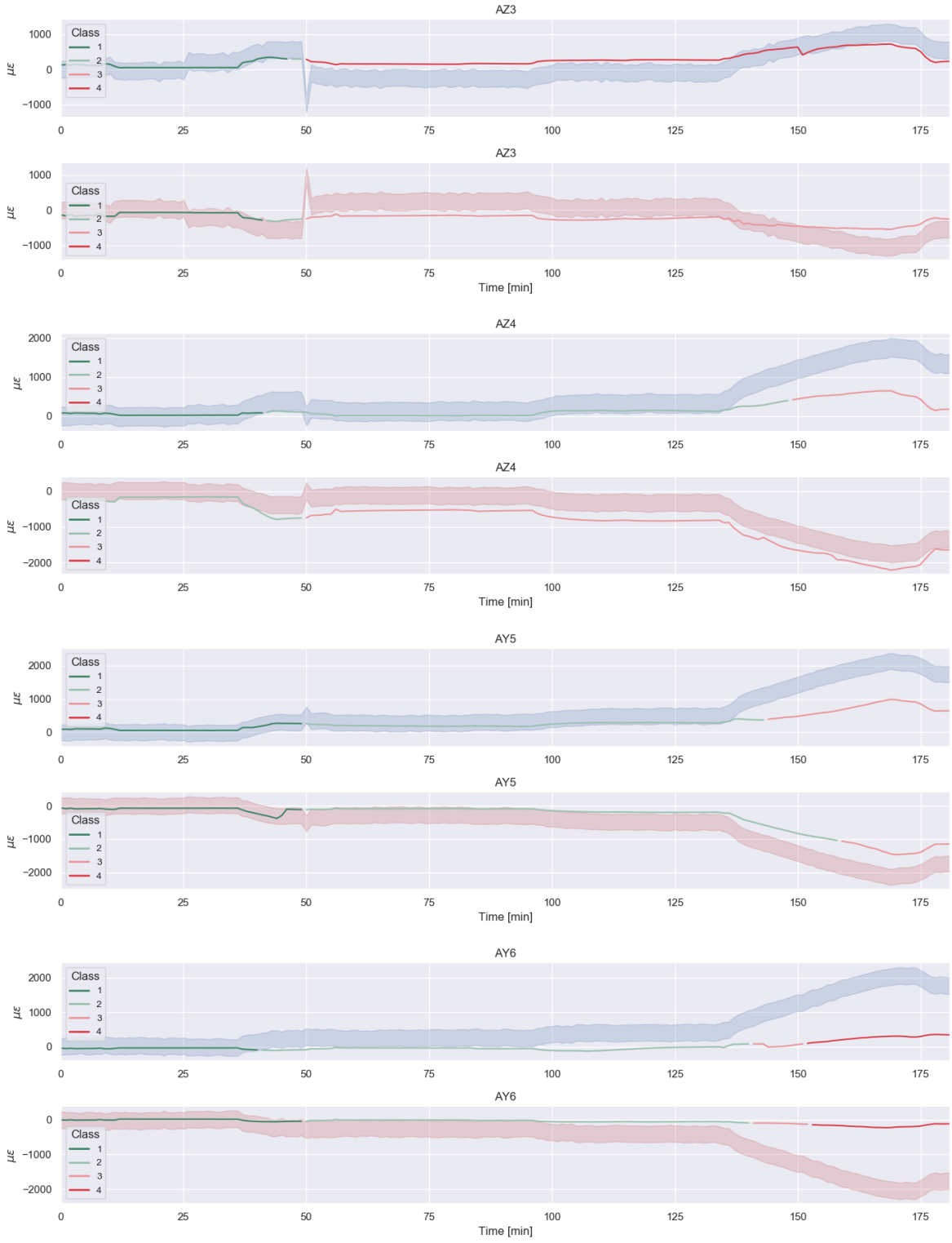

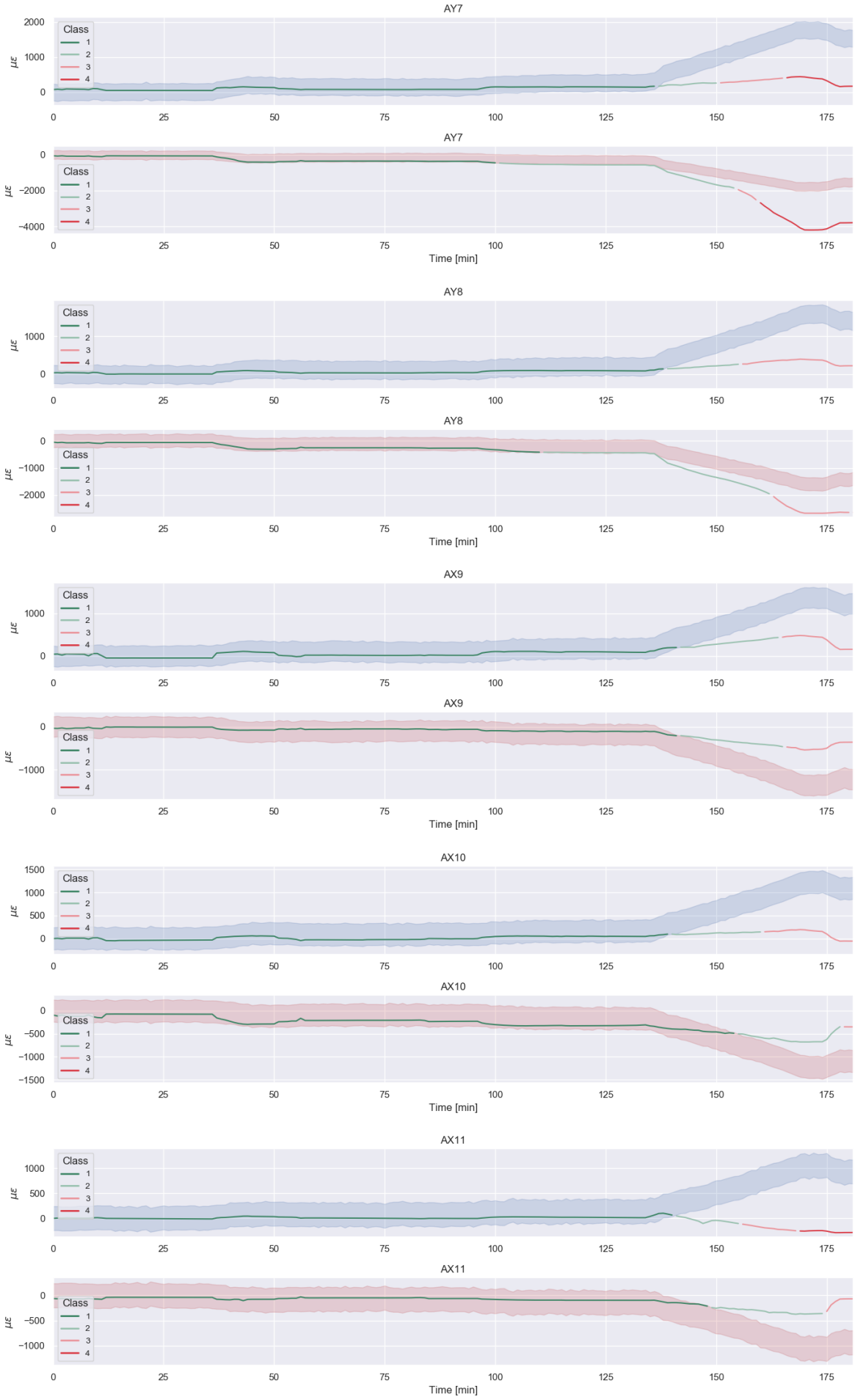
AY7
AY7
AY8
AY8
AX9
AX9
AX10
AX10
AX11
AX11
Class
1
2
3
4
με
Time [min]

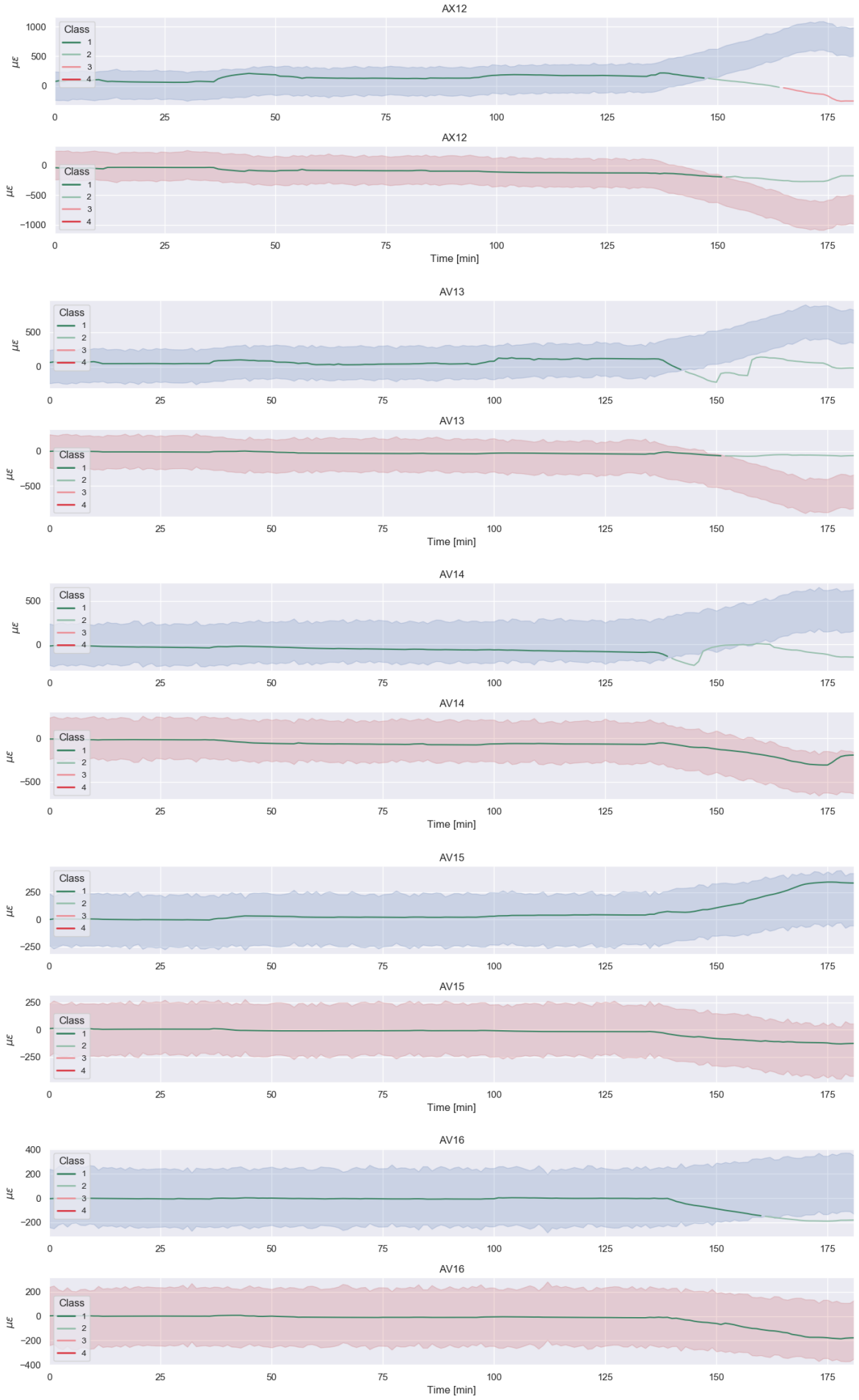
AX12
AX12
AV13
AV13
AV14
AV14
AV15
AV15
AV16
AV16
Class
1
2
3
4
με
Time [min]

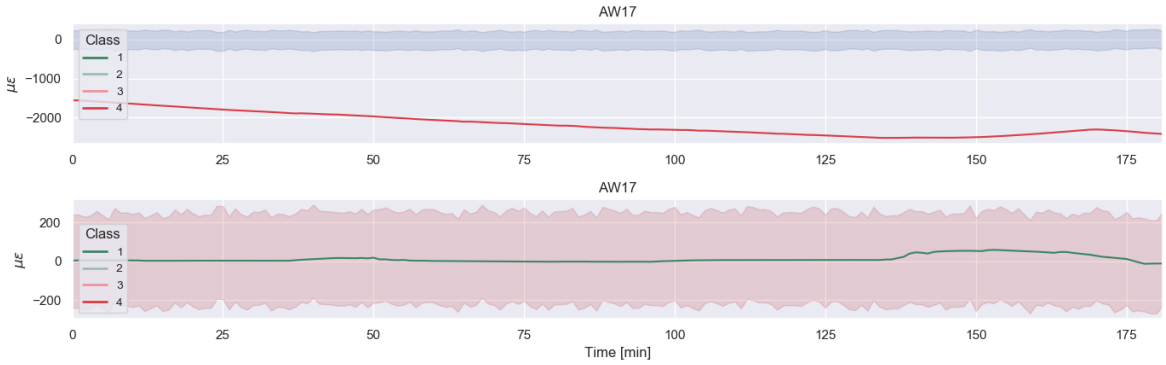
AW17
Class
1
2
3
4
με
0
−1000
−2000
0
25
50
75
100
125
150
175
AW17
Class
1
2
3
4
με
200
0
−200
0
25
50
75
100
125
150
175
Time [min]

B.3. GU8N

B.3.1. Install configuration

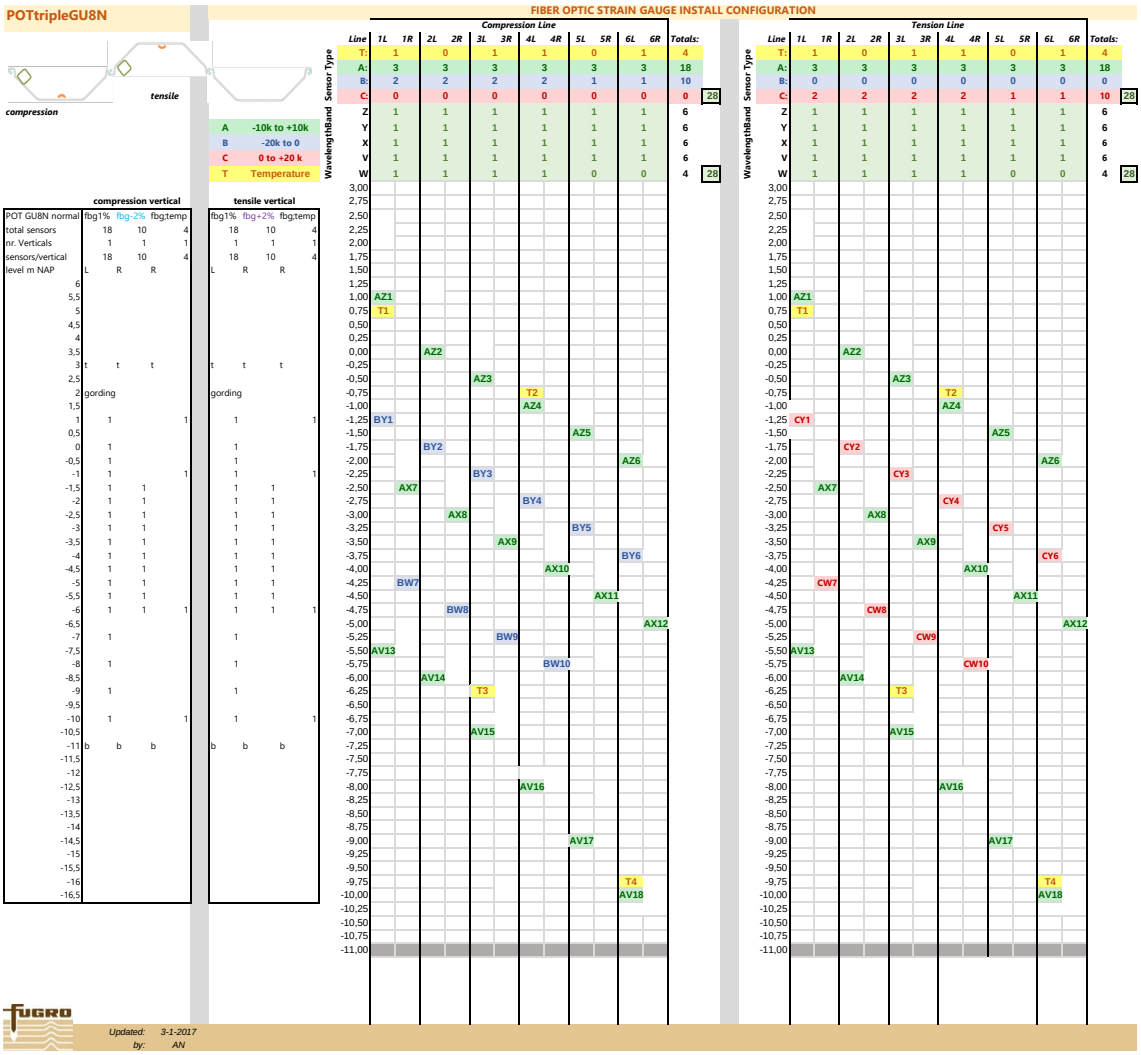

B.3.2. Load verification

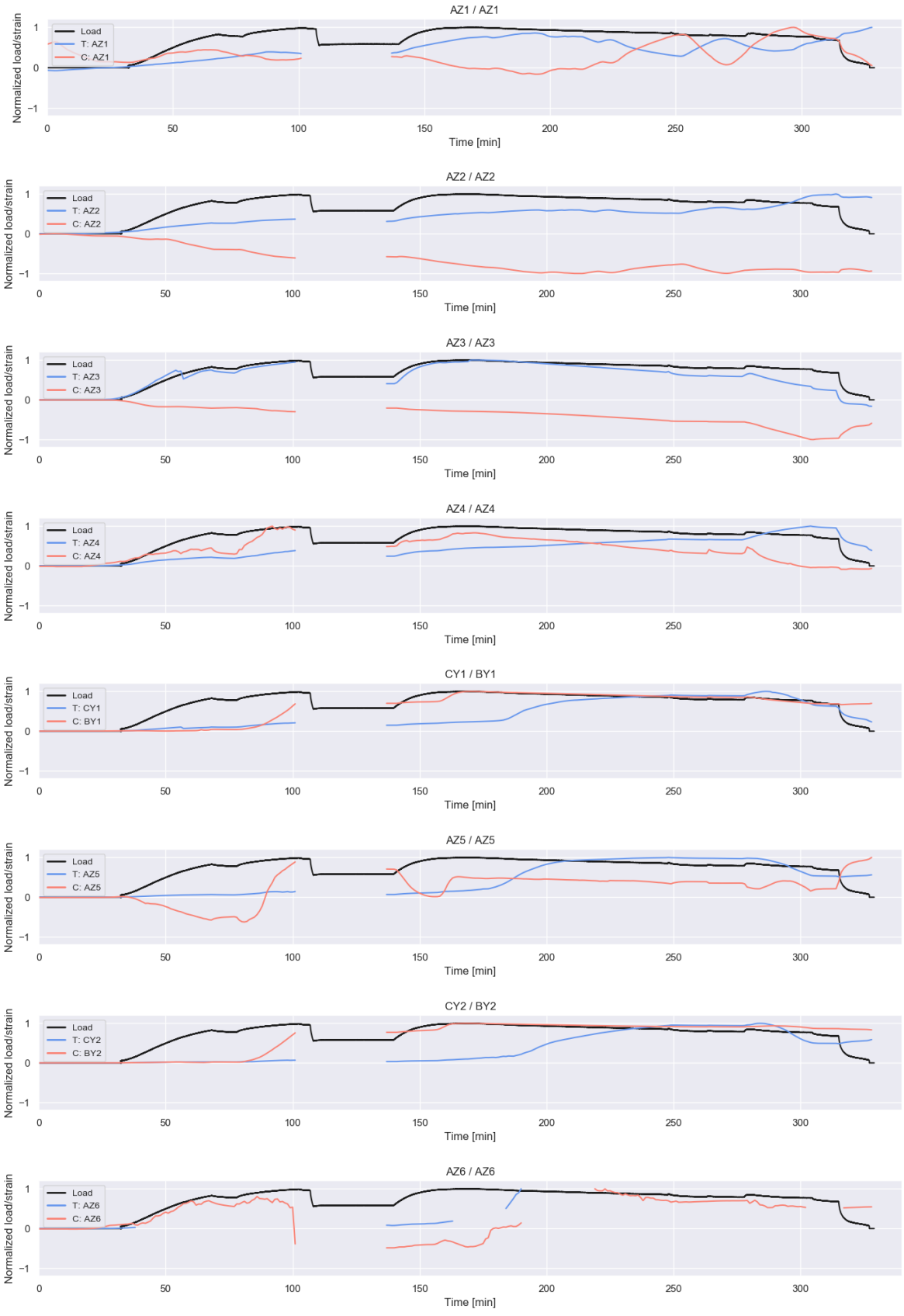

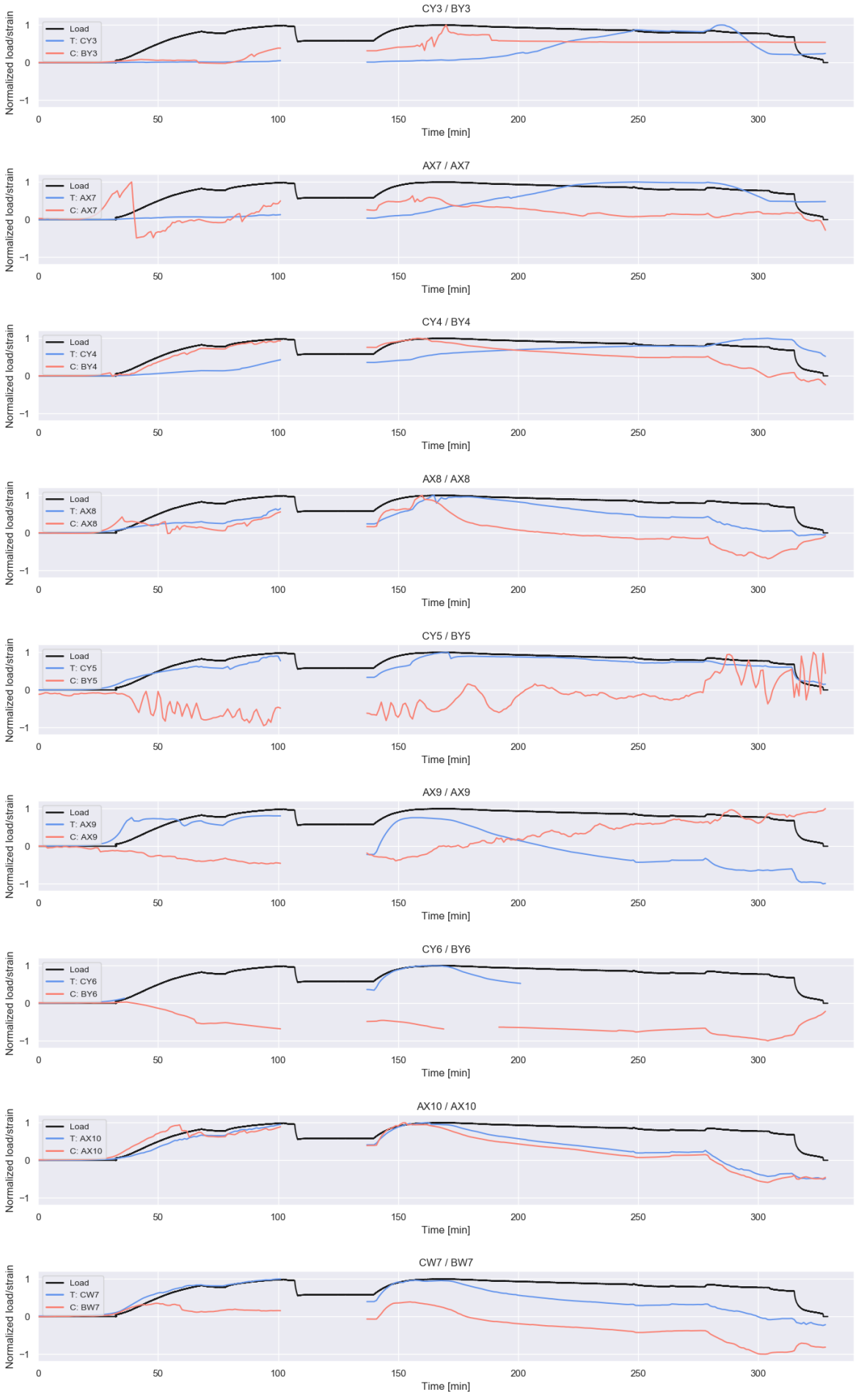
CY3 / BY3
Load
T: CY3
C: BY3
AX7 / AX7
Load
T: AX7
C: AX7
CY4 / BY4
Load
T: CY4
C: BY4
AX8 / AX8
Load
T: AX8
C: AX8
CY5 / BY5
Load
T: CY5
C: BY5
AX9 / AX9
Load
T: AX9
C: AX9
CY6 / BY6
Load
T: CY6
C: BY6
AX10 / AX10
Load
T: AX10
C: AX10
CW7 / BW7
Load
T: CW7
C: BW7
Normalized load/strain
Time [min]

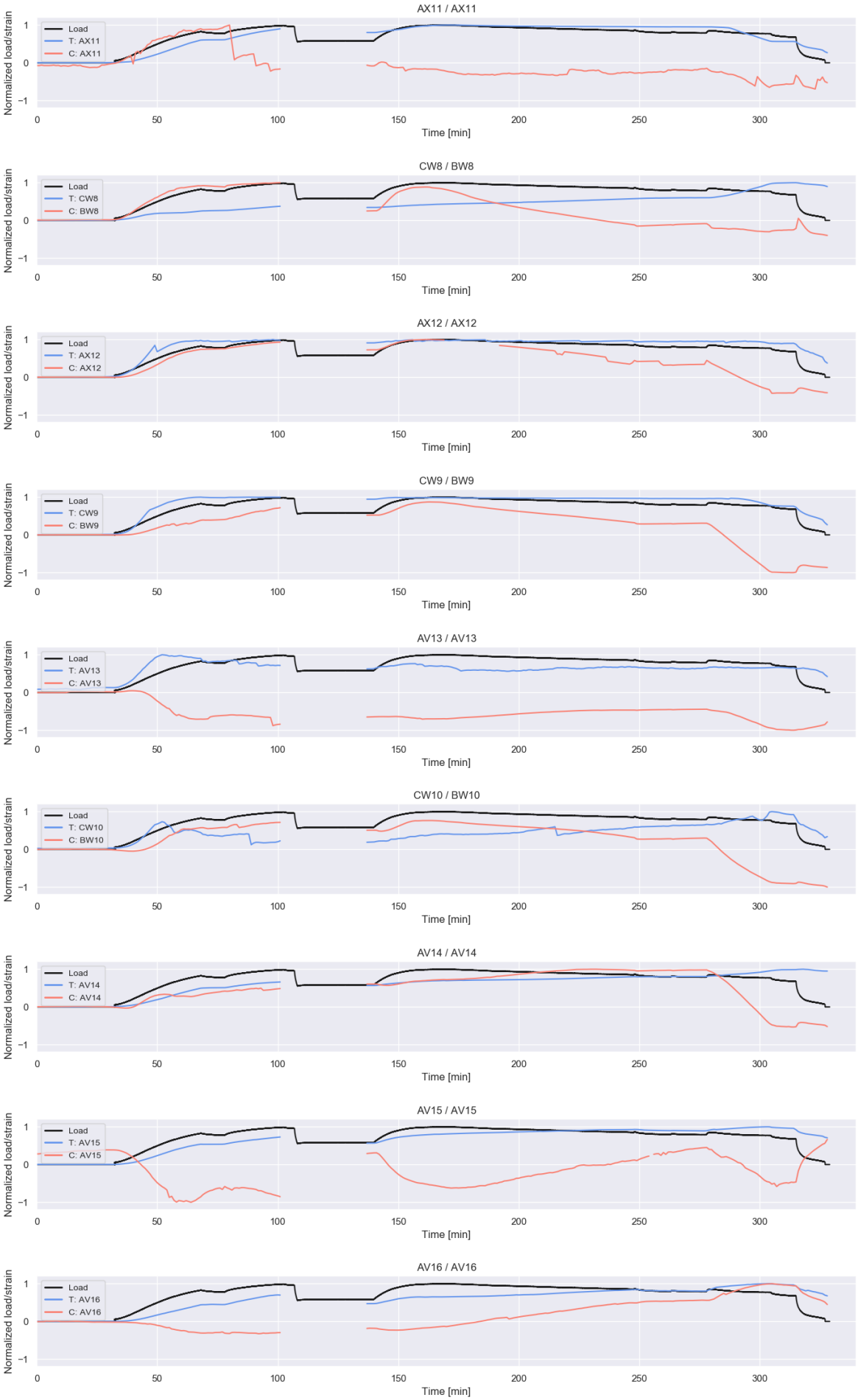
AX11 / AX11
Load
T: AX11
C: AX11
CW8 / BW8
Load
T: CW8
C: BW8
AX12 / AX12
Load
T: AX12
C: AX12
CW9 / BW9
Load
T: CW9
C: BW9
AV13 / AV13
Load
T: AV13
C: AV13
CW10 / BW10
Load
T: CW10
C: BW10
AV14 / AV14
Load
T: AV14
C: AV14
AV15 / AV15
Load
T: AV15
C: AV15
AV16 / AV16
Load
T: AV16
C: AV16
Normalized load/strain
Time [min]

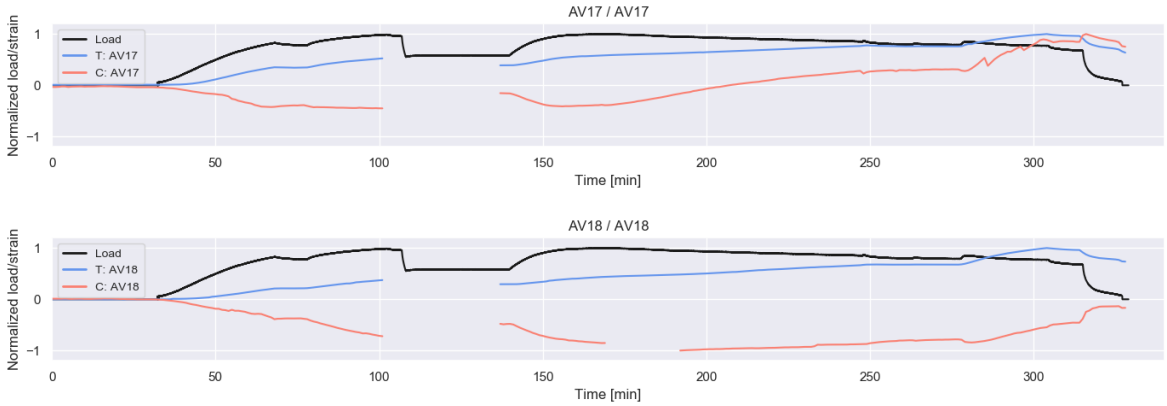
AV17 / AV17
Load
T: AV17
C: AV17
Normalized load/strain
Time [min]
AV18 / AV18
Load
T: AV18
C: AV18
Normalized load/strain
Time [min]

B.3.3. SAAF verifciation

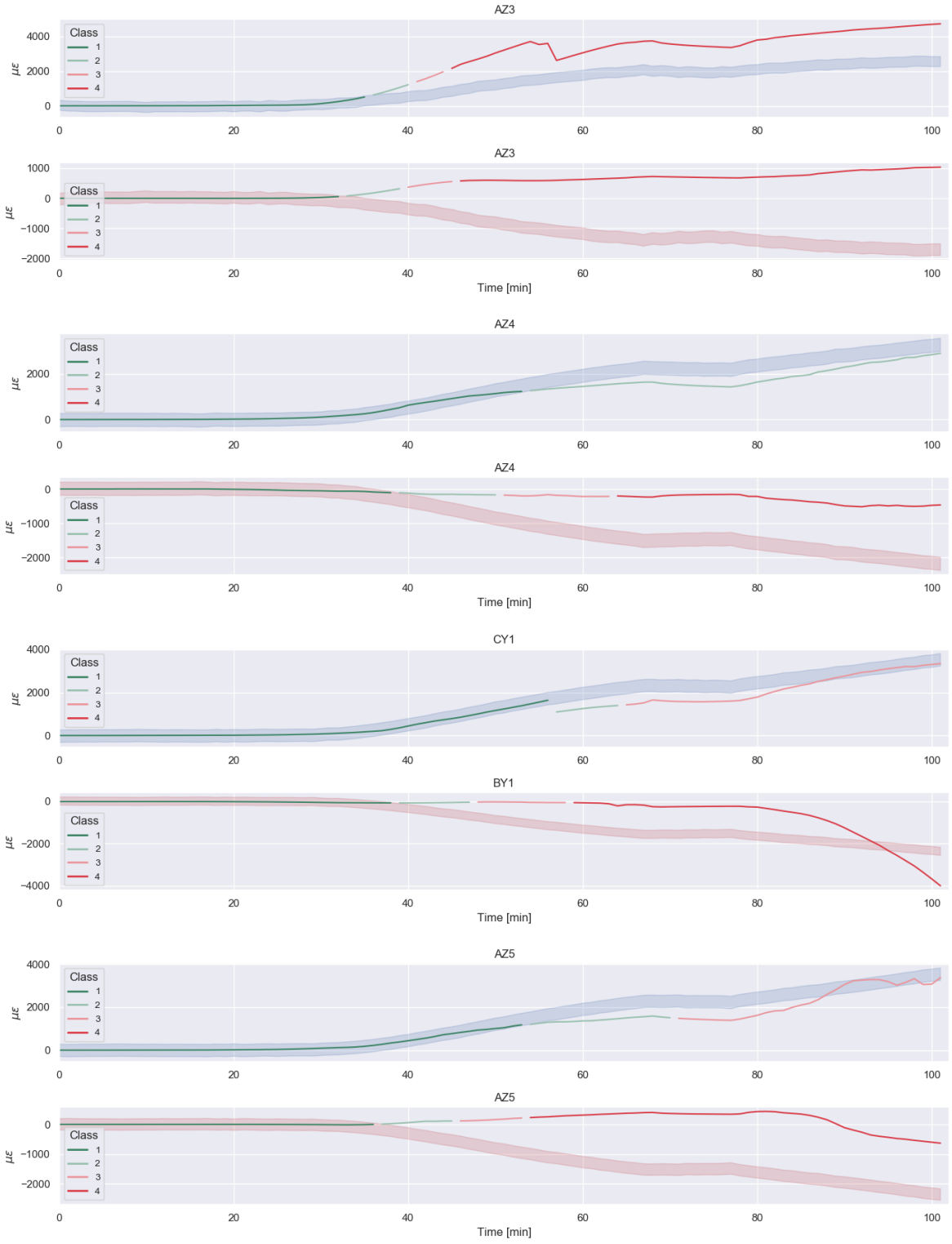

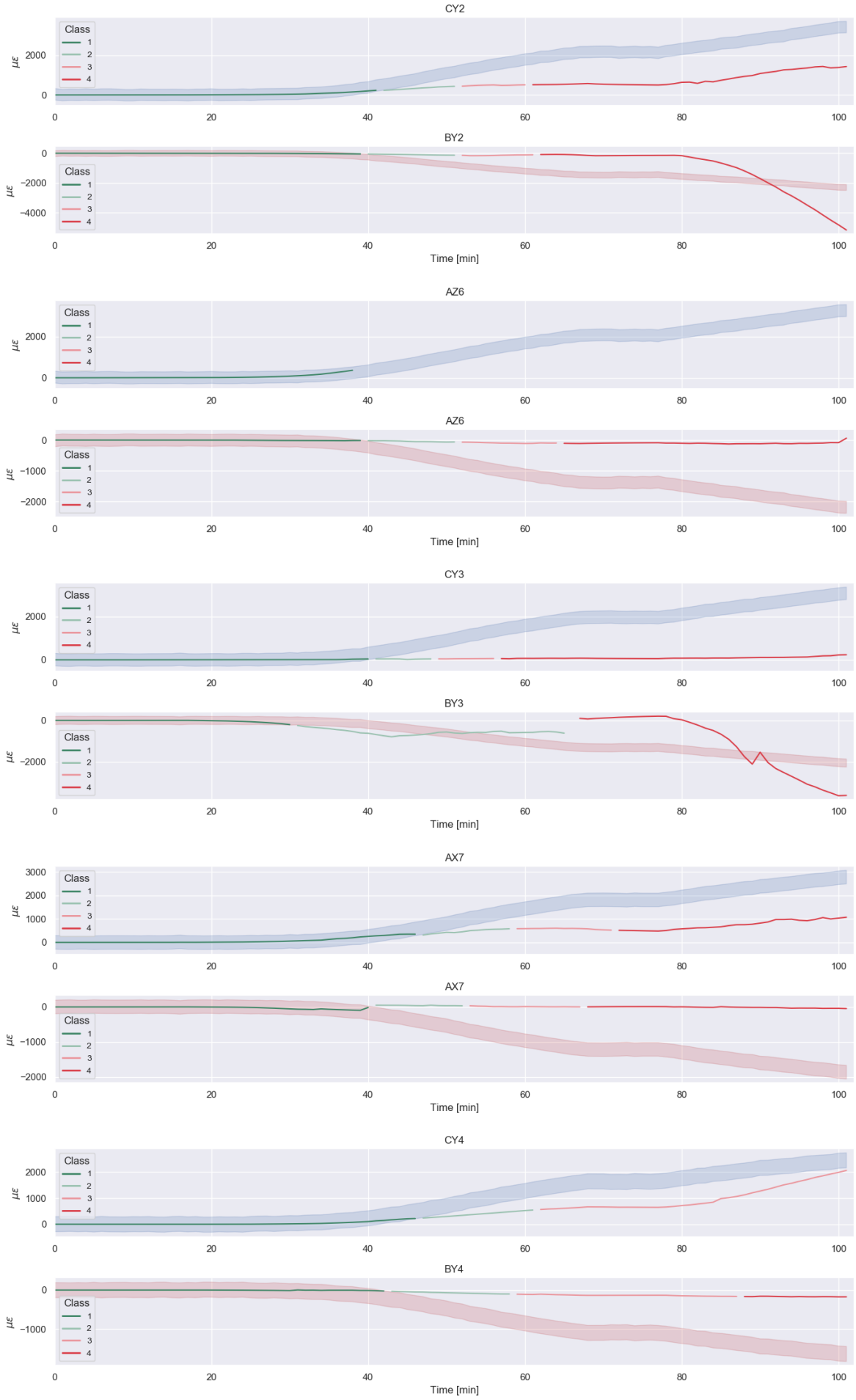
CY2
BY2
AZ6
AZ6
CY3
BY3
AX7
AX7
CY4
BY4
Class
1
2
3
4
με
Time [min]

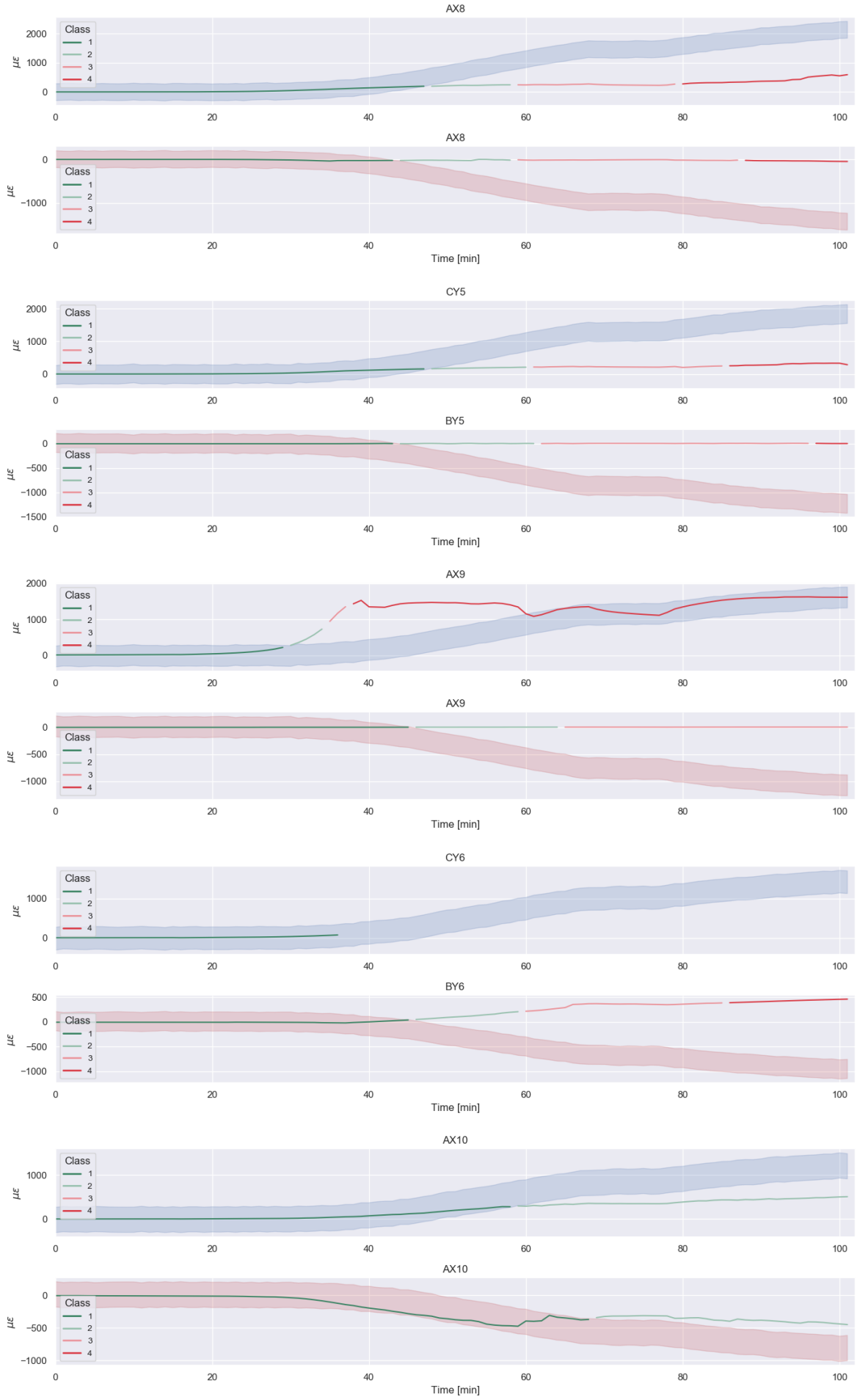
AX8
Class
1
2
3
4
με
Time [min]
CY5
BY5
AX9
CY6
BY6
AX10

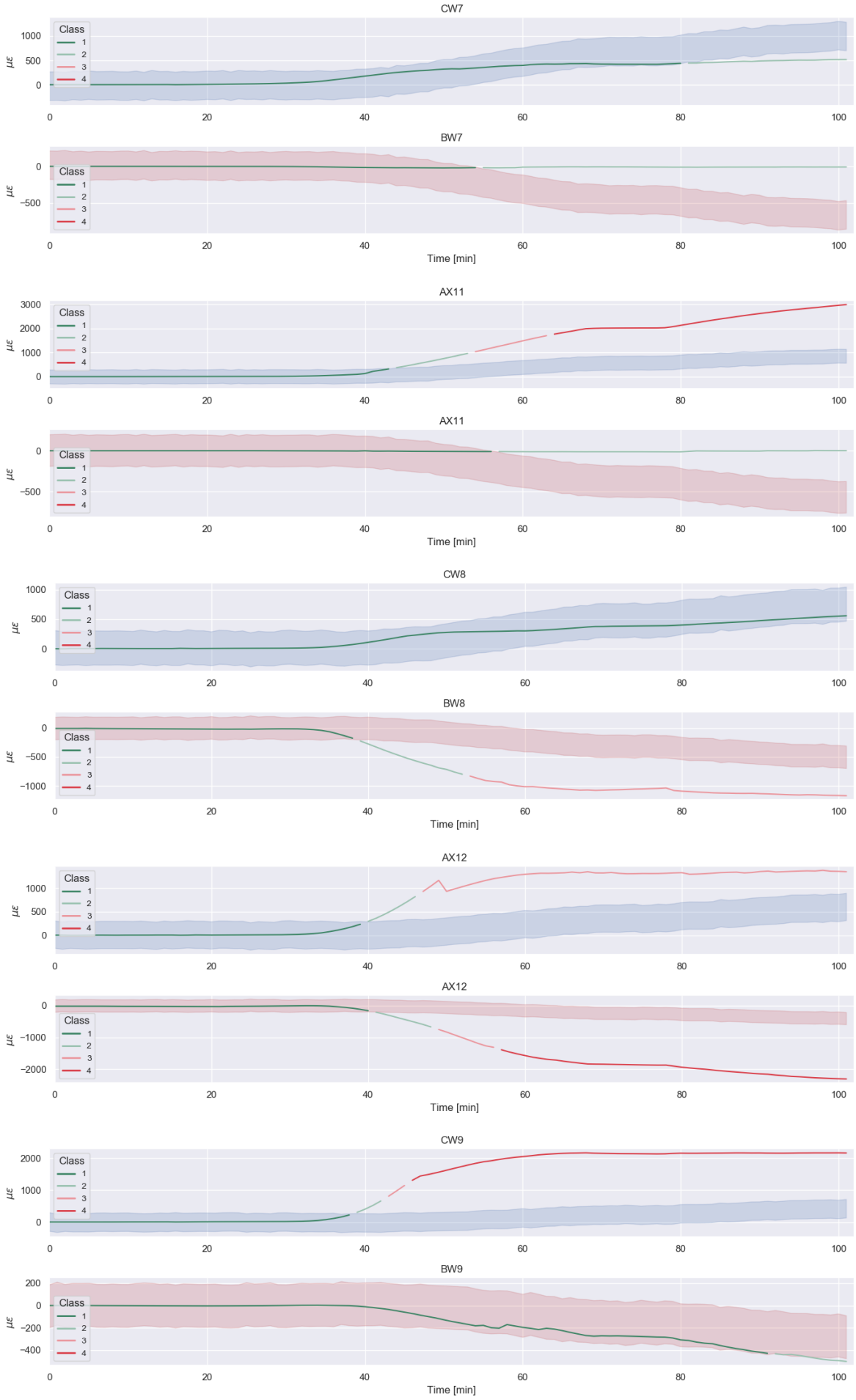
CW7
BW7
AX11
AX11
CW8
BW8
AX12
AX12
CW9
BW9
Class
1
2
3
4
με
Time [min]

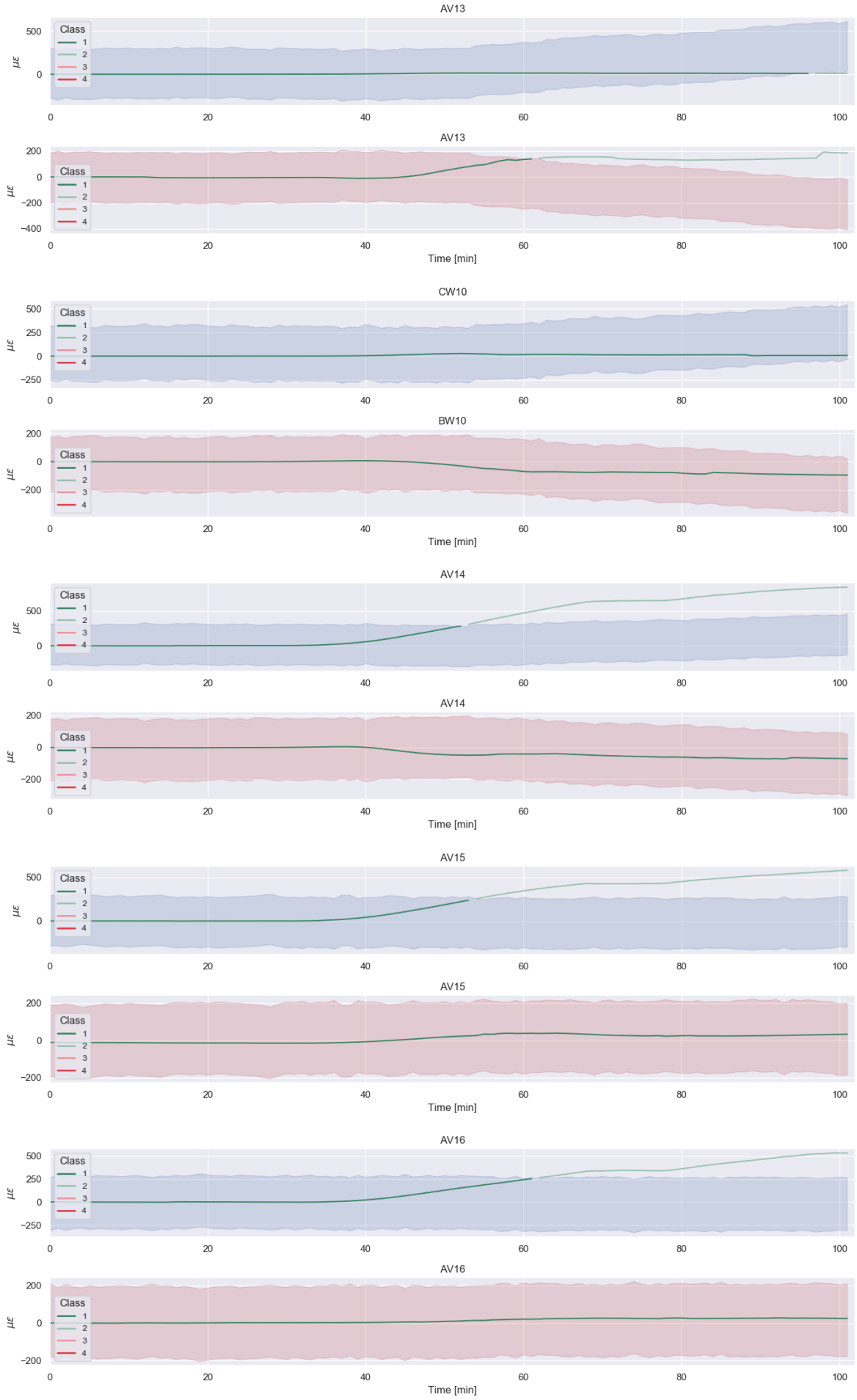
AV13
Class
1
2
3
4
με
Time [min]
CW10
BW10
AV14
AV15
AV16

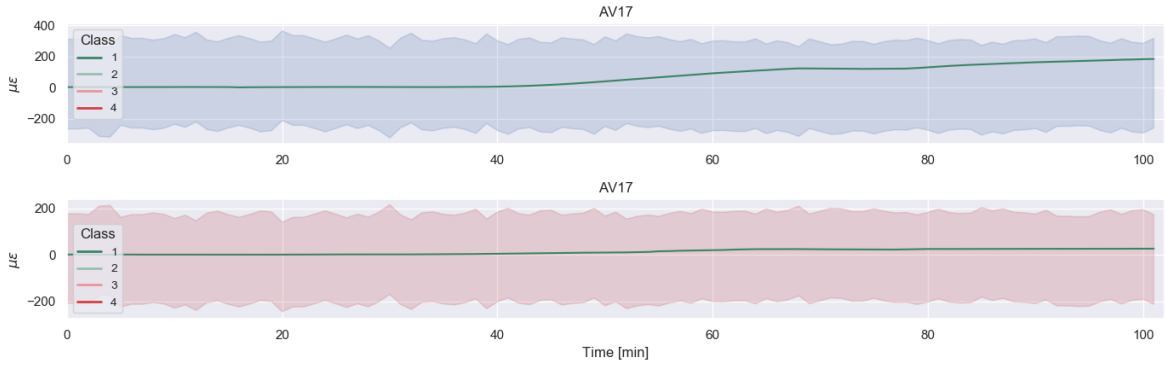
AV17
Class
1
2
3
4
με
400
200
0
−200
0
20
40
60
80
100
AV17
Class
1
2
3
4
με
200
0
−200
0
20
40
60
80
100
Time [min]

B.4. GU8R

B.4.1. Install configuration

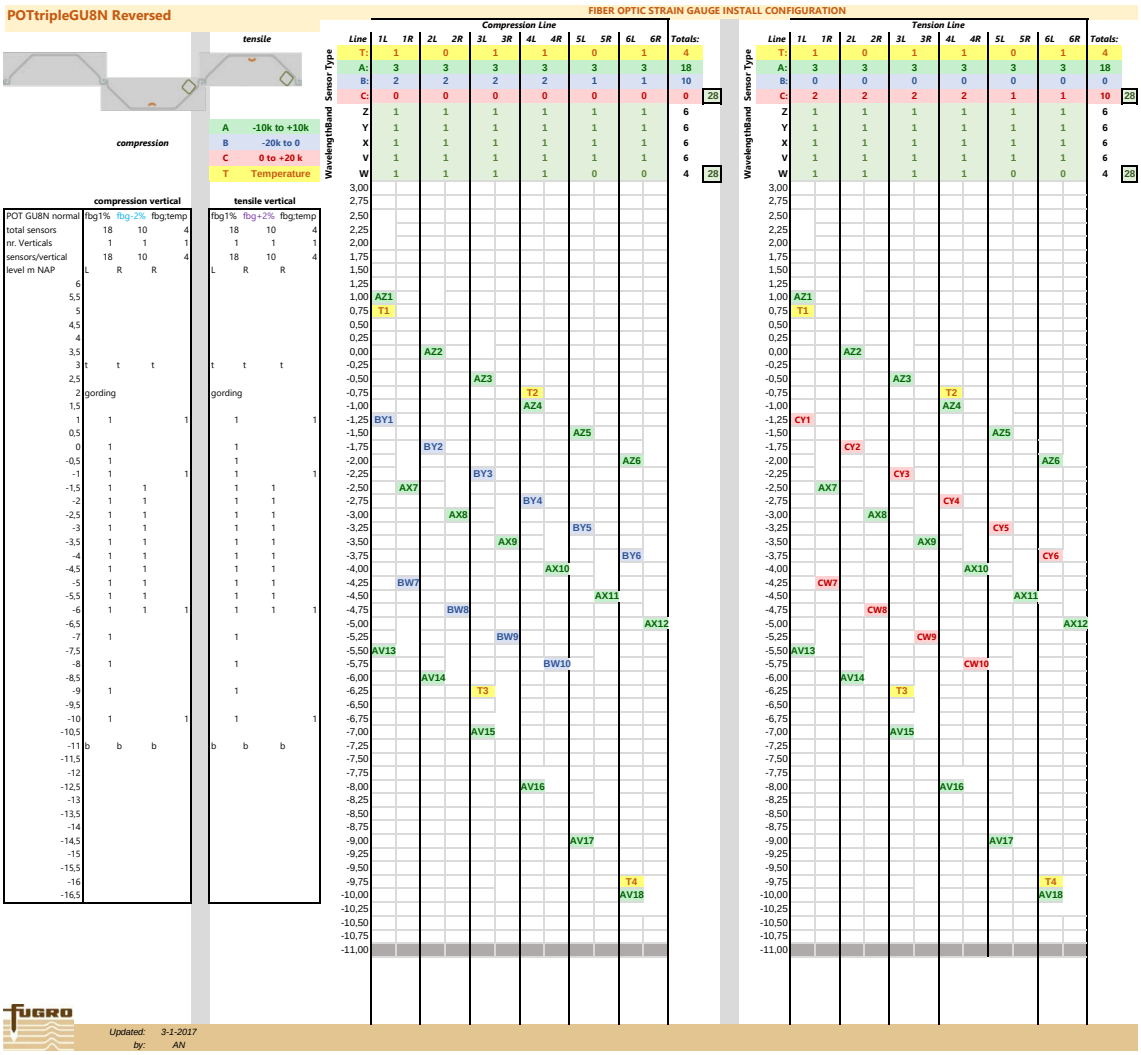

B.4.2. Load verification

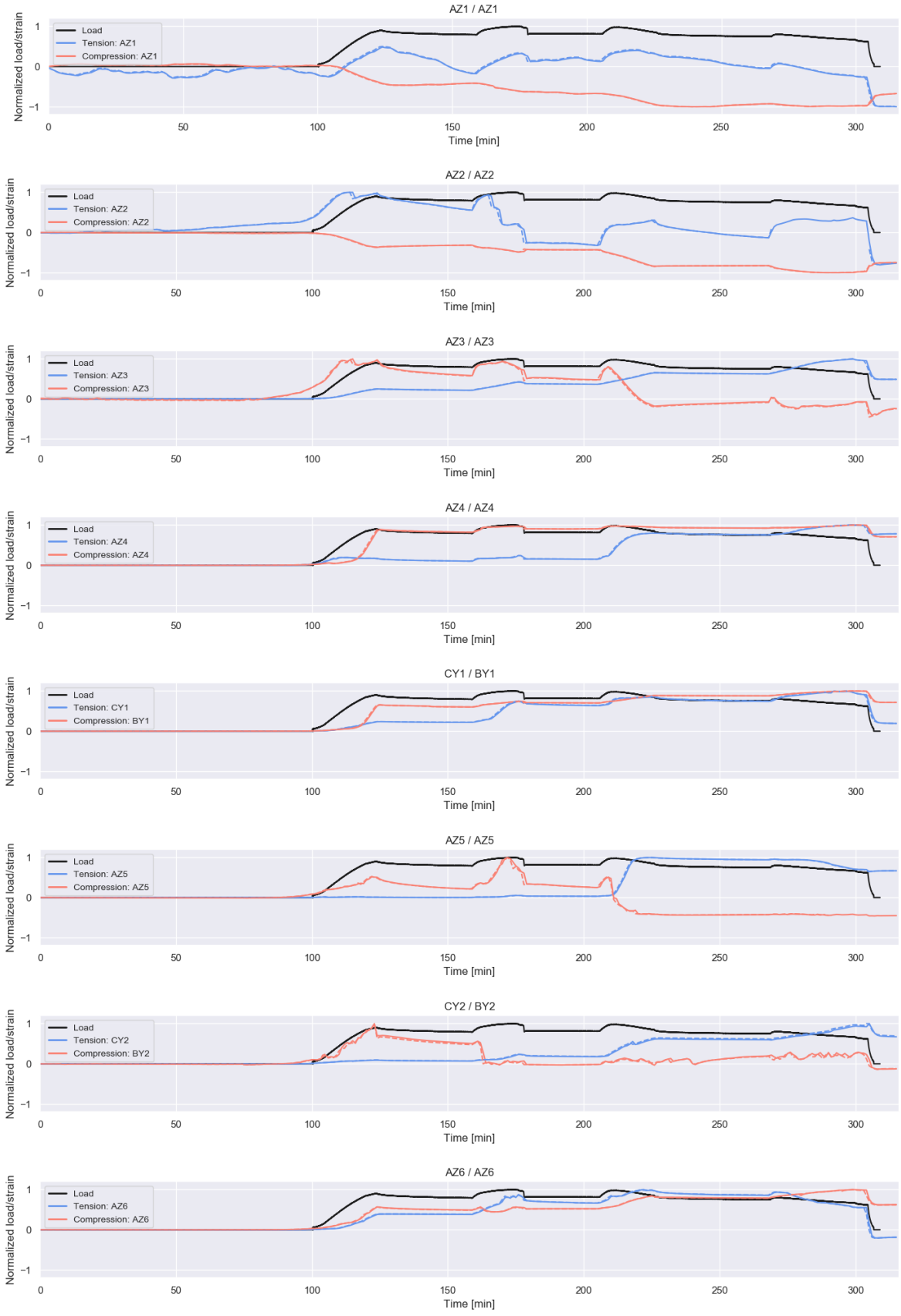

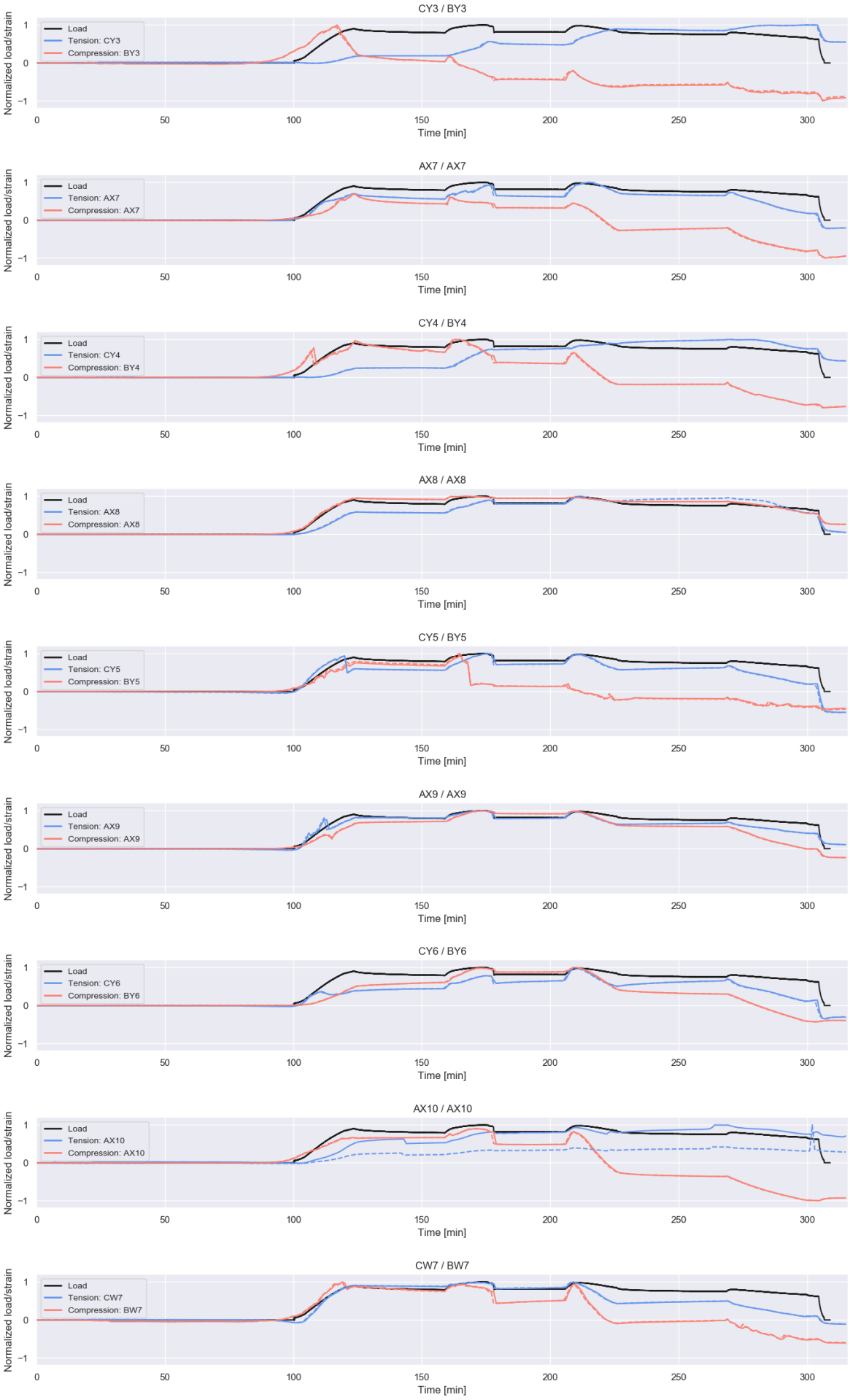
CY3 / BY3
Load
Tension: CY3
Compression: BY3
AX7 / AX7
Load
Tension: AX7
Compression: AX7
CY4 / BY4
Load
Tension: CY4
Compression: BY4
AX8 / AX8
Load
Tension: AX8
Compression: AX8
CY5 / BY5
Load
Tension: CY5
Compression: BY5
AX9 / AX9
Load
Tension: AX9
Compression: AX9
CY6 / BY6
Load
Tension: CY6
Compression: BY6
AX10 / AX10
Load
Tension: AX10
Compression: AX10
CW7 / BW7
Load
Tension: CW7
Compression: BW7
Normalized load/strain
Time [min]

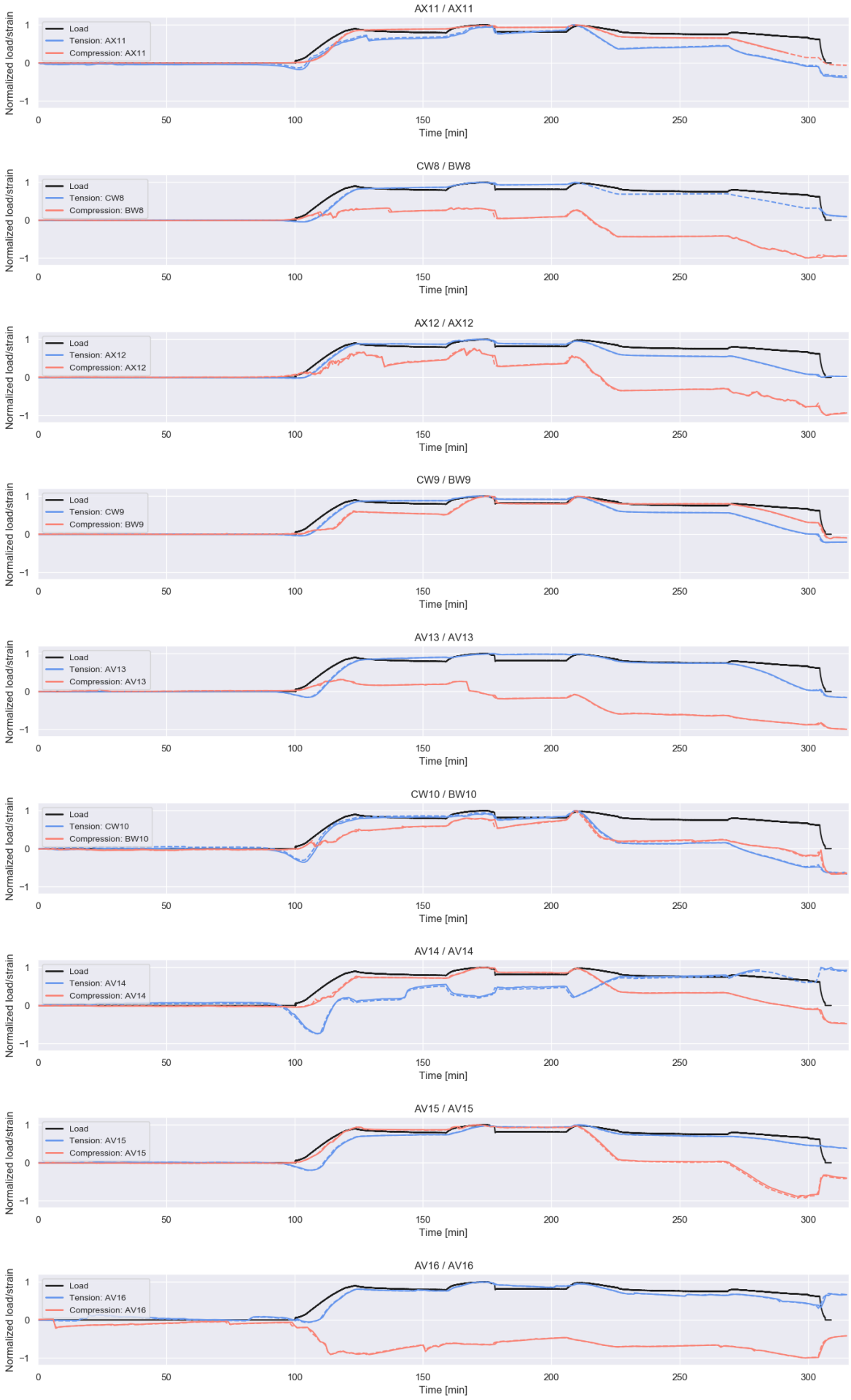
AX11 / AX11
Load
Tension: AX11
Compression: AX11
CW8 / BW8
Load
Tension: CW8
Compression: BW8
AX12 / AX12
Load
Tension: AX12
Compression: AX12
CW9 / BW9
Load
Tension: CW9
Compression: BW9
AV13 / AV13
Load
Tension: AV13
Compression: AV13
CW10 / BW10
Load
Tension: CW10
Compression: BW10
AV14 / AV14
Load
Tension: AV14
Compression: AV14
AV15 / AV15
Load
Tension: AV15
Compression: AV15
AV16 / AV16
Load
Tension: AV16
Compression: AV16
Normalized load/strain
Time [min]

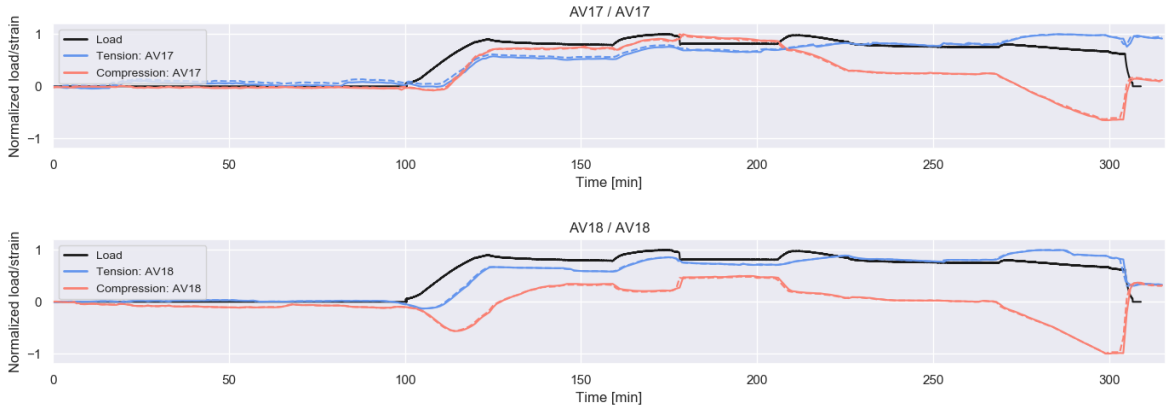
AV17 / AV17
Load
Tension: AV17
Compression: AV17
Normalized load/strain
1
0
−1
0
50
100
150
200
250
300
Time [min]

AV18 / AV18
Load
Tension: AV18
Compression: AV18
Normalized load/strain
1
0
−1
0
50
100
150
200
250
300
Time [min]

B.4.3. SAAF verifciation

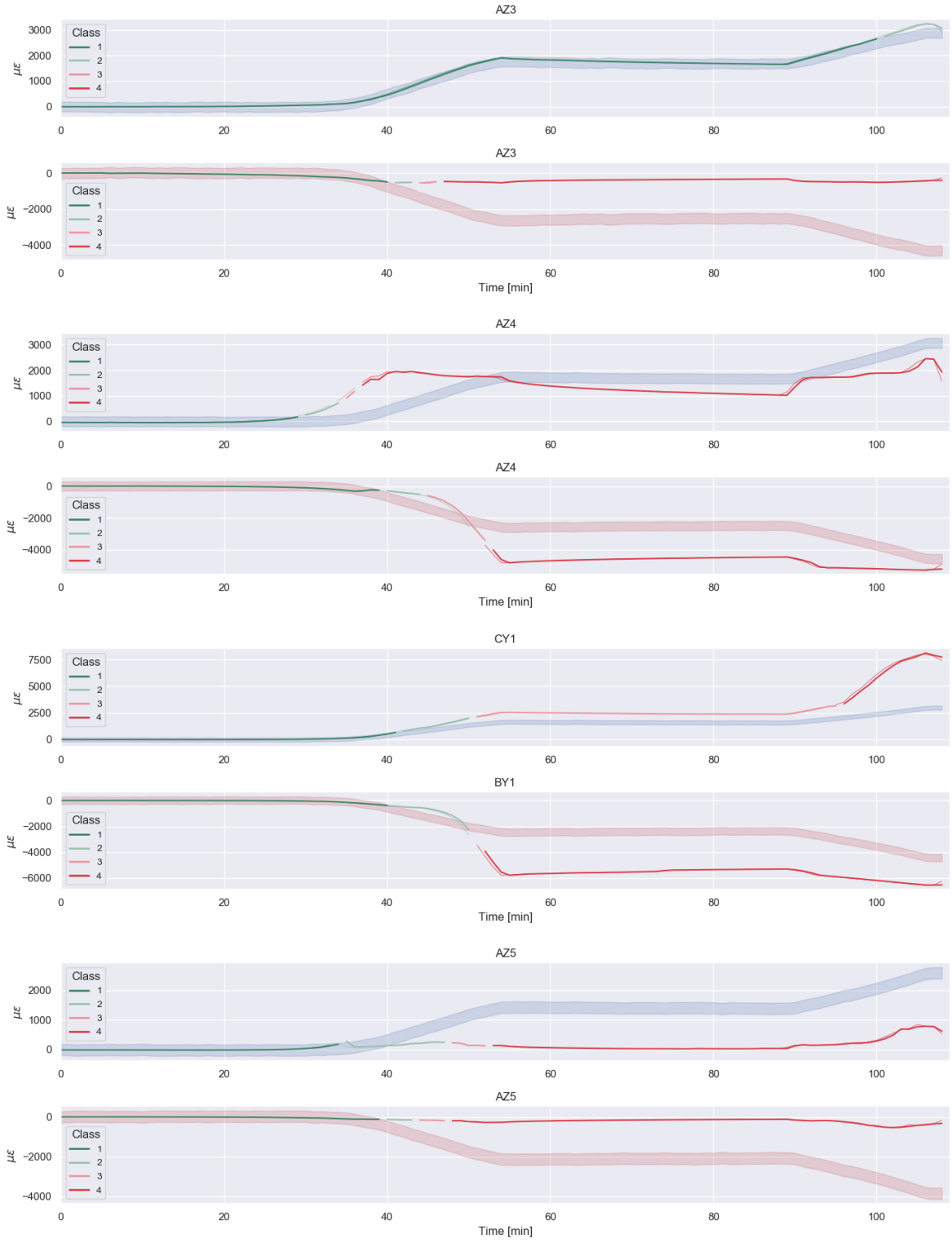

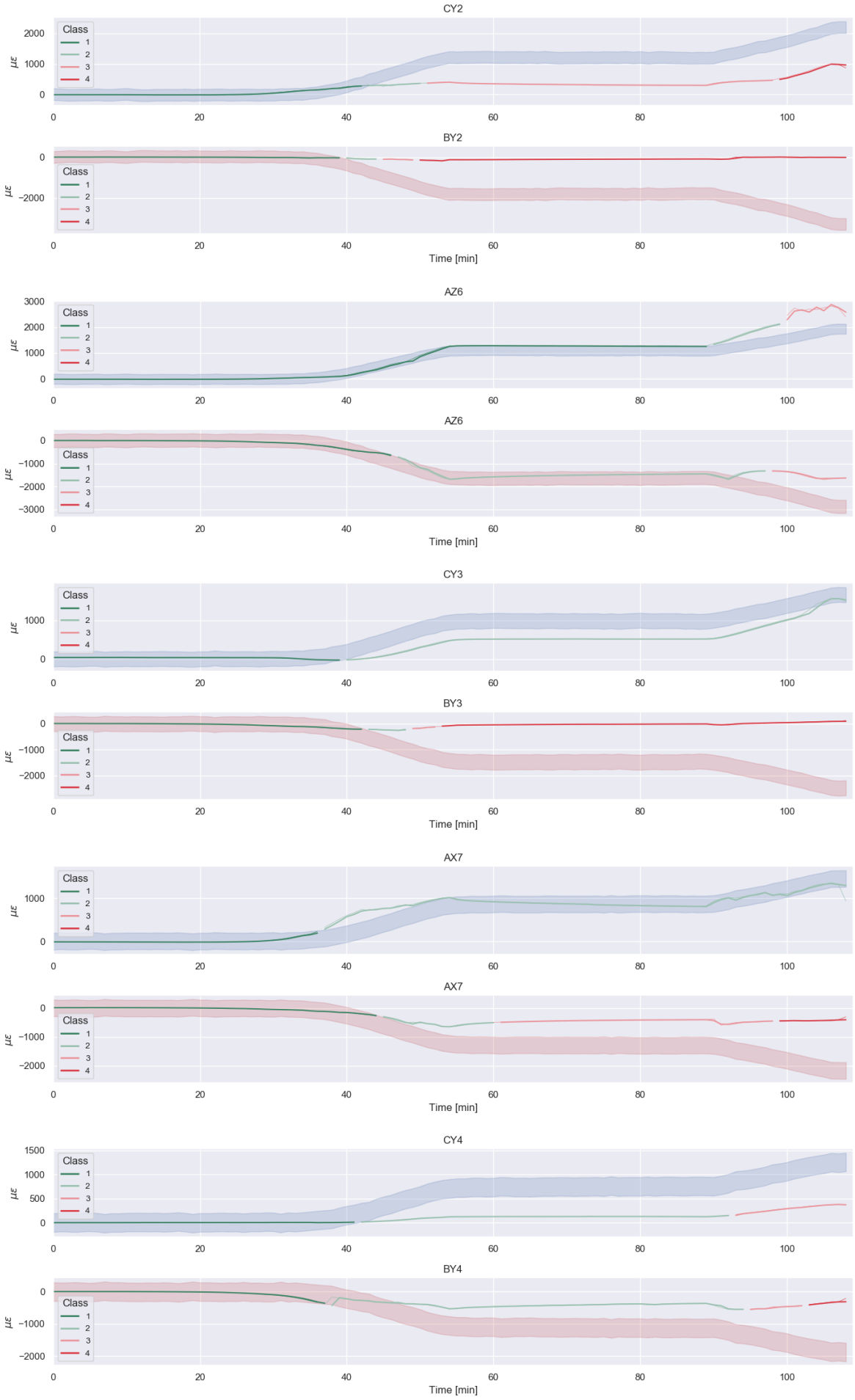
CY2
BY2
AZ6
AZ6
CY3
BY3
AX7
AX7
CY4
BY4
Class
1
2
3
4
με
Time [min]

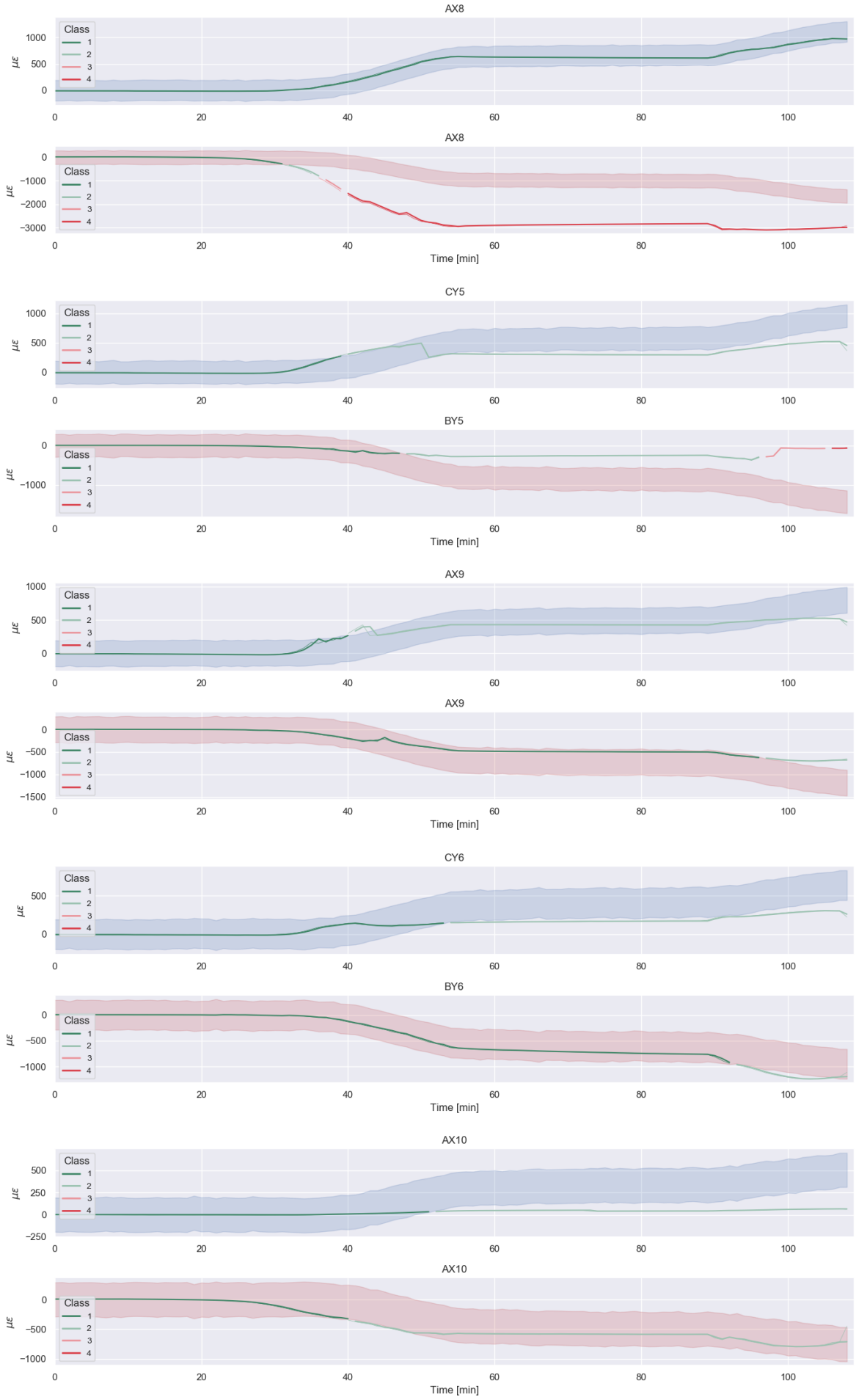
AX8
Class
1
2
3
4
με
1000
500
0
0
20
40
60
80
100
AX8
Class
με
0
−1000
−2000
−3000
Time [min]
CY5
Class
με
1000
500
0
BY5
Class
με
0
−1000
Time [min]
AX9
Class
με
1000
500
0
AX9
Class
με
0
−500
−1000
−1500
Time [min]
CY6
Class
με
500
0
BY6
Class
με
0
−500
−1000
Time [min]
AX10
Class
με
500
250
0
−250
AX10
Class
με
0
−500
−1000
Time [min]

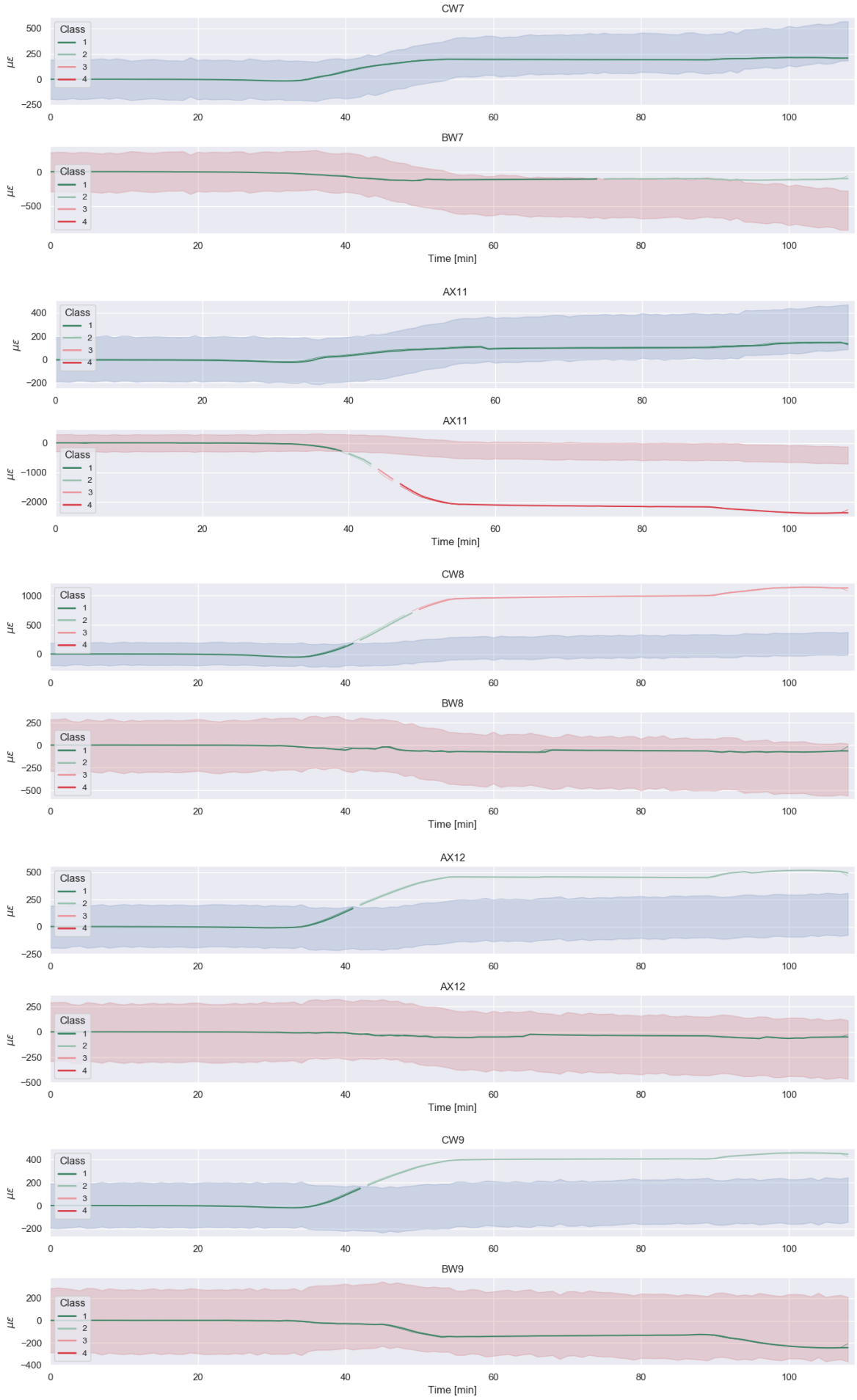
CW7
BW7
AX11
AX11
CW8
BW8
AX12
AX12
CW9
BW9
Class
1
2
3
4
με
Time [min]

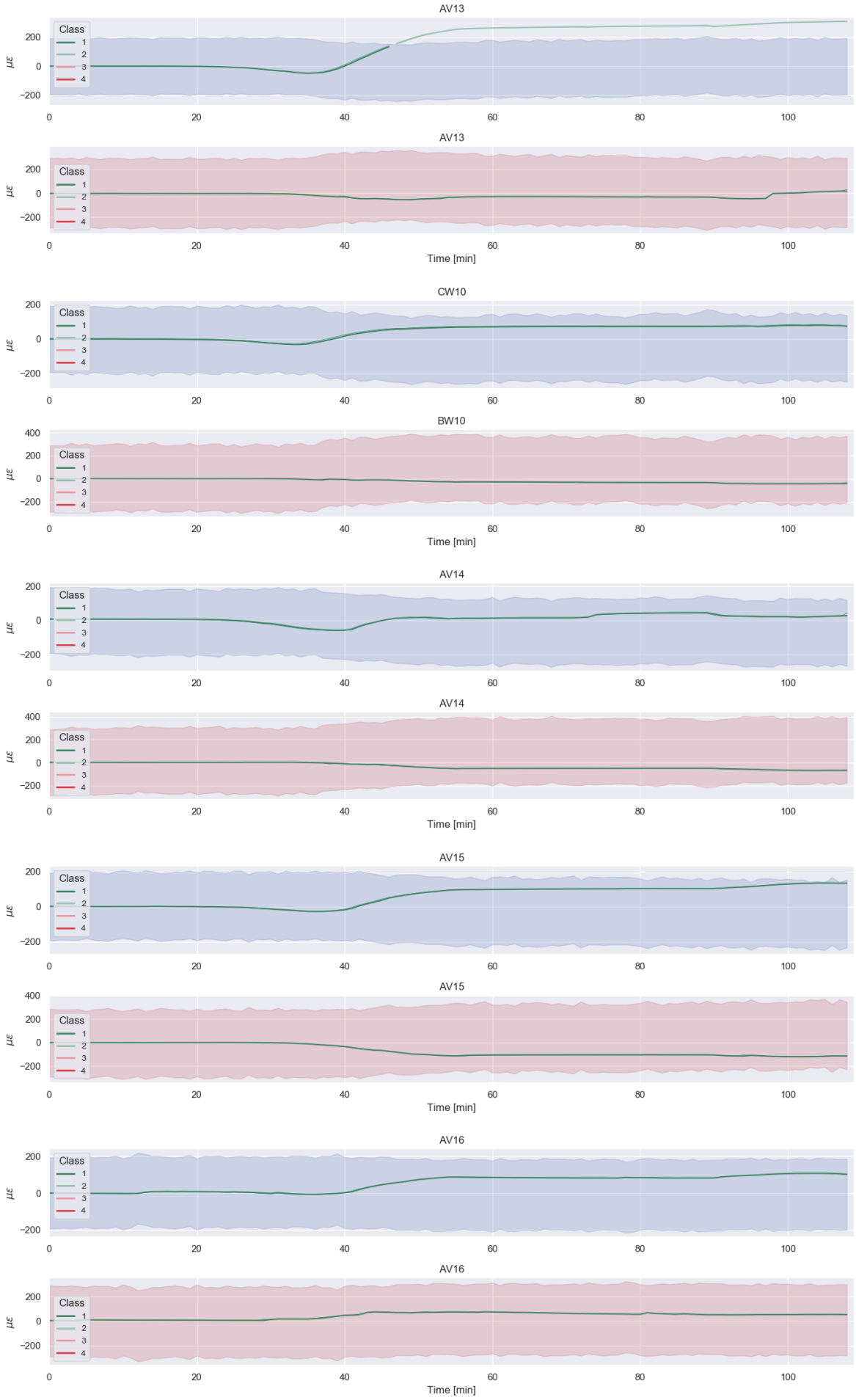
AV13
Class
1
2
3
4
με
200
0
−200
0
20
40
60
80
100
AV13
Time [min]
CW10
BW10
400
AV14
AV15
AV16

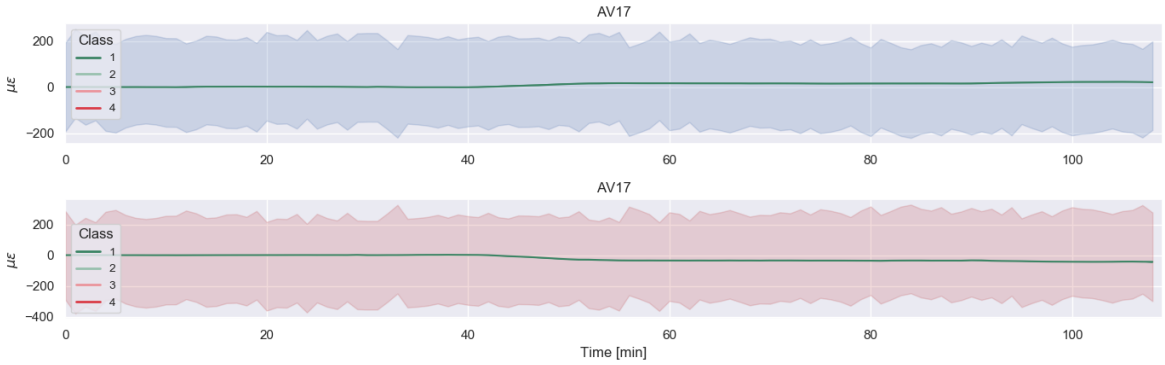
AV17
Class
1
2
3
4
200
0
−200
με
0
20
40
60
80
100
AV17
Class
1
2
3
4
200
0
−200
−400
με
0
20
40
60
80
100
Time [min]